Burning and Suppression of Solids–II (BASS–II) Summary Report

Sandra L. Olson
Glenn Research Center, Cleveland, Ohio

Paul V. Ferkul
Universities Space Research Association, Cleveland, Ohio

Subrata Bhattacharjee and Fletcher J. Miller
San Diego State University, San Diego, California

Carlos Fernandez-Pello and Shmuel Link
University of California, Berkeley, Berkeley, California

James S. T'ien
Case Western Reserve University, Cleveland, Ohio

Indrek Wichman
Michigan State University, East Lansing, Michigan

NASA STI Program . . . in Profile

Since its founding, NASA has been dedicated to the advancement of aeronautics and space science. The NASA Scientific and Technical Information (STI) Program plays a key part in helping NASA maintain this important role.

The NASA STI Program operates under the auspices of the Agency Chief Information Officer. It collects, organizes, provides for archiving, and disseminates NASA's STI. The NASA STI Program provides access to the NASA Technical Report Server—Registered (NTRS Reg) and NASA Technical Report Server— Public (NTRS) thus providing one of the largest collections of aeronautical and space science STI in the world. Results are published in both non-NASA channels and by NASA in the NASA STI Report Series, which includes the following report types:

- TECHNICAL PUBLICATION. Reports of completed research or a major significant phase of research that present the results of NASA programs and include extensive data or theoretical analysis. Includes compilations of significant scientific and technical data and information deemed to be of continuing reference value. NASA counter-part of peer-reviewed formal professional papers, but has less stringent limitations on manuscript length and extent of graphic presentations.

- TECHNICAL MEMORANDUM. Scientific and technical findings that are preliminary or of specialized interest, e.g., "quick-release" reports, working papers, and bibliographies that contain minimal annotation. Does not contain extensive analysis.

- CONTRACTOR REPORT. Scientific and technical findings by NASA-sponsored contractors and grantees.

- CONFERENCE PUBLICATION. Collected papers from scientific and technical conferences, symposia, seminars, or other meetings sponsored or co-sponsored by NASA.

- SPECIAL PUBLICATION. Scientific, technical, or historical information from NASA programs, projects, and missions, often concerned with subjects having substantial public interest.

- TECHNICAL TRANSLATION. English-language translations of foreign scientific and technical material pertinent to NASA's mission.

For more information about the NASA STI program, see the following:

- Access the NASA STI program home page at http://www.sti.nasa.gov

- E-mail your question to help@sti.nasa.gov

- Fax your question to the NASA STI Information Desk at 757-864-6500

- Telephone the NASA STI Information Desk at 757-864-9658

- Write to:
  NASA STI Program
  Mail Stop 148
  NASA Langley Research Center
  Hampton, VA 23681-2199

NASA/TM-20210011385

Burning and Suppression of Solids–II (BASS–II) Summary Report

Sandra L. Olson
Glenn Research Center, Cleveland, Ohio

Paul V. Ferkul
Universities Space Research Association, Cleveland, Ohio

Subrata Bhattacharjee and Fletcher J. Miller
San Diego State University, San Diego, California

Carlos Fernandez-Pello and Shmuel Link
University of California, Berkeley, Berkeley, California

James S. T'ien
Case Western Reserve University, Cleveland, Ohio

Indrek Wichman
Michigan State University, East Lansing, Michigan

National Aeronautics and
Space Administration

Glenn Research Center
Cleveland, Ohio 44135

October 2021

Acknowledgments

Level of Review: This material has been technically reviewed by technical management.

Available from

NASA STI Program	National Technical Information Service
Mail Stop 148	5285 Port Royal Road
NASA Langley Research Center	Springfield, VA 22161
Hampton, VA 23681-2199	703-605-6000

This report is available in electronic form at http://www.sti.nasa.gov/ and http://ntrs.nasa.gov/

Contents

Burning and Suppression of Solids—II (BASS–II)
Summary Report

Sandra L. Olson
National Aeronautics and Space Administration
Glenn Research Center
Cleveland, Ohio 44135

Paul V. Ferkul
Universities Space Research Association
Cleveland, Ohio 44135

Subrata Bhattacharjee and Fletcher J. Miller
San Diego State University
San Diego, California 92182

Carlos Fernandez-Pello and Shmuel Link
University of California, Berkeley
Berkeley, California 94720

James S. T'ien
Case Western Reserve University
Cleveland, Ohio 44106

Indrek Wichman
Michigan State University
East Lansing, Michigan 48824

Summary

The Burning and Suppression of Solids (BASS) experiment hardware is a small flow duct that provides containment for small scale burning of solid samples within the Microgravity Science Glovebox (MSG) aboard the International Space Station (ISS). A video camera with a data overlay and a 35-mm still camera record the combustion events. The controls (ignition, fan speed, etc.) are operated by an astronaut while the principal investigator team monitors the experiment from the ground and communicates directly with the astronaut. For the first time on ISS, BASS–II utilized MSG working volume dilution with gaseous N_2. We developed a perfectly stirred reactor model to determine the N_2 flow time and flow rate to obtain the desired reduced O_2 concentration in the working volume for each test. We calibrated the model with the Compound Specific Analyzer-Combustion Products (CSA-CP) O_2 readings offset using the Major Constituents Analyzer reading of the ISS ambient atmosphere data for that day. This worked out extremely well for operations, and added a new vital variable, ambient O_2 level, to our test matrices. The main variables tested in BASS–II were ambient O_2 concentration, ventilation flow velocity, and fuel type, thickness, and geometry. BASS–II also utilized the onboard CSA-CP for O_2 and CO readings, and the Carbon Dioxide Monitor for CO_2 readings before and after each test. Readings from these sensors allow us to evaluate the completeness of the combustion. The O_2 and CO_2 readings before

and after each test were analyzed and compared very well to stoichiometric ratios for a one-step gas-phase reaction. The CO versus CO_2 followed a linear trend for some datasets, but not for all the different geometries of fuel and flow tested. We calculated the heat release rates during each test from the O_2 consumption and burn times, using the constant 13.1 kJ of heat released per gram of O_2 consumed. The results showed that most of the tests had heat release rates well below 100 W. Lastly, the global equivalence ratio for the tests is estimated to be fuel rich, 1.3 on average using mass loss and O_2 consumption data.

Acronyms

1D	one dimensional
2D	two dimensional
3D	three dimensional
BASS–II	Burning and Suppression of Solids—II experiment in the MSG aboard ISS (Refs. 1 to 3)
CDM	Carbon Dioxide Monitor, sensor aboard ISS (CO_2) (Ref. 4)
CSA-CP	Compound Specific Analyzer-Combustion Products, sensor aboard ISS (O_2, CO, and others) (Refs. 5 and 6)
CSTR	continuously stirred tank reactor
DNS	direct numerical simulation
FDS	fire dynamic simulator
GMT	Greenwich Mean Time, standard time on ISS
GN_2	Gaseous nitrogen
HDPE	high-density polyethylene
HRR	heat release rate, W
ISS	International Space Station
LPM	liters per minute
MCA	Major Constituents Analyzer, a mass spectrometer-based system that measures the major atmospheric constituents on ISS, calibrated O_2 reference (Refs. 7 and 8)
MSG	Microgravity Science Glovebox, a facility aboard ISS (Ref. 9)
NCA	narrow channel apparatus
NIST	National Institute of Standards and Technology
PMMA	polymethylmethacrylate (acrylic)
RGB	red green blue
RTD	resistance thermal detector
RTDFS	Residence Time Driven Flame Spread
SDSU	San Diego State University
SIBAL	Solid Inflammability Boundary at Low Speeds
SMAC	spacecraft maximum allowable concentration

Symbols

P	pressure
R	gas constant; 82.05 cc·atm/gmol·K
T	temperature
V	volume of MSG working volume, 0.25 m^3
r	flow rate of gaseous N_2, 0.0005 m^3/min maximum, adjustable
t	time
Φ_{global}	global equivalence ratio, Equation (1.2)

1.0   Summary of Burning and Suppression of Solids—II Experiments

The first section of the report provides an overview of the experiment operations and results. Each of the five principal investigators (PIs) for Burning and Suppression of Solids—II (BASS–II), in alphabetical order, have summarized their research in separate sections of this report. Appendix A includes test matrices from each PI, Appendix B describes the dilution model and verification testing, Appendix C describes the anomalies encountered, Appendix D describes a thermal analysis, while Appendix E contains the BASS and BASS–II current papers and presentations created through the summer of 2020.

1.1   Background

BASS–II tests the hypothesis that materials in microgravity, with adequate ventilation, burn as well if not better than the same material in normal gravity with other conditions being identical (pressure, O_2 concentration, temperature, etc.). NASA tests and controls materials from a flammability perspective using an upward burning test in normal gravity, which is considered to be the worst-case geometry for flammability of the material on Earth. However, it may not be conservative for flammability in space.

One objective of the BASS–II tests is to identify what is the worst case for material flammability in spacecraft environments, and how does that compare to the terrestrial upward burning used to screen the materials for safe use aboard spacecraft.

Detailed combustion models can be validated by data obtained in the simpler flow environment in microgravity. Once validated, they can be used to build more complex combustion models needed to capture the important details of flames burning in normal gravity. These models have wide applicability to the general understanding of many terrestrial combustion problems.

The main variables tested were the effects of ambient O_2 concentration, ventilation flow velocity, and fuel type, thickness, and geometry. Many of the tests focused on finding a minimum O_2 concentration or flow velocity where a material will burn in space, to compare with the Earth-based limits. Flame growth rates are also of interest, to determine how quickly a fire in space can grow and if the flames reach a finite size or continue to grow. This has implications for firefighting strategies in spacecraft.

BASS–II utilized the gaseous nitrogen (GN_2) available on International Space Station (ISS) to vitiate the atmosphere in the Microgravity Science Glovebox (MSG) from standard ISS "air" down to the low O_2 flammability limits. BASS–II also utilized onboard O_2, CO, and CO_2 sensors to evaluate the completeness of the combustion.

A total of 126 tests were conducted as part of BASS–II. This is more than the planned 103 tests, since some samples were burned more than once. There are some samples that could be burned further, should future operational time become available.

For the first time on ISS, BASS–II utilized MSG working volume vitiation with GN_2. We developed a perfectly stirred reactor model to determine the GN_2 flow time and flow rate to obtain the desired reduced O_2 concentration in the working volume for the tests. This worked out extremely well for operations, and added a new vital variable, ambient O_2 level, to our test matrices.

1.2   Experiment Description

The MSG in the Destiny Lab of the ISS provides a contained atmosphere in which fire safety experiments can be conducted (Ref. 9). The MSG, shown in Figure 1.1, has a set of filter banks that capture particulates and convert the CO to CO_2 using an ambient temperature catalyst. The BASS–II hardware is shown inside the MSG working volume in Figure 1.1.
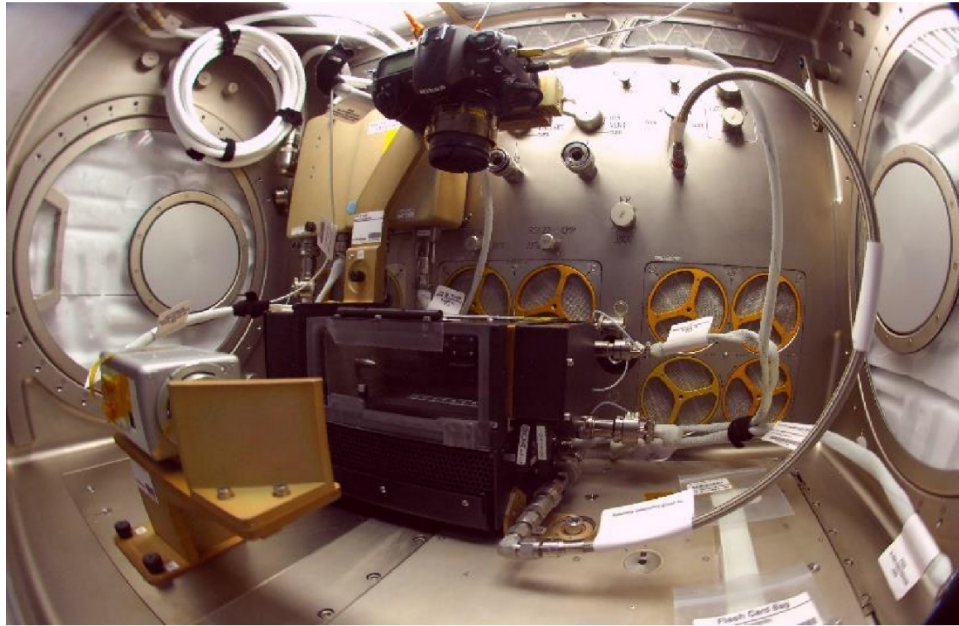
Figure 1.1.—Microgravity Science Glovebox Facility (MSG) working volume aboard the International Space Station (ISS) with the Burning and Suppression of Solids—II (BASS–II) experiment hardware installed. Working volume of MSG was diluted using ISS N_2 gas. Compound Specific Analyzer-Combustion Products (O_2 and CO) and Carbon Dioxide Monitor (CO_2) sensors were used to obtain before and after burn gas concentrations.

The BASS–II hardware consists of a flow duct, still camera, video camera, video and power boxes, external control box and associated plumbing, and mounting systems. The black anodized 7.6- by 7.6- by 17-cm rectangular flow duct with rounded corners was originally built to perform gas jet diffusion flame studies (Ref. 10). It was adapted to accommodate solid samples for the BASS experiments.

The flow was blown through the duct using a variable speed fan. Two additional flow restrictors could be used at the fan inlet to increase the pressure drop and thus reduce the flow through the duct to the desired value for the test point. With no restrictors, the maximum flow velocity was ~55 cm/s, and with two restrictors this was reduced to ~35 cm/s. The flow then passed through a honeycomb flow straightener and an inlet screen to reduce swirl. An omnidirectional spherical airspeed transducer (TSI Incorporated 8475) was positioned between the honeycomb and the screen and was used to measure the steady-state flow through the duct. The air velocity transducer probe had a response time of approximately 1 minute.

The test section was 17 cm long. Inside the test section was a nozzle for N_2 flow, a movable scale, and an Oriel® 71768 thermopile detector (Newport Corporation) with a CaFl window (spectral range of 0.13 to 11 μm) in the downstream top back corner of the duct viewing the upstream direction. The test section of the duct had two orthogonal windows; the top one was replaced for BASS to provide a mounting rail system for the solid samples. The top window was used by a Nikon D300s 12.3-megapixel digital color still camera with a 60-mm lens that provided 4,320- by 2,968-pixel images. The duct exit contained a perforated copper plate followed by a brass screen to provide heat rejection and a cold surface for soot deposition. The flow turned 90° to exit the duct, which facilitated mixing of the hot combustion gases with the cool ambient air.

The front window opened to provide access to the test section for sample and igniter change out. The front window also had interlocks for the igniter and N_2 flow. A Panasonic Corporation color video camera

WV–CP654 (760- by 480-pixel array) with a turning mirror looked in the front window. The video camera had an overlay that displayed the N_2 flow rate (cm^3/min), fan voltage (10× V), air velocity transducer reading (cm/s), and the radiometer signal. The fan voltage was calibrated with the airspeed transducer at the end of every operations day. The radiometer signal was not calibrated but provided a measure of the flame dynamics and steadiness. The external control box had controls for the fan voltage, N_2 flow rate, enable switches for the igniter and N_2 flow, and a radiometer gain level setting.

A number of sample geometries were used in BASS–II: cast polymethylmethacrylate (PMMA) samples were shaped as rods of various diameters (6.35 to 12.7 mm), thin to thick slabs (0.125 to 5 mm), or a section of a 4-cm-diameter sphere. In addition, flat cotton-fiberglass blended fabric samples were also burned. These samples could generally be mounted so that they could be burned in either the opposed or concurrent flow direction. The flat samples were 1 or 2 cm wide. The samples were manually ignited with a Kanthal® A–1 29-gauge hot-wire igniter coil with a nominal hot wire resistance of 0.8 to 1 Ω, powered by 3.5 to 3.8 amps when the astronaut manually pulled the deployment lever to move the igniter into position. Samples were burned within the duct and the combustion products exited the duct and mixed with the gas in the work volume. Example flame images are shown in Figure 1.2. Samples were returned to Earth and evaluated for mass loss.

To evaluate the levels of combustion products produced during microgravity fires, BASS–II requested the use of available onboard sensors to measure the O_2 depletion and the completeness of combustion (CO and CO_2) for microgravity combustion tests under spacecraft ventilation flow rates to provide scientific data on the stoichiometry of the diffusion flame reactions and heat release rates (HHRs). The data reported here is the first extensive data on the stoichiometry and toxicity of combustion products in microgravity.
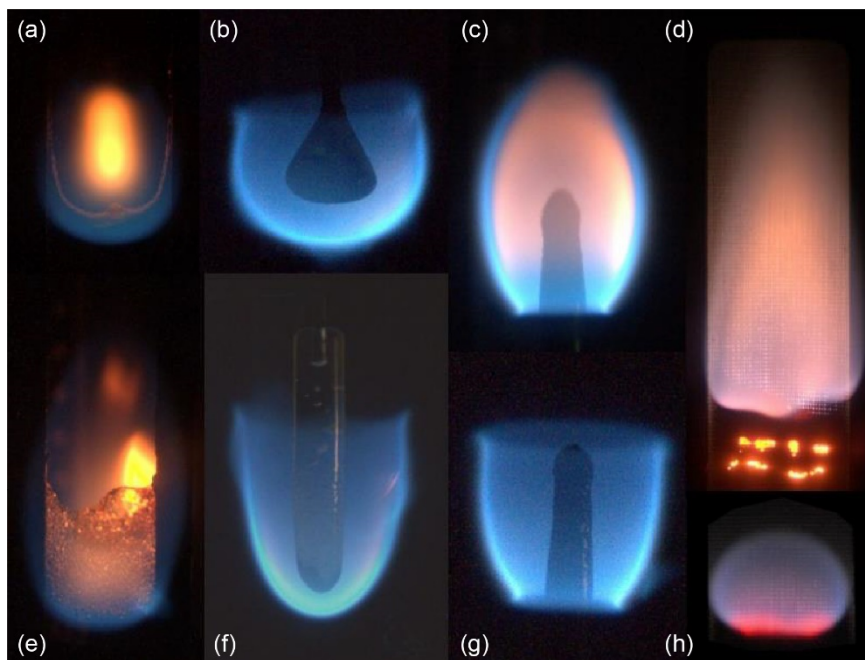
Figure 1.2.—Flame geometries tested in Burning and Suppression of Solids—II (BASS–II). Sample images from different geometries: (a) opposed thin slab, (b) spherical section, (c) opposed rod higher flow, (d) flat fabric sample at higher flow, (e) opposed thick slab, (f) concurrent rod, (g) opposed rod at low flow with open tip (similar to concurrent rod), and (h) flat fabric sample at low flow. Forced flow is up in all images.

The O_2, CO_2, and CO measurements required two portable, battery powered instruments in the working volume during testing: Carbon Dioxide Monitor (CDM), and Compound Specific Analyzer-Combustion Products (CSA-CP) (Refs. 3 to 5). The O_2 sensor (CSA-CP) is not recalibrated on orbit, so we also used the Major Constituents Analyzer (MCA) (Refs. 6 and 7) data to determine the O_2 sensor offset on a daily basis. The resolution of the O_2 sensor in the CSA-CP was 0.1 percent O_2. O_2 concentrations in the MSG working volume were varied during the testing from ambient ISS O_2 levels (~21 percent O_2) down to ~14 percent O_2 for very near limit flames. The CO sensor in the CSA-CP is zero calibrated every 60 days, with a range of 0 to 1,000 ppm and a resolution of 1 ppm. The CO_2 sensor was within its calibration window and had a range of 0 to 5 percent and a resolution of 0.1 percent by volume of CO_2. The sensor data provided initial and final conditions for repeated tests in a sealed working volume and allowed us to determine when the working volume needed to be purged. The O_2 decreased during each burn and the CO and CO_2 increased accordingly.

Many of the BASS–II tests required a diluted atmosphere, which typically took 1 to 3 h to achieve by dilution of the MSG working volume using ISS N_2 (from the hose connecting the BASS–II duct to the back wall of MSG in Figure 1.1). The N_2 was regulated with a small (<0.5 liters per minute (LPM)) MKS Instruments 179A mass flowmeter and entered the flow duct through a small nozzle just downstream of the fan. The fan in the flow duct was turned to maximum (>100 LPM) during the N_2 flow to mix and blow the gas into the working volume and circulate it continuously throughout the hours-long dilution.

1.3 Validation of Microgravity Science Glovebox Dilution—Continuously Stirred Tank Reactor Model

To utilize the capabilities of MSG to reduce the O_2 in the working volume in a controlled manner, a dilution model based on a continuously stirred tank reactor (CSTR) model was developed. In this model, the mixing in the working volume (via the BASS–II duct fan) is assumed to be "instantaneous," so that the outflow "leak" concentration from the MSG work volume to the ISS cabin is the perfectly mixed instantaneous concentration. This perfect mixing approximation is valid as long as the residence time (volume per flow rate or V/R) is at least 5 to 10 times as long as the mixing time, which is met by the 100 LPM N_2 flow rate during dilution (250 liters/100 LPM ~ 2.5 min mixing time). For the MSG volume and N_2 flow rates, the working volume residence time is $V/R = 500+$ min, and the mixing time is shorter than 50 min, so the assumption is valid. The model assumes the work volume is at constant pressure and temperature and constant volume. Thus, the leak rate out of the work volume is equal to the rate of N_2 supplied (r). The details of the model and the on-orbit validation testing using the Major Constituents Analyzer (MCA) (Ref. 11) are provided in Appendix B.

1.4 Combustion Products

Sensor readings were taken before and after each BASS–II test. The sensor data is used to measure the O_2 depletion and the completeness of combustion (CO and CO_2) for each microgravity combustion test under spacecraft ventilation flow rates.

The O_2 depletion data is compared to the CO_2 production for each BASS–II test that used PMMA as the fuel.

The PMMA stoichiometric equation is

$$C_5H_8O_2 + 6\,O_2 > 5\,CO_2 + 4\,H_2O \tag{1.1}$$

The data, taken over a wide range of initial O_2 concentrations, forced opposed or concurrent flow velocities, and using various sample geometries, is compared with this 6:5 stoichiometric ratio of O_2 to CO_2 in Figure 1.3. As shown, the data agrees very well with stoichiometric ratios for the wide range of test conditions.

Other than unburned fuel (primarily methylmethacrylate vapor), which does contain some O_2 as shown in Equation (1.4), the only other (nontrace quantity) potential species with O_2 is CO, which was also measured, as shown in Figure 1.4 to Figure 1.6. Figure 1.4 shows that the concurrent rods produced on average 550 ppm of CO for every 1 percent of CO_2. The opposed rods had a very nonlinear response, which may be indicative of a flow effect.

The longer the burn, the more CO_2 was formed, and the nominal test procedure for most samples was to turn the flow down in increments. At very low velocities, the tail region of the opposed-flow flames opened up, which presumably allowed incomplete combustion products to escape the flame zone. Interestingly, the concurrent procedure was very similar, but the concurrent flame always had an open tail, allowing incomplete combustion products to exit throughout the burn. The opposed thick slabs fall somewhere in between, producing on average 370 ppm of CO for every 1 percent of CO_2.

The one outlier point from Figure 1.3 at 2.8 percent CO_2 is not included in Figure 1.4 since the CO sensor was over-ranged for this test (>1,000 ppm full scale), so we have no quantitative value for CO for this test. During this test, the long burn of the relatively strong flame caused overheat damage to the downstream lower corner of the front window in the area where a flow duct leak was occurring. The leak was repaired on orbit, and operations proceeded without further incident.
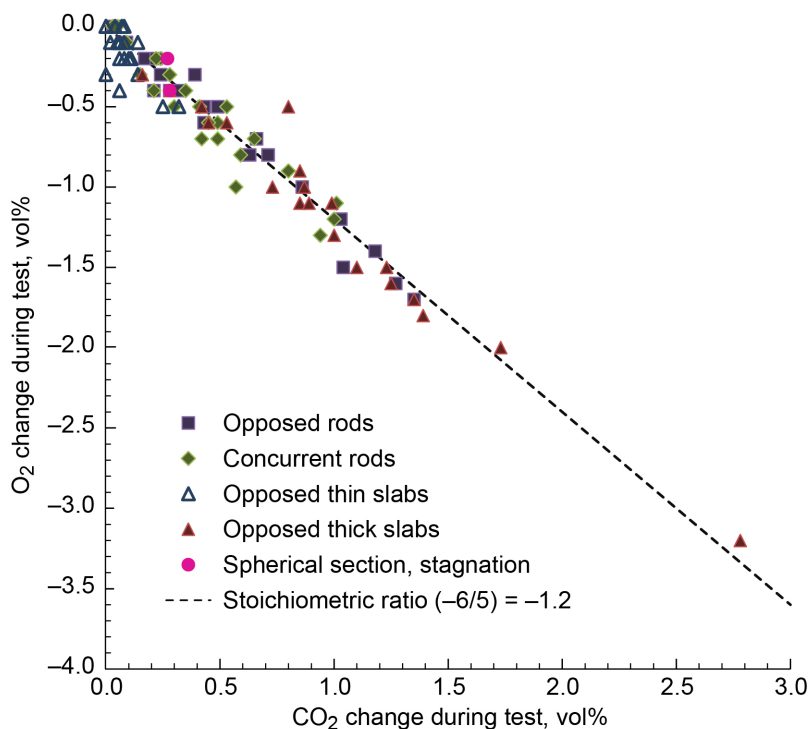
Figure 1.3.—O_2 depletion and CO_2 production during Burning and Suppression of Solids—II (BASS–II) tests with polymethylmethacrylate fuel. Data from different geometries, flows, and initial O_2 concentrations all agree with expected stoichiometric trend (shown by dashed line).
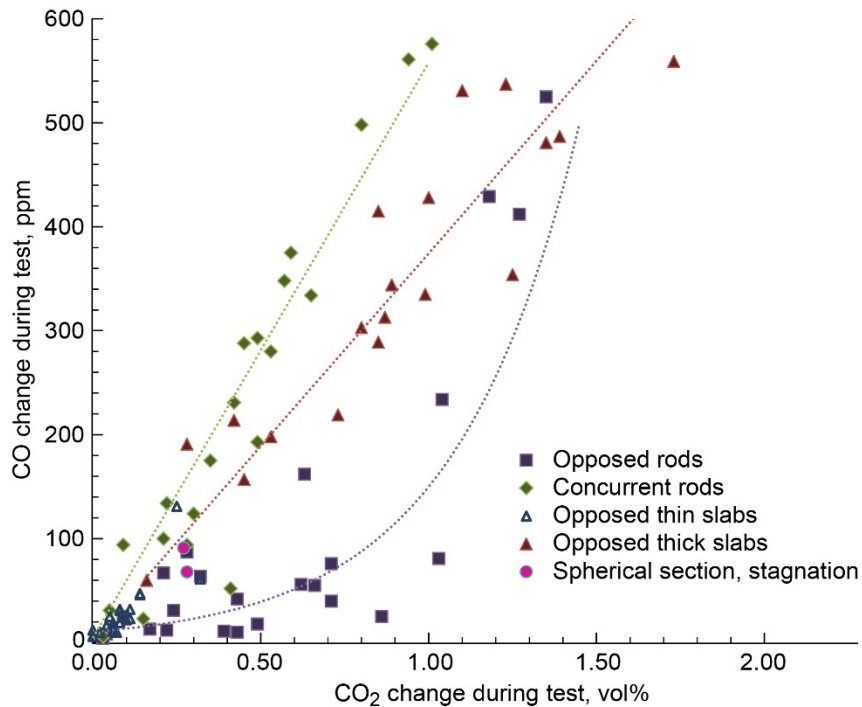
Figure 1.4.—CO generated compared to CO_2 generated in each test. CO generated appears to be clustered by geometric and flow configurations. Concurrent rod geometry produced most CO per CO_2, and opposed rods showed very nonlinear trend of CO versus CO_2 production. Thick opposed-flow slabs fell in between the two.

Of interest to the combustion community is the ratio of CO to CO_2, a measure of completeness of combustion, which is plotted in Figure 1.5 as a function of the initial O_2 concentration in the working volume. For efficiently burned flue gases (boilers, furnaces, etc.), this ratio is typically less than 0.004. As can be seen, most of our data is well above that, indicating that microgravity flames are comparatively inefficient. A similarly sized smoldering event would produce significantly more CO. On the Mir space station, a smoldering carbon bed in the Trace Contaminant Control System caused very high CO levels throughout the space station before it was detected.

Although the absolute values of CO are very high in the 250-L MSG free working volume, the MSG contained and converted the CO to CO_2 during the posttest work volume purge. Since the ISS is quite large, the combustion products from a fire of the scale of a BASS–II test would quickly be diluted, so that even within just the U.S. Lab (106-m^3 pressurized volume), the CO levels in the lab would only be 1.5 ppm, well below spacecraft maximum allowable concentration (SMAC) values for even long-term exposure (10 ppm), let alone the 1 hour SMAC of 55 ppm (Ref. 12).

Lastly, the HRRs from these small microgravity fires can be estimated using Huggett's O_2 consumption calorimetry (Ref. 13) and the burn time for each test. Using his constant of 13.1 kJ/g O_2, we estimate the HRRs to be typically well below 100 W, as shown in Figure 1.6. There is a trend of increasing HRR with increasing ambient O_2 concentration, and the scatter is attributed to the different duct flows between and even within the tests.

The one long opposed thick slab test that caused the lower downstream corner of the front window damage released close to 100 W. A prior relatively brief concurrent rod test that released almost 110 W did not cause any damage.
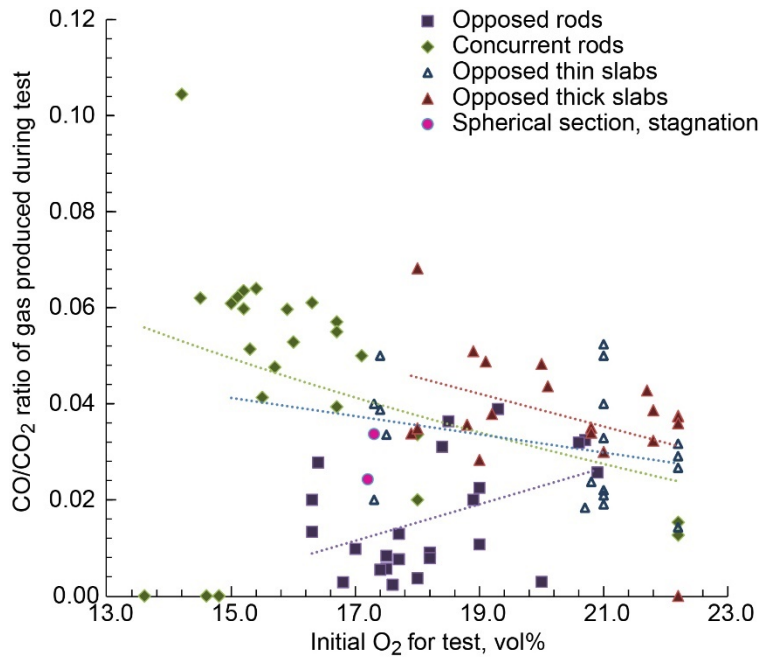
Figure 1.5.—CO to CO$_2$ ratio as function of initial O$_2$ concentration for each test. There is some clustering apparent in data, which shows that lower O$_2$ concentrations produce higher levels of CO per CO$_2$ for concurrent rods, especially when compared to opposed rods, which show opposite trend. Opposed slab data has similar trend to concurrent rod data, although scatter is large.
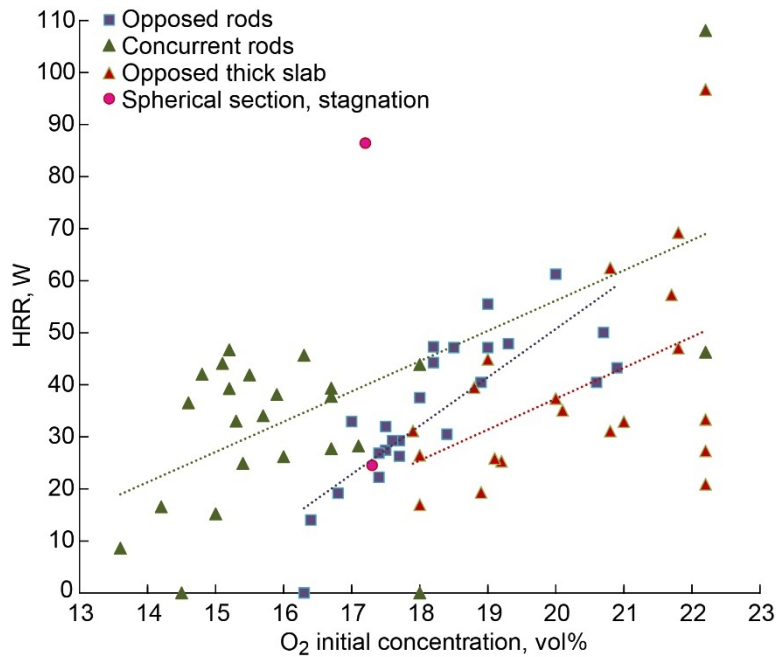
Figure 1.6.—Heat release rate (HRR) during each test using O$_2$ consumption calorimetry. Data from Figure 1.3 is converted to watts using burn time and Huggett's constant, plotted against initial O$_2$, showing HRR generally increases with increasing ambient O$_2$ concentration. Magnitude of HRR is modest for these small flames under conditions tested.
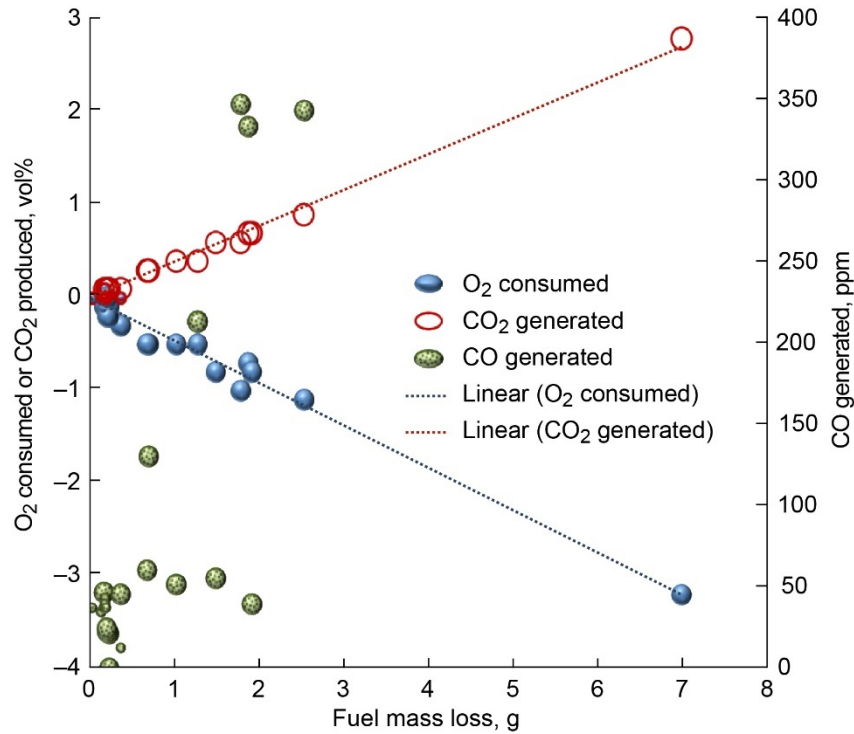
Figure 1.7.—O_2 consumed, CO_2 and CO generated per gram of fuel mass loss for two different fuels tested (cellulose (small circles) and polymethylmethacrylate (large circles)).

1.5   Global Equivalence Ratio

To date, 34 burned BASS–II samples have been returned to Earth for postflight analysis. Eight of those samples had been used for multiple tests and were altered on orbit by having their burned fuel cut off and/or their built-in igniter leads removed. As a result, the preflight and postflight weights for these modified samples cannot be used to determine the mass loss due to combustion. Also, seven additional samples had burns that were so short that no O_2 consumption was measured, so are not usable for the global equivalence ratio estimates.

For the remaining 19 samples, mass loss is compared to O_2 consumption, as shown in Figure 1.7.

There are clear trends observed for O_2 consumption and CO_2 generation relative to measured fuel mass loss. Given the previous stoichiometric relation between O_2 and CO_2, it is not surprising that the two trends mirror each other. The CO data is more scattered, but CO generation generally increases with increasing fuel mass loss and O_2 consumption. The 7-g fuel mass loss test had over 1,000 ppm of CO (above the range of the sensor).

We can evaluate the fuel to O_2 ratio based upon these test results. The global equivalence ratio Φ_{global} can be expressed for either cellulose or PMMA fuel stoichiometry as

$$\Phi_{global} = \frac{\dfrac{gmol_{fuel}}{gmol_{O_2}}}{\dfrac{1}{6}} \tag{1.2}$$

Using the ideal gas law, the free volume of the MSG $V = 250{,}000$ cc, ideal gas constant $R = 82.05$ cc·atm/gmol K, pressure $P = 1$ atm, the change of O_2 percent volume, and temperature $T = 300$ K, the gmol of O_2 consumed is calculated as

$$\text{gmol}_{O_2 \text{ consumed}} = \frac{PV}{RT} = \frac{1\left(\dfrac{\Delta O_2 \text{ vol\%}}{100}\right)250{,}000}{82.05 \cdot 300} \qquad (1.3)$$

The gmol of fuel consumed is simply:

$$\text{gmol}_{\text{fuel}} = \frac{\text{grams of fuel}}{\text{molecular weight}} \qquad (1.4)$$

Using the observed slope of 0.4582 O_2 vol% per gram of fuel, and the molecular weight for PMMA of 100 g/gmol for the majority of the data, we can use the above equations to solve for the effective equivalence ratio for the tests: $\Phi_{\text{global}} = 1.3$, which is fuel rich. So, in general, the flames were under-ventilated and did not burn all of the vaporized fuel. Some fuel ended up as soot, some as CO, and some as unburned hydrocarbons.

1.6   Overall Conclusions

As part of the Burning and Suppression of Solids—II (BASS–II) experiment, we conducted a number of tests with different geometries, flow velocities, and initial O_2 concentrations. The last variable was enabled using gaseous N_2 to dilute the working volume. To adequately characterize this dilution, we developed a continuously stirred tank reactor model and verified it against sensor readings.

Sensor data from the tests showed that the O_2 was burning nearly stoichiometrically to CO_2, and that CO levels appear to be a function of geometry and, in some cases, the flow velocity and geometry combination. The CO to CO_2 ratios for these fires are an order of magnitude higher than for efficient flue gases, indicating that these flames are not efficient. The heat release was estimated for the tests using O_2 consumption calorimetry. This showed that most of the tests released well below 100 W. In the one long test that released close to 100 W, we sustained some damage to the downstream corner of the front window, due to a leak that directed the heat from this energetic flame to that location during the prolonged burn. Using the mass loss and O_2 consumption data, the global equivalence ratio for the tests is estimated to be 1.3 on average, which indicates the flames were burning fuel rich under the low-velocity forced-flow conditions.

1.7   Acknowledgments

This work could not have been done without the intense efforts of the BASS operations team (Jay Owens, Chuck Bunnell, Tibor Lorik, and Carol Reynolds). We also want to acknowledge the ground support teams at Glenn Research Center, Johnson Space Center, and Marshall Space Flight Center (especially the Microgravity Science Glovebox team) that supported the BASS–II operations and assisted in the anomaly resolutions.

1.8   References

1. Olson, S.L., et al.: Burning and Suppression of Solids—II Fire Safety Investigation for the Microgravity Science Glovebox. Presented at the 29th Annual Meeting of the American Society for Gravitational and Space Research (ASGSR) and the 5th International Symposium on Physical Sciences in Space (ISPS), Orlando, FL, 2013.
   https://www.researchgate.net/publication/265684820_Burning_and_Suppression_of_Solids_-_II_Fire_Safety_Investigation_for_the_Microgravity_Science_Glovebox Accessed June 17, 2021.
2. National Aeronautics and Space Administration: Burning and Suppression of Solids—II. Space Station Research Explorer on NASA.gov.
   http://www.nasa.gov/mission_pages/station/research/experiments/1262.html Accessed June 16, 2021.
3. National Aeronautics and Space Administration: Burning and Suppression of Solids. Space Station Research Explorer on NASA.gov.
   http://www.nasa.gov/mission_pages/station/research/experiments/735.html Accessed June 17, 2021.
4. Limero, Thomas; Beck, Steve; and James, John T.: Evaluation of a Portable Carbon Dioxide Monitor for Use Aboard the International Space Station. SAE Technical Paper 2000–01–2433, 2000.
5. Limero, Thomas; Beck, Steve; and James, John T.: Development and Performance of the Oxygen Sensor in the CSA–CP Aboard the International Space Station. SAE Technical Paper 2004–01–2337, 2004.
6. Limero, Thomas; Beck, Steve W.; and James, John T.: The Portable Monitor for Measuring Combustion Products Aboard the International Space Station. SAE Technical Paper 2002–01–2298, 2002.
7. Steiner, G., et al.: Assessment of the Major Constituent Analyzer. SAE Technical Paper 2005–01–2893, 2005.
8. Reysa, R., et al.: International Space Station (ISS) Major Constituent Analyzer (MCA) On-Orbit Performance. SAE Technical Paper 2004–01–2546, 2004.
9. Spivey, Reggie A.; Sheredy, William A.; and Flores, Ginger: An Overview of the Microgravity Science Glovebox (MSG) Facility, and the Gravity-Dependent Phenomena Research Performed in the MSG on the International Space Station (ISS). AIAA 2008–812, 2008.
10. Dotson, K.T., et al.: Laminar Smoke Points of Coflowing Flames in Microgravity. Fire Saf. J., vol. 46, 2011, pp. 550–555.
11. Mass Constituents data from ISS, data available online at
    https://mod2.jsc.nasa.gov/di/di52/constituentmonitor/
12. National Aeronautics and Space Administration: Spacecraft Maximum Allowable Concentrations for Airborne Contaminants. JSC 20584, 1999.
13. Huggett, Clayton: Estimation of Rate of Heat Release by Means of Oxygen Consumption Measurements. Fire Mater., vol. 4, no. 2, 1980, pp. 61–65.

2.0 Individual Principal Investigator Report: Bhattacharjee

2.1 Residence Time Driven Flame Spread

The objective of the Residence Time Driven Flame Spread (RTDFS) experiment of Burning and Suppression of Solids—II (BASS–II) was to examine how thermal and species fields can diverge and lead to microgravity flame extinguishment by varying fuel thickness.

Symbols

t time, s
V_g opposed-flow velocity

2.1.1 Test Matrix

Samples were 1- and 2-cm-wide thin films of plastic (PMMA (polymethylmethacrylate)). Thicknesses were between 0.1 and 0.4 mm. The test matrix is listed in Appendix A.

2.1.2 Results

Twenty-two test points were obtained with the BASS–II experiments. The wealth of data has been catalogued at http://flame.sdsu.edu.

2.1.2.1 Extinction Velocity

Each test is started by establishing a steady flame spread in the presence of a forced flow and then reducing the flow velocity in a gradual manner, as shown in Figure 2.1. In the first test, a steady flame was established over a 100-μm sample. After the flame propagated across half the sample length at a steady spread rate of 2.2 mm/s, the flow was abruptly cut off and the flame was observed to extinguish within 2 s, as shown by the radiometer signal drop in Figure 2.2. To pin down the extinction flow velocity, a second test was done under the same conditions except the flow velocity was set at 3 cm/s and after the flame propagated about half the sample length, the flow was gradually reduced. The flame spread rate of the leading edge, as plotted in Figure 2.3, shows that the flame extinguishes at about 30 s after ignition. The fan voltage at that time indicates a flow velocity of about 1.1 cm/s. The sequence of images in Figure 2.1 shows the pathway to radiative extinction. As the flow speed is gradually reduced from about $t = 27$ s, the flame size starts shrinking and the orange color disappears and the flame becomes completely blue, most possibly because of the temperature drop brought about by radiative losses, which is enhanced by the increased residence time at low flow velocity. The signal from the radiometer, shown in Figure 2.2, is also consistent with a cooling and shrinking flame as the signal starts decreasing from right about $t = 27$ s. After $t = 30$ s, there is no visible flame and the radiometer data (Figure 2.2) indicate a sudden change in slope at that time, possibly because the radiation is emitted mostly by the sample holder with the combustion products swept away by the flow.

When tests are repeated with samples of different thicknesses, the extinction velocities are found to be about 1 cm/s for 100, 200, and 300 μm and about 1.5 cm/s for 400 μm. At all these thicknesses, the fuel can be considered thermally thin because the maximum spread rate was found to be inversely proportional to fuel thickness (Ref. 1), a hallmark of a thermally thin regime. However, it must be mentioned that there are significant uncertainties in these values as the calibration at such low velocity has high error bars. The boundary layer formed by the fuel and the tunnel walls would influence the flow velocity seen by the flame. Also, there is a time lag between when the velocity is reduced and when the reduced velocity reaches the flame. However, we assume that the time lag works the same way when the
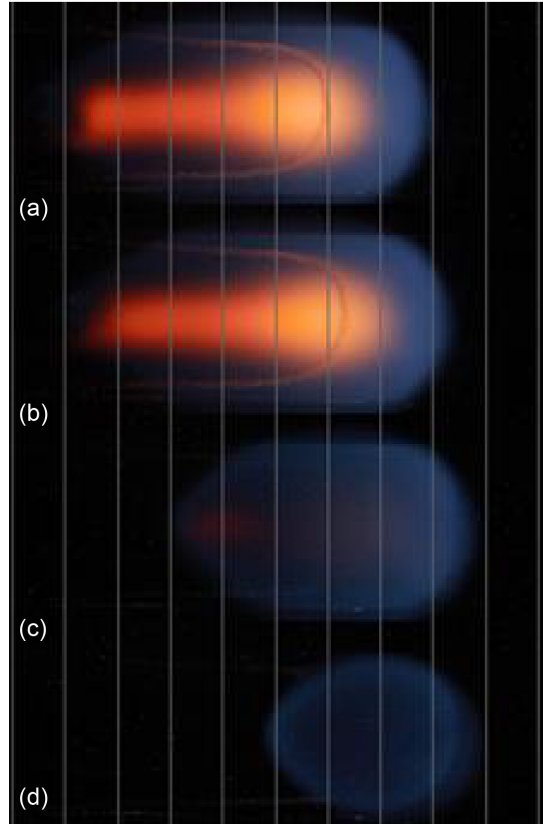
Figure 2.1.—Flame images as function of opposed-flow velocity V_g during radiative extinction. (a) Time (t) = 27 s; V_g = 3.0 cm/s. (b) t = 28 s; V_g = 1.5 cm/s. (c) t = 29 s; V_g = 1.1 cm/s. (d) t = 30 s; V_g = 1.1 cm/s.
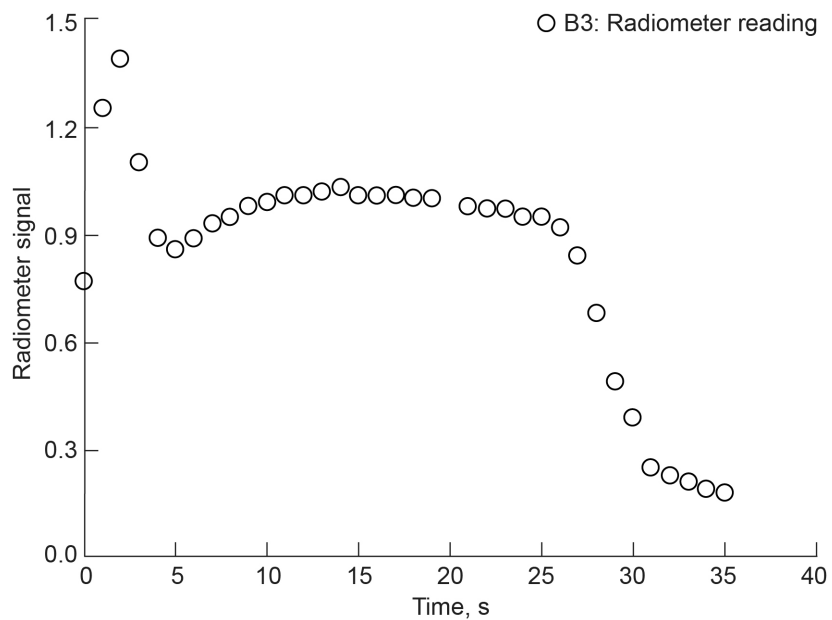
Figure 2.2.—Radiometer signal for entire duration of test. Discontinuity at time (t) = 30 s coincides with disappearance of visible flame.
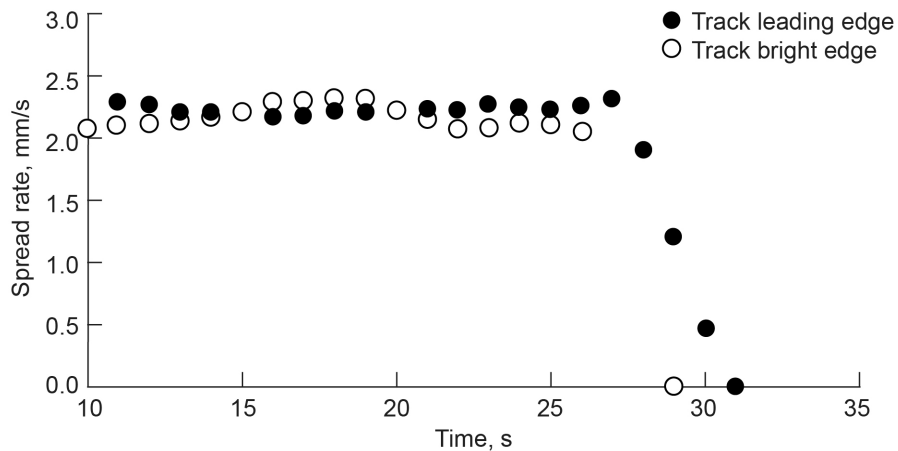
Figure 2.3.—Flame spread rate obtained by tracking leading edge and location of peak intensity.

fuel thickness is changed. When a few of these tests were repeated, the results were very similar. It can be safely concluded that the extinction velocity does not depend on the fuel thickness. Tests were also conducted at a lower O_2 level of about 16 percent for two different thicknesses and the extinction velocities were found to be about 2.6 cm/s for 100 μm and about 4 cm/s for 200 μm. It should be mentioned that the width of the sample was different, 20 mm for the 100-μm sample and 10 mm for the 200-μm sample. Even though there is insufficient data at the lower O_2 level, it is clear that the extinction velocity significantly increases as the O_2 level is reduced and is independent of the fuel thickness.

2.1.2.2 Complementary Normal-Gravity Data

RTDFS acquired further ground data from the San Diego State University (SDSU) flame stabilizer on downward flame spread over PMMA (with thickness varying from the thin to the thick regime). The results were compared with data obtained from the BASS–II experiments. A manuscript written on this comparison was published in the Fire Safety Journal. The manuscript is included in its entirety in Section 2.3.

SDSU Flame Tunnel—While the flame stabilizer is ideal for experiments with downward spreading flame (Ref. 2), it is difficult to create a forced opposed flow, given the diagnostic probes around the setup. The flame tower (Ref. 3) helps create an opposing (or concurrent) flow by moving the sample. However, given the fixed height (8 m) of the tower, the total time available is inversely proportional to the relative flow created; therefore, sufficient time is not available to study flame extinction due to blowoff.

The SDSU vertical flame tunnel (see Figure 2.4) has a cross section of 10 by 10 cm, similar to the combustion tunnel used by Hirano (Ref. 4) at the test section and an opposed flow up to 100 cm/s can be created by an array of fans controlled by a microcontroller. Two resistance thermal detectors (RTDs), one actively heated and one used as reference, are placed right below the sample holder to monitor the flow velocity. The RTDs were calibrated using the flame tower, where the velocity probe can be traversed in stationary air at any prescribed velocity.

One of the major improvements made to the tunnel is the ability to rotate it and set it at any desired angle (see Figure 2.5).

We have collected data for both cellulosic fuels and PMMA sheets.

Figure 2.4.—San Diego State University
flame tunnel has same dimensions as
Hirano tunnel.
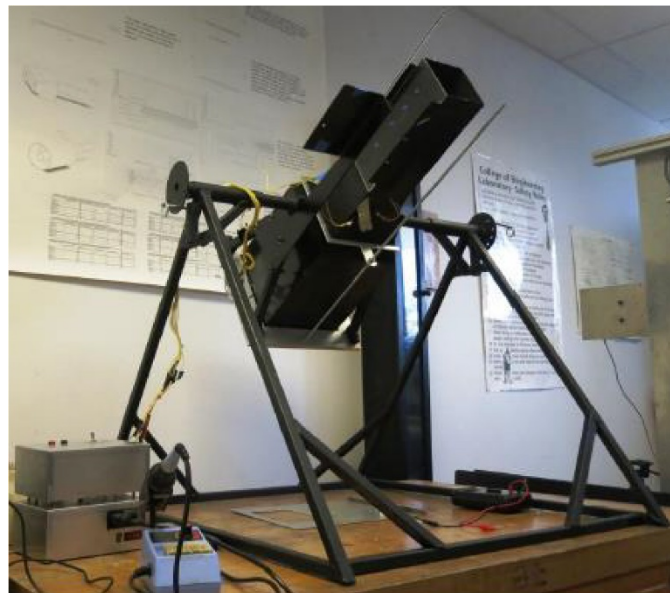
Figure 2.5.—San Diego State University flame tunnel can be
turned to different angles to alter effect of buoyancy-
induced flow.

To establish the boundary layer effect on flame spread rate, experiments were carried out with ashless filter paper with the opposing flow velocity as the control variable. While the blowoff extinction velocity is assumed to be only a function of chemical kinetics, these experiments clearly establish the boundary layer development as an important parameter. The experiments are quite repeatable, and a correlation has been obtained for cellulosic fuel.

2.1.3   Concluding Remarks

The Residence Time Driven Flame Spread (RTDFS) experiment of Burning and Suppression of Solids—II (BASS–II) resulted in the publication of two archival journal articles, several conference papers, and two manuscripts submitted to the 36th International Symposium on Combustion. RTDFS vindicated the theoretical and computational findings that the critical opposed-flow velocity at which radiative extinction occurs in a microgravity environment is independent of fuel thickness, the manuscript published in Combustion and Flame is included in its entirety in Section 2.2.

2.1.4   References

1. Fernandez-Pello, A.C.; and Hirano, T.: Controlling Mechanisms of Flame Spread. Combust. Sci. Technol., vol. 32, nos. 1–4, 1983, pp. 1–31.
2. Bhattacharjee, Subrata, et al.: A Novel Apparatus for Flame Spread Study. Proc. Combust. Inst., vol. 34, no. 2, 2013, pp. 2513–2521.
3. Paolini, Christopher, et al.: Flame Tower: A Novel Apparatus to Study Flame Spread at Low Concurrent or Opposed Flow Velocity. Presented at the 8th U.S. National Combustion Meeting, paper 070FR–0141, 2013. https://sutherland.che.utah.edu/USCI2013/PAPERS/2H04-070FR-0141.pdf Accessed June 18, 2021.
4. Hirano, T.: Flame Spread. Fire Safety Science. Proceeding, 5th AOSFST, Newcastle, Australia, 2001, pp. 40–54.

2.1.5   Publications Resulting from This Work

Journal Articles

- Bhattacharjee, S., et al.: Opposed-Flow Flame Spread: A Comparison of Microgravity and Normal Gravity Experiments to Establish the Thermal Regime. Fire Saf. J., vol. 79, 2016, pp. 111–118. DOI: 10.1016/j.firesaf.2015.11.011 Accessed June 18, 2021.
- Bhattacharjee, S., et al.: The Critical Flow Velocity for Radiative Extinction in Opposed-Flow Flame Spread in a Microgravity Environment: A Comparison of Experimental, Computational, and Theoretical Results. Combust. Flame, vol. 163, 2016, pp. 472–477. DOI: 10.1016/j.combustflame.2015.10.023 Accessed June 18, 2021.

Conference Articles and Presentations

- Bhattacharjee, S., et al.: The Critical Flow Velocity for Radiative Extinction in Opposed-Flow Flame Spread in a Microgravity Environment: A Comparison of Experimental, Computational, and Theoretical Results. Presented at the 9th Mediterranean Combustion Symposium, Rhodes, Greece, 2015.
- Olson, Sandra L., et al.: Results From On-Board CSA–CP and CDM Sensor Readings During the Burning and Suppression of Solids—II (BASS–II) Experiment in the Microgravity Science Glovebox (MSG). ICES–2015–196, 2015.
- Bhattacharjee, S.; and Carmignani, L.I.: The Effect of Boundary Layer on Blow-Off Extinction in Opposed-Flow Flame Spread: Results of Experiments and Simplified Analysis. ATEM'15:

International Conference on Advanced Technology in Experimental Mechanics 2015, Toyohashi, Japan, 2015.

- Bhattacharjee, S.; Simsek, A.; and Ivisic, I.: The Role of Fuel Thickness in Opposed-Flow Flame Spread in a Quiescent Microgravity Environment. Western States Section (WSS) Technical Meeting of the Combustion Institute, Provo, UT, 2015.
- Grayson, L.; Kievens, K.; and Bhattacharjee, S.: Measurement of Thermal Radiation in Stabilized Downward Spreading Flame. Western States Section (WSS) Technical Meeting of the Combustion Institute, Provo, UT, 2015.
- Simsek, A.; and Bhattacharjee, S.: Effect of Boundary Layer on Blow-Off Extinction in Opposed-Flow Flame Spread: A Computational Study. Presented at the 9th So Cal Fluids Symposium, San Diego, CA, 2015.
- Laue, M.; Ivisich, I.; and Bhattacharjee, S.: A Comparison of Radiation Signature From Spreading Flames in Normal and Zero Gravity Environment. Presented at the 8th Annual Student Research Symposium, San Diego, CA, 2015.
- Bhattacharjee, S., et al.: Opposed-Flow Flame Spread: A Comparison of Microgravity and Normal Gravity Experiments Establishing the Thermal Regime. Presented at the 8th International Symposium for Physical Sciences in Space, Alexandria, VA, 2015.

2.2 Critical Flow Velocity for Radiative Extinction in Opposed-Flow Flame Spread in Microgravity Environment: Comparison of Experimental, Computational, and Theoretical Results[1]

2.2.1 Abstract

The effect of opposing flow on flame spread rate over thin solid fuel is investigated with the help of scaling theory, a comprehensive computational model, and experiments conducted aboard the International Space Station. While spread rate over thin fuels is independent of the opposing flow velocity in the thermal regime, in the microgravity regime, where the opposing flow can be very mild or even completely absent in the absence of buoyancy-induced flow, the spread rate is known to decrease as the opposed flow is reduced. Under certain conditions, this can lead to flame extinguishment at a low enough flow velocity. This report combines scaling arguments with computational results to predict a critical flow velocity for such flame extinction. Results from the recently conducted limited number of space-based tests, presented in this report, seem to confirm the prediction validating the closed-form formula for the critical extinction velocity.

Symbols

c	specific heat at constant pressure, kJ/kg·K
F	de Ris flame coefficient
L	length scale, m
T	temperature, K
t	time, s
V_f	absolute spread rate
V_g	opposed-flow velocity
V_r	velocity relative to the flame, $V_r = V_g + V_f$
W	width
α_g	thermal diffusivity of gas, evaluated at T_v, m²/s
ε	surface emissivity
λ_g	gas-phase conductivity evaluated at T_v, kW/m·K
η_f	nondimensional spread rate
η_g	nondimensional flow velocity
ρ_g	gas density evaluated at T_v, kg/m³
ρ_s	solid density, kg/m³
τ	fuel half-thickness, m
σ	Stefan-Boltzmann constant, kW/(m²K⁴)
$\Re_0$	nondimensional radiation number

Subscripts

cr   critical
f   adiabatic flame
g   gas phase
radiative
res residence
s   solid phase
thermal
v   vaporization
x, y coordinates
∞   ambient

2.2.2   Introduction

Opposed-flow flame spread over thermally thin fuels is one of the most fundamental topics in the study of fire spread. The physics of flame spread is considerably simplified in this configuration because the flame spreads steadily and the fuel can be assumed to be uniformly heated across its thickness. Moreover, in the thermal regime, gas-phase and pyrolysis chemistry can be considered infinitely fast compared to the resident time $t_{res} \approx L_g / V_g \approx \alpha_g / V_g^2$, the time spent by the oxidizer as it passes through the length $L_g \approx \alpha_g / V_g$ of the flame leading edge for thermal diffusivity α_g, producing a simplified closed-form expression for the thermal limit (Refs. 1 and 2) of the flame spread rate. The spread rate is independent of flow velocity V_g, inversely proportional to the fuel thickness, and directly proportional to a nondimensional coefficient known as the de Ris coefficient $F = (T_f - T_v)/(T_v - T_\infty)$, where T_f is the adiabatic flame temperature, T_v is the fuel vaporization temperature, and T_∞ is the ambient and virgin fuel temperature. As the opposed-flow velocity is increased, the residence time being inversely proportional to the square of velocity, finite-rate kinetics in the gas phase becomes important leading ultimately to the blowoff extinction. This kinetic regime has been experimentally (Ref. 3) and computationally (Ref. 4) studied and the spread rate, normalized by its thermal limit, has been correlated to the nondimensional Damköhler number, the ratio of the chemical and residence time. The downward spread in a quiescent 1g environment can be considered a special case of opposed-flow flame spread with buoyancy-induced flow providing the opposing flow velocity (Ref. 5).

In a microgravity environment, the opposing flow can be very mild and even completely absent in the perfectly quiescent situation of zero gravity. Numerical (Refs. 6 and 7) and experimental (Refs. 8 and 9) studies have established the radiative regime in the mild opposed-flow environment in which the flame spread rate decreases as the opposed-flow velocity is reduced leading to flame extinguishment (Ref. 10) if the flow velocity is sufficiently low. This result is also dependent on other ambient conditions as steady spread over thin fuels in a perfectly quiescent environment has been established at higher O_2 levels (Ref. 11). The critical velocity, defined as the opposed-flow velocity below which steady spread rate is not observed in a microgravity environment, has been shown to depend on O_2 level, but its dependence on other parameters such as fuel thickness are still not well known. There is no closed-form formula, verified by experimental results that can be used to predict the critical velocity.

In this work, recent experimental work for flame spread over thin sheets of polymethylmethacrylate (PMMA) performed in the International Space Station (ISS) is reported. The experimental results are analyzed to determine the critical velocity for different fuel thicknesses and ambient O_2 levels. The results are compared with predictions from a simplified analysis and computational results from a two-

dimensional (2D) steady-state flame spread model. A predictive formula for the critical velocity is proposed in this work.

2.2.3   Experimental Setup

The Burning and Suppression of Solids—II (BASS–II) apparatus (Ref. 12) in the ISS is depicted in Figure 2.6. It is a combustion tunnel, a 76-mm square duct, where the PMMA fuel samples, 20 mm wide and about 95 mm long with the thickness ranging from 100 to 400 µm, are burned in an opposed-flow configuration. A fan forces a flow of an O_2-N_2 mixture through flow straighteners from the right to the left and the sample is ignited at the left end. Depending on the flow velocity and O_2 concentration, a steady flame is established that spreads from the left end of the sample towards the right end. The O_2 level can be adjusted to 21 percent or below and the flow velocity can range from 0 to 50 cm/s. A hot wire anemometer is used to calibrate the flow velocity with fan voltage, which is used to determine the flow velocity.

Experiments were conducted in the Microgravity Science Glovebox of the ISS by two crew members. Operation instructions were communicated from NASA Glenn Operations Center in realtime as the experiment progressed. Each test starts by creating a desired opposing flow by adjusting the fan voltage. After the flow stabilizes, the igniter is turned on until a visible flame is observed. The igniter is then turned off and the flame is photographed with a high-resolution digital still camera with a frame rate of 1 per second. A radiometer is used to confirm flame extinction when the visible flame goes out. In some of the tests, the flow velocity is changed during the spread to maximize the test matrix without having to burn additional samples.
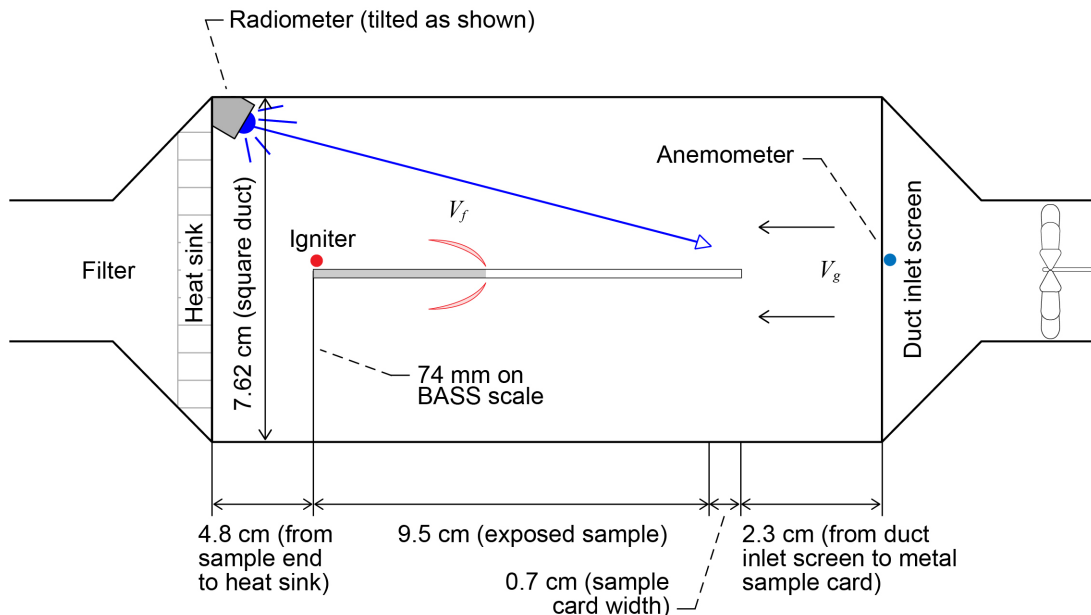
Figure 2.6.—Schematic of Burning and Suppression of Solids—II (BASS–II) combustion tunnel. Absolute spread rate (V_f). Opposed-flow velocity (V_g).

2.2.4   Data Analysis

An image processing application that is based on MATLAB® (The MathWorks, Inc.) has been developed at San Diego State University to obtain flame spread rate and other information from the sequence of top-view digital photographs. A typical color image of the top view 10 s after ignition is shown in Figure 2.7(a) for flame spread over 100-µm-thick PMMA sheet for the ambient conditions of 20.7 percent O_2, 1 atm, and an opposed-flow velocity of 2.5 cm/s. The dots along the axis, 6 mm apart, are superimposed on the image to help display the spatial resolution of the image. The ignition wire, glowing red at x = 36 mm, and the burnout location, the black line at x = 42 mm are visible in this picture. To eliminate the effect of edge propagation, the central part of the flame, bracketed between the two white lines parallel to the axis and about 14 mm apart, is isolated. The red green blue (RGB) values of each pixel of the central slice are then converted to an intensity value using built-in MATLAB® tools. Across the width of the section, these intensity values are averaged, producing a 2D representation of the flame as shown in Figure 2.7(b). The variation of the width-averaged intensity along the x direction (axis) is shown in Figure 2.7(c). The leading edge of the flame is determined by locating a fixed threshold intensity. A value of 30 for the threshold value was found to work well for tracking the flame leading edge for almost all the tests. The location of the maximum intensity is identified by finding the maxima of the intensity curve (Figure 2.7(c)).

A number of consecutive locations are used to obtain the flame spread rate by finding the slope of the linear regression analysis. The uncertainty in the spread rate calculations through this method depends on the sample size, but five consecutive locations have been found to be a good compromise between noise and temporal precision. Spread rates obtained by tracking the leading edge and bright edge (the maximum intensity location) are shown in Figure 2.8. The result has been found to be reproducible within 5 percent uncertainty regardless of how the flame movement is tracked.
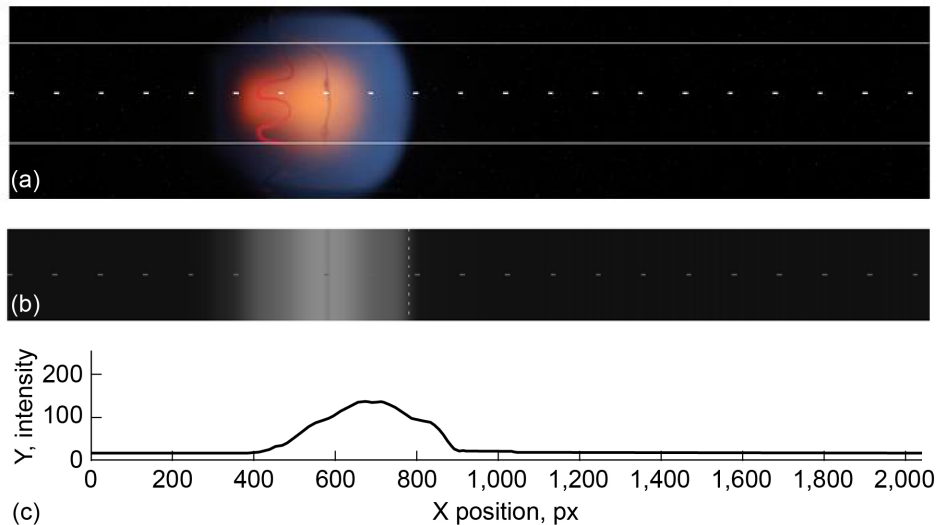
Figure 2.7.—Image processing of top view. (a) Color image. (b) Image averaged over central section between white lines. (c) Variation of intensity along dotted line. Leading edge is located at x = 887 pixel for a threshold intensity of 30.
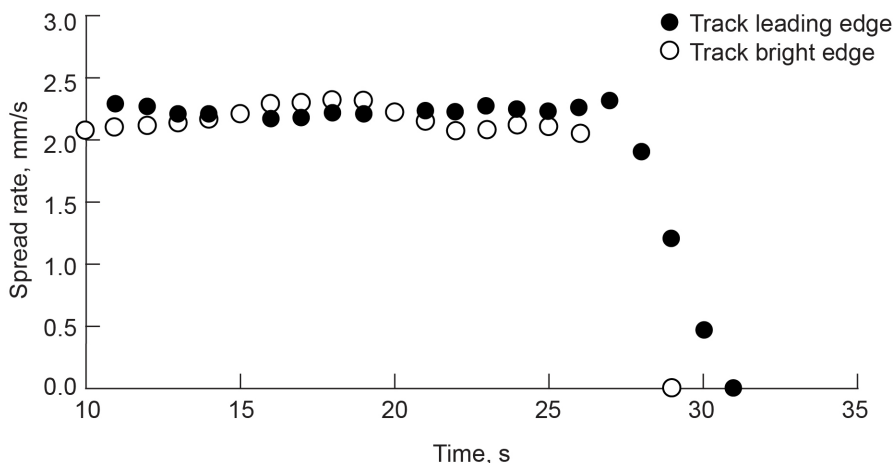
Figure 2.8.—Flame spread rate obtained by tracking leading edge and location of peak intensity.

2.2.5 Extinction Velocity

Each test is started by establishing a steady flame spread in the presence of a forced flow and then reducing the flow velocity in a gradual manner. In the first test, a steady flame was established over a 100-μm sample. After the flame propagated across half the sample length at a steady spread rate of 2.2 mm/s, the flow was abruptly cut off and the flame was observed to extinguish within 2 s. To pin down the extinction flow velocity, a second test was done under the same conditions except the flow velocity was set at 3 cm/s and after the flame propagated about half the sample length, the flow was gradually reduced. The flame spread rate of the leading edge, as plotted in Figure 2.8, shows that the flame extinguishes at about 30 s after ignition. The fan voltage at that time indicates a flow velocity of about 1.1 cm/s. The sequence of images in Figure 2.9 shows the pathway to radiative extinction. As the flow speed is gradually reduced from about $t = 27$ s, the flame size starts shrinking and the orange color disappears and the flame becomes completely blue, most possibly because of the temperature drop brought about by radiative losses, which is enhanced by the increased residence time at low flow velocity. The signal from the radiometer, shown in Figure 2.10, is also consistent with a cooling and shrinking flame as the signal starts decreasing from right about $t = 27$ s. After $t = 30$ s, there is no visible flame and the radiometer data (Figure 2.10) indicate a sudden change in slope at that time, possibly because the radiation is emitted mostly by the sample holder with the combustion products swept away by the flow.

When tests are repeated with samples of different thicknesses, the extinction velocities are found to be about 1 cm/s for 100, 200, and 300 μm and about 1.5 cm/s for 400 μm. At all these thicknesses, the fuel can be considered thermally thin because the maximum spread rate was found to be inversely proportional to fuel thickness (Ref. 13), a hallmark of thermally thin regime. However, it must be mentioned that there are significant uncertainties in these values as the calibration at such low velocity has high error bars. The boundary layer formed by the fuel and the tunnel walls would influence the flow velocity seen by the flame. Also, there is a time lag between when the velocity is reduced and when the reduced velocity reaches the flame. However, we assume that the time lag works the same way when the fuel thickness is changed. When a few of these tests were repeated, the results were very similar. It can be safely concluded that the extinction velocity does not depend on the fuel thickness. Tests were also conducted at a lower O_2 level of about 16 percent for two different thicknesses and the extinction
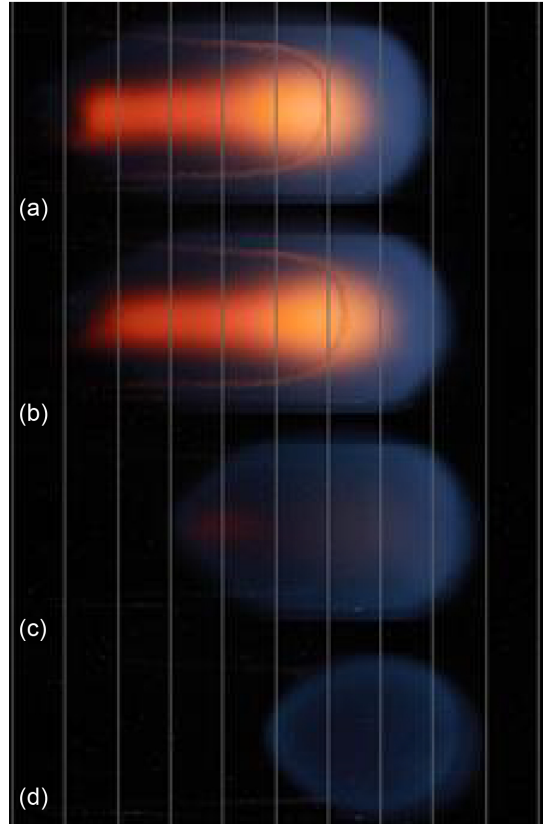
Figure 2.9.—Flame images as function of opposed-flow velocity (V_g) during radiative extinction. (a) Time (t) = 27 s; V_g = 3.0 cm/s. (b) t = 28 s; V_g = 1.5 cm/s. (c) t = 29 s; V_g = 1.1 cm/s. (d) t = 30 s; V_g = 1.1 cm/s.
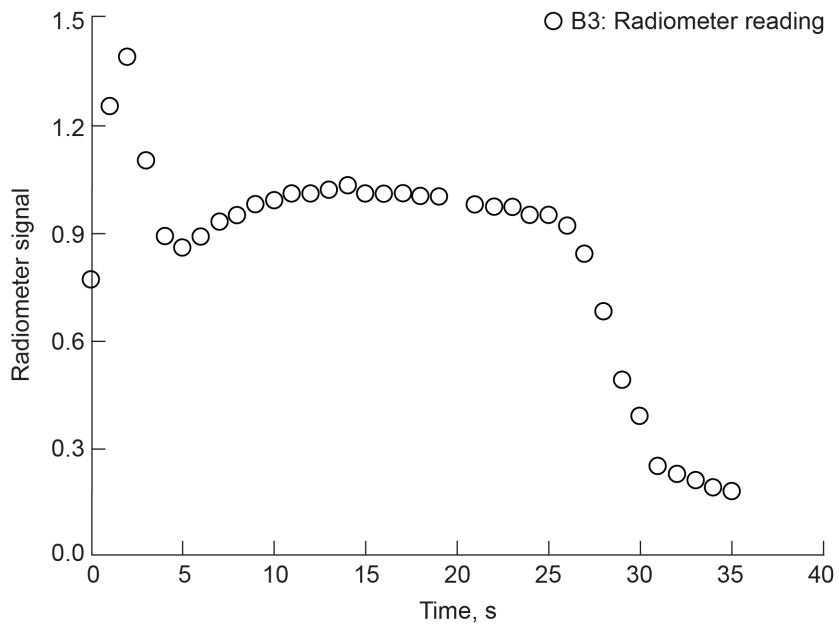
Figure 2.10.—Radiometer signal for entire duration of test. Discontinuity at time t = 30 s coincides with disappearance of visible flame.

velocities are found to be about 2.6 cm/s for 100 μm and about 4 cm/s for 200 μm. It should be mentioned that the width of the sample was different, 20 mm for the 100-μm sample and 10 mm for the 200-μm sample. Even though there is insufficient data at the lower O_2 level, it is clear that the extinction velocity significantly increases as the O_2 level is reduced and is independent of the fuel thickness.

2.2.6 Computational Results

The mathematical model consists of the 2D, steady, elliptic, partial differential equations describing conservation of energy, species mass, total mass, and momentum in the gas phase and ordinary differential equations for the conservation of mass and energy in the solid phase. In the numerical model, the gas and solid phases, coupled through interface conditions, are solved sequentially using the SIMPLER algorithm (Ref. 14). A single-step global reaction with second-order kinetics in the gas phase and a first-order pyrolysis kinetics is used in modeling fuel vaporization. Details of the model, including the properties used, can be found elsewhere (Ref. 15), but the model has been validated by reproducing (Ref. 4) several analytical solutions including Emmons problem and de Ris solution for thin and thick fuels.

The global-balance radiation model (Ref. 6) is used for modeling gas and surface radiation. While the computational fluids dynamics solution is 2D, the radiation model calculates the Planck mean absorption coefficient, used in calculating the radiative source term, by equating the thin-gas expression for radiative losses from the entire computational domain to three-dimensional radiative loss from the domain, accurately calculated using a narrow band model (Ref. 16). The radiation calculation (Ref. 17) accounts for losses due to the finite width of the sample.

A large set of computations is carried out by varying opposed-flow velocity and fuel thicknesses for the ambient conditions of 21/79 (percent by volume) mixture of O_2 and N_2 at 1 atm pressure. The resulting spread rates are shown in Figure 2.11. At relatively large values of the opposed-flow velocity V_g, the spread rate V_f can be seen to be relatively independent of the opposing flow velocity and inversely proportional to the fuel thickness as predicted by the thermal theory (Ref. 1). However, as V_g is reduced, V_f decreases, leading to flame extinguishment that is seen in the experiments. Moreover, the extinction velocity is identical at 1.5 cm/s for all the four thicknesses studied. This finding has been ascertained by making sure that the results are independent of grid density and the computational domain. The computational results also reproduce the experimental trend of the increase of the extinction velocity at
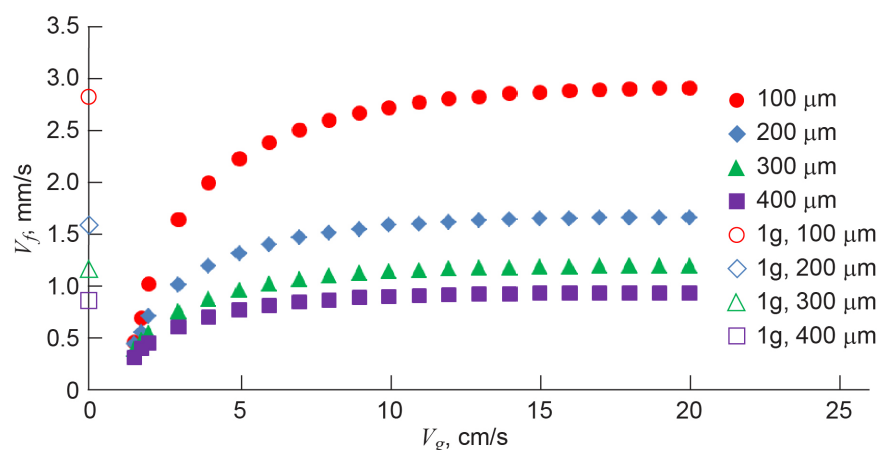
Figure 2.11.—Computational spread rate for flame spread over thin polymethylmethacrylate. Although spread rate can be seen to be function of fuel thickness, extinction velocity is same at 1.5 cm/s for each thickness. Spread rates for downward spread configuration are indicated by empty symbols. Absolute spread rate (V_f). Opposed-flow velocity (V_g).
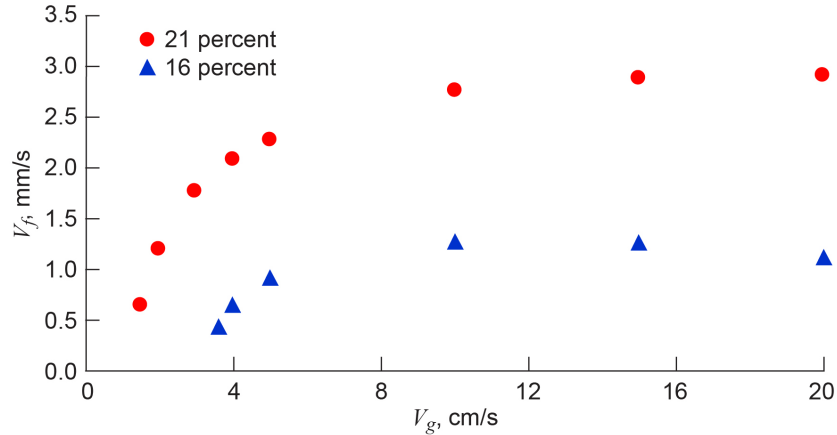
Figure 2.12.—Computational spread rate for flame spread over 100-μm-thick sheet of polymethylmethacrylate at two different O_2 levels. Extinction velocity increases from 1.5 cm/s at 21 percent O_2 to 3.5 cm/s at 16 percent, closely matching experimental results.

lower O_2 levels. For flame spread over 100-μm-thick sheet of PMMA, the calculations were repeated at a lower O_2 level of 16 percent and the two sets of spread rates are compared in Figure 2.12. At a lower O_2 level, the spread rate can be seen to significantly lower and the kinetic effect sets in early for V_g greater than 16 cm/s. The extinction velocity is found to be 3.5 cm/s as opposed to 1.5 cm/s at 21 percent O_2. This is consistent with the experimental finding discussed in the previous section.

It should be mentioned that when the computational model is used (Ref. 15) for downward spread configuration in a quiescent 1g environment, a steady spread results for 21 percent O_2 with spread rates of 2.8, 1.6, 1.2, and 0.9 mm/s, for 100, 200, 300 and 400 μm, respectively, as shown in Figure 2.11. At 16 percent O_2, however, the buoyancy-created flow is strong enough to cause blowoff extinction.

2.2.7   Scale Analysis: Expression for Extinction Velocity $V_{g,cr}$

In a microgravity environment, an opposing flow can be quite mild or even absent, raising the residence time to the point that both gas and surface radiation can become significant compared to other heat transfer mechanisms. Numerical studies (Refs. 6 and 7) have shown that both gas and surface radiation primarily act as a loss mechanism, depressing the flame temperature. As V_g decreases, the radiative loss effect intensifies and V_f, deviating from its thermal limit, decreases as shown in Figure 2.11 and Figure 2.12. If N_2 in the oxidizer is replaced with highly radiating species such as CO_2, the gas radiation feedback may become important (Ref. 18). It can be shown that the surface radiation loss, gas-phase radiation loss, and gas to surface radiation feedback (see Figure 2.13) scale the same way with the residence time $t_{res} \approx \alpha_g / V_g^2$, that is, as V_g decreases, all these radiative effects become more severe. Assuming radiation feedback to be negligible (Ref. 19), the surface radiation loss can be used as a representative radiation term in the energy balance on the surface. It is well known that forward conduction through the thin solid with density ρ_s and heated layer L_{sy} is negligible (Ref. 20), leaving the difference between the conduction from the gas phase and radiative losses supplying the net forward heat transfer necessary to raise the temperature of the virgin fuel from T_∞ to T_v. The thermal conductivity of the gas is λ_g, c_s is the heat capacity of the solid, and ε is the surface emissivity.

$$V_f \rho_s c_s L_{sy} W (T_v - T_\infty) \sim \lambda_g \frac{(T_f - T_v)}{L_{gy}} L_{gx} W - \varepsilon \sigma (T_v^4 - T_\infty^4) L_{sx} W \tag{2.1}$$

Here W is an arbitrary width, and the solid-phase horizontal and vertical-length scales, L_{sx}, and L_{sy}, and gas phase vertical and horizontal length scales L_{gx} and L_{gy} are shown in Figure 2.13. Because the gas phase is the only source of heating, the gas-phase length scales are comparable: $L_{gx} \sim L_{gy}$. Also, by equating (in the scaling sense) the convective term with x and y conduction in the gas phase at the leading edge, we can establish that $L_{gx} \sim L_{gy} \sim \alpha_g/V_g$ provided $V_g \gg V_f$. Introducing these simplifications into Equation (2.1) and substituting L_{sy}, the heated layer thickness in Figure 2.13, with the half-thickness τ of the fuel, which is uniformly heated across its thickness (an assumption that defines thermally thin fuels), and neglecting the radiative loss, we obtain the thermal limit:

$$V_{f,\text{thermal}} \sim \frac{\lambda_g}{\rho_s c_s \tau} F \quad \text{where } F = \frac{(T_f - T_v)}{(T_v - T_\infty)} \tag{2.2}$$

Using the thermal limit expression for the spread rate as the velocity scale, Equation (2.1) can be made nondimensional as follows:

$$\eta_f \eta_g \sim \eta_g - \mathcal{R}_0; \quad \Rightarrow \eta_f \sim 1 - \frac{\mathcal{R}_0}{\eta_g}; \quad \Rightarrow V_{f,\text{radiative}} \sim V_{f,\text{thermal}} \left(1 - \frac{\mathcal{R}_0}{\eta_g}\right) \tag{2.3}$$

where

$$\mathcal{R}_0 \equiv \frac{1}{F^2} \frac{\rho_s c_s}{\rho_g c_g} \frac{\varepsilon \sigma \tau}{\lambda_g} \left(\frac{T_v^4 - T_\infty^4}{T_v - T_\infty}\right), \quad \eta_g \equiv \frac{V_g}{V_{f,\text{thermal}}}, \quad \eta_f \equiv \frac{V_f}{V_{f,\text{thermal}}} \tag{2.4}$$

and c_g is the specific heat of gas.
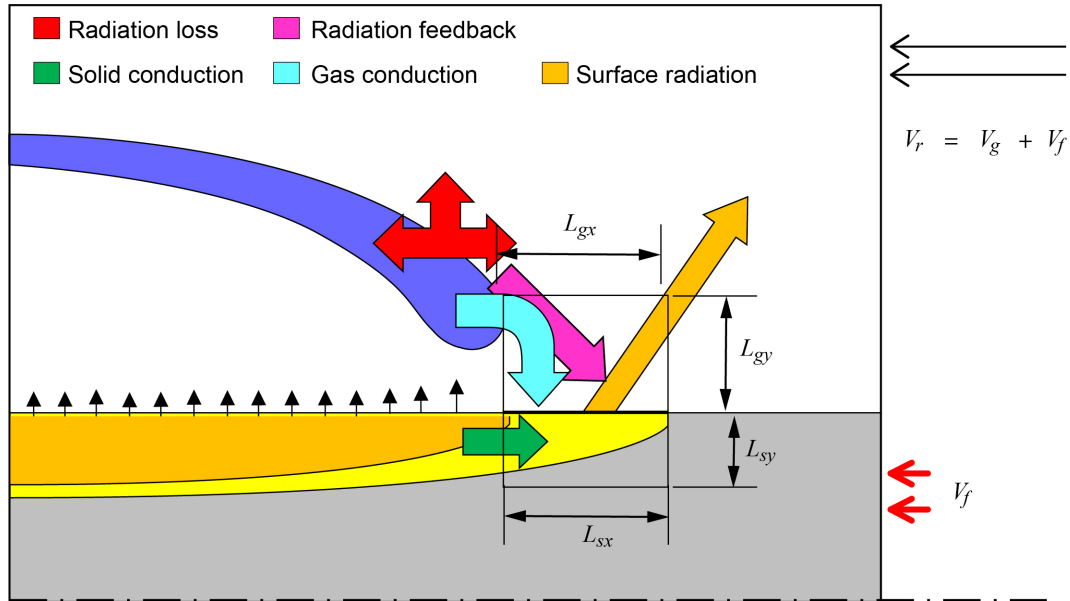
Figure 2.13.—Different modes of heat transfer and length scales (L) at leading edge of flame. For thermally thin fuel, $L_{sy} \leq \tau$. Solid (s). Gas phase (g). Absolute spread rate (V_f). Opposed-flow velocity (V_g). Velocity relative to flame (V_r). Fuel half thickness (τ).

TABLE 2.1.—COMPARISON OF EXTINCTION VELOCITY $V_{g,cr}$
FOR THIN POLYMETHYLMETHACRYLATE AT 1 atm

$V_{g,cr}$, mm/s			
O_2, percent	Experiment	Computation	Theory, Equation (2.5)
21	10±5	15	7.5
16	30±5	35	10

Equation (2.3) establishes that the spread rate in the radiative regime decreases with an increase in the radiation number $\mathfrak{R}_0$ and a decrease in the nondimensional flow velocity η_g. Note that the fuel thickness does not affect the ratio $\mathfrak{R}_0/\eta_g$; therefore, the inverse relation between flame spread rate and fuel thickness, a typical thermal regime behavior, also extends to the radiative regime. Setting the nondimensional spread rate η_f to zero in Equation (2.3), we obtain the condition for radiative extinction as

$$\eta_g \leq \mathfrak{R}_0; \quad \Rightarrow V_g \sim V_{g,cr} \quad \text{where } V_{g,cr} \equiv \frac{\varepsilon\sigma}{c_g\rho_g} \frac{\left(T_v^4 - T_\infty^4\right)}{\left(T_f - T_v\right)} \tag{2.5}$$

As found in the experiments and computations, Equation (2.3) confirms that the extinction velocity is not a function of fuel thickness. Using the properties used in the numerical simulation (which produces a linearized flame temperature of 2,199 K) and a vaporization temperature of 673 K, the critical extinction velocity $V_{g,cr}$ can be evaluated at different O_2 levels. Table 2.1 compares the prediction from this formula with computational and experimental results. Given the uncertainties associated with the experiments, simplified nature of the mathematical model, and errors associated with scale analysis, the agreement seems reasonable.

2.2.8 Conclusions

Recently conducted space-based experimental results on flame extinction at low opposing flow velocity are presented in this report. A critical flow velocity below which steady spread cannot be sustained is experimentally determined for various fuel thicknesses and two O_2 levels. Results from four different fuel thicknesses indicate that fuel thickness does not affect the critical velocity, which increases if the O_2 level is decreased. A two-dimensional computation model confirms this finding. A simplified scale analysis produces a closed-form expression $V_{g,cr} \equiv \left(\varepsilon\sigma/c_g\rho_g\right)\left[\left(T_v^4 - T_\infty^4\right)/\left(T_f - T_v\right)\right]$ for the critical velocity, where ε is surface emissivity, σ is Stefan-Boltzmann constant, c_g is the specific heat of gas, ρ_g is gas density evaluated at T_v, T_v is the vaporization temperature, T_∞ is ambient temperature, and T_f is adiabatic flame temperature. It establishes that even though the flame spread rate is inversely proportional to the fuel thickness, the critical velocity is independent of the fuel thickness. Prediction from this formula agrees remarkably well with the experimental and computational results.

2.2.9 Acknowledgment

NASA ground support teams at Glenn Research Center, Johnson Space Center, and Marshall Space Flight Center that supported the BASS–II operations.

2.2.10 References

1. De Ris, J.N.: Spread of a Laminar Diffusion Flame. Proc. Combust. Inst., vol. 12, no. 1, 1969, pp. 241–252.
2. Delichatsios, Michael A.: Flame Heights in Turbulent Wall Fires With Significant Flame Radiation. Combust. Sci. Technol., vol. 39, nos. 1–6, 1984, pp. 195–214.
3. Fernandez-Pello, A.C.; Ray, S.R.; and Glassman, I: Flame Spread in an Opposed Forced Flow: The Effect of Ambient Oxygen Concentration. Proc. Combust. Inst., vol. 18, no. 1, 1981, pp. 579–589.
4. West, Jeffrey S.: Forced Opposed-Flow Flame Spread Over Flat Solid Fuels in the Thermal, Near-Quiescent and Chemical Kinetic Regimes. Ph.D. Dissertation, Univ. of California, San Diego, 1998.
5. Bhattacharjee, Subrata, et al.: Downward Flame Spread Over Poly(methyl)methacrylate. Proc. Combust. Inst., vol. 28, no. 2, 2000, pp. 2891–2897.
6. Bhattacharjee, Subrata; and Altenkirch, Robert A.: Radiation-Controlled, Opposed-Flow Flame Spread in a Microgravity Environment. Proc. Combust. Inst., vol. 23, no. 1, 1991, pp. 1627–1633.
7. Kumar, Chenthil; and Kumar, Amit: On the Role of Radiation and Dimensionality in Predicting Flow Opposed Flame Spread Over Thin Fuels. Combust. Theory Model., vol. 16, no. 3, 2012, pp. 537–569.
8. Takahashi, Shuhei, et al.: Effect of Radiation Loss on Flame Spread Over a Thin PMMA Sheet in Microgravity. Proc. Combust. Inst., vol. 29, no. 2, 2002, pp. 2579–2586.
9. Olson, S.L.: Mechanisms of Microgravity Flame Spread Over a Thin Solid Fuel: Oxygen and Opposed Flow Effects. Combust. Sci. Technol., vol. 76, nos. 4–6, 1991, pp. 233–249.
10. Olson, Sandra; Ferkul, Paul V.; and T'ien, James S.: Near-Limit Flame Spread Over a Thin Solid Fuel in Microgravity. Proc. Combust. Inst., vol. 22, no. 1, 1989, pp. 1213–1222.
11. Bhattacharjee, Subrata; Altenkirch, Robert A.; and Sacksteder, Kurt: Implications of Spread Rate and Temperature Measurements in Flame Spread Over a Thin Fuel in a Quiescent, Microgravity, Space-Based Environment. Combust. Sci. Technol., vol. 91, 1993, pp. 225–231.
12. Reckart, T.A.: Space Flight System at GRC: Burning and Suppression of Solids (BASS). National Aeronautics and Space Administration, 2014. https://www1.grc.nasa.gov/space/iss-research/msg/bass/ Accessed June 21, 2021.
13. Bhattacharjee, S., et al.: Opposed-Flow Flame Spread: A Comparison of Microgravity and Normal Gravity Experiments to Establish the Thermal Regime. Fire Saf. J., vol. 79, 2016, pp. 111–118. DOI: 10.1016/j.firesaf.2015.11.011 Accessed June 18, 2021.
14. Patankar, Suhas V.: Numerical Heat Transfer and Fluid Flow. McGraw Hill, New York, NY, 1980.
15. Bhattacharjee, Subrata; King, Matthew D.; and Paolini, Chris: Structure of Downward Spreading Flames: A Comparison of Numerical Simulation, Experimental Results and a Simplified Parabolic Theory. Combust. Theory Model., vol. 8, no. 1, 2004, pp. 23–39.
16. Grosshandler, W.: Radcal: A Narrow-Band Model for Radiation Calculations in a Combustion Environment. NIST Technical Note 1402, 1993.
17. Ivisic, Ivan: Application of a Validated Radiation Model in Flame Spread Rate Over Solid Fuels. M.S. Thesis, San Diego State Univ., 2016.
18. Son, Youngjin; and Ronney, Paul D.: Radiation-Driven Flame Spread Over Thermally Thick Fuels in Quiescent Microgravity Environments. Proc. Combust. Inst., vol. 29, no. 2, 2002, pp. 2587–2594.
19. Bhattacharjee, S., et al.: The Critical Flow Velocity for Radiative Extinction in Opposed-Flow Flame Spread in a Microgravity Environment: A Comparison of Experimental, Computational, and

Theoretical Results. Combust. Flame, vol. 163, 2016, pp. 472–477. DOI: 10.1016/j.combustflame.2015.10.023 Accessed June 18, 2021.

20. Ito, Akihiko; and Kashiwagi, Takashi: Temperature Measurements in PMMA During Downward Flame Spread in Air Using Holographic Interferometry. Proc. Combust. Inst., vol. 21, no. 1, 1988, pp. 65–74.

2.3 Opposed-Flow Flame Spread: Comparison of Microgravity and Normal-Gravity Experiments to Establish Thermal Regime[2]

2.3.1 Abstract

The thermal regime of flame spread over solid fuels constitutes the reference condition for all other flame spread research. Although the theory of flame spread in the thermal regime is well understood, the well-known closed-form formulas for flame spread do not compare well with available experimental data. The comparison is further complicated by the fact that establishing a thermal regime in a normal-gravity environment is difficult because of the buoyancy-induced flow, which may usher in finite-rate kinetics effect. As a result, even the transition thickness, when a fuel can be considered a thermally thick fuel, still lacks a widely accepted formula.

This work presents opposed-flow flame spread data over varying thicknesses of polymethylmethacrylate obtained in the International Space Station where the opposing flow velocity can be reduced arbitrarily without any interference from the gravity-induced flow. It also presents a larger set of spread rate data for the downward spreading configuration at normal gravity. A comparison between the two datasets allow us to establish the thermal limit for thin fuel for which the spread rate is independent of the opposing flow velocity. The classical thin fuel spread rate formula is shown to fit well with the experimental results provided the adiabatic flame temperature is used in the flame coefficient that appears in the formula. The experimentally determined flame coefficient along with downward flame spread data for thick fuels are used to develop a closed-form expression for the transition thickness between thermally thin and thick fuels for downward spread in the thermal regime.

Symbols

a_P	Planck mean absorption coefficient
c	specific heat, kJ/kg·K
F	flame constant, Equation (2.12)
f	radiation view factor for the gas to the solid preheat region
g	gravity
g,rad	gas radiation feedback
$gy,cond$	conduction through gas
L_g	gas-phase diffusion length scale, m
L_{sy}	fuel thickness
s,rad	surface radiation
$sx,cond$	conduction through solid
T	temperature, K
t	time
V_f	absolute spread rate, m/s
V_g	velocity of the oxidizer, m/s
V_r	velocity relative to the flame, $V_r = V_g + V_f$
α_g	thermal diffusivity of gas, evaluated at T_v, m^2/s
α_s	thermal diffusivity of solid
ε	surface emissivity

λ_g	gas-phase conductivity evaluated at T_v, kW/m·K
λ_s	solid thermal conductivity
Ω	ratio $(\rho c_p \lambda)_g / (\rho c_p \lambda)_s$
ρ_g	gas density evaluated at T_v, kg/m^3
ρ_s	solid density, kg/m^3
σ	Stefan-Boltzmann constant, kW/(m^{2}K^4)
τ	fuel half-thickness, m
$\dot{\omega}_F'''$	fuel consumption rate

Subscripts

adb	adiabatic
chem	chemical
cond	conduction
cr	critical
de Ris	
eff	effective
eql	equal
expt	experimental
f	flame
g	gas phase
lin	linear
NC	natural convection
rad	radiation
res	residence
s	solid phase
th	thermal
thick	
thin	
transition	
v	vaporization
x, y	coordinates
∞	ambient

2.3.2 Introduction

Opposed-flow flame spread over solid fuels has been under investigation for about four decades (Refs. 1 to 3). Researchers have long desired to understand and predict the behavior of fire in different situations and under different conditions. While flame spread in the upward configuration is closely related to fire safety studies, it is also quite complex to model because the flame spread process is not steady and the flame size quickly becomes very large. In the downward configuration, where a flame spreads down a solid fuel sample vertically downward, the flame behaves in a two-dimensional (2D), quasi-steady (while the flame spread rate is constant, the flame shape may evolve in an unsteady manner), quasi-laminar (the flame trailing edge may show fluctuating pattern) manner with the steady flame spread rate being a function of fuel and environmental conditions. Because experiments on downward spread can be inexpensive to perform (Ref. 4), theories to describe the mechanism of flame spread in a quantitative manner can be tested and refined. Findings from this simplified configuration can be useful for more

practical configurations, such as upward or horizontal spread, given the commonality of various physics that participate in the mechanism of flame spread (Ref. 5).

Even in this simplified configuration a number of complexities can arise. Based on the thickness of the fuel sample, it may or may not be uniformly heated across its thickness. The pyrolysis chemistry to predict the burning rate of the fuel may not be well known (Ref. 6). The gas-phase chemistry used in computational models mostly assumes an overall single-step reaction. If the buoyancy-generated flow is strong enough or the O_2 level is low enough (or both), a competition between the combustion time and residence time may usher in chemical kinetics effect (Ref. 7) on the flame, leading to a reduction of spread rate or even extinction. Yet another complication can arise if the opposing flow velocity is too low, as in the case of a microgravity environment. A higher residence time makes both surface and gas radiative effects increasingly important (Ref. 8). Obviously, despite the simplification that the assumption of a 2D laminar flow brings in, a theory that includes gas-phase radiation, chemical kinetics in the gas phase, and pyrolysis kinetics is still too complicated to yield a solution without the application of numerical analysis. This is why de Ris (Ref. 9) introduced the thermal regime, where the theory is drastically simplified by assuming that the opposing flow velocity is not too small or not too large so that neither radiation nor chemistry play any significant role in the mechanism of flame spread. As a result an analytical solution of the governing equations is possible with the neglect of radiation and assumption of infinite-rate kinetics; the closed-form spread rate formulas by de Ris and Delichatsios (Refs. 9 and 10) in the thermal regime provide a baseline for nondimensionalizing experimental data and understanding the parametric dependence of flame spread with fuel and environmental conditions.

These well-known formulas for opposed-flow spread rate, however, have some drawbacks. The flame temperature used in the formula is based on a linearized mass diffusion theory and can be quite different than the thermodynamic adiabatic flame temperature. Also, use of constant properties in the theory allows room for significant variability in how properties such as thermal conductivity of air, specific heat, etc., are evaluated. As a result, when an experimental spread rate does not agree reasonably well with the theoretical prediction, it is not clear whether the disagreement is due to incorrect use of properties in the formula or due to more fundamental reason such as the flame spread is not in the thermal regime.

The opposed-flow flame spread experiments, where the opposing flow velocity can be directly controlled in a flow tunnel (Refs. 11 and 12) can easily create a high flow velocity where gas-phase chemistry becomes important due to shortened residence time. However, the opposed flow cannot be arbitrarily reduced. Even in a quiescent environment, there is no guarantee that the buoyancy-created flow is weak enough to justify an assumption of infinite-rate kinetics.

In this work, we use the gravity-free environment of the International Space Station (ISS) to continue the opposed-flow flame spread experiment to its logical conclusion by reducing the opposing flow velocity to any desired value without any interference from buoyancy in search of the elusive thermal regime. We present data from both downward experiments and microgravity experiments for the same fuel under the same environmental conditions (except for gravity level of course) for the first time. A simplified scale analysis is carried out to establish the elusive thermal regime experimentally. The results also help us determine the transition thickness between thermally thin and thermally thick fuels for downward flame spread.

2.3.3 Scale Analysis

Flame spread is determined by the competing physics at the flame leading edge. To establish the thermal regime through a scale analysis, a comprehensive sketch of all the major participants is presented in Figure 2.14, where different types of heat transfers are shown in bold arrows, length scales at the leading edge, and competing timescales with the subscripts g indicating gas phase and s indicating the

solid phase. The heat transfer to the virgin fuel, the driving mechanism of any flame spread (Ref. 5), involves conduction through the gas (*gy,cond*), conduction through the solid (*sx,cond*), surface radiation (*s,rad*), and gas radiation feedback (*g,rad*). Of these, forward conduction through the solid has been shown to be relatively unimportant theoretically (Ref. 9) and experimentally (Ref. 13). It should be mentioned that high lateral (perpendicular to spread rate) thermal conductivity, which can be different from the forward conductivity in composite materials, has been experimentally (Ref. 14) shown to influence the spread process strongly. In this analysis, however, the focus will be on homogeneous fuel such as polymethylmethacrylate (PMMA) ($C_2H_8O_2$). The radiative effects are also neglected (the rational to be discussed later), leaving gas to solid conduction as the dominant heat transfer mode.

By comparing the forward heat conduction to the advection term at the flame leading edge, the diffusion length scale can be established as $L_g \approx \alpha_g/V_g$, where α_g is the thermal diffusivity and V_g is the opposing flow velocity. Therefore, the gas residence time, time spent by the oxidizer at the leading edge, is given as $t_{g,res} \approx L_g/V_g \approx \alpha_g/V_g^2$. Assuming gas-phase conduction is the primary heating mechanism of the preheat zone, L_g must also be the solid-phase heating length. The fuel residence time, time spent by the fuel at the leading edge, is then given by $t_{s,res} \approx L_g/V_f \approx \alpha_g/(V_gV_f)$, where V_f is the flame spread rate, the desired unknown.

The first assumption of the thermal regime is that $V_f \ll V_g$ so that $t_{s,res} \gg t_{g,res}$. The combustion timescale in the gas phase, $t_{g,chem}$, can be defined as the time necessary for the combustion reaction to be complete at the flame leading edge raising the gas temperature to $T_{f,adb}$, the adiabatic flame temperature. Similarly, the chemical timescale in the solid phase for the pyrolysis of fuel, $t_{s,chem}$, can be defined as the time necessary for the fuel temperature to reach a vaporization temperature T_v. By assuming $t_{g,res} \gg t_{g,chem}$ and $t_{s,res} \gg t_{g,chem}$, finite-rate kinetics (Ref. 12) in the gas and solid phases can be
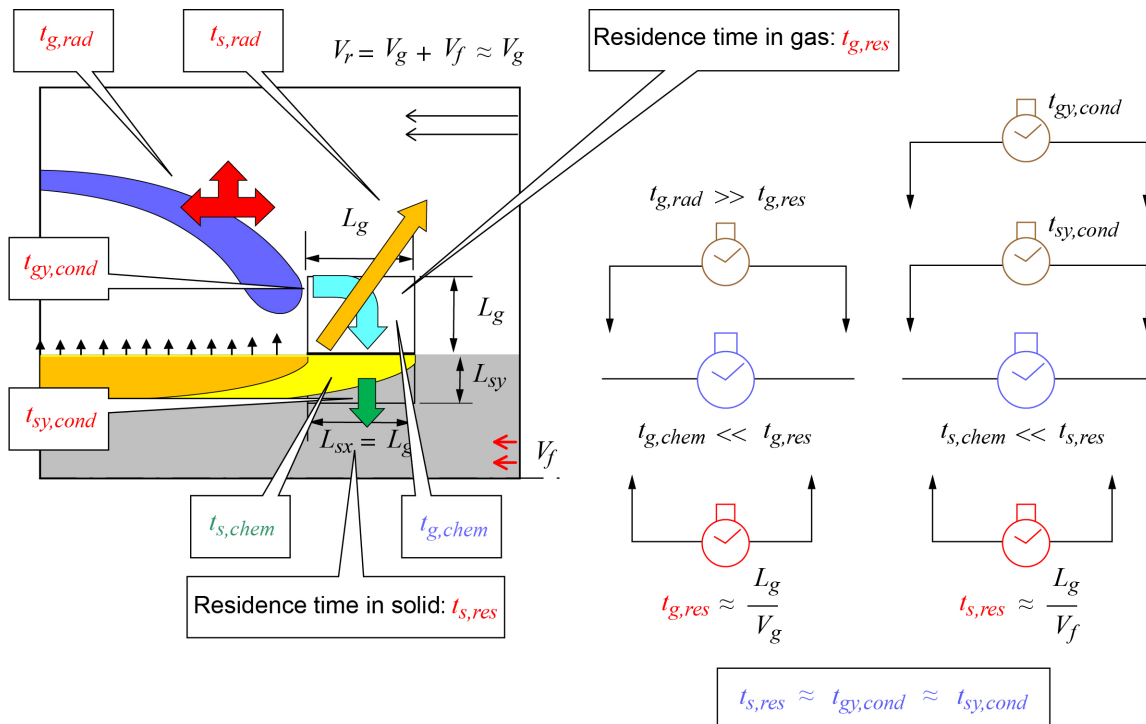
Figure 2.14.—Various time *t* and length scales *L* at leading edge. In thermal regime, fuel preheating *rad* and transverse conduction *cond* through gas *g* and solid *s* are of same order. Chemical (*chem*). Absolute spread rate (V_f). Velocity of the oxidizer (V_g).

eliminated. $T_{f,adb}$ and T_v, therefore, can be considered thermodynamic properties. However, when $t_{g,res}$ is too large, which is a possibility in a microgravity environment where in the absence of buoyancy-induced flow V_g can be quite small or even absent, gas and surface radiation can become important (Ref. 15). In the thermal regime, $t_{g,res}$ is considered large compared to $t_{g,chem}$ but not large enough for the radiative effects to be significant. If the opposed flow is not a fully developed flow, the presence of a boundary layer upstream of the flame leading edge can alter the effective velocity the flame encounters (Ref. 12). For a theoretical solution, the boundary layer effect is routinely neglected, and the opposing flow is considered a slug flow. The remaining assumptions include the neglect of finite width, effect of humidity, and variability of properties with temperature.

With the complications of kinetics and radiation eliminated, the essential mechanism for steady spread rate in the thermal regime reduces to heating up a layer of fuel of thickness L_{sy} (to be determined) from ambient temperature T_∞ to vaporization temperature T_v within the solid-phase residence time $t_{s,res}$. The gas layer of thickness L_g responsible for supplying this heat must itself be heated up from T_∞ to $T_{f,adb}$ in the available time $t_{g,res}$ at the leading edge. As already mentioned, the combustion time, defined as the time to consume the fuel vapor with mass fraction x_F at density (ρx_F) in the volume L_g^2 at the leading edge $t_{g,chem} \approx (\rho x_F)/\dot{\omega}_F'''$, is considered small compared to the residence time $t_{g,res}$ in the thermal regime. If the O_2 level is reduced, the fuel consumption rate $\dot{\omega}_F'''$ decreases increasing $t_{g,chem}$ and finite-rate chemistry becomes important, leading to flame extinction, when $t_{g,chem}$ becomes comparable to $t_{g,res}$. Even if there is sufficient O_2, if V_g is high enough, $t_{g,res}$ can decrease to the point that it becomes comparable to $t_{g,chem}$ and finite-rate kinetics becomes important leading to blowoff extinction.

The timescale for a heat transfer mechanism can be defined as the time it takes to supply or remove the characteristic amount of heat, $\rho_s L_{sy} L_g c_s (T_v - T_\infty)$, necessary to heat up the fuel layer L_{sy} with density ρ_s at the leading edge from T_∞ to T_v. The gas radiation timescale, $t_{g,rad} \approx \left[\left[\rho_s L_{sy} L_g c_s (T_v - T_\infty)\right]\right/ \left[4 a_P \sigma \left(T_f^4 - T_\infty^4\right) L_g^2\right]$, where a_p is the Planck mean absorption coefficient, σ is the Stefan-Boltzmann constant, and T_f, is the flame temperature, can be shown to be much larger than $t_{g,res}$ as long as V_g is not too small; it means gas radiation, both radiative losses and radiative feedback to the fuel, is not a significant participant within the short residence time $t_{g,res}$ of the thermal regime.

In the solid phase, the residence time depends on the gas-phase length and spread rate: $t_{s,res} \approx L_g/V_f$. Within this time, the fuel must start pyrolyzing. It can be shown that the characteristic pyrolysis time is much shorter than $t_{s,res}$ so that T_v can be considered a thermodynamic property of the fuel (Ref. 16). The timescale for surface radiation, $t_{s,rad} \approx \left[\rho_s L_{sy} L_g c_s (T_v - T_\infty)\right]/\left[\varepsilon \sigma \left(T_v^4 - T_\infty^4\right) L_g\right]$, where solid density ρ_s, specific heat of the solid c_s, and emissivity ε are constant while L_{sy} varies, can be shown to be much larger than $t_{s,res}$ for a large enough V_g, meaning surface radiation also can be neglected in the thermal regime. The forward conduction through solid with thermal conductivity λ_s and thermal diffusivity α_s is also neglected in the thermal regime as $t_{sx,cond} \approx \left[\rho_s L_{sy} L_g c_s (T_v - T_\infty)\right]/\left[\lambda_s (T_v - T_\infty)(L_{sy}/L_g)\right] \approx L_g^2/\alpha_s \gg t_{s,res}$ as long as $L_g \gg \alpha_s/V_f$, which is true except for very high V_g.

The surviving timescales, time for gas $t_{gy,cond}$ to solid conduction $t_{sy,cond}$, and interior conduction loss through solid, must be of the same order as the solid residence time (see Figure 2.14). That is,

$$t_{s,res} \approx t_{gy,cond} \approx t_{sy,cond} \tag{2.6}$$

Equating the first two timescales produces an expression for V_f in terms of L_{sy}:

$$\frac{L_g}{V_f} \approx \frac{\rho_s L_{sy} L_g c_s (T_v - T_\infty)}{\lambda_g (T_f - T_v) L_g / L_g}; \quad \Rightarrow V_f \approx \frac{\lambda_g}{\rho_s L_{sy} c_s} F, \quad \text{where } F \equiv \frac{T_f - T_v}{T_v - T_\infty} \tag{2.7}$$

A thermally thin fuel, by definition, is heated across its thickness so that $L_{sy} \approx \tau$, where τ is the half-thickness of the fuel (only the symmetric half of the leading edge is depicted in Figure 2.14). The familiar expression of thin-limit spread rate (Ref. 10) (except for the factor of $\pi/4$) is obtained by substituting $L_{sy} \approx \tau$ in Equation (2.7). For a thick fuel, the last two timescales in Equation (2.6) are equated to produce

$$\frac{\rho_s L_{sy} L_g c_s (T_v - T_\infty)}{\lambda_g (T_f - T_v) L_g / L_g} \approx \frac{\rho_s L_{sy} L_g c_s (T_v - T_\infty)}{\lambda_s (T_v - T_\infty) L_g / L_{sy}}; \quad \Rightarrow L_{sy} \approx \frac{\lambda_s L_g}{\lambda_g F} \approx \frac{\lambda_s}{\rho_g c_g V_g F} \tag{2.8}$$

Substituting this expression in Equation (2.7) produces the familiar de Ris thick limit (Ref. 9):

$$V_{f,\text{thin}} \approx \frac{\lambda_g}{\rho_s c_s \tau} F; \quad \text{and } V_{f,\text{thick}} \approx \frac{\rho_g c_g \lambda_g}{\rho_s c_s \lambda_s} V_g F^2 \tag{2.9}$$

One of the remarkable aspects of these expressions is that the spread rate is independent of opposing flow velocity V_g for thin fuels while it is proportional to V_g for thick fuels. An increase in V_g obviously raises the heat flux (W/m^2) from the gas to the solid, but it also shortens the preheat zone length, making the heat flow (W) independent of flow velocity. This heat is used to raise the temperature of the heated layer, which is the physical half-thickness of a thin fuel sample. For a thick fuel, on the other hand, the heated layer thickness depends on the heat flux: a higher temperature gradient in the solid (in the y direction) and, hence, a thinner heated layer, is necessary to sustain a higher heat flux from the gas and hence the flow velocity. That is how the velocity dependence is introduced for a thermally thick fuel.

Equation (2.8) also provides a simple criterion for transition thickness. A fuel can be considered thermally thin when

$$\tau < \tau_{\text{cr}}; \quad \text{where } \tau_{\text{cr}} \approx \frac{\lambda_s}{\rho_g c_g V_g F} \tag{2.10}$$

Although Equations (2.9) and (2.10) are remarkable in their simplicity, there is no universally accepted procedure for evaluating various parameters. The temperature at which gas properties are evaluated, the value of T_f and T_v to be used in determining F, and how to include the effect of the boundary layer on V_g are all subject to differing interpretation (Refs. 1, 10, and 12).

2.3.4   Onset of Kinetic Effect

One of the major challenges in acquiring data in the thermal regime is the onset of gas-phase kinetic effect when $t_{g,res}$ decreases to the level of the combustion time $t_{g,chem}$. Their ratio, called the Damköhler number, decreases the same as the opposed-flow velocity is increased (at a given O$_2$ level), leading to blowoff extinction. In the downward spreading configuration in a normal-gravity environment, buoyancy-generated flow, which scales with $V_{NC} \approx [\alpha_g g (T_g - T_\infty)/T_\infty]^{1/3}$ (Ref. 17) creates a constant opposing flow for a given O$_2$ level. When a forced opposing flow is superposed, the forced flow cannot have much impact on the flame spread until the strength of forced convection becomes comparable to that of natural convection due to gravity.

To illustrate this, average spread rate data acquired in a vertical combustion tunnel (Ref. 18) for various opposing airflow velocity for spread over a thin sheet of PMMA (50-μm-thick, 2-cm-wide) is plotted in Figure 2.15. The spread rate can be seen to remain relatively independent of the forced opposing flow velocity until it reaches a value of 40 cm/s. Similar behavior has been observed in flame spread over thin cellulosic fuel (Ref. 12). For thermally thin fuel in the thermal regime, the spread rate is
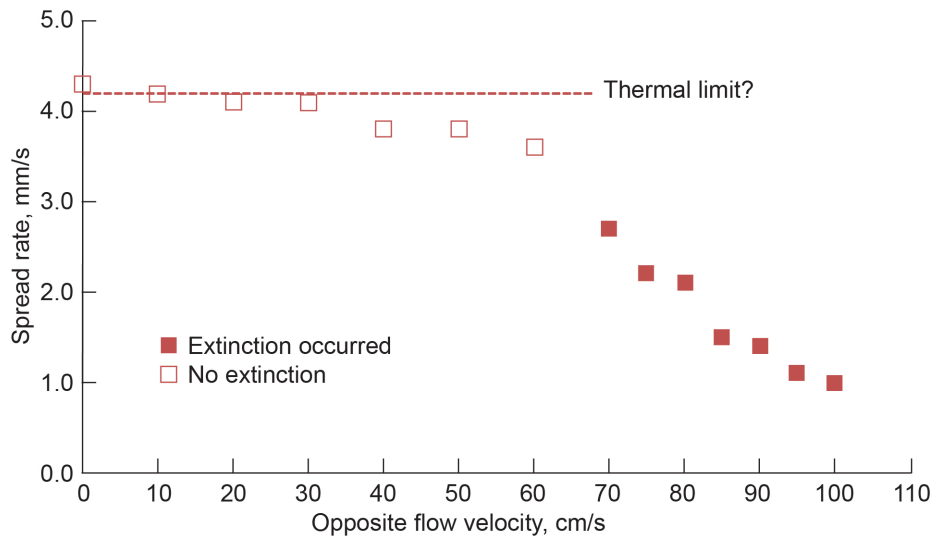
Figure 2.15.—Downward flame spread over polymethylmethacrylate sheets of 50-μm thickness in presence of forced opposed flow of air. Filled symbols represent blowoff extinction.

expected to be independent of opposing flow velocity as dictated by Equation (2.9). So, does the constant spread rate for up to a velocity of 40 cm/s in Figure 2.15 indicate the existence of thermal regime? Based on computational work (Ref. 17) that used a one-step second-order global kinetics model, it was concluded that kinetic effect may be present even at 21 percent O_2 level. The independence of spread rate with opposing flow velocity was interpreted as a constant kinetic effect by the buoyancy-generated flow. However, given the simplicity of the chemical kinetic model (one-step overall reaction) used in the computational model, a definitive conclusion cannot be made from computational results alone.

One way to experimentally establish if there is kinetic effect in downward spread rate is to reduce the strength of the buoyancy-generated flow or eliminate it altogether as in a microgravity environment. If the flow velocity is reduced below 40 cm/s, the increased residence time would reduce and weaken the kinetic effect and the spread rate can be expected to increase (in a kinetically controlled flame) until the thermal limit is reached. On the other hand, if the thermal limit is already established in the downward experiment (see Figure 2.14), then the spread rate is expected to remain unaltered as the opposing flow velocity is reduced in the absence of buoyancy. A comparison of experiments in the downward configuration with that in a microgravity environment, therefore, can be used to establish the thermal regime for a given O_2 level.

2.3.5 Microgravity and Normal-Gravity Experiments

There are only a handful of experiments conducted on flame spread in a microgravity environment, an excellent review of which can be found as a book chapter by T'ien (Ref. 19). The only long-duration opposed-flow experimental facility is offered by the BASS–II apparatus (Ref. 20) in the ISS. It is depicted in Figure 2.16. It is a combustion tunnel, a 76-mm square duct, where the PMMA ($C_2H_8O_2$) fuel samples, 20 mm wide and about 95 mm long with the thickness ranging from 100 to 400 μm, are burned in an opposed-flow configuration. A fan forces a flow of an O_2-N_2 mixture through flow straighteners from the right to the left and the sample, 2 cm wide, is ignited at the left end. Depending on the flow velocity and O_2 concentration, a steady flame is established that spreads from the left end of the sample towards the right end. The oxidizer mixture consists of O_2 and N_2 where the O_2 level can be adjusted at 21 percent or below. During the experiment, an O_2 sensor monitors the O_2 level, which has been found to drift by less

than 0.1 percent. A hot wire anemometer is used to calibrate the flow velocity with the voltage of the fan (see Figure 2.16) used for creating a flow of 50 cm/s or below. The total pressure is also monitored, which varied from 99.2 to 99.5 kPa in the tests reported.

Experiments were conducted in the Microgravity Science Glovebox of ISS by two crew members. Operation instructions were communicated from NASA Glenn Operations Center in realtime as the experiment progressed. Each test starts by creating a desired opposing flow by adjusting the fan voltage. After the flow stabilizes, the igniter is turned on until a visible flame is observed. The igniter is then turned off and the top view of the flame propagation is photographed with a high-resolution digital still camera with a frame rate of 1 per second. A video camera captures the side view of the flame propagation. In some of the tests, the flow velocity is changed during the spread to maximize the test matrix without having to burn additional samples.

For downward spreading experiments, the Flame Stabilizer apparatus (Ref. 4) is used, where a 2-cm-wide sample of PMMA is held vertically by a stainless steel sample holder and ignited at the top with a top-view camera recording the flame spread. The sample holders used in the microgravity and downward experiments are shown in Figure 2.17. While the BASS sample holder has a built-in igniter, piloted ignition is used in the downward experiments. The downward experiments were performed in the atmospheric condition (pressure 101 kPa, O_2 level 21 percent).

Ideally, the controllable parameters in a flame spread experiments include oxidizer mixture (percent of O_2 by volume), oxidizer pressure, oxidizer velocity, fuel type, fuel thickness, fuel width, fuel length, and external radiation. In the data presented, the fuel thickness is the most important parameter of interest.
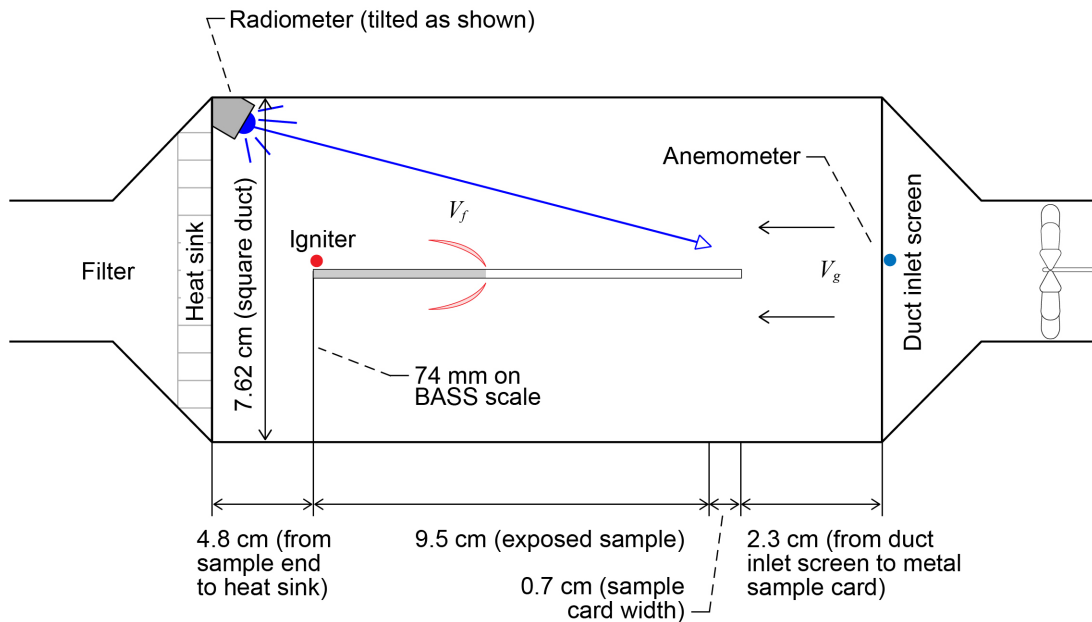
Figure 2.16.—Experimental setup aboard International Space Station used for opposed-flow flame spread research. Absolute spread rate (V_f). Velocity of the oxidizer (V_g).
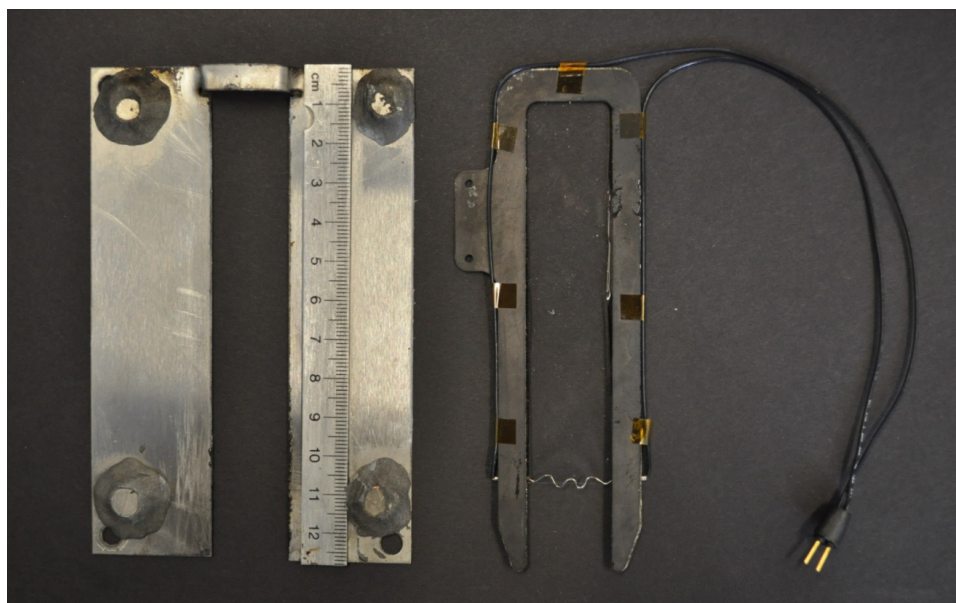
Figure 2.17.—Sample holder used for downward (left) and microgravity Burning and Suppression of Solids (BASS) (right) experiments.

2.3.6 Data Analysis

The still images from the BASS experiments are converted to videos and posted along with those from the downward experiments at http://flame.sdsu.edu. A MATLAB®- (The MathWorks, Inc.) based image processing application called Flame Analyzer has been developed at San Diego State University (SDSU) to obtain flame spread rate and other information from a top-view video. Video analysis has been used in fire research for a long time not just for tracking flame spread (Ref. 21) but also for estimating flame temperature (Ref. 22). But the Flame Analyzer is designed to automate the process of finding instantaneous flame spread rate.

A typical color image of the top view 18 s after ignition is shown in Figure 2.18(a) for downward flame spread over a 75-µm-thick sample. The dots along the axis, 6 mm apart, are superimposed on the image to help display the spatial resolution of the image. The red green blue (RGB) values of each pixel of the central slice are then converted to an intensity value using built-in MATLAB® tools. Across the width of the section, these intensity values are averaged, producing a 2D representation of the flame as shown in Figure 2.18(b). The variation of the width-averaged intensity along the x direction (axis) is shown in Figure 2.18(c). The leading edge of the flame is determined by deciding on a fixed threshold intensity. A value of 70 for the threshold value was found to work well for tracking the flame leading edge for this test.

For flame spread over 100-µm-thick samples, the leading edge locations during microgravity and downward spreads are shown in Figure 2.19(a). Most conditions are kept similar between the microgravity and downward experiments except in the microgravity experiment, the opposing flow velocity is 3 cm/s. A number of consecutive leading edge locations are used to obtain the flame spread rate by finding the slope of the linear regression analysis. The resulting spread rates are plotted in Figure 2.19(b). The uncertainty in the spread rate calculations by tracking the leading edge in this manner has been shown to be less than 5 percent except near ignition time when the flame bursts into its spreading form (Ref. 4). Once away from the ignition zone, averaging over 5 s of propagation have been found to produce spread rates that are reproducible within 5 percent variability. The error bar remains the same (at 5 percent or under) for all the data reported.
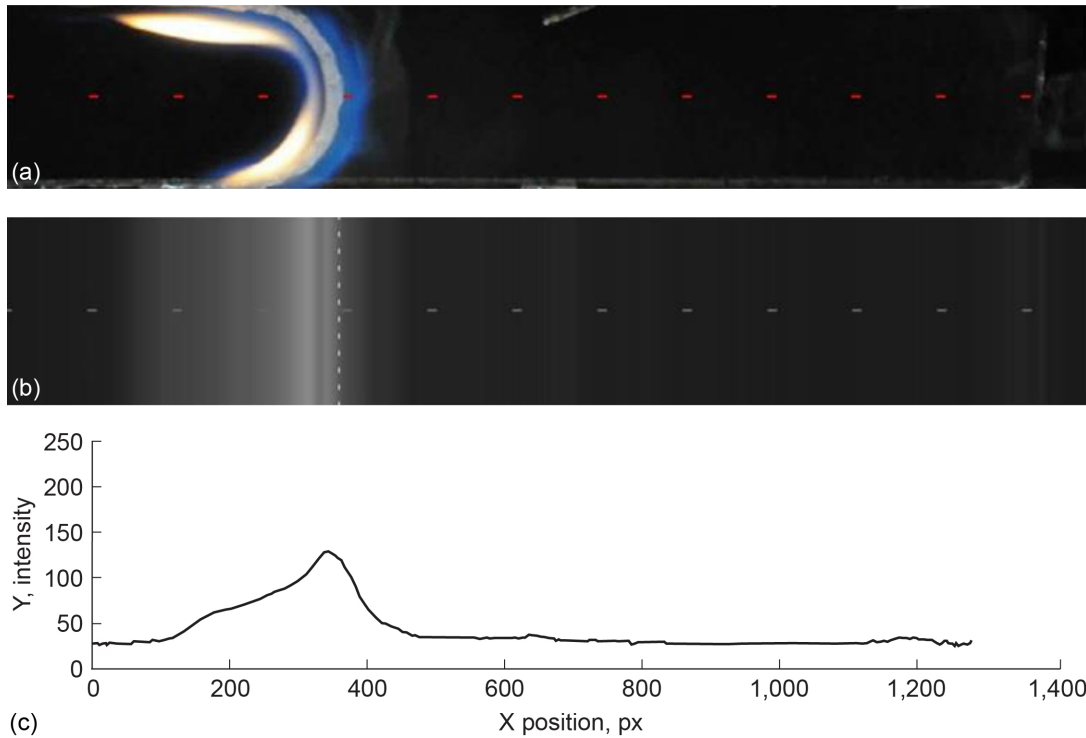
Figure 2.18.—Flame data. (a) Top view of flame 18 s into video, (b) two-dimensional representation of flame from averaged intensity values, and (c) variation of width-averaged intensity in x direction.
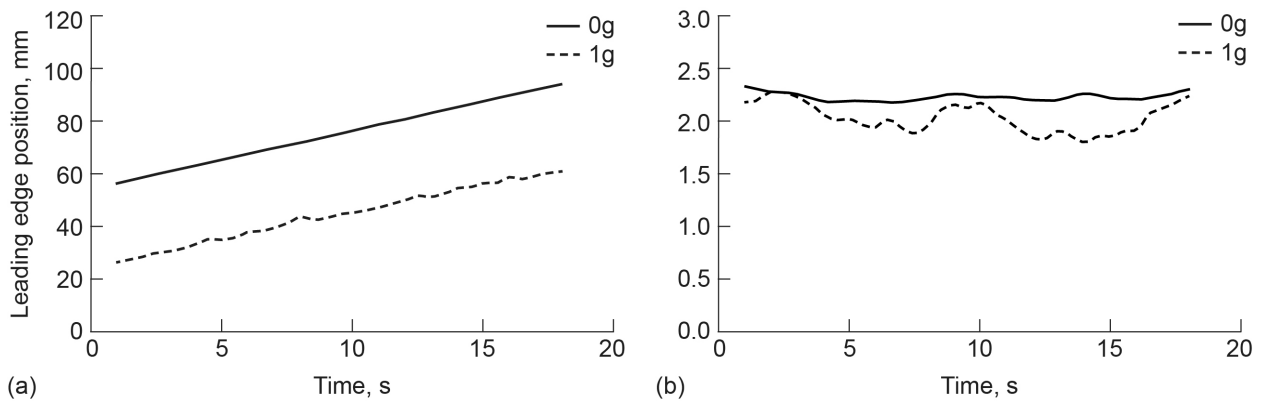
Figure 2.19.—Microgravity and downward configuration results. (a) Leading edge location versus time in microgravity (solid line) and downward configurations. (b) Spread rate versus time in microgravity (solid line) and downward configurations.

2.3.7 Results and Discussion

The average spread rate over the 100-μm-thick sample in the normal-gravity experiments is found to be 2.0 mm/s (see Figure 2.19(b)). Although the instantaneous spread rate fluctuates slightly, the average spread rate and the flame shape remain relatively steady throughout the experiment. The opposed flow being generated by buoyancy, a steady spread is expected. Any variation is probably due to surface irregularities and other random factors. In a microgravity environment, the opposed flow is much lower with experiments conducted mostly at very mild opposed-flow velocities. For the same fuel thickness, the highest spread rate obtained is about 2.2 mm/s even though the opposing flow velocity was varied from

about 40 cm/s to about 1 cm/s. At very high flow velocity, kinetically driven blowoff extinction was observed and at very low velocity (at about 1 cm/s) radiative extinction was observed. The highest spread rate in the microgravity environment, 2.2 mm/s, is about the same as the downward spread rate. The overall flame shapes are also quite similar as shown in Figure 2.20(a) and (b) where flame images for spread over samples of different thicknesses are compared. The leading edges in the downward spread show slight dripping effect and the flame is sootier, but the overall shape and size are quite similar as are the spread rates. This indicates that at 21 percent O_2 level, downward spread over PMMA can be considered thermally controlled with minimal kinetic effect.

Because gas-phase kinetics (or precisely, the Damköhler number, the ratio of the residence time to the gas-phase combustion time) is independent of fuel thickness, downward or microgravity spread over different fuel thicknesses should follow Equation (2.9). Using properties as listed in the nomenclature, de Ris formula for the thin limit, Equation (2.9) modified with a factor of $\pi/4$, can be expressed as

$$V_{f,\text{thin}} = \frac{\pi}{4}\frac{\lambda_g}{\rho_s c_s \tau}F = 2.34\times10^{-8}\frac{F}{\tau}; \quad \text{and } V_{f,\text{thick}} = \frac{\rho_g c_g \lambda_g}{\rho_s c_s \lambda_s}V_g F^2 = 9.72\times10^{-5}V_g F^2 \quad \left(\frac{\text{m}}{\text{s}}\right) \tag{2.11}$$
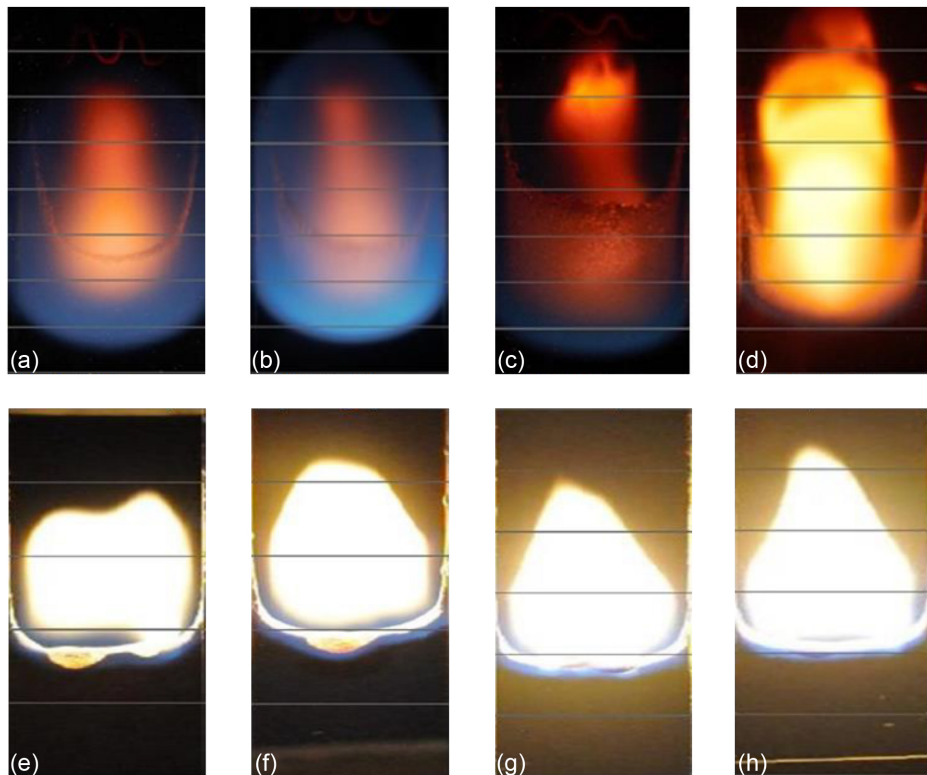
Figure 2.20.—Image array comparing microgravity and downward flame spread for different thicknesses of polymethylmethacrylate (PMMA). Velocity of oxidizer (V_g). Absolute spread rate (V_f). PMMA (NASA) in 0g on International Space Station, 2-cm sample with 10.x cm in 20.7 percent O_2 and 79 percent N_2 at 1 atm. (a) Burning and Suppression of Solids—II (BASS–II) B03 sample; 100 μm thick. (b) BASS–II B11; 200 μm thick. (c) BASS–II B4; 300 μm thick. (d) BASS–II B13; 400 μm thick. PMMA (NASA and Astra) in 1g at San Diego State University, 2-cm sample with 10.x cm in 20.7 percent O_2 and 79 percent N_2 at 1 atm. (e) PMMA at NASA; 100 μm thick. (f) PMMA at Astra; 200 μm thick. (g) PMMA at NASA; 300 μm thick. (h) PMMA at NASA; 400 μm thick.

For the experimental value of $V_{f,\text{thin}} = 2.2$ mm/s for $\tau = 50$ μm, the value of the de Ris flame coefficient F can be calculated from Equation (2.9) as 4.76. This experimentally (expt) determined value compares with different values used in literature as follows:

$$F_{\text{expt}} = \frac{\tau V_{f,\text{thin}}}{2.34 \times 10^{-8}} = 4.76; \quad F_{\text{de Ris}} \equiv \frac{T_{f,lin} - T_v}{T_v - T_\infty} = 5.54; \quad F_{adb} \equiv \frac{T_{f,adb} - T_v}{T_v - T_\infty} = 4.89; \quad F_{eql} \equiv \frac{T_{f,eql} - T_v}{T_v - T_\infty} = 4.41 \qquad (2.12)$$

Although de Ris expression for spread rate is based on the linearized (*lin*) flame temperature (the theory neglects advection in the normal direction to the fuel bed, replacing it with enhanced linearized diffusion that leads to the closed-form expression for flame spread rate in terms of a linearized flame temperature), the adiabatic (*adb*) flame temperature is easier to compute and can be seen to produce good agreement with the experimentally (*expt*) determined value of the equilibrium (*eql*) flame coefficient.

Using F_{adb} in Equation (2.11), spread rates calculated for different fuel thicknesses are plotted in Figure 2.21. Spread rate data for all four different fuel thickness studies are superposed along with data from downward experiments with nine different fuel thicknesses. The thermal regime formula for the thin fuel, Equation (2.11), seems to fit the experimental results quite well. Further downward experiments are conducted with progressively higher fuel thicknesses. Use of extruded PMMA produces considerable dripping (possibly because the methylmethacrylate chains are broken during extrusion making it easier for PMMA to drip) producing unsteady spread, while cast PMMA is less susceptible to dripping, producing a steady spread. Data for 2-cm-wide samples are added in Figure 2.22 with the purpose of creating a thick limit and delineating thermally thin fuel. Although for thicker fuels, the spread rate is slightly width dependent, a value of 0.042 mm/s for a 10-cm-wide sample (Ref. 23) as opposed to 0.044 mm/s for the 2-cm-wide sample, an average value of 0.044 mm/s is selected as the average spread rate for downward spread over PMMA in the thick limit.

The value of the flame coefficient F is not affected by the fuel thickness; therefore, F_{adb} that works so well with the thin fuel formula can also be applied to the thick-limit formula of Equation (2.11). However, the flow velocity V_g is an unknown for downward spread and should be replaced by an effective velocity.
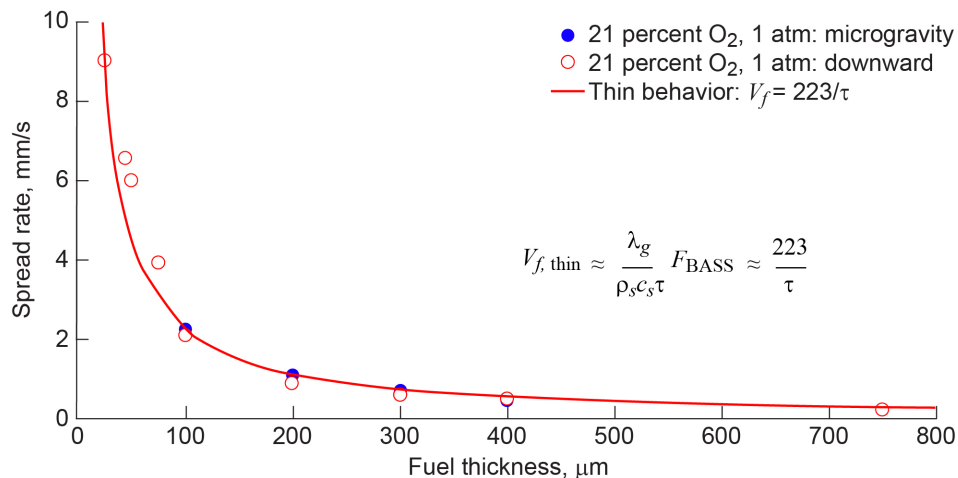
Figure 2.21.—Comparison of microgravity and downward flame spread at different thicknesses of polymethylmethacrylate. Absolute spread rate (V_f). Specific heat (c_s). Flame constant for Burning and Suppression of Solids (F_{BASS}). Gas-phase conductivity (λ_g). Solid density (ρ_s). Fuel half-thickness (τ).
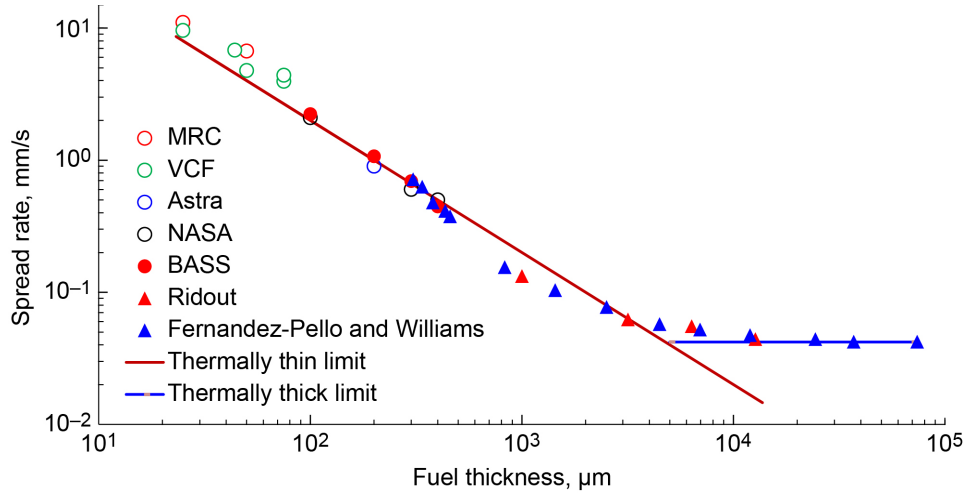
Figure 2.22.—Comparison of microgravity, downward flame spread, and Fernandez-Pello and Williams experimental data at different thicknesses of polymethylmethacrylate. Also showing thin and thick fuel theoretical thermal limits.

Using the experimental value of $V_{f,\text{thick}} = 0.044$ mm/s, the effective value of the opposing flow created by natural convection can be calculated from Equation (2.11) as

$$V_{g,\text{eff}} = \frac{V_{f,\text{thick,expt}}}{\Omega F_{adb}^2} = 0.019 \ \frac{\text{m}}{\text{s}} = 1.9 \ \frac{\text{cm}}{\text{s}} \tag{2.13}$$

where Ω is the ratio $(\rho c_p \lambda)_g/(\rho c_p \lambda)_s$.

In earlier computation work (Ref. 17), the effective velocity was calculated as 6 cm/s based on a more complex definition of the flame coefficient. The current experimental result, on the other hand, is based on F defined in terms of adiabatic flame temperature. The characteristic buoyancy-driven natural convection flow can be shown to scale with $V_{NC} \approx \left[\alpha_g g \left(T_g - T_\infty\right)/T_\infty\right]^{1/3}$. Using T_v as the characteristic gas temperature near the flame leading edge, we calculate $V_{NC} = 10.2$ cm/s, which is about the same order as the effective velocity.

The transition thickness between the thermally thin and thick fuels can be obtained by equating the experimentally verified thin and thick fuel spread rate expressions.

$$V_{f,\text{thin,expt}} = V_{f,\text{thick,expt}}; \quad \Rightarrow \tau_{\text{transition}} = \frac{\pi}{4} \frac{\lambda_s}{\rho_g c_g V_{g,\text{eff}} F_{adb}} \ \ (\text{m}) \tag{2.14}$$

The transition thickness $(2\tau_{\text{transition}})$ can be calculated from this expression as 5.19 mm for downward flame spread in ambient air. In a general opposed-flow environment, the transition thickness will vary with the opposing flow velocity and the boundary layer development length through its dependence on $V_{g,\text{eff}}$, with pressure through its dependence on ρ_g, and O_2 level through its dependence on F_{adb}.

2.3.8   Conclusion

In this work, results of experiments on flame spread over thin sheets of polymethylmethacrylate (PMMA) in the quiescent downward configuration and opposed-flow configuration in the microgravity environment are compared. A curve fit of maximum spread rate against fuel thickness using de Ris

formula for the thermal regime was used to determine the de Ris coefficient *F* as 4.76 for an oxidizing mixture of 21 percent O_2 and 79 percent N_2. Based on adiabatic flame temperature, *F* is only about 3 percent greater. Data from downward spread in ambient air is shown to correlate well (within the experimental uncertainty) with the microgravity data, establishing that the thermal limit is extended to downward spreading configuration in atmospheric condition on Earth. With *F* evaluated, experimental data for flame spread over thick PMMA is used to determine the effective velocity induced by buoyancy as 1.9 cm/s. Equating the thermal regime spread rate expressions for thin and thick limits, a formula for the transition between thin and thick fuels for downward spread in ambient atmosphere is obtained. For PMMA in ambient air, this transition thickness is evaluated to be 5.2 mm.

2.3.9   Acknowledgment

2.3.10   References

1. Wichman, Indrek S.: Theory of Opposed-Flow Flame Spread. Prog. Energy Combust. Sci., vol. 18, no. 6, 1992, pp. 553–593.
2. Blasi, C.D.: Modeling and Simulation of Combustion Processes of Charring and Non-Charring Solid Fuels. Prog. Energy. Combust. Sci., vol. 19, 1993, pp. 71–104.
3. Fernandez-Pello, A.C.; and Hirano, T.: Controlling Mechanisms of Flame Spread. Combust. Sci. Technol., vol. 32, nos. 1–4, 1983, pp. 1–31.
4. Bhattacharjee, S., et al.: A Novel Apparatus for Flame Spread Study. Proc. Combust. Inst., vol. 34, no. 2, 2013, pp. 2513–2521.
5. Williams, F.A.: Mechanism of Fire Spread. Proc. Combust. Inst., vol. 16, no. 1, 1977, pp. 1281–1294.
6. Torero, J.L., et al.: The Effect of Gravity on a Laminar Diffusion Flame Established Over a Horizontal Flat Plate. Proc. Combust. Inst., vol. 25, no. 1, 1994, pp. 1701–1709.
7. Altenkirch, R.A.; Eichron, R.; and Shang, P.C.: Buoyancy Effects on Flames Spreading Down Thermally Thin Fuels. Combust. Flame, vol. 37, 1980, pp. 71–83.
8. Bhattacharjee, Subrata, et al.: Opposed-Flow Flame Spread in Microgravity-Theoretical Prediction of Spread Rate and Flammability Map. Proc. Combust. Inst., vol. 30, no. 2, 2005, pp. 2279–2286.
9. De Ris, J.N.: Spread of a Laminar Diffusion Flame. Proc. Combust. Inst., vol. 12, no. 1, 1969, pp. 241–252.
10. Delichatsios, M.A.: Exact Solution for the Rate of Creeping Flame Spread Over Thermally Thin Materials. Combust. Sci. Technol., vol. 44, nos. 5–6, 1986, pp. 257–267.
11. Hirano, Toshisuke; and Sato, Kenji: Effects of Radiation and Convection on Gas Velocity and Temperature Profiles of Flames Spreading Over Paper. Proc. Combust. Inst., vol. 15, no. 1, 1975, pp. 233–241.
12. Bhattacharjee, Subrata; Nagarkar, Rohit; and Nakamura, Yuji: A Correlation for an Effective Flow Velocity for Capturing the Boundary Layer Effect in Opposed-Flow Flame Spread Over Thin Fuels. Combust. Sci. Technol., vol. 186, no. 8, 2014, pp. 975–987.

13. Ito, Akihik; and Kashiwagi, Takashi: Measurement Technique for Determining the Temperature Distribution in a Transparent Solid Using Holographic Interferometry. Appl. Optics, vol. 26, no. 5, 1987, pp. 954–958.

14. Di Blasi, C.; and Wichman, I.S.: Effects of Solid-Phase Properties on Flames Spreading Over Composite Materials. Combust. Flame, vol. 102, no. 3, 1995, pp. 229–240.

15. Bhattacharjee, Subrata; and Altenkirch, Robert A.: Radiation-Controlled, Opposed-Flow Flame Spread in a Microgravity Environment. Symposium (International) on Combustion, vol. 23, no. 1, 1991, pp. 1627–1633.

16. Bhattacharjee, S.; Bhaskaran, K.K.; and Altenkirch, R.A.: Effects of Pyrolysis Kinetics on Opposed-Flow Flame Spread Modeling. Combust. Sci. Technol., vol. 100, nos. 1–6, 1994, pp. 163–182.

17. Bhattacharjee, Subrata, et al.: Downward Flame Spread Over Poly(methyl)methacrylate. Proc. Combust. Inst., vol. 28, no. 2, 2000, pp. 2891–2897.

18. Carmignani, Luca: Flame Spread Over Solid Fuels Facing an Opposing Flow: Experimental Investigation of the Aerodynamic Effects on Spread Rate and Extinction. M.S. Thesis, Univ. of Pisa, 2015.

19. Ross, H.D.: Microgravity Combustion: Fire in Free Fall. Appl. Mech. Rev., vol. 55, no. 6, 2002, pp. B116–B117.

20. Reckart, T.A.: Space Flight System at GRC: Burning and Suppression of Solids (BASS). National Aeronautics and Space Administration, 2014. https://www1.grc.nasa.gov/space/iss-research/msg/bass/ Accessed June 21, 2021.

21. Klimek, Robert; and Wright, Ted: Spotlight–8 Image Analysis Software. NASA/TM—2006-214084, 2006. https://ntrs.nasa.gov

22. Audoin, L., et al.: Average Centreline Temperatures of a Buoyant Pool Fire Obtained by Image Processing of Video Recordings. Fire Saf. J., vol. 24, no. 2, 1995, pp. 167–187.

23. Fernandez-Pello, A.C.; and Williams, F.A.: Laminar Flame Spread Over PMMA Surfaces. Proc. Combust. Inst., vol. 15, no. 1, 1975, pp. 217–231.

3.0   Project Scientist Report: Ferkul

3.1   Nomex® Flammability

The objective of the Nomex® (DuPont™) sample tests was to evaluate the flammability of Nomex®, since it is heavily used aboard the International Space Station (ISS) as a fire barrier. A secondary objective was to burn any unused Burning and Suppression Solids—I (BASS–I) samples, of which there was a single wax candle. The test matrix is in Appendix A.

3.1.1   Results

The three Nomex® samples did not ignite, which is an excellent result for fire safety aboard the ISS.

The wax candle test successfully ignited in an opposed flow (akin to holding a candle upside down) and burned at five different flow velocities corresponding to the test matrix potentiometer settings as shown in Figure 3.1. At the initial 3 cm/s, the sooty flame has an aspect ratio that is longer rather than wide. As the flow reduced, the flame became hemispherical. At the lowest pot setting, the flame becomes short rather than wide and turns mostly blue.

The ejected wax droplet shown in Figure 3.1(b) typifies the flame spread hazard associated with melting plastics in microgravity. If the melt viscosity is low enough, burning droplets can be ejected and possibly ignite other materials.
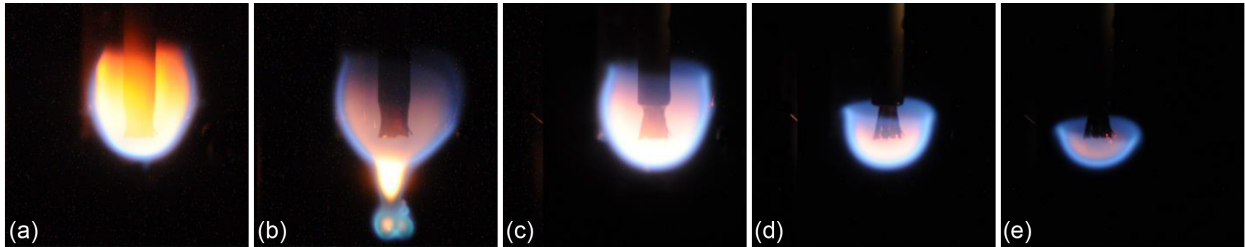
Figure 3.1.—Candle wick burning with opposed flow (upward flow). (a) Postignition at 3 cm/s (potentiometer or pot 0.6); (b) Pot 0.4, wick ejects droplet of wax directly upstream; (c) Pot 0.35; (d) Pot 0.32; and (e) Pot 0.31.

4.0   Individual Principal Investigator Report: Fernandez-Pello

4.1   Opposed-Flame Spread Task

The scientific objective of the Burning and Suppression Solids—II (BASS–II) opposed-flow flame spread test is to further understand the mechanisms controlling the spread of flames over the surface of solid combustible materials, particularly in a spacecraft environment. For this purpose, experiments were conducted aboard the International Space Station (ISS) to determine the effects of microgravity on the spread of flames over polymethylmethacrylate (PMMA) rods of different diameters subjected to different O_2 concentrations and low flow velocities. These are parameters that in addition to low pressure are expected in spacecraft environments. By conducting these tests aboard the ISS and then comparing the results to ground-based data, it is expected that a better understanding of the governing mechanisms of flame spread in microgravity can be obtained. In addition, by conducting the tests with cylindrical samples, the effect on the flame spread process of geometrical factors such as the transverse curvature of the surface can be better studied.

4.1.1   Experiment and Test Matrix

The tests were conducted in the BASS–II hardware placed inside the Microgravity Science Glovebox (MSG) in the Destiny Lab of the ISS. The BASS–II hardware consists of a flow duct, still camera, video camera, external control box, and associated plumbing and mounting systems along with the fuel samples for the BASS–II experiments.

The tests for the present task were conducted with rods of cast PMMA with diameters of 6.35, 9.525, and 12.7 mm (1/4, 3/8, and 1/2 in., respectively) and were 57.15 mm in length. All cylindrical rods tested started with rounded (hemispherical) ends in order to minimize the flow disturbance associated with the abrupt bluff body transition at the sample's downstream edge. Ignition of the PMMA was accomplished by using a hot wire placed to heat the PMMA surface in the downstream edge of the rods.

Table 4.1 and Table 4.2 present the test conditions for the opposed-flow flame spread tests conducted in this task. The majority of the tests were conducted with black PMMA, because rods of black PMMA are also used in the Material Ignition and Suppression Test (MIST) project to reduce effects of in-depth absorption of thermal radiation. For this reason, the results presented in this report are limited to those for black PMMA. A few tests were conducted with clear PMMA for comparison purposes, but the data is too limited to present it here.

TABLE 4.1.—ROD DIAMETERS TESTED FOR BOTH CLEAR AND BLACK POLYMETHYLMETHACRYLATE (PMMA) ABOARD INTERNATIONAL SPACE STATION AS PART OF BURNING AND SUPPRESSION SOLIDS—II (BASS–II) CAMPAIGN

Size, m	0.00635	0.009525	0.0127	Total
Black PMMA				
Test conditions	23	12	12	47
Samples burnt	9	4	4	17
Clear PMMA				
Test conditions	4	3	0	7
Samples burnt	2	1	0	3

TABLE 4.2.—RANGE OF OXIDIZER AND ESTIMATED MIXED (FORCED AND FREE) FLOW CONDITIONS BY
DIAMETER EMPLOYED ABOARD INTERNATIONAL SPACE STATION AS PART OF BURNING
AND SUPPRESSION SOLIDS—II (BASS–II) CAMPAIGN

Sample diameter, m	0.00635	0.009525	0.0127
O_2 concentration, vol%	16.8 to 18.9	17.5 to 20.9	17.6 to 20.7
Flow velocity, m/s	0.0041 to 0.075	0.043 to 0.02	0.0137 to 0.0164

Table 4.2 exhibits the range of oxidizer and flow conditions employed in these tests. The focus of these experiments was on low O_2 concentrations and characteristic flow velocities below those achievable in 1g environments due to the effects of buoyancy. The low-flow velocities in microgravity environments allow for the investigation of conditions unachievable in a 1g environment. As a means of comparison, from standard Grashof number arguments one can derive a characteristic buoyant velocity induced by the heated sample (Ref. 1), and at the point of ignition it is approximately 0.50 m/s, which is an order of magnitude greater than the largest forced-flow velocity tested in the BASS–II experiments, as can be seen in Table 4.2.

4.1.2   Results

Multiple test conditions were accomplished for each PMMA sample by igniting the sample at a high opposed-flow velocity and then subsequently reducing the opposed-flow velocity until extinction was observed, pausing along the way to allow steady-state flame spread. The results presented herein comprise the effects of O_2 concentration and flow velocity on the rate of microgravity opposed-flame spread over black PMMA rods in microgravity. Figure 4.1(a) presents a summary of the results of the effect of flow velocity on the opposed-flow flame spread rate for 0.00635-, 0.009525-, and 0.0127-m-diameter rods of black cast PMMA. The data points are at different O_2 concentrations, which explains some of the scatter in the data. Figure 4.1(b) presents the effect of O_2 concentration at different flow velocities.

As can be seen in Figure 4.1(a), the average flame spread rate increases with opposed-flow velocity, even within the small range of flow velocities tested. Sustained flame spread for the conditions tested was not observed for opposed-flow velocities below approximately 4 mm/s for the 0.00635- and 0.009525-m-diameter rods. Visually it was observed that at very low flow velocities the flames appear to be very small, blue, faint, and open at their downstream ends. As the flow velocity rises towards 20 mm/s and above, the flames become much more luminous, with bright yellow flames, and a closed downstream tip.

In Figure 4.1(b), the data exhibits an upward trend in spread rate with increasing O_2 concentration, which is especially marked in the results of the 6.35-mm-diameter rods. Both of these sets of observations are similar to those of previous work on flame spread in microgravity. Near the quenching limit, not only is diffusion playing a bigger role in providing the oxidizer flow to the flame, but also, the flame becomes very faint and the reradiation from the sample surface becomes increasingly important (Refs. 2 and 3).

To facilitate the comparison of the data for the different conditions, all the data points are presented in Figure 4.2. Figure 4.2 presents the same data as Figure 4.1, but presents all three rod diameters in one plot, and colors the data points by their respective O_2 concentration (Figure 4.2(a)) or flow velocity (Figure 4.2(b)).
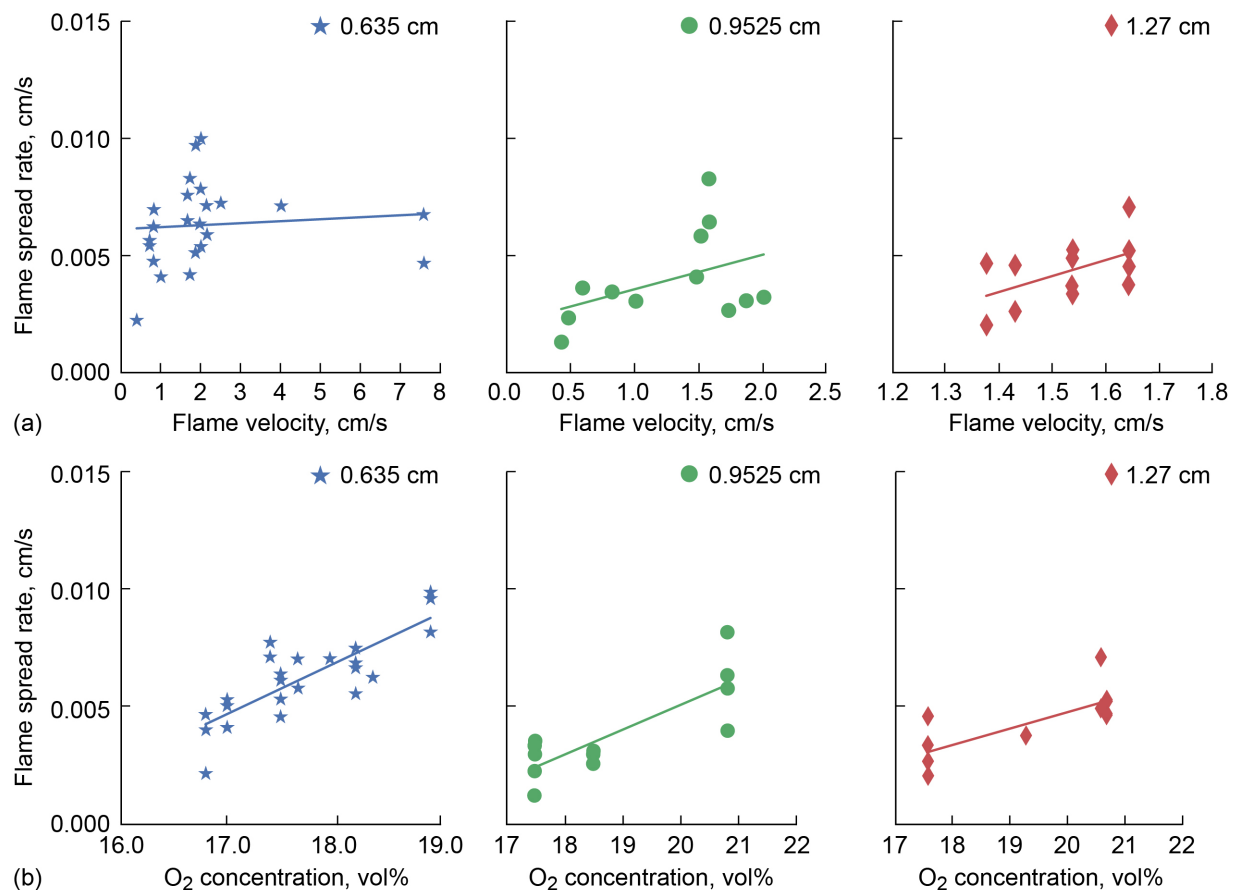
Figure 4.1.—Flame spread rate versus opposed-flow velocity and O_2 concentration for three diameters of black polymethylmethacrylate rods in microgravity. (a) Opposed-flow velocity. (b) O_2 concentration.

In comparing the experimental results from ground-based experiments with those conducted aboard the ISS, a number of complications arise. First and foremost, due to the effect of buoyancy, the effective opposed-flow velocity felt by the flame in the 1g experiments is an order of magnitude greater than the velocities tested in microgravity experiments. As has been shown elsewhere, the difference in flame spread rate between natural convective conditions and an opposed-flow velocity of 0.25 m/s in 1g is relatively negligible. On the other hand, for the microgravity tests presented herein, the flow velocities under investigation are near the quenching limit, below those normally expected from the air supply and recirculation systems currently employed on the ISS.

In addition to difficulties regarding the use of comparable flow velocities, in the microgravity experiments only the two largest diameter rods were tested at near 21 percent O_2 by volume, with the highest O_2 concentration tested for the 6.35-mm-diameter rods being approximately 19 percent by volume. The only O_2 concentration at which all three rod diameters employed in the microgravity experiments were tested was at approximately 17.5 percent O_2 by volume. In the 1g experiments, the lowest O_2 concentration at which all four tested rod diameters were successfully burnt without the addition of an external radiant heat source was 19 percent by volume.

Thus, in comparing the datasets, some compromises were made. In particular, as can be seen in Figure 4.3, the ranges of O_2 concentrations and rod diameters employed do not completely overlap. Yet, the trend in flame spread rate in terms of both O_2 concentration and rod diameter are still quite apparent even after discounting the fact that the flow velocities are not strictly comparable.

The most important result of the comparison is that of the minimum O_2 concentration for flame spread in normal and microgravity. While in microgravity, flame spread was observed at O_2 concentrations as low as 17.5 percent, in normal gravity, flame spread was not observed below 19 percent. This result is probably due to the lower opposed-flow velocity in the microgravity tests in comparison with those induced by buoyancy in normal gravity.
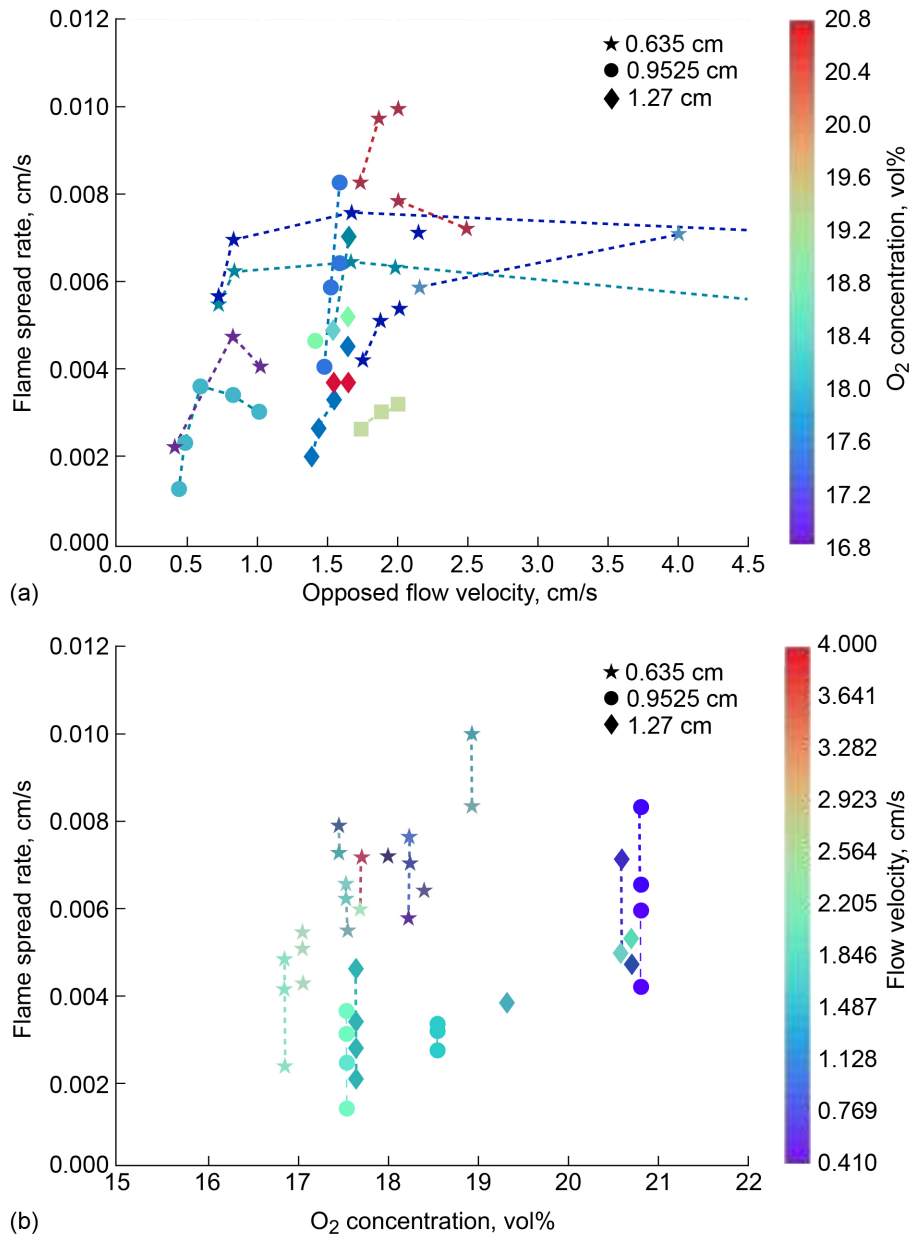
Figure 4.2.—Flame spread rate versus opposed-flow velocity and O_2 concentration for three diameters of black polymethylmethacrylate rods in microgravity where independent variable not on abscissa is represented as color of data point. (a) Opposed-flow velocity. (b) O_2 concentration.
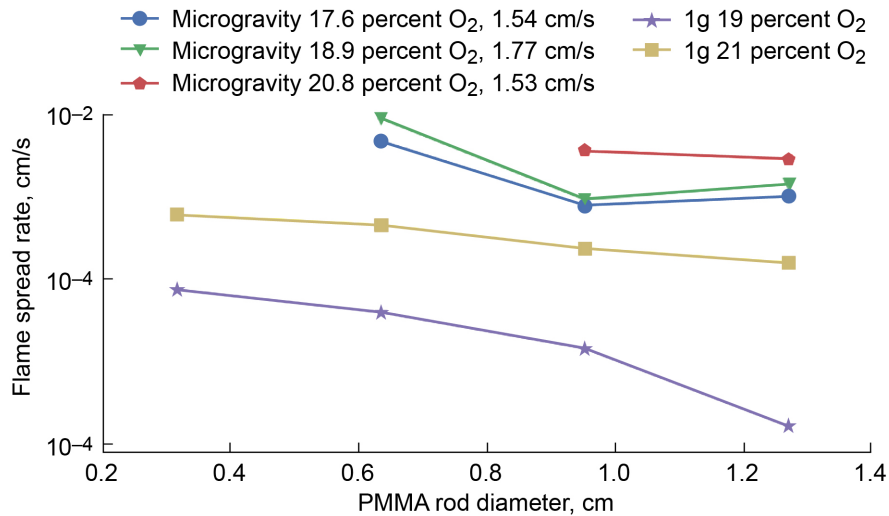
Figure 4.3.—Comparison of flame spread rates for black cast polymethylmethacrylate (PMMA) rods as function of gravity, O_2 concentration, and rod diameter. All data are for experiments carried out in absence of external radiant heating. All O_2 concentrations and flow velocities for microgravity experiments are averaged over associated test conditions.

Decreasing the rod diameter increases the flame spread rate in both 1g and microgravity environments, as shown in Figure 4.3. It is also apparent that flame spread in microgravity is appreciably faster than in 1g for cylindrical rods of PMMA. These results agree well with similar comparisons of 1g and microgravity results for opposed-flow flame spread on wire insulation (Refs. 4 and 5), as well as theoretical considerations of the problem (Ref. 6).

The rods were ignited at the downstream end, and the flame was allowed to spread across the rod for a period of time at each velocity. A typical test is shown in Figure 4.4(a) to (e), where the flame is initially sooty. As the flow velocity is reduced, the sooting decreases and then disappears. The flame tail opens up as it continues to spread along the rod. The rod extends past the end of the flame as the spreading continues. This wide-open flame tail with rod remaining behind is unique to microgravity.

In normal gravity, the flame burns away the rod in a conical regression, and the rod tip is always within the flame. The regression angle of the cone increases as the forced-flow velocity increases (Ref. 6). At relatively high flow rates (120 cm/s and higher) (Refs. 6 and 7), the flame is small and flat behind a flat rod tip (regression angle 90°). In other words, the flame is stabilized in the recirculation zone behind the rod. It is quite difficult to blowoff this flame, as was predicted (Ref. 8). The distinction between flame spread and regression is important when one considers the classic limiting O_2 index test (Ref. 9), where a small sample is burned like a candle flame in a 4-cm/s oxidizer flow velocity, and the O_2 concentration is reduced until the flame extinguishes. The small flames in 1g sit at the top of the sample instead of spreading down the sample near the extinction limit.

A similar shaped flame is observed at very low O_2 concentration in the space experiment, as shown in Figure 4.4(f). The flame survived under the low-O_2 conditions until the initially hemispherical rod tip regressed to a flat surface. It never spread along the outer surface of the rod. It is hypothesized that the flame quenched when the local flow velocity in the flame zone decreased as the flame transitioned to a wake flame, and the sample thickness that needed heating exceeded the ability of the weakened flame to heat it.
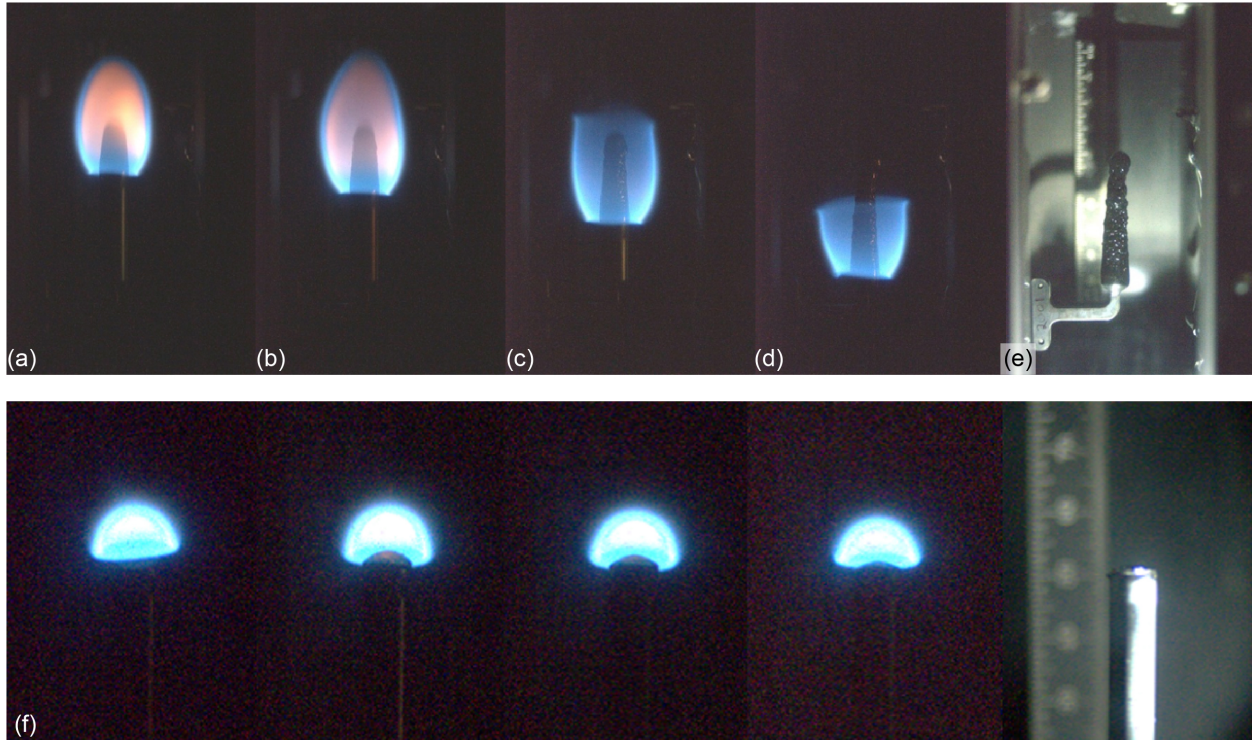
Figure 4.4.—Two flame sequences showing very different burning behavior. Black polymethylmethacrylate (PMMA) rod, 4.76 mm, 18.5 percent O_2, with decreasing flow at (a) 1.9 cm/s, (b) 1.7 cm/s, (c) 1.6 cm/s, and (d) 1.5 cm/s. (e) Posttest rod, showing general conical burn shape except blunt melted tip of the rod. (f) Black PMMA rod, 3.18 mm, 16.3 percent O_2, at 5 cm/s. Cap-shaped flame burned away initial hemispherical tip of rod to flat surface and then extinguished.

The postburn rod samples in Figure 4.5 preserve bubble layers for the opposed flow and for concurrent flow (Olson tests). The opposed-flow rod exhibits a dense white bubble layer starting abruptly near the flame leading edge and extends downstream as the rod regresses symmetrically until the full thickness of the rod is heated to the point that the molten tip forms a sphere to minimize surface tension. At the leading edge of the flame, the upstream solid-phase preheat length is relatively short, and the flame must provide an adequate heat flux to preheat the upstream rod.

In contrast, the concurrent PMMA rod molten tip is upstream, and the dense bubble layer varies with the flame length. Due to the convective heating of the downstream rod, large widely spaced internal bubbles are formed well downstream of the flame. These bubbles are full of methylmethacrylate vapor under pressure from polymer chain scission. When they reach the surface of the material, they rupture and form a vapor jet that ignites in the presence of a flame. After extinction, the hot material can continue to produce fuel for some time until it cools. Premixed flame oscillations along the rod have been observed for the concurrent rod geometry that persist much longer in microgravity than in normal gravity due to the lower rate of convective cooling of the rod. This suggests that spacecraft fire suppression efforts should be maintained until the burning material has cooled and stopped emitting vapors.

Figure 4.5.—Polymethylmethacrylate rod bubble layers (a) opposed and (b) concurrent.

4.1.3 References

1. Schlichting, Herrmann; and Gersten, Klaus: Boundary-Layer Theory. Springer, Berlin, Germany, 2001.
2. Altenkirch, Robert A., et al.: Opposed-Flow Flame Spreading in Reduced Gravity. The Second International Microgravity Combustion Workshop Proceedings, NASA CP–10113, 1993, pp. 237–243. https://ntrs.nasa.gov
3. Bhattacharjee, Subrata, et al.: Extinction Criteria for Opposed-Flow Flame Spread in a Microgravity Environment. Seventh International Workshop on Microgravity Combustion and Chemically Reacting Systems Proceedings, NASA/CP—2003-212376/REV1, 2003, pp. 201–204. https://ntrs.nasa.gov
4. Kikuchi, Masao et al.: Experimental Study on Flame Spread Over Wire Insulation. Proc. Combust. Inst., vol. 27, no. 2, 1998, pp. 2507–2514.
5. Fujita, Osamu; Nishizawa, Katsuhiro; and Ito, Kenichi: Effect of Low External Flow on Flame Spread Over Polyethylene-Insulated Wire in Microgravity. Proc. Combust. Inst., vol. 29, no. 2, 2002, pp. 2545–2552.
6. Higuera, F.; and Linan, A.: Flame Spread Along a Fuel Rod in the Absence of Gravity. Combust. Theory Model., vol. 3, no. 2, 1999, pp. 259–265.

7. Bhattacharjee, Subrata; and Carmignani, Luca: Burn Angle in Forced and Natural Convection: A Simplified Scaling Approach. Combust. Theory Model., vol. 23, no. 5, 2019, pp. 956–968.

8. Link, Shmuel, et al.: The Effect of Gravity on Flame Spread Over PMMA Cylinders. Sci. Rep., vol. 8, no. 120, 2018.

9. Ikeda, G.: Oxygen Index Tests to Evaluate the Suitability of a Given Material for Oxygen Service. Flammability and Sensitivity of Materials in Oxygen-Enriched Atmospheres, ASTM STP812, B. Werley, ed., American Society for Testing and Materials, West Conshohocken, PA, 1983, pp. 56–67.

5.0   Individual Principal Investigator Report: Miller and Wichman

5.1   Narrow Channel Apparatus as Microgravity Flame Spread Surrogate

Combustion of clear cast polymethylmethacrylate (PMMA) samples 10 cm long by either 1 or 2 cm wide with thicknesses ranging from 1 to 5 mm was investigated in opposed flow. Tests included both one-sided and two-sided burns. The samples were burned in a flow duct within the Microgravity Science Glovebox (MSG) on the International Space Station (ISS) to ensure true microgravity conditions. The experiment took place in opposed flow with a varying O_2 concentration (uncontrolled) and varying flow velocities (controlled). Flames are recorded on two cameras and later tracked to determine spread rate.

Assuming a linear profile between O_2 concentration at the start and the end of each test, we made graphs of O_2 concentration versus time for each test. From these, we created flammability maps showing the flame behavior at different O_2 concentrations and flow velocities. Additionally, we have conducted an extinction analysis, plotting the O_2 concentration against the flow velocity at the time of extinction with respect to type of test (one sided or two sided). Currently we are modeling combustion of flat PMMA samples in microgravity using Fire Dynamic Simulator (FDS; v5.5.3; National Institute of Standards and Technology (NIST)). The entire modeling for Burning and Suppression of Solids—II (BASS–II) is performed in Direct Numerical Simulation (DNS) mode because of the laminar conditions and small domain. The model employs the same test sample and MSG geometry as the experiment. The model predicts a higher flame spread rate than that observed in experiments. So, we look to modify the chemical kinetics and materials properties to improve the model. Also, we plan to do a domain study and grid sensitivity analysis in future.

5.2   Introduction

The NASA Burning and Suppression of Solids—II (BASS–II) tests examine the combustion of different solid materials and geometries in microgravity. While flames in microgravity are driven by diffusion and weak advection due to ventilation systems and crew movement, the current NASA spacecraft material selection test method (NASA–STD–6001 Test 1) (Ref. 1) is driven by buoyant forces since gravity is present. So, the BASS–II results will be used in comparison with ground-based experimental setups aimed at replacing NASA's current test method for screening materials used onboard spacecraft. The data gathered will also help us understand and know more about behavior of fires in space so that space travel can be made safer in the future. The BASS–II experiments have provided us with an extensive thick fuel microgravity database that did not exist previously. Previously, thick-fuel true microgravity data was obtained by Olson and others in a study involving Sounding Rocket experiments (Ref. 2). The study comprised a series of combustion experiments on polymethylmethacrylate (PMMA) at very low velocity opposed flow and external radiant flux.

The institutions taking part in BASS–II operations are Case Western Reserve University; University of California, Berkeley; NASA Glenn Research Center; San Diego State University; and Michigan State University (Ref. 3). There are three categories of samples: flat samples, rod samples, and a section of a large solid sphere. The flat sample materials will include acrylic films and sheets of different thicknesses, and a cotton-fiberglass fabric blend Solid Inflammability Boundary at Low-Speeds (SIBAL) fuel. The rod samples are made of black or clear acrylic and will provide solid fuel regression rates and extinction limits for both opposed and concurrent flow. The large solid spherical section, also made of acrylic, will be used to study ignition of thick materials and flame growth over the thick material.

5.3   Experimental Setup and Summary

The BASS–II hardware shown in Figure 5.1 comprises a small flow duct with an igniter and a small nozzle along with exchangeable fuel samples. The BASS–II flow duct is placed inside the Microgravity Science Glovebox (MSG) (255 L) (Ref. 5) onboard the International Space Station (ISS). A radiometer placed at the top measures the intensity of the flame. A fan is used to produce forced flow of air in the duct. Also present is an anemometer that measures the velocity of air entering into the duct. A Nikon digital camera (Nikon Corporation) looks through the top of the flow duct normal to the sample surface and a high-definition video camera uses a mirror to look through the front door of the duct at the edge of the flat sample (orthogonal to the high-definition camera). A total of 20 PMMA flat samples were burnt during the BASS–II experimentation (Table 5.1). The sample thickness varied from 1 to 5 mm thick. The samples burnt were all either 1 or 2 cm wide. All the burns are either one sided or two sided. The airflow was always opposed. Airflow speeds ranging from as low as 3 cm/s up to 20 cm/s were used in the flow duct.

Prior to the start of testing at each session, a crew member installs the hardware in the MSG. The fan calibration is set before the flame is ignited. Once ignited, the flame is allowed to stabilize at first and then the airflow is adjusted throughout the test. Fan speed, radiometer reading, and the time is monitored during the entire test. The airflow is turned off after the test. Videos and data are downlinked to Earth (Ref. 3). The still images and videos from the data are tracked using Spotlight–16 (NASA image tracking software) (Ref. 6). Data are then imported to Excel® (Microsoft®) to obtain flame spread rates. A graph of the position versus time for one of the tests is found in Figure 5.2. The black line in the plot represents the O_2 concentration profile during the duration of the test. A secondary y-axis shows the O_2 concentration in percent by volume. The red portion on the graph represents the part of experiment where the opposed-flow velocity was 10 cm/s. Similarly, the green and purple regions represent flow speeds of 6 and 5 cm/s, respectively.
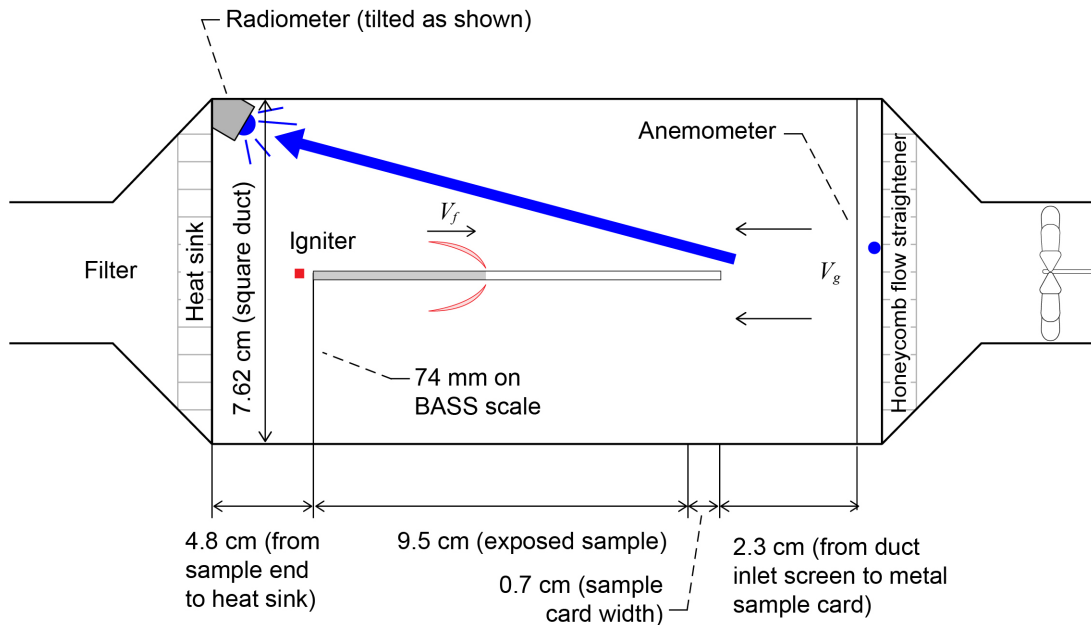
Figure 5.1.—BASS–II duct (Ref. 4). Absolute spread rate (V_f). Opposed-flow velocity (V_g).

TABLE 5.1.—TWENTY BURNING AND SUPPRESSION OF SOLIDS—II (BASS–II) TESTS

Test no.	Thickness, mm	Width, cm	One or two sides burning	Velocity, cm/s	Spread rate, mm/s	Burn time, min	Initial O_2, vol%	Final O_2, vol%
M1	1	2.2	1	9	0.071	6.4	22.2	21.9
M2	3	2.2	1	20 and 15	0.052 and 0.033	22.9	22.2	21.2
M3	5	2.2	1	10 and 20	0.029 and 0.024	20.1	20.8	19.7
M4	5	2.2	2	5 and 3	0.045 and 0.033	19.8	21.8	19.8
M5	3	2.2	2	10	0.071	27.2	22.2	19
M6	1	2.2	2	10 and 8	Not tracked	16.8	21.8	20.7
M7	1	1.2	2	10, 6, 5, and 3	0.106, 0.099, 0.083, and 0.07	18.4	18.9	18.4
M8	2	1.2	2	10, 6, and 5	0.057, 0.056, and 0.04	25.2	19.1	18.2
M9	3	1.2	2	14	0.025	16.8	18	17.6
M10	4	1.2	2	15 and 10	0.0373 and 0.03	30.5	20.1	18.6
M11	5	1.2	2	21, 15, and 13	0.048, 0.028, and 0.022	28.5	20	18.5
M12	2	2.2	2	12 and 10	Not tracked	16.2	21.7	20.4
M13	4	2.2	2	6, 5, and 4	0.047, 0.035, and 0.033	20.5	20.8	19
M14	2	2.2	1	15, 14, and 10	0.0624, 0.055, and 0.0353	15.4	22.2	21.6
M15	4	2.2	1	20	0.045	22.0	21	20
M16	1	2.2	2	5, 3, and 2	0.144, 0.1309, and 0.1062	8.4	19.2	18.7
M17	2	2.2	2	5, 4, and 3	0.053, 0.042, and 0.026	30.7	18.8	17.1
M18	3	2.2	2	10 and 8	0.026 and 0.013	25.5	17.9	16.8
M19	4	2.2	2	10 and 6	0.027 and 0.0159	25.7	19	17.4
M20	5	2.2	2	10	0.012	16.5	18	17.4
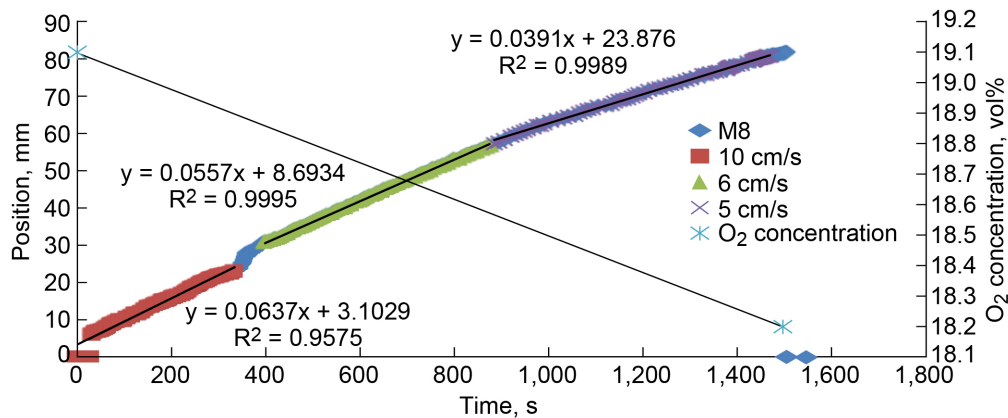
Figure 5.2.—Position versus time graph for test M8. Red, green, and purple symbols at constant flow are overlaid on overall test sequence blue symbols.

Figure 5.3.—M17 still images at different flow velocities. Last image is just before extinction as flow is turned off.

Figure 5.3 shows flame still images taken by the Nikon camera during one experiment as the flow is turned down incrementally. O_2 is also decreasing slightly during the experiment. Soot decreases as flow decreases, and flame is all blue prior to extinction.

Flat PMMA samples have been burned in the narrow channel apparatus (NCA) to simulate microgravity conditions (Refs. 7 and 8). In the flight experiment, five thicknesses of PMMA slab (1 to 5 mm), in two widths (1.2 and 2.2 cm), and one-sided versus two-sided burning were studied in various O_2 concentrations (Refs. 9 to 11). Flow velocity was varied to obtain spread rates at different flow conditions. Some tests lasted more than 30 min. The goal of these experiments is to begin gathering data for sample materials of finite thickness, in which case the sample regression and consumption plays a more important role than when the sample is extremely thin (Refs. 7 and 8). The objective was to obtain microgravity data for flame spread over a thick fuel and compare the results to data from the normal-gravity NCA that uses a small-height flow duct to suppress buoyant flow. Quenching extinction data was also obtained at finite flow rates for most of the tests. Preliminary comparisons have been published (Refs. 7 and 10).

There was a clear difference in how the material burned as ambient O_2 concentration was decreased. At near-air O_2 concentrations, the flames spread over the fuel surface without burning through for both one-sided and two-sided samples. As O_2 concentrations were reduced to approximately 19 percent however, the flames could no longer spread across the surface of the two-sided fuel, but rather completely consumed the fuel from the trailing edge. This is shown in Figure 5.4 for 2-mm-thick by 2.2-cm-wide samples. Note that the velocities listed are the quenching velocities.

Figure 5.4(a) and (b) show regression behavior that is similar to what is found in normal-gravity downward flame spread experiments. The fuel is completely consumed a few millimeters downstream of the leading edge of the flame. The curved shape of the melt layer occurs because of heat losses to the holder sides. There is a similarity to the last image in Figure 5.3 for a much thinner material, down to the ring-shaped tail. The flame shape in Figure 5.4 also shows curvature due to heat losses to the sample holder, increasing as the forced-flow velocity decreases.

Figure 5.4(c) and (d) are of a higher O_2 level, showing how the flame spread across the material, leaving behind a very long bubbled sample. The two sides of the flame extinguished separately on each side of the sample, within a few seconds of each other. Figure 5.4(e) and (f) is a single-sided sample whose flame was quite weak despite the high flow rate and the high O_2 concentration. Heat loss to the metal substrate clearly weakened this flame. It too left behind a long bubbled sample.

Spread rates decrease as thickness increases, and also decrease as forced-flow velocity decreases (Ref. 10). Figure 5.5 shows that, for the one-sided samples, there was a clear trend that as thickness increased, the O_2 concentration for extinction decreased but the forced-flow velocity for extinction increased. For the two-sided samples that spread across the surface, there was not a clear trend with thickness, but the extinction velocities were significantly lower than for the one-sided samples, indicating that heat loss to the substrate for the one-sided flame was significantly greater than the two-sided flame without a substrate. There was no clear dependence on thickness for the extinction limits for both the 1- and 2.2-cm-wide regressing samples, but the 1.2-cm-wide samples did extinguish approximately 1 percent O_2 higher than the 2.2-cm-wide samples, most likely due to increased relative heat losses to the sample holder.
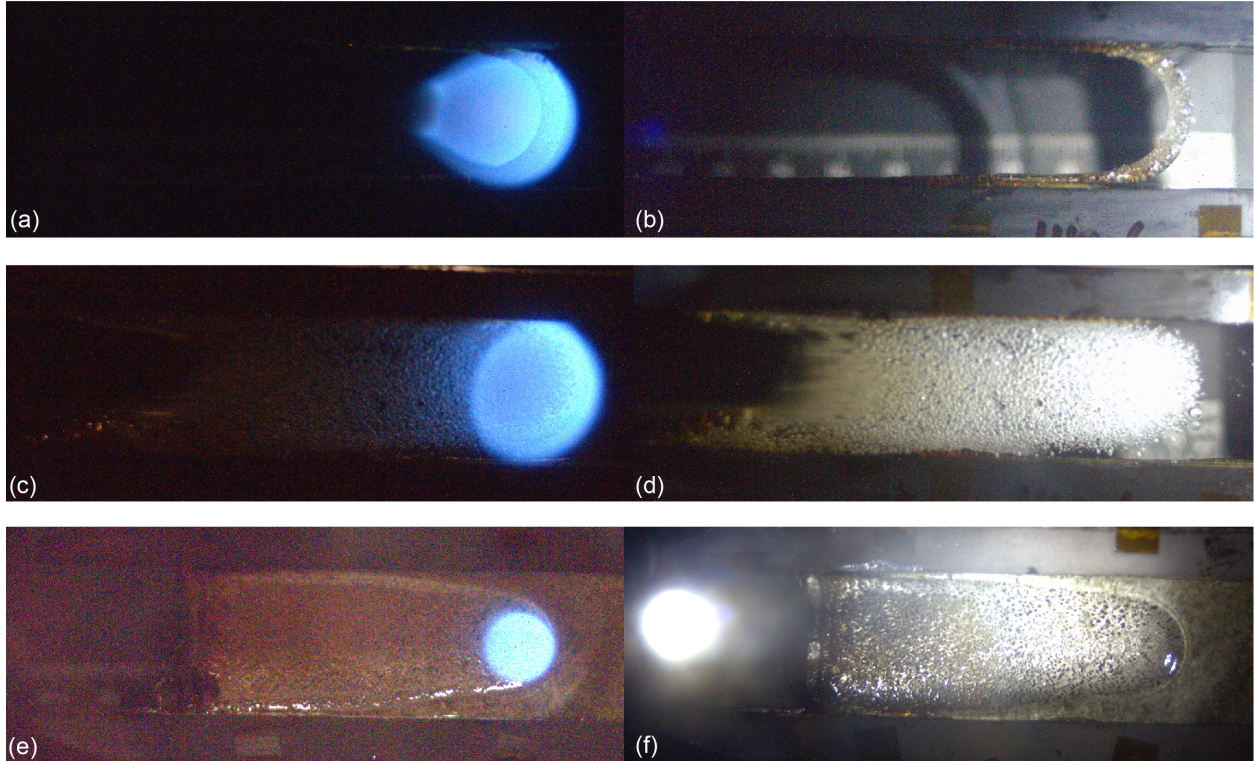
Figure 5.4.—Polymethylmethacrylate (PMMA) slab tests. 2-mm-thick by 2.2-cm-wide PMMA slab tests.
(a) Preextinction flame, two sided, 18.8 percent O_2, 3 cm/s. (b) Postburn sample from (a). (c) Preextinction flame, two sided, 21.7 percent O_2, <1 cm/s. (d) Postburn sample from (c). (e) Preextinction flame, two sided, 22.2 percent O_2, 11 cm/s. (f) Postburn sample from (e).
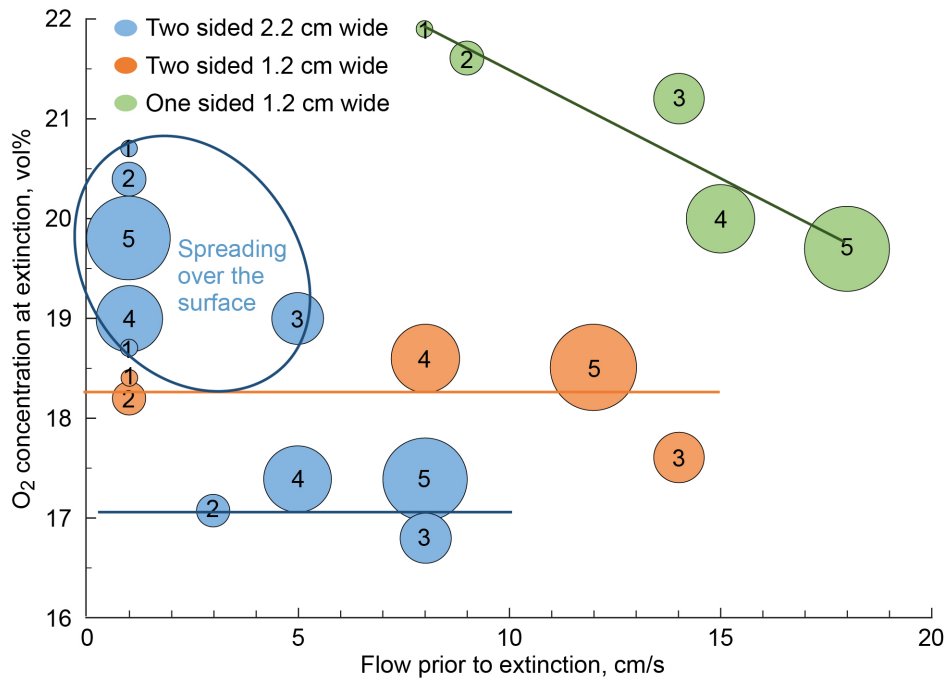
Figure 5.5.—Extinction limits for Miller and Wichman tests. Symbol sizes and numbers reflect fuel thickness, and other geometry variations are noted in legend.

5.4   Oxygen Concentration Analysis

The BASS hardware does not have a provision to measure O_2 concentration throughout the entire experiment. We have O_2 data available at only the start and end of the test. Assuming a linear profile between these two points; we made O_2 concentration graphs for each test (see Figure 5.2 for an example). This helps us estimate the O_2 concentration at any given time during the experiment. Next, the average O_2 concentration was calculated for each flow speed. Plots were created summarizing the average O_2 concentration (vol%) versus opposed-flow speed (cm/s) for the one-sided and two-sided tests separately. The data points on these graphs are characterized according to the flame spread rate. Additionally, the data points at which the flame extinguishes are also added to the summary graphs to see the effects of varying O_2 concentration through the duration of test. This analysis will serve as a reference point when more BASS operations are conducted in the future.

5.5   Numerical Modeling

We are modeling combustion of flat PMMA samples in microgravity using Fire Dynamics Simulator (FDS; v5.5.3; National Institute of Standards and Technology (NIST)) (Ref. 12), which is a computational fluid dynamics model of fire-driven fluid flow. The entire modeling for BASS–II is done in Direct Numerical Simulation (DNS) mode because of the laminar conditions and small domain. The model employs the same test sample and approximate BASS flow duct geometry as the experiment. The results are viewed in Smokeview (NIST), which is a visualization package that goes with FDS. The experimental data gave upstream velocity at several points using an anemometer. A flow profile for the inlet velocity is obtained using MATLAB® (The MathWorks, Inc.) and input into the model (note that the measured flow profile for the BASS–II duct is quite irregular). Figure 5.6 shows the geometry setup for the model.
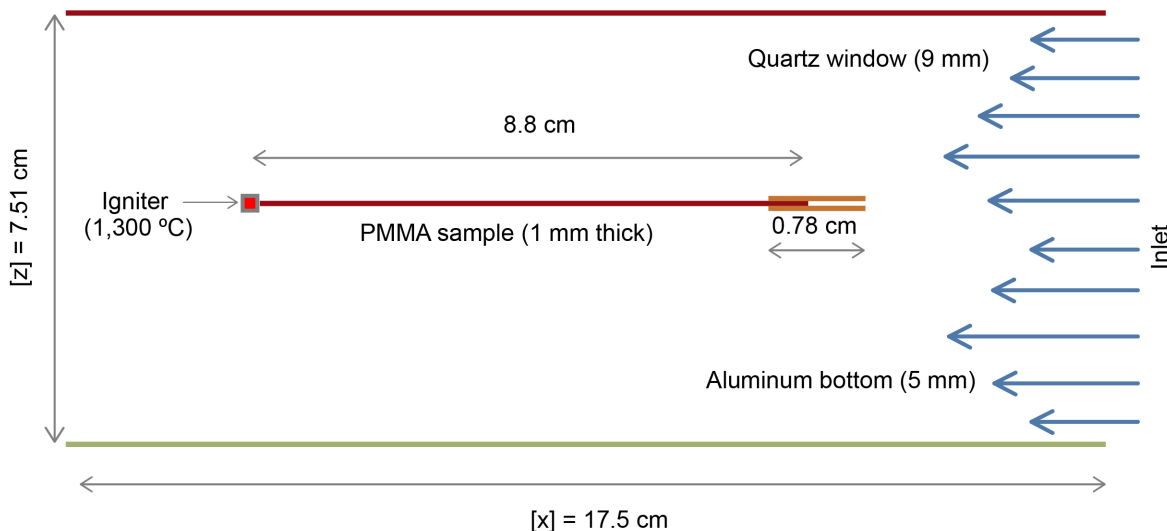
Figure 5.6.—Geometry setup for two-dimensional model. Polymethylmethacrylate (PMMA).
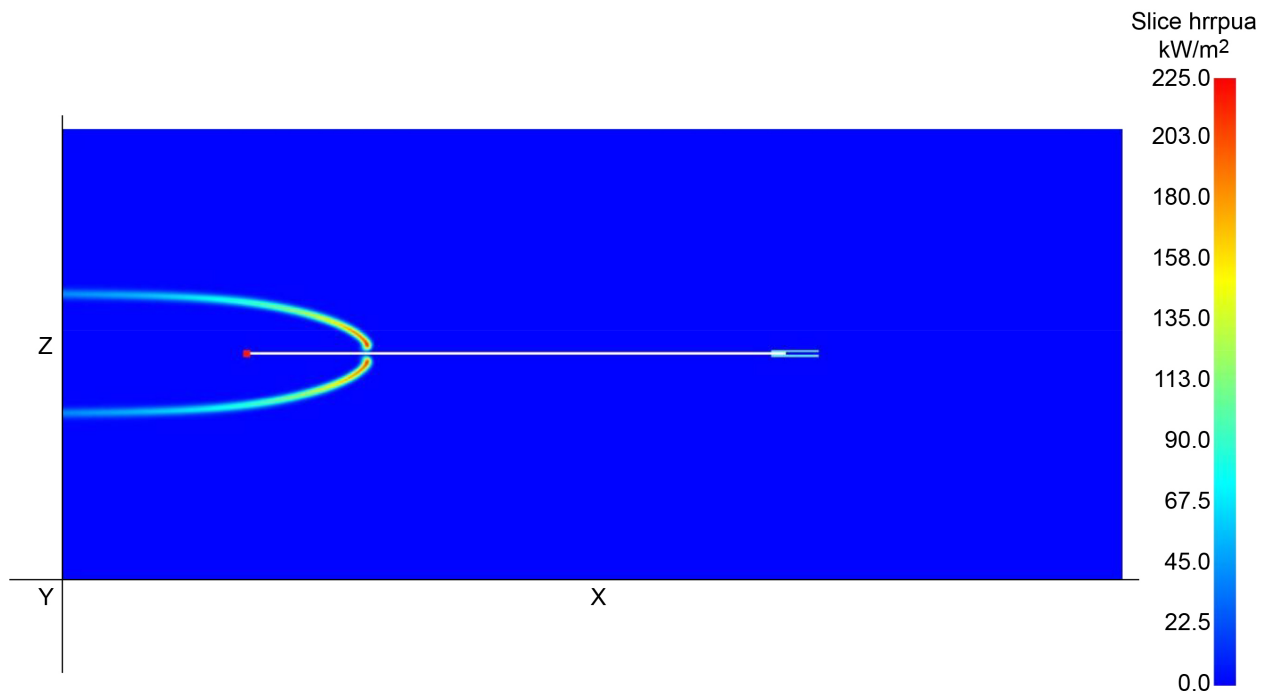
Figure 5.7.—Smokeview (National Institute of Standards and Technology (NIST)) heat release rate in kW/m^2.

For this case, the fuel sample used was 3 mm thick. The averaged opposed-flow rate is 10 cm/s. A grid size of 0.389 mm in the x direction and 0.376 mm in the z direction was used for the computation. At the start of simulation, we have only cold flow. The flow is allowed to stabilize for 1 s of simulation time and then the igniter is turned on. It is on for around 5 s and then ramped down and finally turned off. Figure 5.7 shows the heat release rate (HRR) per unit area profile for this case. The maximum HRR obtained in the two-dimensional simulation was 225 kW/m^2. Smokeview can also be used to obtain quantities like temperature, mass flux, net heat flux, etc.

5.6   Experimental and Modeling Results

Currently, we have formed summary graphs for one-sided and two-sided BASS–II experiments that show certain behaviors. Shown in Figure 5.8 is a summary graph for two-sided burns with data from the model as well.

As you see, the graph illustrates that the higher the flow velocity, or the thinner the sample, the higher the spread rate is. The triangles represent the two model data points, which show a much higher spread rate than experiments (Refs. 9 and 10). On further observation, we can see that the plot exhibits a clear width effect. For thin fuels (1-mm-thick), especially, the 2-cm-wide samples show a higher spread rate than the 1-cm-wide samples. These trends will help researchers decide sample sizes for future planned experimentation aboard ISS.

As shown in Figure 5.9, the one-sided samples burned more slowly than the two-sided samples, and also needed a higher opposed-flow rate to keep burning. Symbol size reflects the estimated O_2 concentration at the velocity, based on an assumed linear O_2 decay during the test.
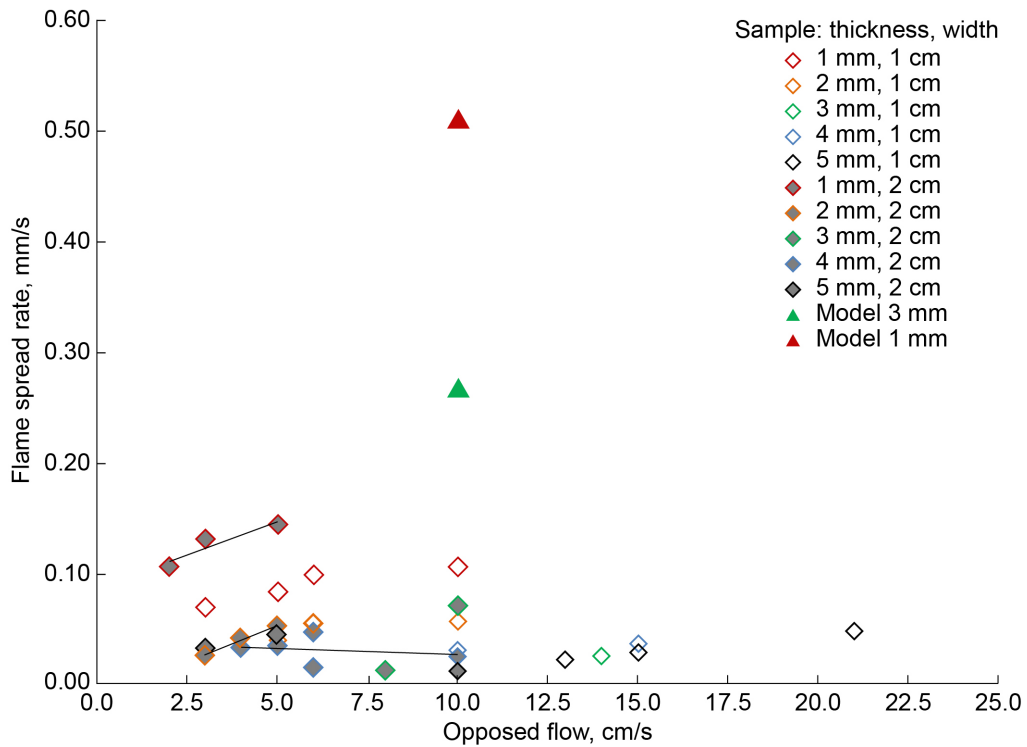
Figure 5.8.—Flame spread rate versus opposed-flow velocity (two-sided tests).
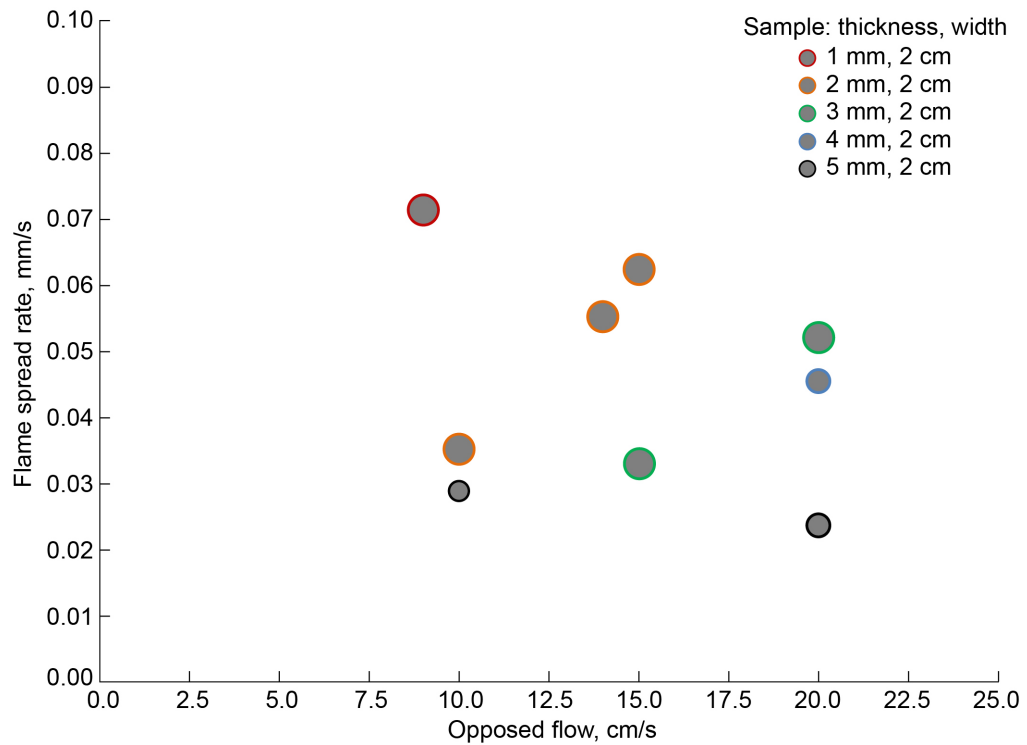
Figure 5.9.—Flame spread rate versus opposed-flow speed (one-sided tests).

5.7   Conclusions

The Burning and Suppression of Solids (BASS) experiments gave some of the first ever data regarding combustion of thick fuels in microgravity. The two-sided summary graphs show that for thin fuels, sample width affects the spread rate. In general, the flames spread faster for two-sided burns compared to one-sided burns. The greater the thickness of the fuel, the greater is the time taken for the flame to spread and so the lower is the spread rate. This is clearly evident in the different thicknesses that we have tested. The model currently predicts much higher spread rates than those obtained in the experiment. We need to modify chemical kinetics and material properties to improve model accuracy and results.

5.8   Acknowledgments

5.9   References

1. National Aeronautics and Space Administration: Flammability, Offgassing, and Compatibility Requirements and Test Procedures. NASA–STD–6001B, 2011.
2. Olson, S.L., et al.: Sounding Rocket Microgravity Experiments Elucidating Diffusive and Radiative Transport Effects on Flame Spread Over Thermally Thick Solids. Combust. Sci. Technol., vol. 176, no. 4, 2004, pp. 557–584.
3. Reckart, T.A.: Space Flight System at GRC: Burning and Suppression of Solids (BASS). National Aeronautics and Space Administration, 2014. https://www1.grc.nasa.gov/space/iss-research/msg/bass/ Accessed June 21, 2021.
4. Bhattacharjee, S.: Research on Flame Spread at SDSU: The Bhattacharjee Group. http://flame.sdsu.edu/ Accessed August 27, 2015.
5. Wikipedia contributors: Microgravity Science Glovebox. Wikipedia, The Free Encyclopedia, 2021. https://en.wikipedia.org/wiki/Microgravity_Science_Glovebox Accessed June 22, 2021.
6. Klimek, Robert; and Wright, Ted: Spotlight–8 Image Analysis Software. NASA/TM—2006-214084, 2006. https://ntrs.nasa.gov
7. Bornand, G.R., et al.: Opposed-Flow Flame Spread in a Narrow Channel Apparatus Over Thin PMMA Sheets. Presented at the 8th U.S. National Combustion Meeting, paper 070FR–0418, 2013.
8. Bornand, Garrett Randall: Polymethylmethacrylate Combustion in a Narrow Channel Apparatus Simulating a Microgravity Environment. M.S. Thesis, San Diego State Univ., 2015.
9. Winter, Kelsey Gloria: Experimental Measurements of PMMA Combustion in Simulated Microgravity Along the Normoxic Curve. M.S. Thesis, San Diego State Univ. 2019.
10. Shah, Tirthesh J., et al.: Modeling and Analysis of Intermediate Thickness PMMA Sheets Burning in Microgravity Opposed Flow. Presented at the Western States Section of the Combustion Institute—Fall 2015 Meeting, paper 134HC–0056, 2015.
11. Shah, Tirthesh Jayesh: Flame Spread Over Thick Polymethylmethacrylate Samples in a Simulated and Actual Microgravity Environment. M.S. Thesis, San Diego State Univ., 2016.
12. McGrattan Kevin, et al.: Fire Dynamics Simulator (Version 5) User's Guide. NIST Special Publication 1019–5, 2007.

6.0 Individual Principal Investigator Report: Olson

6.1 Microgravity Flammability Boundary for Polymethylmethacrylate Rods in Axial Stagnation Flow: Experimental Results and Energy Balance Analyses

6.1.1 Abstract

For the first time, a series of concurrent rod flammability tests were conducted in microgravity aboard the International Space Station. A small flow duct was used to create 0- to 55-cm/s flows past the three sizes of clear and black polymethylmethacrylate rods. The ambient O_2 concentration in the Microgravity Science Glovebox was varied from 13.6 to 22.2 percent. O_2, CO_2, and CO gas sensors provided initial and final readings for each test and indicate that the flames are globally stoichiometric at higher O_2 concentrations, but become more globally fuel rich as the minimum O_2 concentration is approached due to excess pyrolyzate leakage out of the open tail of the hemispherical flames. Quenching extinction occurs at very low forced flows, where the flame shrinks to a hemispherical blue flame and oscillates with increasing amplitude just before going out. Blowoff extinction is initiated by the formation of a hole in the flame sheet in the stagnation region of the flame. A critical Damköhler number formulation is applied across the flammability boundary, and the critical flame temperature is derived. This critical flame temperature is then used in a Nusselt number correlation to estimate the convective heat flux to the stagnation region of the rod. A model of surface energy balance is formulated that uses the critical flame temperature and convective heat flux to derive the mass burning rate along the boundary. The rod regression rates calculated from this model compare favorably with the experimental measurements. The surface energy balance reveals that along the blowoff branch, heat losses are negligible whereas in the quenching region, surface radiative loss dominates. At the bottom of the flammability map, the transition from blowoff to quenching occurs when the convective flows become the same order of magnitude as diffusive flows, shifting the critical Damköhler number from residence time limitations to diffusive time limitations.

Symbols

a	stretch rate, $3/2\ U/r\ (r/r_o)^{1/2}$, s^{-1}
a_s	absorptivity of the PMMA surface
A	area, cm^2
A_r	cross section of rod
A_h	hemispherical rod tip surface area $= 2\ A_r$
Bi	Biot number, $h\ r/\lambda_s$
D	diameter
Da	Damköhler number, Equation (6.2), normalized by 7.35×10^7 (Ref. 1)
E	activation energy, 1.45×10^5 J/mol
F	surface to flame hemispherical radiative view factor, $= 0.93$
h	heat transfer coefficient
L	length of the flame, stagnation standoff to flame tails, cm, or rod initial length
L_o	rod initial length, 5.9 cm
L_v	latent heat of vaporization, 1700 J/g
$\dot{m}''$	hemispherical surface average burning rate, g/cm^2 s, $=V_r\ \rho_s \cdot A_r/A_h$
Nu	Nusselt number, convective heat flux and conductive heat flux, Equation (6.3)
Pe	Peclet number, $L_o V/\alpha_s$
Pr	Prandtl number of air at T_m, 0.69
$\dot{q}''$	heat flux, W/cm^2, Equation (6.4)

$\dot{q}$	heating rate, W, Equation (6.4)
r	radius, cm
R	ideal gas constant, 8.314 J/(gmol K)
Re	Reynolds number, UD/v
s	flame standoff distance, measured to outer bright cyan zone of flame, cm
T	temperature, T_m = 800 °C
t	time, s
t_s	solid-phase response time, 0.7 r^2/α_s, s
ΔT	$T_{crit} - T_s$
U	forced-flow velocity, cm/s
U_D	diffusion velocity, 2 cm/s
V_r	measured rod tip regression velocity, cm/s
X	percent by volume (mole percent)
Y	nondimensional $y = y/L$
y	distance along the rod, cm
α	thermal diffusivity of air at T_m, 1.19 cm²/s, of PMMA 1.2×10^{-3} cm²/s
β	preexponential constant, 1.3×10^{16} cm³/ gmol s
ε	surface emissivity, 0.8 surface, 0.02 gas, also surface absorptivity via Kirchhoff's law
λ	thermal conductivity of air at T_m, 0.000577 W/cm K, or of solid at T_∞, 2.09×10^{-3} W/cm K
v	kinematic viscosity at T_m, 0.822 cm²/s
ρ	gas density of air at T_m, 0.0441 g/cc, solid density 1.19 g/cc
θ	nondimensional temperature
σ	Stefan-Boltzmann constant, experimental, 5.729×10^{-12} W/cm² K⁴
ℓ	thermal length scale, cm, $(\alpha_g/a)^{1/2}$
τ	nondimensional solid phase response time, $= t/t_s$

Subscripts

conv	convective
crit	flame extinction condition
D	diffusion
f	fuel, assumed unity at the fuel surface
g	gas
ign	ignition
m	mean, at 800 K
o	base size of rod, 0.318 cm
O_2	oxygen
rad	radiative
s	surface, at 675 K, or solid
tot	total feedback to surface
vap	vaporization
∞	ambient, at 300 K

6.1.2   Introduction

Early work (Ref. 2) on flammability limits has demonstrated that using a hemispherical stagnation flow geometry provides a good way to obtain the flammability limits of various fuels as a function of upward flowing oxidizer gas. Similar limiting O_2 concentrations (13 to 14 percent) and flame temperatures (1,450 to

1,500 °C) have been noted for many heavier hydrocarbons. The stagnation flow geometry is amenable to asymptotic analyses (Refs. 3 and 4), numerical modeling (Refs. 5 to 7), and experimental blowoff extinction work for both axisymmetric and two-dimensional geometries (Refs. 8 to 11).

The importance of radiative heat loss was examined (Refs. 4 and 5) and found to primarily reduce the flame temperature. The flammability map in terms of O_2 and stretch rate a (Ref. 5) was shown to consist of a blowoff and new quenching branch where the low power flame (due to the reduced temperature) is too weak to compensate for the surface radiative heat loss. It was pointed out that this is likely only observable in microgravity. Experimentally, the first observed solid fuel quenching extinction limits were observed in microgravity opposed-flow flame spread tests over thermally thin cellulose fuel (Ref. 12).

Very few solid fuel stagnation flow extinction studies have been performed in reduced gravity to eliminate buoyant flow effects. Concurrent-flow flame spread with plastic rods was tested aboard the Mir Space Station in the Skorost hardware (Ref. 13). The extruded polymethylmethacrylate (PMMA), polyoxymethylene (POM), and high-density polyethylene (HDPE) rods all showed the same tendency to melt beneath the flame and form accumulating molten balls on the stagnation end of the rod, with the flame wrapped around the molten ball. At low flows, the small hemispherical flame at the stagnation tip of the rod propagated simply through rod regression (bulk burning) rather than through a concurrent flame spread along the rod. Flames survived at airflow less than 1 cm/s.

This stagnation geometry was selected for this work to study material flammability in microgravity. Concurrent-flow flame spread tests burned an axisymmetric cylindrical PMMA rod having low heat losses to the downstream sample support pin. Other intrinsic heat losses (surface radiation loss and conduction along the rod axis) will be estimated in Section 6.1.5.5. The objective of these tests was to obtain the lower portion of the concurrent microgravity flammability map as a function of ventilation flow and ambient O_2 concentration.

6.1.3 Experimental Setup

The BASS–II hardware used for these tests has been described in detail in Reference 14. It consists of a black-anodized flow duct that provides a low-reflection backdrop for imaging flames with a color video camera at 30 frames per second and an orthogonal digital still camera (4,320 by 2,968 pixel images) at ~1 frame per second. The tests were performed in the 250-L free volume Microgravity Science Glovebox (MSG) in the Destiny Lab of the International Space Station (ISS). The hardware setup is shown in Figure 6.1. The flow duct measured 7.6 by 7.6 by 17 cm with rounded internal corners for smooth laminar flow through the duct. The front window opened to install samples and igniters. A top window allowed still camera imaging. A noncalibrated radiometer in the downstream top back corner of the flow duct provided a relative flame strength reading at 5 Hz. The three primary variables were flow velocity through the duct, PMMA rod radius, and O_2 concentration of the working volume.

The flow was generated using a small variable-speed fan at the upstream end of the duct. The voltage to the fan was displayed and could be set. Up to two flow restrictors could be used at the fan inlet to increase the pressure drop and thus change the output flow range. With no restrictors, the maximum flow velocity was ~55 cm/s, and with two restrictors this was reduced to a maximum of ~35 cm/s. The flow then passed through a honeycomb flow straightener and an inlet screen to reduce swirl. An omnidirectional spherical air velocity transducer (TSI Incorporated 8475) was positioned between the honeycomb and the screen and was used to measure the steady-state flow through the duct. The air velocity transducer probe had a response time of approximately 1 min and its digital display only read out to the units place (no decimals) yielding an effective resolution of ±0.5 cm/s. A fan calibration was performed at the end of each operational day to associate the fan voltage with the flow velocity for each flow restrictor, after the fan had adequate time for warmup.

To obtain the desired O_2 concentration for the test, the initial ISS air filling the MSG working volume was diluted using N_2 as described in Reference 14. A continuously stirred tank reactor (CSTR) model was used to time the N_2 flow to obtain the desired initial O_2 concentrations down to as low as 13.6 percent O_2. O_2 sensor readings, calibrated with the onboard mass spectrometer, provided initial and final O_2 concentrations for each test. The readings were used to verify the CSTR model and measure the O_2 consumption within the test. Onboard CO and CO_2 sensors were also used to provide initial and final product gas concentrations for each test, to evaluate the average burning efficiency for each test.

Clear cast PMMA rods, shown in the top left corner of Figure 6.1, were mounted inside the flow duct for each test. The stagnation tips of the rods were initially hemispherical. Three radii r of clear cast PMMA cylindrical rods were tested (primarily 0.318 cm; but also 0.476 and 0.635 cm). Two black PMMA rods ($r = 0.318$ cm, blackened with a small amount of soot during polymerization) were also tested, but no obvious differences in flammability were noted compared to the clear rods.

A control box external to the MSG allowed the astronaut to dynamically change the fan voltage, set the N_2 flow, turn the igniter on and off, and adjust the radiometer gain, as shown in the lower right corner of Figure 6.1. The Burning and Suppression of Solids—II (BASS–II) science team monitored the real-time video on the ground and talked directly to the astronaut running the experiment, calling up real-time flow changes, still camera imaging adjustments, ignition instructions, etc.

The samples were ignited manually by the astronaut at the initially hemispherical stagnation tip with a hot-wire igniter, typically at a flow speed of 5 cm/s. The hook-shaped 29-gauge Kanthal® wire igniter had a resistance of 1 Ω and was powered by a 4-A circuit. Ignition times to achieve sustained flames varied and could be as long as 230 s. At very low O_2 concentrations, even longer ignition times (up to 500 s) did not result in a sustained flame even when the initial flow was varied up to 10 cm/s and down to 2 cm/s. Once successfully ignited, the flow was reduced incrementally until the flame extinguished via
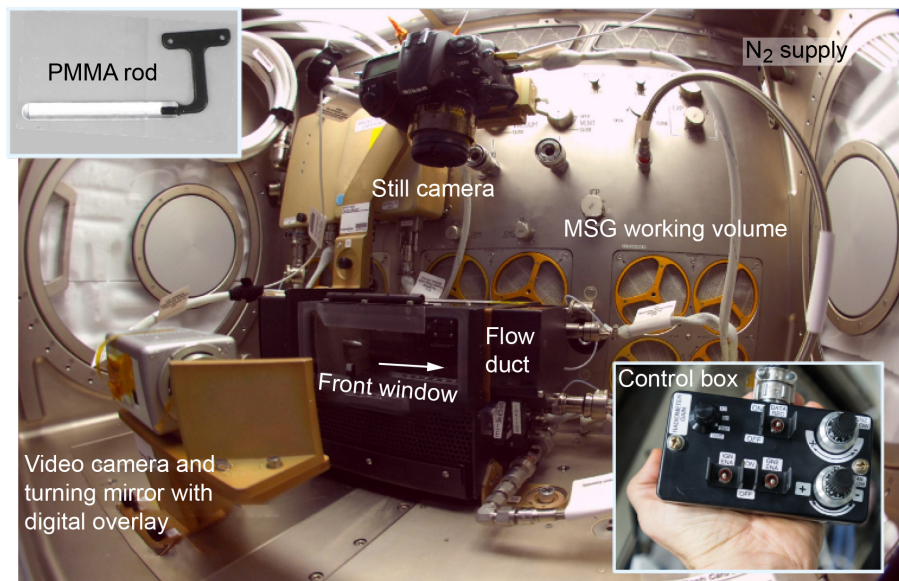
Figure 6.1.—Hardware used for Burning and Suppression of Solids—II (BASS–II) tests. Gas sensors are not shown. Polymethylmethacrylate (PMMA). Microgravity Science Glovebox (MSG).

quenching. For blowoff tests, the flow was increased until blowoff occurred. After each test, there was a minimum of 9 min for cooldown to safe sample touch temperatures before the setup of the next experiment could begin.

Complementary 5.18-s Zero Gravity Research Facility blowoff drop tests were conducted to compare with long-duration microgravity, using the microgravity wind tunnel drop rig (Ref. 15). The rod was ignited in 1g to establish a flame at a flammable O_2 flow. The gas flow source was switched to a reduced O_2 level and the package dropped just as this test oxidizer flow reached the flame zone. Blowoff extinction could be observed in the drop tests because the characteristic time for extinction was less than the available drop time. However, it was not possible to observe quenching extinction because its characteristic time was substantially longer than the available drop time.

6.1.4   Experimental Results

6.1.4.1 Ignition Delay Time

The astronaut would manually position the igniter within a millimeter of the tip of the rod and activate the igniter until a stable flame was achieved. It could be difficult to see the flame in the glare of the igniter, so the astronaut would turn off the igniter to assess flame viability. If the flame appeared to be going out, the astronaut would quickly turn the igniter back on to strengthen the flame and again check flame viability after a few seconds of applying power. This igniter on and off cycle might occur several times in a given test. The ignition delay (t_{ign}) in each test was defined as the time from when the igniter was first turned on to the last time the igniter was turned off and a stable flame persisted. Ignition generally occurred at a forced flow of 5 cm/s, so the ignition delay is plotted in Figure 6.2 against the initial O_2 concentration alone. The symbol sizes reflect the initial rod radius. Because the igniter is positioned and activated manually, there is some inherent scatter in the ignition time, but some trends are clear.

At higher O_2 concentrations, ignition occurred within approximately 40 s. Below an initial O_2 concentration of 16 percent, the ignition delay time increased significantly. Larger rods take longer to ignite, especially at lower O_2 concentrations (up to 230 s). This suggests that the weaker flames at low O_2 cannot be sustained when the fuel rod is cold because too much of the heat from the flame is lost to conduction into the fuel. Only after a significant ignition time does the initially cold fuel rod become warm enough to allow the flame to persist. Section 6.1.5.5 examines the importance of conductive heat loss down the rod.

Below an initial O_2 concentration of ~14.5 percent O_2, a sustained ignition could not be achieved even though flames were observed when the igniter was on and briefly after the igniter was turned off before extinguishing.

On the right axis of Figure 6.2, the ignition delay is normalized by the characteristic solid phase response time ($t_s = 0.7\ r^2/\alpha_s$) where α is the thermal diffusivity of the solid. If the sample is not ignited within this nondimensional time τ (the empirical factor 0.7 is selected so that $\tau = 1$ at the ignition limit), it is likely not flammable, as shown for all values $\tau \geq$ ~1 that fall below the ignition limit of ~14.5 percent O_2.

Despite this limiting O_2 concentration for ignition, flames ignited at a higher O_2 survived to final O_2 concentrations as low as 13.6 percent O_2, indicating that the high heat loss to the initially cold rod will quench a postignition flame while a developed solid phase temperature profile allows a sustained flame down to these low ambient O_2 concentrations.

This difference between O_2 ignition limits and O_2 extinction limits is an important factor to consider for a flammability test. For example, NASA's Test 1 (Ref. 16) is an upward flame spread test that has a fixed ignition time of ~25 s, which is shown in Figure 6.2 as the bottom shaded region. If the material is

not ignited by this time, it passes the test. However, as one can see from Figure 6.2, a longer ignition time may successfully ignite the material, especially at the lower O_2 concentrations.
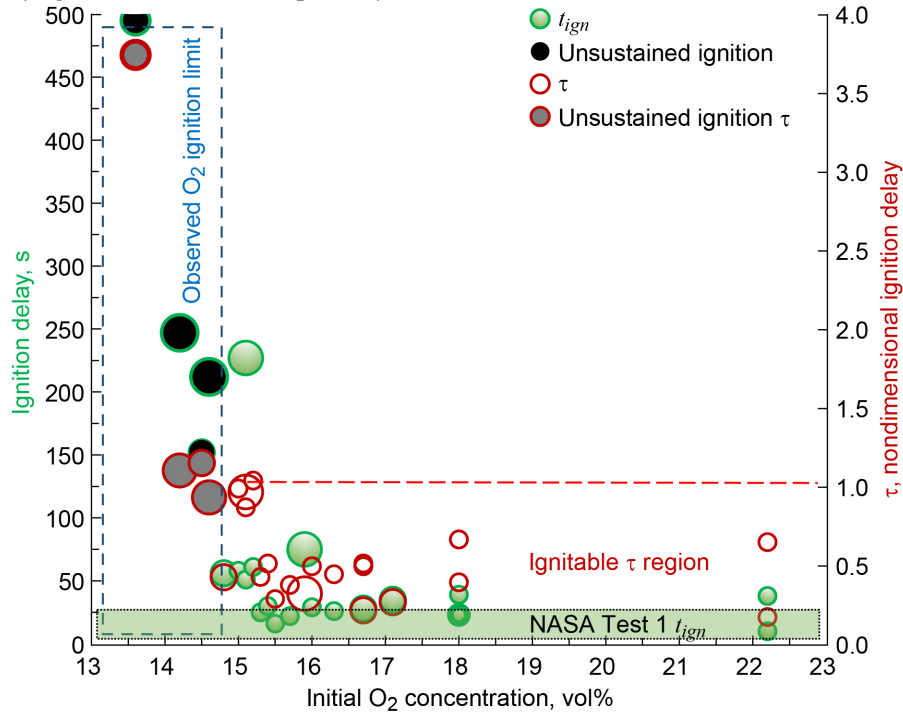
Figure 6.2.—Ignition delay time (left axis) and nondimensional ignition delay time τ (right axis) as function of initial O_2 concentration. Successful ignitions occur in nondimensional ignitable region, and with ignition delay times as long as 230 s. NASA Test 1 25-s ignition time may be too short for flammability test and so may be an ignition test.

6.1.4.2 Quenching Extinction

Samples burned within the flow duct and the combustion products exited the duct and mixed with the gas in the 250-L free working volume of the MSG, so the O_2 very gradually decreased during the test. To determine the quenching limit, the flow was decreased incrementally, and the solid-phase temperature distribution was allowed to equilibrate to the new flame for at least 100 s before the flow was changed again, to ensure each flame was steady. Quench tests lasted up to 28 min. Near-quenching flames for each rod size are shown in Figure 6.3(a) to (c). Flow and O_2 are not the same, but each represent the lowest O_2 test for that rod size. These all-blue flames are roughly hemispherical in shape.

Figure 6.4 shows a detailed time history of flame measurements (flame length, width, standoff distance, aspect ratio, rod tip position, and radiometer reading) of the lowest O_2 quenching test, where the initial O_2 setting was 14.8 percent O_2 (by volume) and the final O_2 reading was 13.6 percent O_2. The prequenching flame from this $r = 0.476$ cm rod radius test is the center top image in Figures 6.3. The flow was incrementally decreased throughout the test, as shown by the red stepped line. The flame length stopped growing at the 2- to 1.5-cm/s flow change, and shortly thereafter the rod regression reached an apparently steady-state regression rate of 0.0385 mm/s.

Flame measurements show that the flame standoff distance is nearly constant. The flame length asymptotes down to nearly constant length at each subsequent flow until the last one leading to extinction. The flame length and radiometer signal track each other very closely. The flame width shows a smooth

increase up to the 2- to 1.5-cm/s flow change, and then a slow decrease until the last flow change where it decreases more quickly. The aspect ratio (L/W) decreases incrementally to 0.5 at extinction, indicating a hemispherical flame at the quenching limit. Quenching occurred over 100 s after the last flow change, which is on the order of the solid-phase response time t_s. The cause of quenching extinction is evaluated further in Section 6.1.5.3.
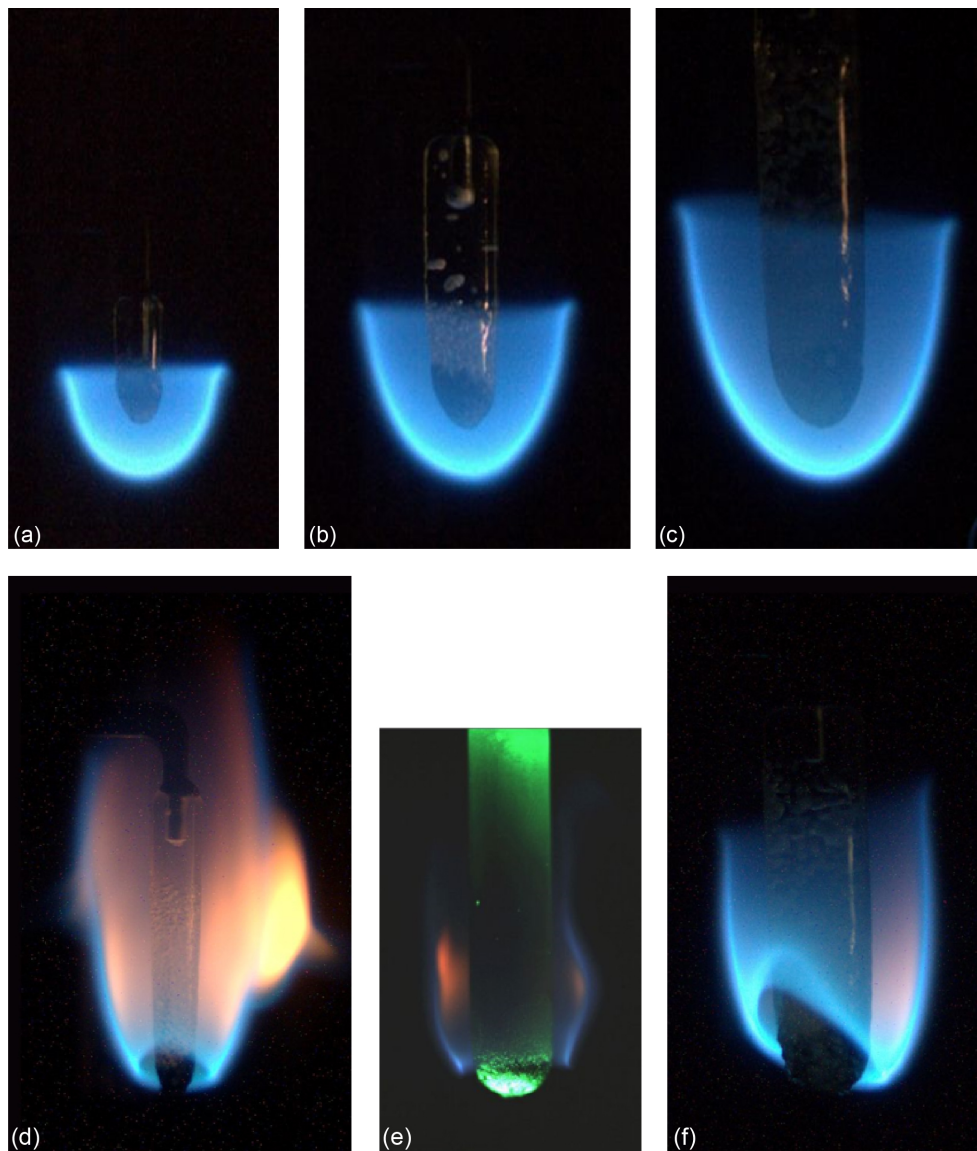
Figure 6.3.—Representative limit flames for three rod sizes tested. Near-quenching limit flame (a) Radius r = 0.318 cm. (b) r = 0.476 cm. (c) r = 0.635 cm. Blowoff after stagnation tip opens up. (d) r = 0.318 cm. (e) r = 0.476 cm. (f) r = 0.635 cm.
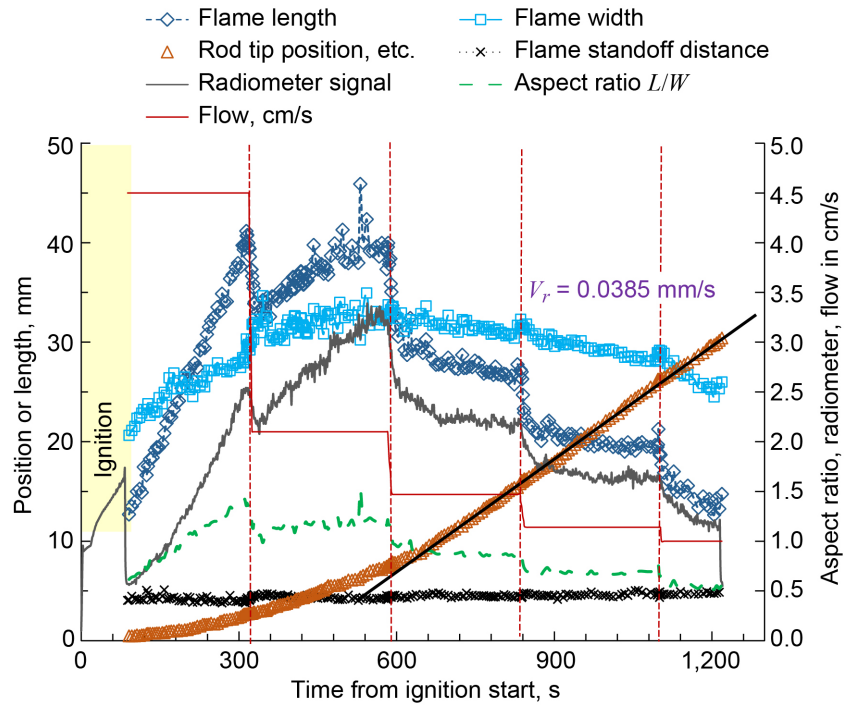
Figure 6.4.—Time history of flame measurements and flow from lowest O_2 quenching test for 0.476-cm-radius rod.
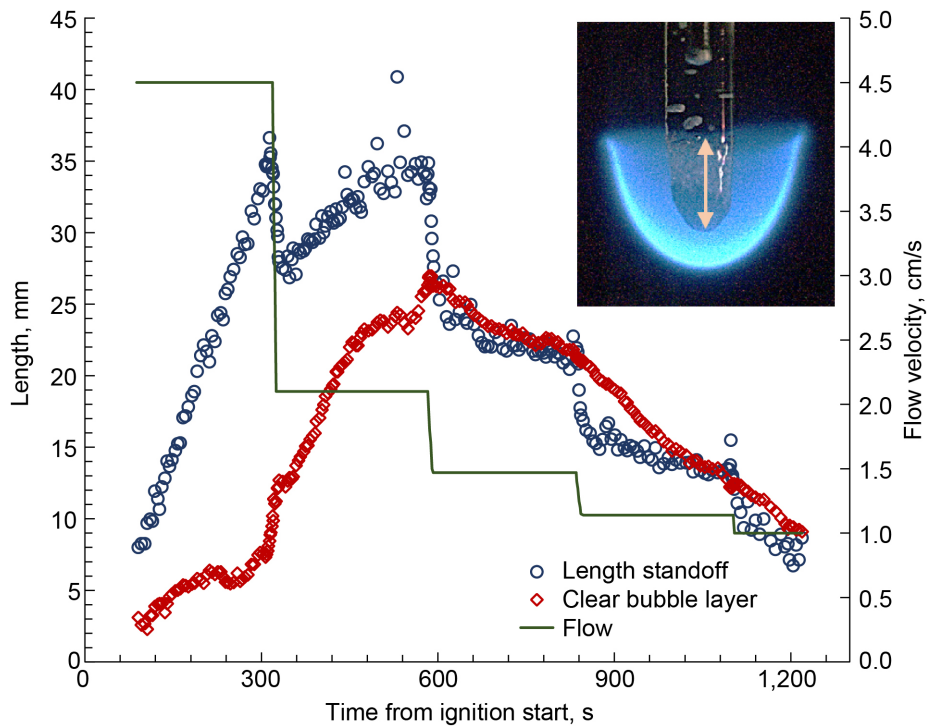
Figure 6.5.—Flame length compared to clear bubble layer length. Inset flame image shows bubble layer length. Data is from same test as Figure 6.4.
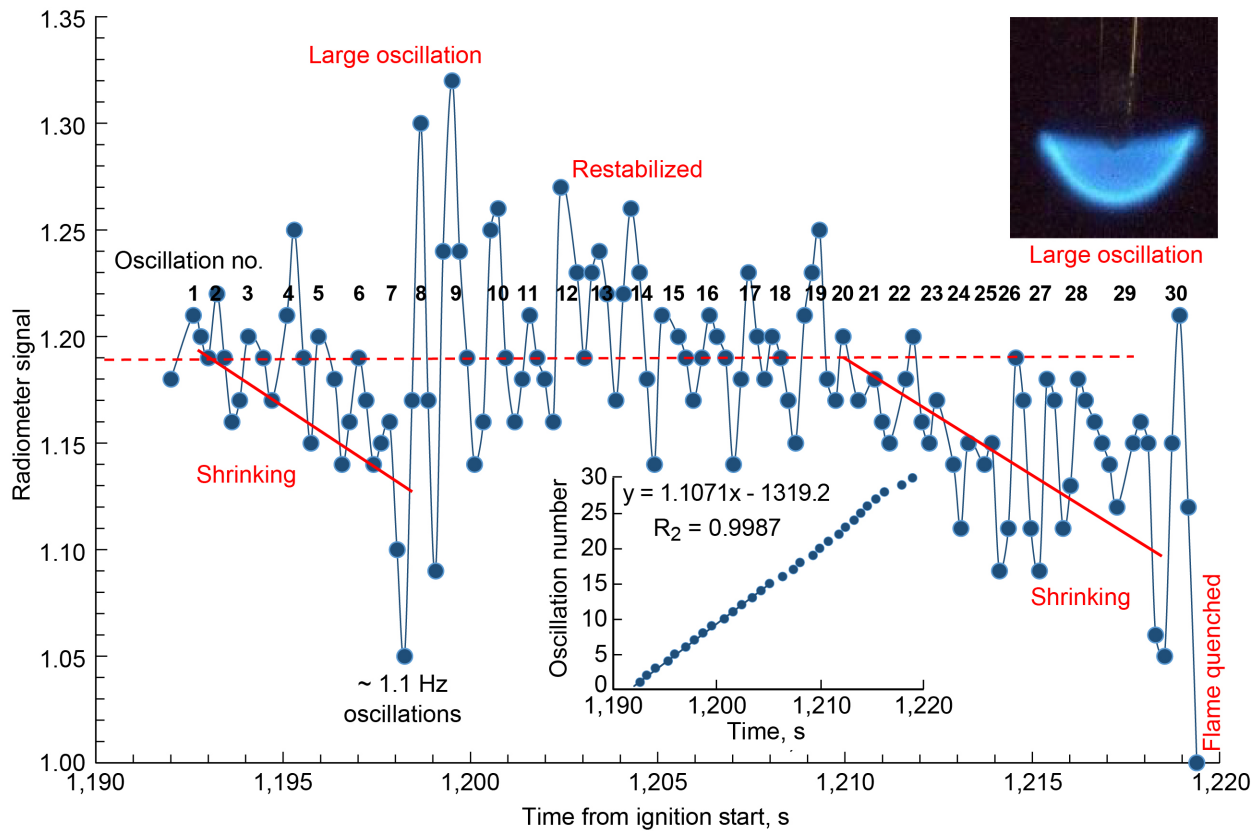
Figure 6.6.—Flame oscillations prior to quenching extinction, detected by radiometer. Data is from same test as Figure 6.4. Inset graph shows oscillation frequency to be steady at 1.1 Hz.

The flame length minus the standoff distance matches the clear bubble layer length just before each flow change, as shown in Figure 6.5, indicating that the bubble layer formation is due to heat flux from the flame, as shown in the flame image inset in Figure 6.5 (at 1,100 s). The dense small clear bubble layer (indicated by the arrow in the flame inset image) tracks the length closely except just after the flow is turned down. The flame adjusts immediately to the flow change, but the bubble layer length can only shrink at the rate of the tip regression. It is interesting that at quenching extinction, the bubble layer length has shrunk to approximately the same length as the rod diameter, which is another indication of the hemispherical shape of the flame prior to quenching extinction.

After the last flow change, the flame length does not reach a steady size, but shrinks and begins to oscillate. The radiometer signal provides the best temporal reading of these oscillations. The radiometer reading for the last 30 s of the test are shown in Figure 6.6. The radiometer signal oscillates at approximately 1.1 Hz as shown in the inset to Figure 6.6, and drops to a value of 1.05 over a period of a few seconds followed by a large oscillation. The flame appears to recover back to smaller scale oscillations. After a few seconds, the radiometer signal again drops to 1.05 followed by another large oscillation. The flame then extinguishes. A still flame image also inset into Figure 6.6 shows a similar test that captured a flame just prior to extinction, showing the flame length shrinks forward to basically the flame standoff distance on its way to quenching extinction.

These oscillations are very similar to those observed for candle flames in a quiescent environment (Ref. 17), since the ~1-cm/s convective flow is at the level of diffusive flows. The open tail of the small hemispherical flame allows fuel vapor to escape downstream. This mixes with O_2 and forms a flammable

mixture. The flame flashes downstream through this mixture and consumes the reactants. This larger flame locally depletes the O_2 concentration, weakening the flame briefly. For a large amplitude oscillation, the local O_2 depletion becomes low enough to destabilize the flame anchor at the stagnation region, and the flame extinguishes entirely. The oscillation frequency is controlled by the diffusive transport (mixing) rates of the reactants and the inherent heat losses (Ref. 17). The radiative loss has been shown to have the same effect as changing the thermal-diffusivity of the reactants (Ref. 18) resulting in oscillations with thermodiffusive characteristics even for unity Lewis number.

6.1.4.3 Blowoff Extinction

Blowoff limits were typically determined after a stable rod regression was established at a modest flow speed. The astronaut would then turn up the flow to obtain blowoff. Blowoff was defined as the instant when the stagnation region developed a hole (Ref. 19) as shown in the lower row of flame images in Figure 6.3. The center blowoff image is of a 5.18-s Zero Gravity Research Facility drop test since no ISS blowoff tests were obtained with the intermediate rod size. A green light-emitting diode (LED) illuminates the drop test rod. The flames in the drop tower blowoff tests are significantly smaller than the ISS flames, as can be seen in Figure 6.3, due to the reduced level of fuel preheating resulting from the short burn time prior to blowoff. Previous research (Refs. 6, 7, 20, and 21) and Section 6.1.5.5 indicate that blowoff extinction is not sensitive to heat losses.

After the stagnation region blows off, the subsequent annular flame leading edge would oscillate upstream and downstream multiple times before completely blowing off. During one test, we attempted to reestablish the envelope flame after local blowoff. Only once could we successfully reestablish the stagnation region after local blowoff by quickly reducing the flow to a value below the blowoff velocity. A second attempt was not successful.

The a and radiometer data from these blowoffs are shown in Figure 6.7. In each blowoff, the astronaut quickly turns up the flow from a low a to a high a and the flame blows downstream. The astronaut then quickly turns the flow down to a near the minimum flammability (discussed in Section 6.1.4.4). Figure 6.7 shows that the two attempts were quite similar, but the results were not. For the first blowoff, the flame hole is initially about 9 mm in diameter, but within 2 s moves back forward of the rod tip position (yellow line in Figure 6.8) and closes up in 7 s after the flow is turned down, as shown in Figure 6.8(a). The radiometer signal is higher since the flow is slightly higher and the flame is visibly longer than the preblowoff flame.

A subsequent attempt 55 s later resulted in a slightly larger initial flame hole of 10 mm that was not able to move forward of the flame tip and reestablish the stagnation region, as shown in Figure 6.8(b). This 10-mm flame hole persisted for over a minute even after the flow was turned down again to the initial flow before the flame destabilized and blew off completely.

While the flow profile was quite similar for the two blowoffs, the O_2 had depleted more by the second blowoff. This is apparent in the reduced sooting for the second preblowoff flame. This second blowoff is interpreted as indicating that once the flame is stabilized farther than the thermal length downstream of the stagnation region ($\ell = 2$ mm), the flame is unable to repropagate upstream for the low O_2 levels tested (X_{O_2} final = 14.5 percent for this test) even though the fuel is already preheated. This is consistent with tests for opposed-flow flame spread over rods that were also done as part of BASS–II (Ref. 14), where opposed-flow flame spread was not observed below 16.4 percent O_2 at any flow.
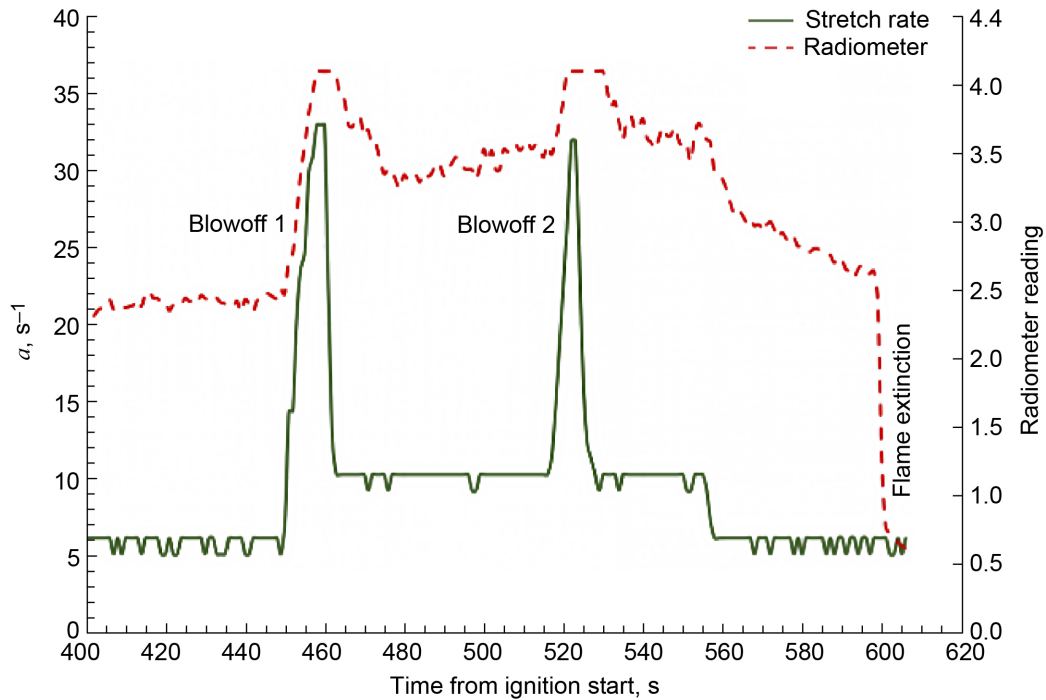
Figure 6.7.—Time history of stretch rate a and radiometer signal for two local blowoffs for 0.318 cm rod.
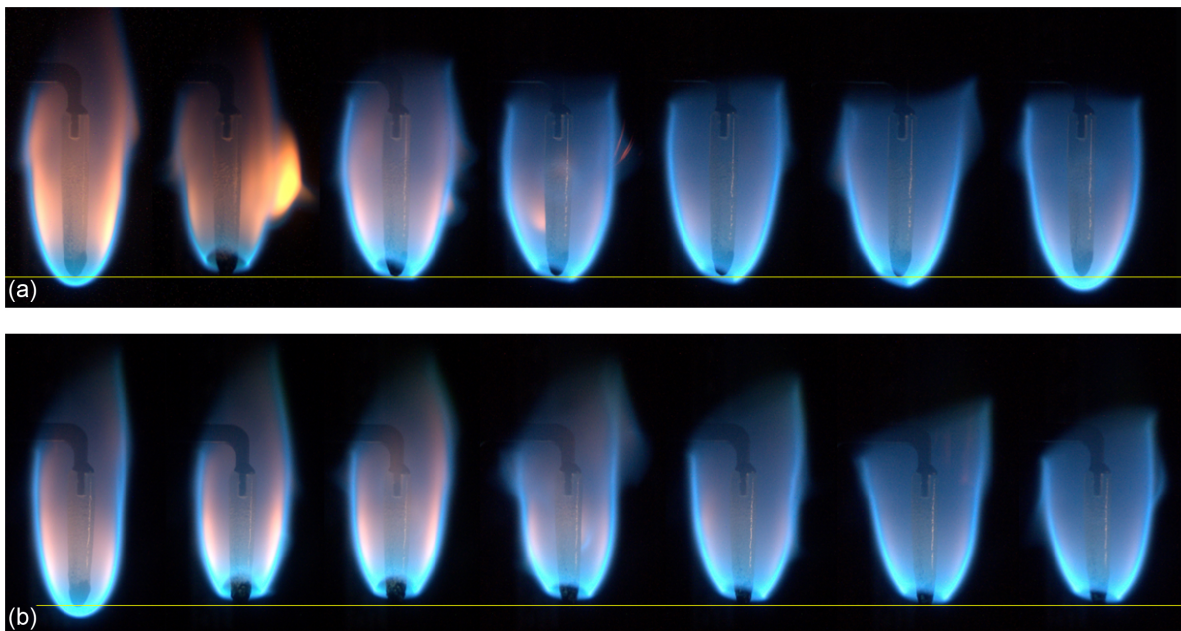
Figure 6.8.—Sequence of still flame images from two local blowoffs. Images in each set are 1 s apart. Yellow horizontal lines reflect position of rod tip. (a) Blowoff 1. (b) Blowoff 2.

6.1.4.4 Flammability Boundary

For each test, the flow speed at which the flames extinguished and the last flow speed at which a stable flame was observed (or the flow at which the flame did not blow out in the drop time for drop

tests), along with the postburn O_2 sensor reading were used to generate a flammability boundary, shown in Figure 6.9. Error bars reflect the uncertainties in O_2 and flow and are mostly smaller than the symbols.

The x-axis of Figure 6.9 uses a forced a, which is defined as $a = (3/2)(U/r)(r/r_o)^{1/2}$ where U is the free stream velocity. The square root modifying factor is used to correct for the different rod sizes. The gas phase ℓ scale (Ref. 7) is defined as $\ell = (\alpha/a)^{1/2}$, which is proportional to $r^{1/2}$ for a given velocity. All a are normalized to the base rod radius ($r_o = 0.318$ cm) using the ratio of these ℓ s.

The thick gray flammability boundary in Figure 6.9 represents the border between stable flames and extinguished flames. Along this boundary, the flame is sensitive to stochastic perturbations that can lead to extinguishment (Ref. 22). The O_2 concentration (X_{O_2}) versus a boundary is defined by the combined empirical equations shown by the red (quenching branch, exponential expression) and black (blowoff branch, linear expression) dashed lines.

$$X_{O_2} = 6\exp(-0.5a) + 0.0167a + 13.4 \qquad (6.1)$$

The minimum in this boundary occurs at $a = 8$ to 12 s^{-1} at approximately 13.5 percent O_2, in good agreement with the predicted a at the minima in the flammability boundary (Refs. 6, 7, 20, and 21).

The drop tower blowoff data, given by the purple dashed line, agrees very well with the flight data. The fact that the blowoff boundary is linear with flow makes it possible to extrapolate blowoff data down to zero a and use that O_2 value as an accurate but conservative estimate of the minimum O_2 concentration for material flammability in space. This may provide a consistent methodology to derate materials based on normal-gravity flammability tests accounting for buoyant flow to ensure the material will not burn in space.
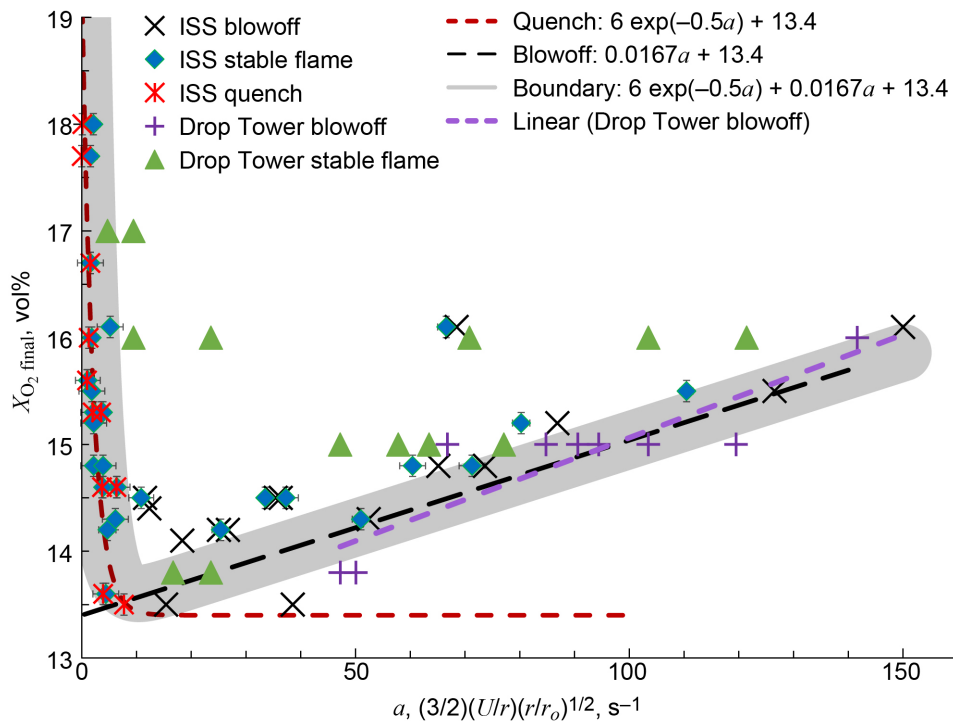
Figure 6.9.—Flammability boundary obtained in Burning and Suppression of Solids—II (BASS–II) tests with linear axis. Complementary drop tower test results are also shown. International Space Station (ISS). Stretch rate (a). Final O_2 concentration (X_{O_2}). Forced-flow velocity (U). Rod radius (r).

The quenching branch is fitted using an exponential decay (red dashed curve). In this region, heat losses dominate to cool the flame to extinction through the strong dependence of reaction rate in the Arrhenius term, as was modeled by References 6, 7, 20, and 21, and will be evaluated in Section 6.1.4.3. This boundary is very steep for small a when plotted on a linear x-axis as shown in Figure 6.9.

Figure 6.10 replots the same data as Figure 6.9 but with a logarithmic x-axis. Note that the classic U-shaped flammability boundary is evident when a logarithmic x-axis is used. This expands the quenching branch while making the linear blowoff branch appear curved. It also emphasizes the uncertainty in the flow at the very low velocities (<1 cm/s) along the quenching branch. The minimum O_2 concentration of 13.5 percent O_2 at a of 8 to 12 s^{-1} is significantly lower than the observed upward flame spread limit of 15.4 percent O_2 (in normal gravity with an additional 4-cm/s forced flow (Ref. 23)), indicating the material remains flammable under the weak ventilation only obtainable in microgravity. This "Goldilocks" zone of flow is unfortunately typical of spacecraft ventilation flows near surfaces. Earthbound flammability tests need a reliable method to account for this extension of flammability in microgravity environments. Extrapolation of the normal-gravity blowoff boundary to zero stretch may be a viable method to estimate this enhanced flammability if a buoyant stretch can be included.
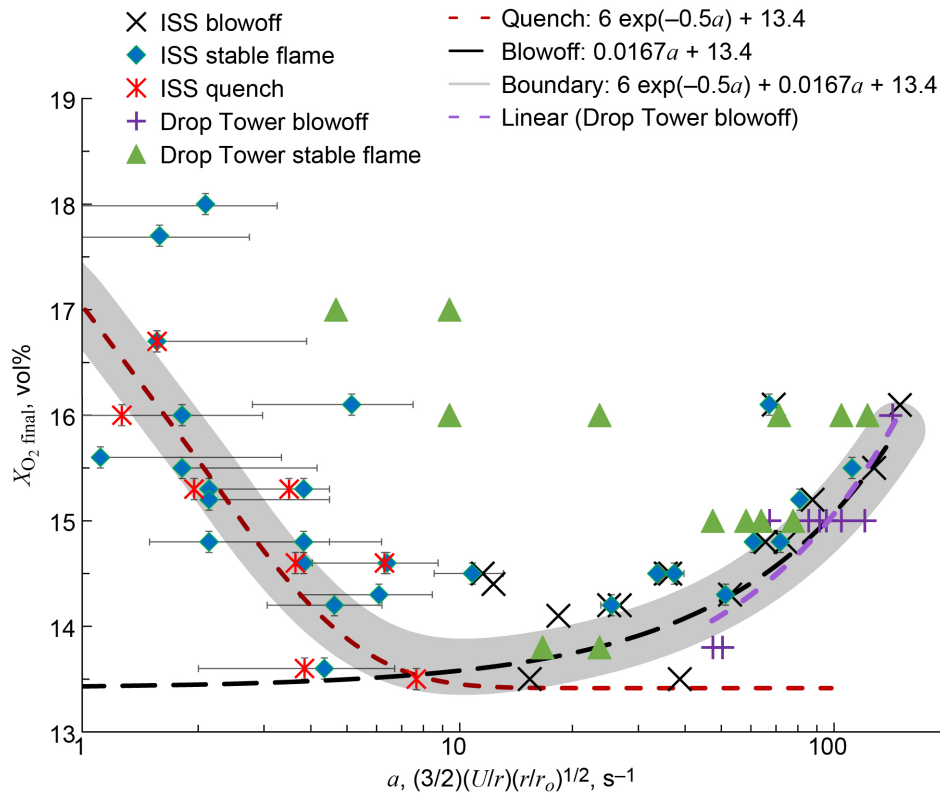
Figure 6.10.—Flammability boundary shown with logarithmic x-axis, which expands quenching region and exhibits classic U-shaped flammability map. International Space Station (ISS). Stretch rate (a). Final O2 concentration (X_{O_2}). Forced-flow velocity (U). Rod radius (r).

6.1.4.5 Flame Standoff Distance

The flame standoff distance at the stagnation point, just prior to extinction (blowoff or quenching), was measured for each test using the high-resolution digital still images. These measurements are used in Section 6.1.5.2 to estimate the convective heat flux from the flame to the rod in the stagnation region. The standoff distances measured are at the outer boundary of the bright cyan edge (peak temperature) of the flames shown in Figure 6.3.

The measured standoff distance as a function of O_2 concentration is shown in Figure 6.11 for all three radii and also for the type of extinction, quenching, or blowoff. The flame standoff distance shows a trend reversal on the two sides of the flammability boundary. On the blowoff side, as O_2 is reduced, the standoff distance increases. There is a turning point at a minimum O_2 concentration, and on the quenching side, as O_2 increases, the standoff distance also increases.

Figure 6.12 shows the same measured standoff distance data plotted against the a. The standoff distance shows a seven-fold increase as a is reduced by two orders of magnitude. Error bars reflect the uncertainty of the a at very low values due to the resolution limitations of the flow velocity sensor. A power law curve fit to the data shows the standoff distance is approximately proportional to cube root of the a, not the square root dependence of the characteristic ℓ predicted by theory (Ref. 7). The square root dependence (dotted line in Figure 6.12) appears to capture the trend in the blowoff region, but not in the quenching region.
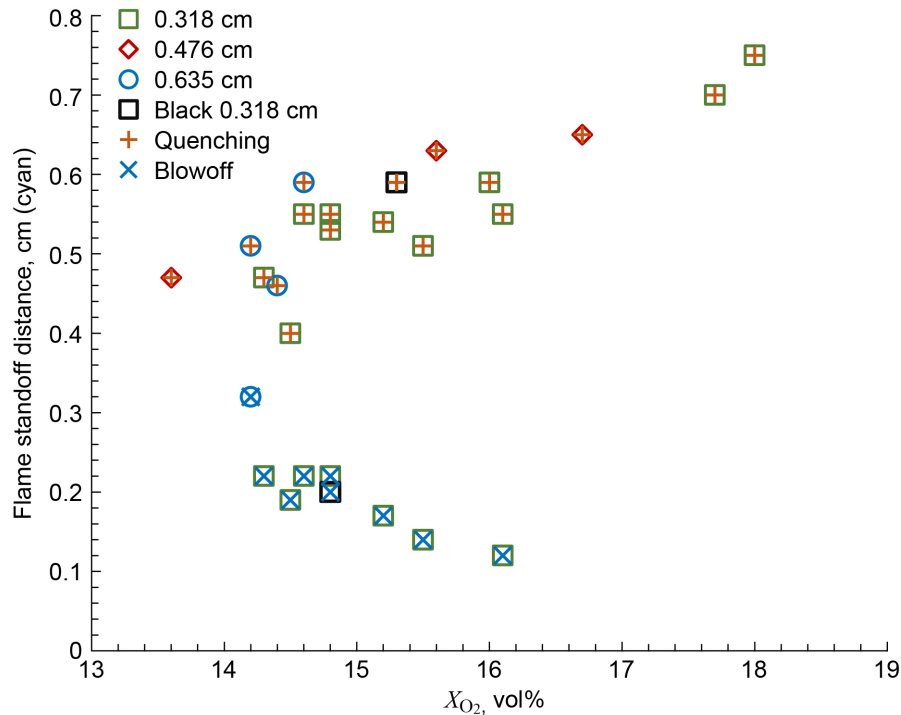
Figure 6.11.—Flame standoff distance as function of oxygen, showing both quenching and blowoff branches. O_2 concentration (X_{O_2}).
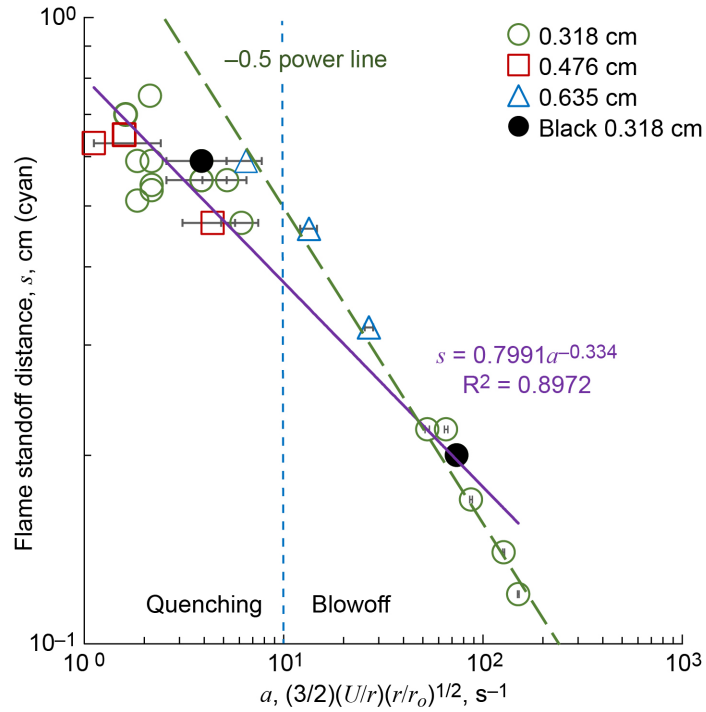
Figure 6.12.—Flame standoff distance as function of stretch rate a with power law fit. Forced-flow velocity (U). Rod radius (r).
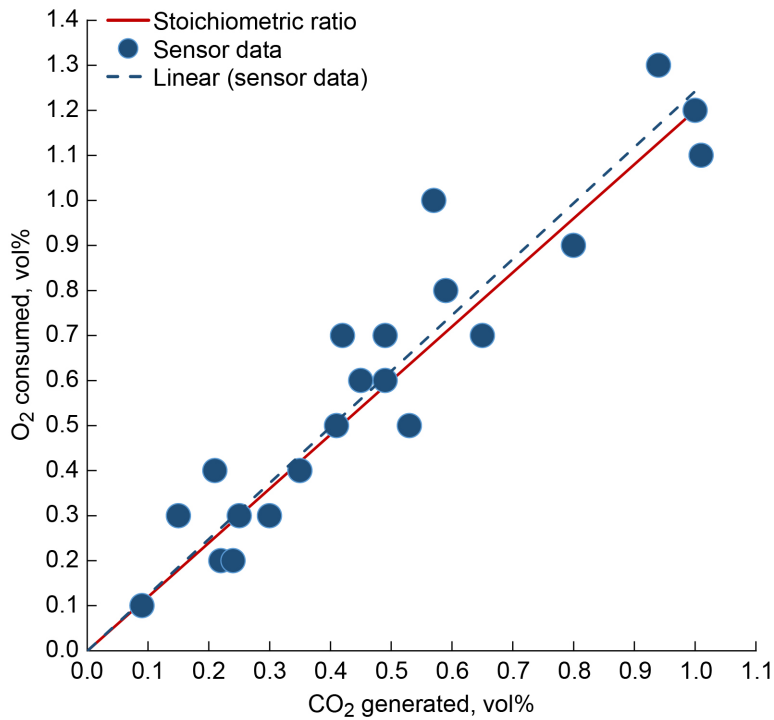
Figure 6.13.—O_2 consumed compared to CO_2 generated.

6.1.4.6 Gas Sensor Results

The initial and final O_2, CO_2, and CO readings were recorded for each test. Although flow and O_2 concentrations do change within each test, the averages still provide insight into the overall processes. The O_2 consumed can be compared to the CO_2 generated, as shown in Figure 6.13. While there is scatter in the data, the linear trend agrees very well with the stoichiometric ratio for PMMA (6 O_2 to 5 CO_2). This indicates that the O_2 was burning primarily to the expected CO_2 and water.

The CO produced is plotted against CO_2 in Figure 6.14. There is a fairly linear relationship between the two, with approximately 600 ppm of CO produced for every 1 vol% of CO_2 produced. The CO to CO_2 ratio is plotted against the initial O_2 concentration in Figure 6.15, and shows that as the initial O_2 concentration decreases, the CO to CO_2 ratio increases. These values are an order of magnitude greater than the 1g values found in the cone calorimeter for PMMA (Ref. 24), indicating very inefficient burning at low ambient O_2 levels in microgravity.

The O_2 consumed and the fuel burned were used to estimate the global stoichiometry for each test. The amount of rod burned away was measured from the still images in each test. The bubble layer effect on density was not accounted for, so there is scatter in the data most likely due to this factor. The O_2 consumed was calculated by using the MSG free work volume of 250 L (Ref. 14) and the ideal gas law. The fuel to oxidizer molar ratio is divided by the stoichiometric ratio (1 monomer unit per 6 O_2). The resulting global stoichiometric ratios for each test are shown in Figure 6.16. At higher O_2 concentrations, the flames are nearly stoichiometric. At lower O_2 concentrations, the global equivalence ratio increases. This indicates that the limiting reactant is the O_2 rather than the fuel. It is likely that at the low O_2 levels (and low flow rates) that there is significant fuel leakage out the open back of the flame. This is consistent with the near-extinction oscillation mechanism of fuel leakage downstream, mixing, and flame flashback through the premixed region. This is also consistent with the CO to CO_2 ratio trend of inefficient burning.
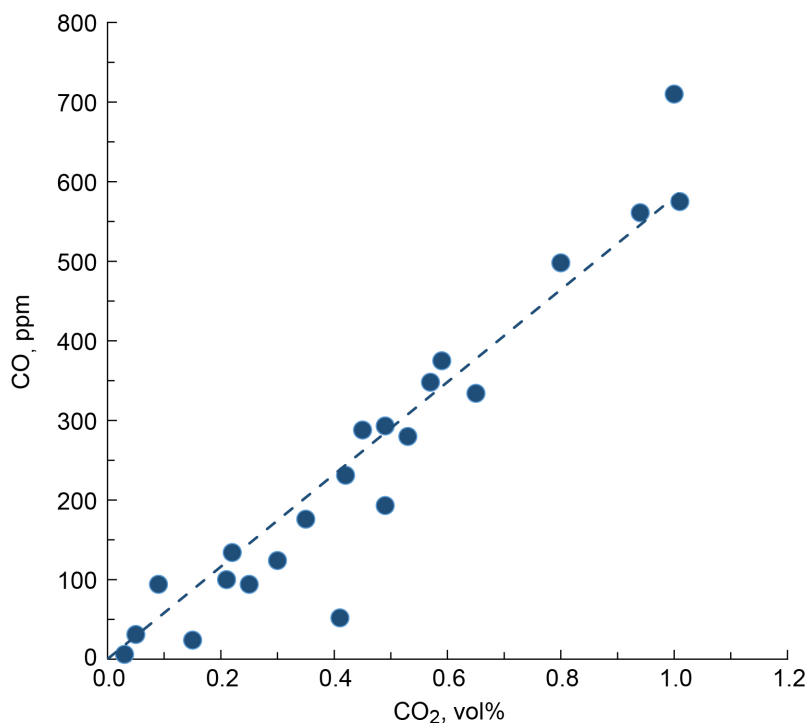
Figure 6.14.—CO generated compared to CO_2 generated.
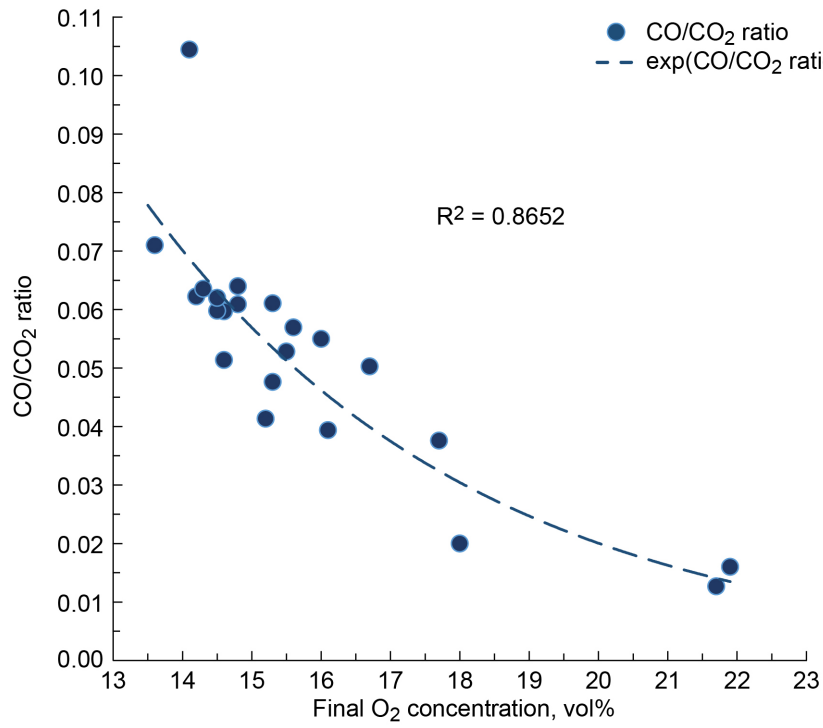
Figure 6.15.—CO to CO_2 ratio as function of final O_2 concentration.
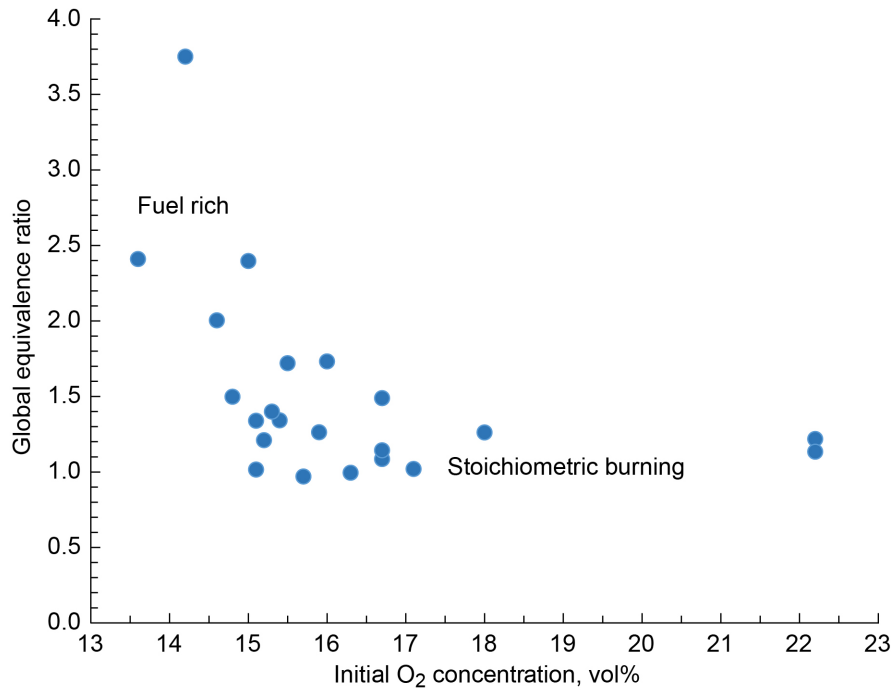
Figure 6.16.—Global equivalence ratio as function of initial O_2 concentration.

6.1.5   Analyses

In this section, the experimental flammability boundary (Eq. (6.1)) is applied to a constant critical Damköhler number formulation (Section 6.1.5.1) to estimate the critical flame temperatures along the extinction boundary. The critical temperatures and measured flame standoff distances are then used in a Nusselt number correlation (Section 6.1.5.2) to estimate the convective heat flux to the rod from the flame along the flammability boundary. A surface energy balance (Section 6.1.5.3) utilizes the deduced convective heat flux to evaluate the importance of radiative exchange and heat losses on the blowoff versus quenching sides of the extinction boundary. A comparison of measured versus predicted rod regression rates is presented (Section 6.1.5.4). Lastly, the relative heat losses across the flammability boundary are examined to understand the physics of the transition from blowoff to quenching. It should be noted that a constant base rod size is used in all subsequent analysis so the correction factor for radius in the a expression is unity.

6.1.5.1 Damköhler Number Analysis

The critical Damköhler number (Da_{crit}) analysis presented here is applied to both blowoff and quenching sides of the flammability boundary since finite rate chemistry applies along the entire flammability boundary. For both blowoff and quenching, the Da_{crit} becomes too small. At blowoff, the flow rate is too large to allow the relatively fast reactions to occur, while at quenching, the reaction rate becomes too small due to slow mixing of the reactants.

A critical Damköhler number (Da_{crit}) is defined as

$$Da_{crit} = \frac{\text{flow time}}{\text{reaction time}} \sim \frac{\text{reaction rate}}{\text{flow rate}} = \frac{\beta\rho\left(X_f\right)\left(X_{O_2}\right)e^{\left(-E/RT_{crit}\right)}}{a} \tag{6.2}$$

where β is the preexponential factor, ρ is the gas density at the mean temperature, X_f and X_{O_2} are the fuel and oxidizer concentrations, E is the activation energy, R is the ideal gas constant, and T_{crit} is the critical temperature.

The Da_{crit} is assumed to be constant along the entire flammability boundary (Ref. 1), and equal to unity to reflect a critical balance in the flow and reaction times. The reaction constants are close to those for extinction conditions given by Reference 8 and their β is normalized with a reported blowoff Da from Reference 1 to obtain the unity Da. The fuel concentration is assumed to be unity at the fuel surface. Equation (6.2) is solved for the temperature along the extinction boundary, T_{crit} (not a constant) by using the O_2 and stretch dependence from Equation (6.1).

The resultant critical flame temperature along the flammability boundary is shown in Figure 6.17 as a function of a. The critical temperature drops as a decreases. For quenching extinction ($a < \sim 10$ s^{-1}), the critical flame temperature drops more precipitously. This is due to the reduction in heat flux from the flame relative to the intrinsic heat losses, as will be shown in Section 6.1.5.3. Critical flame temperature is used in the next section to estimate heat flux from the flame to the fuel.
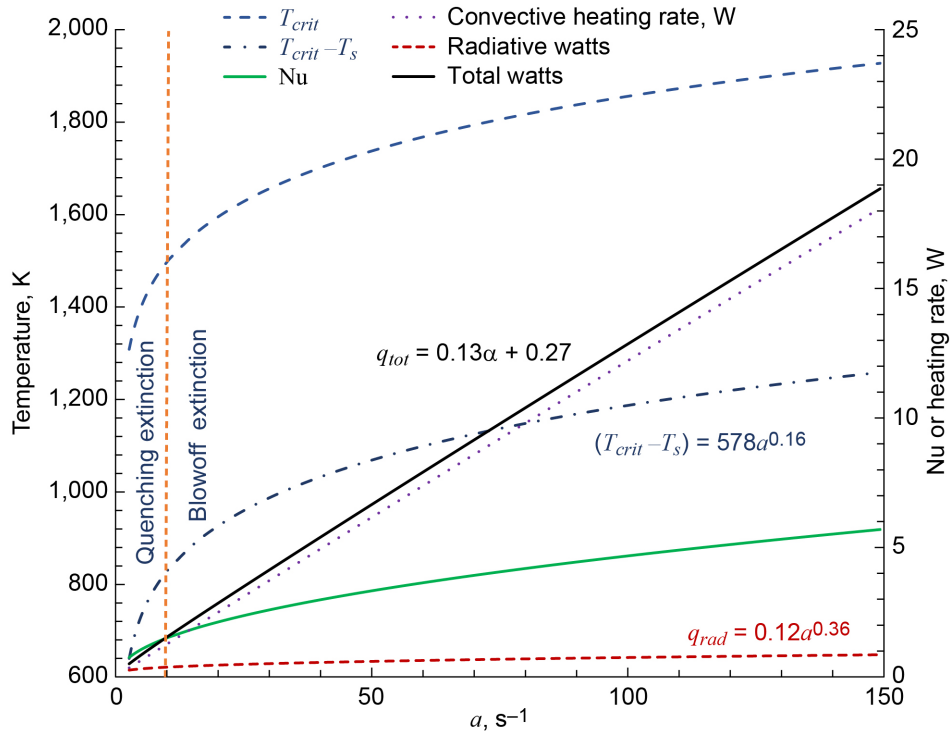
Figure 6.17.—Predicted temperature along extinction boundary T_{crit} (Eq. (6.2)), Nusselt number Nu (Eq. (6.3)), decay of heating rate $\dot{q}''$ with stretch rate a (Eq. (6.4)), and radiative heat q_{rad} and total heat q_{tot} from Equation (6.5). Solid temperature (T_s). Convective heating rate $\dot{q}_{conv}$.

6.1.5.2 Heat Transfer Estimates

To estimate the heat transfer rates to the stagnation region of the rod, the Nusselt number Nu correlation developed by Sibulkin (Ref. 25) is used, which evaluates the convective heat transfer near the forward stagnation point of a hemispherically tipped body of revolution as a function of Reynolds (Re) and Prandtl (Pr) numbers.

$$Nu = 1.32\,Re^{0.5}\,Pr^{0.4} \qquad (6.3)$$

This correlation neglects dissociation (thermochemical heat release) for the low temperatures and high nitrogen dilution levels along the flammability boundary (Ref. 26), and neglects gas radiation for the nonluminous flames per Reference 27. The Re is based on the diameter. The convective heat flux $\dot{q}_{conv}$ to the stagnation region is thus:

$$\dot{q}_{conv}'' = Nu\,\frac{\lambda\left(T_{crit} - T_s\right)}{s} \qquad \text{so, } \dot{q}_{conv} = \dot{q}_{conv}''\,A_h = h\left(T_{crit} - T_s\right)A_h \qquad (6.4)$$

Where λ is the thermal diffusivity at the mean gas temperature, T_s is the surface temperature, s is the flame standoff distance, h is the convective heat transfer coefficient, and A_h is the hemispherical rod tip surface area.

The T_{crit} from Figure 6.17 are used with the measured s power law fit from Figure 6.12 to solve for the $\dot{q}_{conv}$ to the stagnation region. The convective heating rate is linear with a, as shown in Figure 6.17. This is an interesting combination of a terms in Equation (6.4): the square root Nu flow dependence (Eq. (6.3)), the approximate minus cube root s dependence (0.334 power from Figure 6.12), and the approximate seventh root temperature difference $(T_{crit} - T_s)$ dependence on a (0.16 power from Figure 6.17). The sum of the powers is thus $0.5 + 0.33 + 0.16 = 0.99 \sim 1$, which means that $\dot{q}_{conv}$ depends linearly on a.

6.1.5.3 Surface Energy Balance

To examine the role of radiation- and solid-phase conductive losses on the flame, a surface energy balance is developed. A two-zone surface energy balance schematic for the rod tip is formulated and shown in Figure 6.18 to account for the three-dimensional (3D) nature of the flame over the nearly spherical tip of the rod. Zone 1 is the area defined by the hemispherical tip of the rod. The entire zone is assumed to be at the pyrolysis temperature T_s, consistent with the observed bubble layer length from Figure 6.5, and consistent with the Biot number $Bi \ll 1$ from Equation (6.4) heat flux levels. Zone 2 is the cylindrical rod, with an interface to Zone 1 at the base of the hemisphere. Only solid conduction loss out of Zone 1 into Zone 2 is considered, using the rod cross-sectional area while the other terms use the tip hemispherical surface area, which is twice as large.
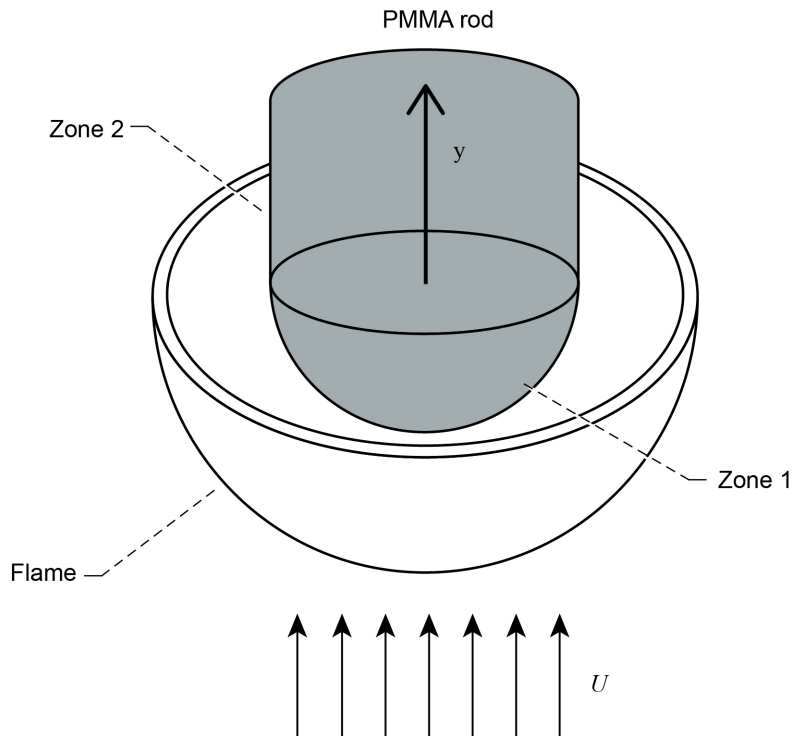
Figure 6.18.—Two-zone surface energy balance.

A surface energy balance is defined as

$$\dot{q}_{tot} = \dot{q}_{conv}'' A_h + \varepsilon_g a_s \sigma F T_{crit}^4 A_h = \dot{m}'' L_{vap} A_h + \varepsilon_s \sigma \left(T_s^4 - T_\infty^4 \right) A_h + \lambda_s \left. \frac{\partial T_{solid}}{\partial y} \right|_0 A_r \qquad (6.5)$$

The total energy $\dot{q}_{tot}$ transferred from the flame to A_h includes convection $\dot{q}_{conv}''$ from Equation (6.4) along with an estimate of the gas-phase radiative feedback to the surface. In the gas-phase radiation term, ε_g is the gas-phase emissivity, α_s is the surface absorptivity, σ is the Stefan-Boltzmann constant, and F is the view factor. Gas-phase flame radiation is included in the surface energy balance because it becomes an important source of energy in the quenching region, as will be shown. Kirchhoff's law is applied to the surface where absorptivity equals emissivity ($a_s = \varepsilon_s$), and ε_g is estimated to be 0.02, primarily from CO_2 and H_2O.

The energy from the flame to the surface goes into vaporizing the fuel, where $\dot{m}''$ is the burning rate and L_{vap} is the latent heat of vaporization, surface radiative loss is estimated using the surface and ambient temperatures T_s and T_∞, and conduction into the rod (Zone 2) for a solid-phase thermal diffusivity λ_s and the solid-phase temperature gradient T_{solid} at the surface through the cross-sectional area of the rod A_r. To estimate surface radiative loss, we assume a constant surface pyrolysis temperature, but this assumption may break down very near quenching.

To solve for the conductive loss to Zone 2, for long burn times with slow convective flow, the solid-phase thermal profile is assumed to have reached an approximate steady state, and we can approximate a one-dimensional (1D) temperature profile along the rod axis. It is assumed that no vaporization occurs in this zone. We also assume for simplicity that the surface radiative loss is counteracted by a convective heat flux from the hot gases flowing slowly past the rod.

There is a balance of heat transfer through the rod via conduction and convection. The convective term is due to the steady surface regression of the rod (measured from the experiment), V_r. It is assumed in this steady analysis that V_r is so small that the length of the sample does not change significantly over the timeframe of interest t_s, over which $\Delta L \ll L$, where L is the characteristic length of the rod. For example, using the regression rate measured in Figure 6.4 for the 0.476-cm radius rod, $t_s = 132$ s and thus $\Delta L = V_r t_s = 0.5$ cm $\ll L_o = 5.9$ cm. This means that changes in the temperature profiles are quasi-steady for a slowly changing L. However, as the rod shortens significantly, this assumption breaks down.

The 1D steady conduction-convection energy balance in the solid can be nondimensionalized with $Y = y/L$, $\theta = (T - T_\infty)/(T_s - T_\infty)$, and the solid-phase Peclet number $Pe = LV_r/\alpha_s$.

$$0 = Pe \frac{\partial \theta_s}{\partial Y} + \frac{\partial^2 \theta_s}{\partial Y^2} \qquad (6.6)$$

Boundary conditions for the solid model include the surface temperature $T = T_s$ at $y = 0$ (circular interface between Zone 1 and Zone 2) and $T = T_\infty$ at $y = L$. Boundary conditions become $\theta(0) = 1$ and $\theta(1) = 0$. This equation is a linear, homogeneous, second-order ordinary differential equation with constant coefficients, with roots 0 and $-Pe$ for the general solution. Using the boundary conditions to evaluate the constants of integration, the solution is

$$\theta(Y) = \frac{\exp(-PeY) - \exp(-Pe)}{1 - \exp(-Pe)} \qquad (6.7)$$

Differentiating this solution, one can evaluate the steady-state temperature gradient at the regressing surface ($Y = 0$) with decreasing Pe. The temperature gradient at the surface as a function of Pe is obtained in dimensional terms:

$$\left.\frac{dT_s}{dy}\right|_{y=0} = \frac{Pe}{\exp(-Pe)-1}\frac{(T_s - T_\infty)}{L_o} \tag{6.8}$$

We can use this to evaluate the conductive loss down the rod in Equation (6.5).

For large Peclet numbers ($Pe \gg 1$), the temperature gradient at the pyrolysis interface is steep since heat conducted along the rod is quickly convected back toward the burning tip via rod regression so that heat cannot penetrate too deeply along the rod. For small Peclet numbers ($Pe \leq 1$), conduction dominates, and the temperature profiles are nearly linear. It is counterintuitive that the slowest burning samples will, in this steady-state, have the least heat loss into the solid.

Using Equations (6.4) and (6.8), we can solve Equation (6.5) for the mass burning rate $\dot{m}''$ as a function of a. The mass flux from the burning tip of the rod is the only unknown in Equation (6.5). It should be noted that as expressed in Equation (6.5), the fuel vaporization rate is from the hemispherical surface, whereas the experiments measure the average rod regression rate. The difference is a factor of 2 due to the different areas.

6.1.5.4 Rod Regression Rates

The predicted 3D average rod regression rates using the two-zone model are compared with the measured average regression rates, as shown in Figure 6.19. There is significant scatter in the measured average regression rates since the flow and O_2 varied during each test, but the values are of the correct magnitude compared to the predicted 3D rod regression rates.

It is also possible to compare the 1D solution to Equation (6.5) with prior pseudo-1D flat flame experiments (Refs. 28 to 30) by assuming all areas for heat transfer are the same and then solving the equation for the regression rate V_r, also shown in Figure 6.19. Stretch rates are also defined as flow velocity U/D for the 1D geometry, using the base rod size. The 1D predicted regression rates agree quite well with existing data (Refs. 28 to 30) where the scale of the flames is much wider than the flame standoff distance, resulting in pseudo-1D flames. The burning rates for the two-zone model are significantly higher than the 1D solution for a given a due to the increased surface area for heat flux and fuel vaporization in the 3D cylindrical geometry.
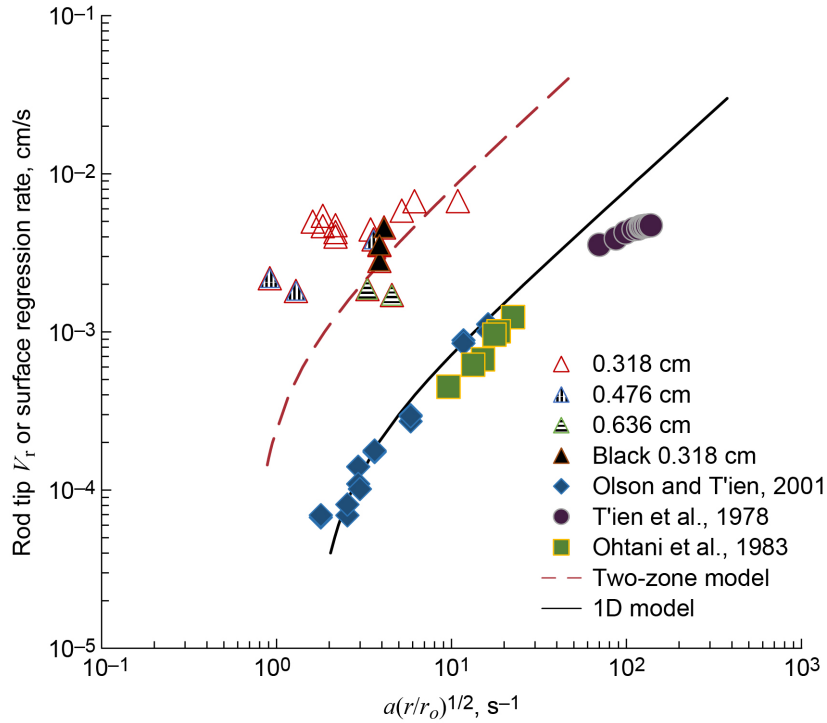
Figure 6.19.—Predicted regression rates from two-zone and one-dimensional (1D) models as function of stretch rate a compared with measured rod regression rates and published pseudo-1D experimental data.

6.1.5.5 Estimate of Heat Loss Along Flammability Boundary

The terms of Equation (6.5) are plotted in Figure 6.20 as a function of a. The graph is plotted with logarithmic axes to expand the quenching region ($a < 10$ s^{-1}) where the heat losses become important. The total flame heating rate to the surface drops linearly with decreasing a as was shown in Figure 6.17. The minimum heat flux at unity a is 1 W/A$_h$ = 1.57 W/cm^2, which is in the range of literature values for the critical heat flux for ignition of PMMA (Ref. 31). Along the blowoff branch ($a > 10$ s^{-1}), fuel vaporization parallels the total flame to surface heat flux. Heat loss is relatively small, with the solid conduction from the surface in depth being most significant, but it decreases with decreasing a, mirroring the Peclet number. Flame radiative feedback to the surface is comparable to surface radiative loss at high a but decreases with decreasing a as the flame temperature decreases. Along the quenching branch, fuel vaporization drops precipitously as the total heat flux to the surface drops and the losses become a significant fraction of the total heat flux to the surface.
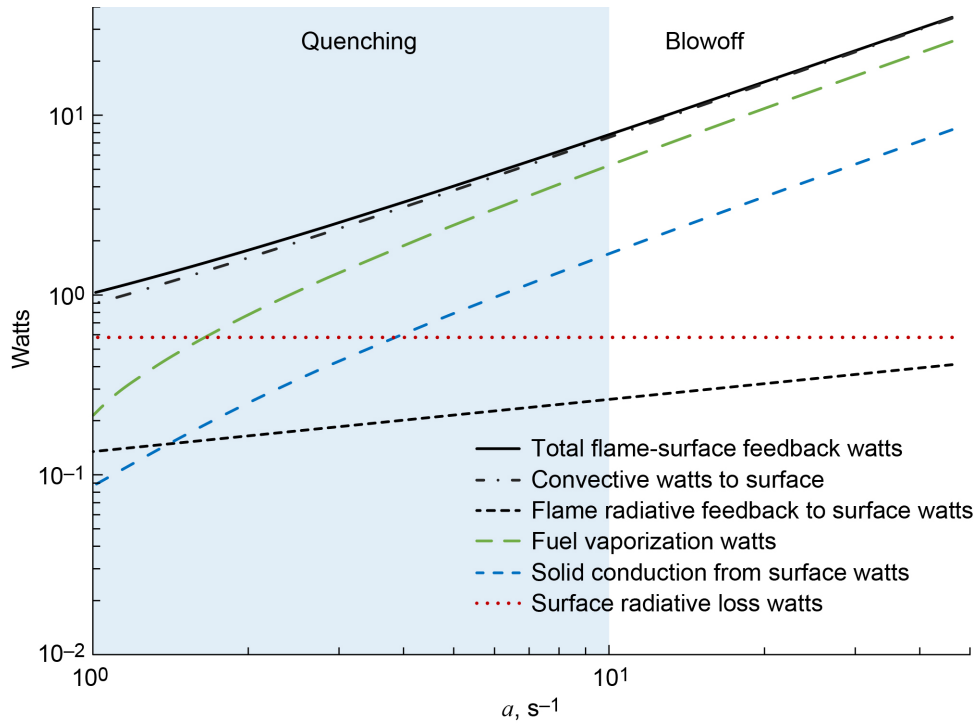
Figure 6.20.—Surface energy balance terms as function of stretch rate a along flammability boundary from Equation (6.5) using the convective heating rate (Eq. (6.4)) and solid conduction (Eq. (6.8)) as input.
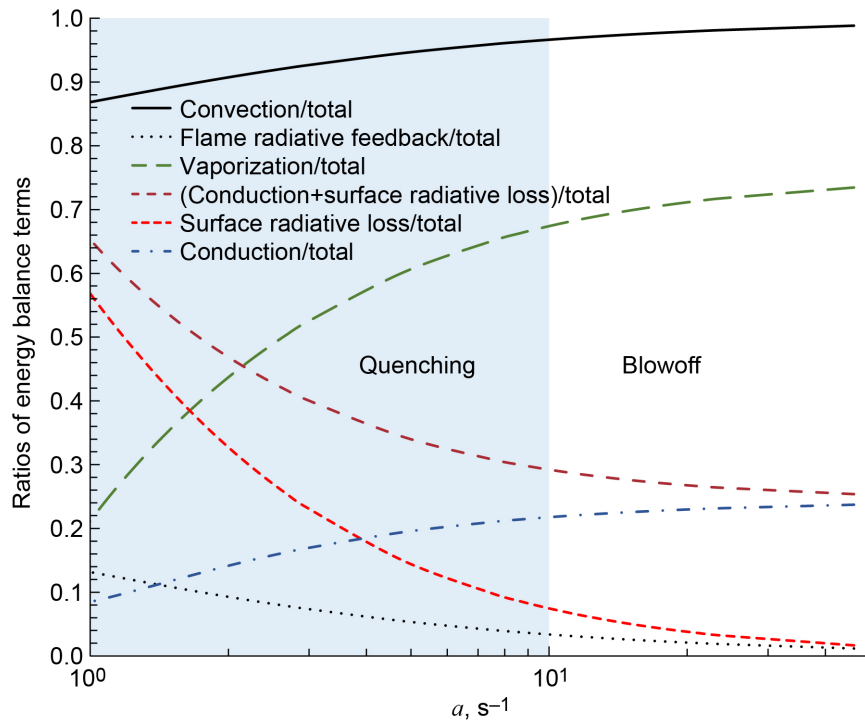
Figure 6.21.—Ratio of energy balance terms to total heat flux from flame to surface, to show relative importance of each term along flammability boundary. Stretch rate (a).

This is shown more clearly in Figure 6.21, which plots the ratio of each term divided by the total energy to the surface (convective plus gas radiative feedback). It is interesting that across the entire blowoff branch, the vaporization ratio is ~70 percent, whereas it drops precipitously to 20 percent at low a along the quenching branch. As a is reduced, the solid-phase conductive loss ratio surprisingly decreases for this geometry, which is consistent with the observation that the slowest burning rods have the least conductive loss. The surface radiative loss ratio becomes increasingly significant as a decreases, not due to an increase in surface loss, but due to the decrease in total energy from the flame to the surface, consistent with Reference 6.

Above $a \sim 10 \ s^{-1}$, corresponding to the blowoff side of the flammability map (Figure 6.9 and Figure 6.10), the surface radiative loss is comparable to the flame radiative feedback, and so radiative exchange in general can be neglected. Interestingly, the flame radiative feedback increases from an insignificant 1 percent (in agreement with Ref. 26) to over 13 percent of the total flame to surface feedback, and thus becomes a significant fraction of the total flame to surface feedback at low a, in general agreement with the more rigorous radiation analysis of Rhatigan et al. (Ref. 20). This additional source of energy extends the flammability to lower a. It is only in the quenching region where surface radiative loss becomes a significant fraction of the total heat release from the flame to the surface. At the lowest a, the total heat loss fraction exceeds 60 percent of the total flame to surface feedback.

It is interesting to note that at the bottom of the flammability map ($a \sim 10 \ s^{-1}$), the losses account for only ~30 percent of the total flame to surface feedback, and yet the transition from blowoff to quenching extinction begins in this region. What causes this transition? As shown in Figure 6.22, the experimental flammability boundary is replotted with the x-axis as forced-flow velocity U divided by a diffusive velocity $U_D = 2$ cm/s. The transition from blowoff to quenching occurs when the forced-flow velocity becomes the same order as the diffusive velocity ($U/U_D = 1$) for this geometry.
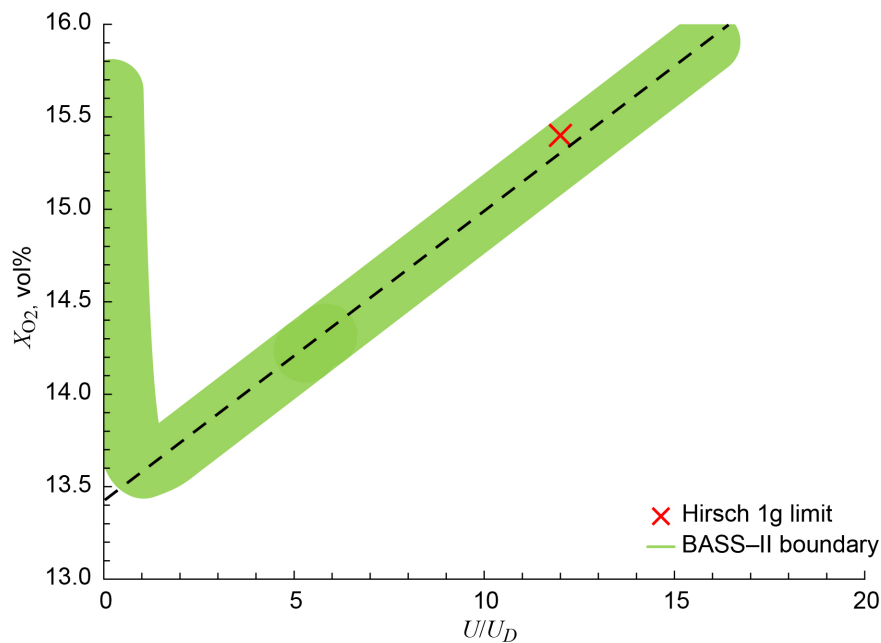
Figure 6.22.—Flammability boundary (Eq. (6.1)) using forced-flow velocity U divided by diffusive velocity U_D in lieu of stretch rate a. X_{O_2} is O_2 concentration in vol%. Normal-gravity flammability limit (Ref. 23) is graphed for comparison.

The normal-gravity upward limiting O_2 concentration of 15.4 percent O_2 (Ref. 23) is plotted for comparison, assuming linear superposition of the buoyant flow velocity at the base of the flame (20 cm/s (Ref. 32)) and the 4-cm/s forced-flow velocity. The normal-gravity upward flammability limit falls within the stochastic boundary. If multiple limits at different forced plus buoyant flows were obtained along the blowoff boundary, one could linearly extrapolate to zero flow velocity and get a reasonable yet conservative estimate of the minimum flammability.

On the quenching branch of Figure 6.22, as the U is reduced, the ambient O_2 concentration at the limit has to increase to create an adequate O_2 gradient for diffusion of O_2 to the flame. The 3D diffusive transport becomes significant. The flow time shifts from the residence time limitations to diffusive time limitations. The flames near quenching are starved for O_2, which is the limiting reactant. Fuel is leaking out of the open tail of the flame. Oscillations begin and mixing layers form and the flame flashes through them, locally depleting the already low ambient O_2 as discussed previously. Ultimately, the flame extinguishes due to the resulting reduced reaction rate that lowers the flame temperature to quenching.

6.1.6 Conclusions

For the first time, a series of concurrent rod flammability tests were conducted in microgravity aboard the International Space Station (ISS). A small flow duct was used to create 0- to 55-cm/s flows past the three sizes of clear and black PMMA rods.

Ignition delay time increased significantly as the minimum limiting O_2 concentration is approached. Ignition limits are found to be at higher O_2 concentrations than the flammability limits due to the added heat loss to the initially cold fuel rod present at ignition. The ignition delay time can be up to almost 10 times longer than the NASA STD–6001 standard igniter on time.

Detailed observations of near-quenching flames are described, including flame standoff distance trend with O_2 and stretch rate a. The flame shrinks to a hemispherical blue shape just before quenching. Prequenching extinction oscillations at 1.1 Hz are observed with a radiometer and are similar to previously reported quiescent candle flame oscillations in microgravity.

As flow speed is increased, blowoff extinction is initiated by the formation of a hole in the flame sheet in the stagnation region of the flame. Once the stagnation region is blown far enough downstream of the stagnation region (greater than one gas-phase thermal length ℓ), the flame is unable to propagate back upstream even when the flow is reduced. This is consistent with observations that at the low O_2 concentrations of interest, an opposed-flow flame cannot be established. Blowoff extinction limits from the ISS experiments agree well with Zero Gravity Research Facility 5.18-s drop test limits.

The lower portion of the flammability boundary, with O_2 concentration and a as coordinates, was outlined as stochastic region between stable flames and extinguished flames. A curve fit including an exponential and linear term was used to empirically define the boundary. The minimum in the flammability boundary is at a of 8 to 12 s^{-1}, where the a is modified to account for the various rod sizes tested through the gas-phase ℓ scale. The linear blowoff branch may lend itself to extrapolation of normal-gravity flammability testing to zero stretch to estimate the lower microgravity flammability limit.

Gas sensor data and rod mass loss estimates indicate that the flames are globally stoichiometric at higher O_2 concentrations but become more globally fuel rich as the minimum O_2 concentration is approached. This is due to excess pyrolyzate leakage out of the open tail of the hemispherical flames. CO production also increases significantly at low O_2 levels. The CO to CO_2 ratio increases as well at low O_2 concentrations. This data suggests that the limiting reactant at the lowest O_2 concentrations is the O_2 rather than the fuel.

A critical Damköhler number formulation is applied across the flammability boundary, and the critical flame temperature is derived. This critical flame temperature is used in a Nusselt number

correlation to estimate the convective heat flux to the stagnation region of the rod. A surface energy balance is formulated that uses the critical flame temperature and convective heat flux to derive the mass burning rate along the boundary. The rod regression rates calculated from this model compare favorably with the experimental measurements.

The terms of the surface energy balance are compared and reveal that in the blowoff branch, heat losses are negligible. In the quenching region, surface radiative loss dominates. Solid conductive loss down the rod is lower and decreases with decreasing stretch due to the low Peclet number. Gas-phase radiative feedback becomes an important heat transfer process that extends the flammability limit to lower a. At the bottom of the flammability map, heat losses are only 30 percent of the total heating rate to the surface, so the transition from blowoff to quenching occurs when the convective flows become the same order of magnitude as diffusive flows, shifting the critical Damköhler number residence time limitations to diffusive time limitations. The transport of the limiting reactant O_2 is limited by concentration gradients, causing the needed ambient O_2 to increase as the a is reduced.

6.1.7   Acknowledgments

6.1.8   References

1. Alkidas, A.; and Durbetaki, P.: Stagnation-Point Heat Transfer: The Effect of the First Damkohler Similarity Parameter. J. Heat Transfer, vol. 94, no. 4, 1972, pp. 410–414.
2. Simmons, R.F.; and Wolfhard, H.G.: Some Limiting Oxygen Concentrations for Diffusion Flames in Air Diluted With Nitrogen. Combust. Flame, vol. 1, no. 2, 1957, pp. 155–161.
3. Linan, Amable: The Asymptotic Structure of Counterflow Diffusion Flames for Large Activation Energies. Acta Astronaut., vol. 1, nos.7–8, 1974, pp. 1007–1039.
4. Sohrab, S.H.; Linan, A.; and Williams, F.A.: Asymptotic Theory of Diffusion-Flame Extinction With Radiant Loss From the Flame Zone. Combust. Sci. Technol., vol. 27, nos. 3–4, 1982, pp. 143–154.
5. T'ien, James S.; and Bedir, Hasan: Radiative Extinction of Diffusion Flames—A Review. Proceedings of the First Asia-Pacific Conference on Combustion, Osaka, Japan, 1997.
6. T'ien, James S.: Diffusion Flame Extinction at Small Stretch Rates: The Mechanism of Radiative Loss. Combust. Flame, vol. 65, no. 1, 1986, pp. 31–34.
7. T'ien, James S.: Some Partial Scaling Considerations in Microgravity Combustion Problems. Progress in Scale Modeling, Springer, Dordrecht, 2008, pp. 281–292.
8. Sohrab, S.H.; and Williams, F.A.: Extinction of Diffusion Flames Adjacent to Flat Surfaces of Burning Polymers. J. Polym. Sci., Polym. Chem. Ed., vol. 19, no. 11, 1981, pp. 2955–2976.
9. Krishnamurthy, L.: Diffusion-Flame Extinction in the Stagnation-Point Boundary Layer of PMMA in O_2/N_2 Mixtures. Combust. Sci. Technol., vol. 10, nos. 1–2, 1975, pp. 21–25.
10. Tsuji, Hiroshi: Counterflow Diffusion Flames. Prog. Energy Combust. Sci., vol. 8, no. 2, 1982, pp. 93–119.
11. Halli, Y.; and T'ien, J.S.: Effect of Convective Velocity on Upward and Downward Burning Limits of PMMA Rods. NBS–GCR–86–507, 1986. Available from National Technical Information Services.

12. Olson, Sandra L.; Ferkul, Paul V.; and T'ien, James S.: Near-Limit Flame Spread Over a Thin Solid Fuel in Microgravity. Proc. Combust. Inst., vol. 22, no. 1, 1989, pp. 1213–1222.

13. Ivanov, A.V., et al.: Experimental Verification of Material Flammability in Space. NASA/CR—1999-209405, 1999. https://ntrs.nasa.gov

14. Olson, Sandra L., et al.: Results From On-Board CSA–CP and CDM Sensor Readings During the Burning and Suppression of Solids—II (BASS–II) Experiment in the Microgravity Science Glovebox (MSG). ICES–2015–196, 2015.

15. Olson, S.L.; and Miller, F.J.: Experimental Comparison of Opposed and Concurrent Flame Spread in a Forced Convective Microgravity Environment. Proc. Combust. Inst., vol. 32, no. 2, 2009, pp. 2445–2452.

16. National Aeronautics and Space Administration: Flammability, Offgassing, and Compatibility Requirements and Test Procedures. NASA–STD–6001B, 2011.

17. Dietrich, D.L., et al.: Candle Flames in Non-Buoyant Atmospheres. Combust. Sci. Technol., vol. 156, no. 1, 2000, pp. 1–24.

18. Wang, H.Y.; and Law, C.K.: On Intrinsic Oscillation in Radiation-Affected Diffusion Flames. Proc. Comb. Inst., vol. 31, no. 1, 2007, pp. 979–987.

19. Nayagam, Vedha; Balasubramaniam, R.; and Ronney, Paul D.: Diffusion Flame-Holes. Combust. Theory Model., vol. 3, no. 4, 1999, pp. 727–742.

20. Rhatigan, Jennifer L.; Bedir, Hasan; and T'ien, James S.: Gas-Phase Radiative Effects on the Burning and Extinction of a Solid Fuel. Combust. Flame, vol. 112, nos. 1–2, 1998, pp. 231–241.

21. Rhatigan, J.L.; Sung, C.J.; and T'ien, J.S.: On Solid Trioxane Combustion in Stagnation Point Flows. Proc. Comb. Inst., vol. 29, no. 2, 2002, pp. 1645–1652.

22. T'ien, James S.: The Effects of Perturbations on the Flammability Limits. Combust. Sci. Technol., vol. 7, no. 4, 1973, pp. 185–188.

23. Hirsch, D., et al.: Issues Related to the Flammability Assessment of Polymers for Hazard Analyses of Oxygen Systems. Flammability and Sensitivity of Materials in Oxygen-Enriched Atmospheres: 10th Volume, ASTM STP1454, T. Steinberg, B. Newton, and H. Beeson, eds., American Society for Testing and Materials, West Conshohocken, PA, 2003, pp. 21–26.

24. Mulholland, G.W.: The Effect of Oxygen Concentration on CO and Smoke Produced by Flames. Fire Saf. Sci., vol. 3, 1991, pp. 585–594.

25. Sibulkin, M.: Heat Transfer Near the Forward Stagnation Point of a Body of Revolution. J. Aeronaut. Sci., vol. 19, no. 8, 1952, pp. 570–571.

26. Baukal, C.E.; and Gebhart, B.: Surface Condition Effects on Flame Impingement Heat Transfer. Exp. Therm. Fluid Sci., vol. 15, no. 4, 1997, pp. 323–335.

27. Chander, Subhash; and Ray, Anjan: Flame Impingement Heat Transfer: A Review. Energy Convers. Manag., vol. 46, nos. 18–19, 2005, pp. 2803–2837.

28. Olson, Sandra L.; and T'ien, James S.: Buoyant Low-Stretch Diffusion Flames Beneath Cylindrical PMMA Samples. Combust. Flame, vol. 121, no. 3, 2000, pp. 439–452.

29. Ohtani, Hideo; Akita, Kazuo; and Hirano, Toshisuke: An Analysis of Bottom Stagnation Region Combustion of Polymeric Material Pieces Under Natural Convection. Combust. Flame, vol. 53, 1983, pp. 33–40.

30. T'ien, J.S., et al.: Combustion and Extinction in the Stagnation-Point Boundary Layer of a Condensed Fuel. Combust. Flame, vol. 33, 1978, pp. 55–68.

31. Lyon, Richard E.; and Quintiere, James G.: Criteria for Piloted Ignition of Combustible Solids. Combust. Flame, vol. 151, no. 4, 2007, pp. 551–559.

32. Hirano, Toshisuke; Noreikis, Stanley E.; and Waterman, Thomas E.: Measured Velocity and Temperature Profiles Near Flames Spreading Over a Thin Combustible Solid. Combust. Flame, vol. 23, no. 1, 1974, pp. 83–96.

6.1.9 Primary Microgravity and Normal-Gravity Research Citations for This Project

- Olson, Sandra; and Ferkul, Paul V.: Microgravity Flammability Boundary for PMMA Rods in Axial Stagnation Flow: Experimental Results and Energy Balance Analyses. Combust. Flame, vol. 180, 2017, pp. 217–229.
- Marcum, Jeremy W.; Ferkul, Paul V.; and Olson, Sandra L.: PMMA Rod Stagnation Region Flame Blowoff Limits at Various Radii, Oxygen Concentrations, and Mixed Convection Stretch Rates. Proc. Comb. Inst., vol. 37, no. 3, 2019, pp. 4001–4008.
- Olson, Sandra L.; Ferkul, Paul V.; and Marcum, Jeremy W.: High-Speed Video Analysis of Flame Oscillations Along a PMMA Rod After Stagnation Region Blowoff. Proc. Comb. Inst., vol. 37, no. 2, 2019, pp. 1555–1562
- Marcum, J.W., et al.: Low Pressure Flame Blowoff of the Stagnation Region of Cast PMMA Cylinder in Axial Mixed Convective Flow. Combust. Flame, vol. 216, 2020, pp. 385–397.

7.0   Individual Principal Investigator Report: T'ien

7.1   Concurrent Flame Growth, Spread, and Extinction Over Composite Fabric Samples in Low-Speed Purely Forced Flow in Microgravity[3]

7.1.1   Abstract

As a part of the NASA Burning and Suppression of Solids (BASS) and BASS–II experimental projects aboard the International Space Station, flame growth, spread, and extinction over a composite cotton-fiberglass fabric blend (referred to as the SIBAL (Solid Inflammability Boundary at Low Speed) fabric) were studied in low-speed concurrent forced flows. The tests were conducted in a small flow duct within the Microgravity Science Glovebox. The fuel samples measured 1.2 and 2.2 cm wide and 10 cm long. Ambient O_2 was varied from 21 percent down to 16 percent and flow speed from 40 cm/s down to 1 cm/s. A small flame resulted at low flow, enabling us to observe the entire history of flame development including ignition, flame growth, steady spread (in some cases), and decay at the end of the sample. In addition, by decreasing flow velocity during some of the tests, low-speed flame quenching extinction limits were found as a function of O_2 percentage. The quenching speeds were found to be between 1 and 5 cm/s with higher speed in lower O_2 atmosphere. The shape of the quenching boundary supports the prediction by earlier theoretical models. These long-duration microgravity experiments provide a rare opportunity for solid fuel combustion since microgravity time in ground-based facilities is generally not sufficient. This is the first time that a low-speed quenching boundary in concurrent spread is determined in a clean and unambiguous manner.

7.1.2   Introduction

Flame spread and extinction over condensed fuels in a microgravity environment has been the subject of extensive theoretical and experimental studies due to the importance of fire safety in human space missions (Refs. 1 to 4). Compared with burning in normal gravity, diffusion flames in microgravity are not affected by buoyancy-induced flow, thus providing a chance to study the fundamental mechanism(s) of low-speed flame quenching (Ref. 5). Transition from solid diffusion flame spreading to quenching extinction is a slow heat loss process characterized by a relative increase in the rates of radiative and conductive heat losses compared to the rate of heat generation (Ref. 3). Long-duration microgravity time is desired for such studies, which in general cannot be achieved by ground-based facilities.

Recently, NASA's Burning and Suppression of Solids (BASS and BASS–II) project examined the burning and extinction characteristics of a variety of solid fuel samples aboard the International Space Station (ISS). Different thermally thin and thermally thick solid fuels were burned in concurrent, opposed, or stagnation flow configurations in a small flow duct. Each experimental run took tens of seconds to minutes, depending on the sample type and flow conditions. The challenge with thin solid samples in concurrent flow, compared with other configurations, is that flame spreads much faster, and flames can become quite long. Because of size limitations, the fuel sample is relatively short and so a concurrent spreading flame may not reach fully steady spread within the sample length. The transient ignition and flame growth process, however, provides a flame spread history that can be useful for the development of transient flame models (Ref. 6). In BASS–II, a N_2 dilution scheme is used whereby the O_2 percentage in the Microgravity Science Glovebox (MSG) can be decreased to a preset value so that flame spread can be

studied with O_2 percentage as an additional variable parameter (Ref. 7). This facilitates the determination of the O_2-flow-velocity flammability boundary of materials.

In this report, BASS and BASS–II results will be discussed in detail. Flame growth, spread, and quenching extinction will be presented for a thin composite cotton-fiberglass fabric burning in various O_2 concentrations and concurrent flow speeds.

7.1.3 Experimental

All tests were conducted in a small flow duct (shown in Figure 7.1) within the MSG aboard the ISS. The sample used is a composite cotton-fiberglass fabric blend (75 percent cotton and 25 percent fiberglass). The thickness of the sample is about 0.32 mm with an area density of 18.2 mg/cm^2. The fabric is custom made for a previous project Solid Inflammability Boundary at Low Speeds (SIBAL) (Ref. 8), hence it is referred to here as the SIBAL fabric. One major advantage of this fuel sample is the retention of sample structure integrity after the combustible (i.e., cotton cellulose) is consumed because of the fiberglass mesh. It does not crack or produce curly ash typically seen in pure cellulose samples such as paper or cloth. In addition to Reference 8, experimental studies using SIBAL fabric can be found in References 9 and 10.

In the experiment, SIBAL fuel samples of two different widths, 1.2 and 2.2 cm, were used. Both have an exposed length of 10 cm. The samples were mounted in stainless steel sample holders. The fuel sample mounted to the holder was placed in the small flow duct of cross-sectional size 7.6 by 7.6 cm. The flow speed could be varied from 1 to 55 cm/s. The tests were conducted in ambient O_2 molar fraction of 16 to 21 percent. Ambient pressure was 1 atm. It should be noted that for a given test the O_2 concentration was fixed while the flow speed could be varied.

A Kanthal® hot wire was used to ignite the fuel sample leading edge so that the flame can spread in a concurrent configuration. The flame growth process was recorded by two cameras. The side-view video camera provided edge-on images of the flat samples at standard video framing rates (29.97 frames per second). The top-view digital camera looked down on the top fuel surface and provided high-resolution still images of the flame at a rate of about one image every 1.2 s. When flow speed and O_2 concentration were low, the flame became very dim blue and was difficult to see in the side video camera. The top-view
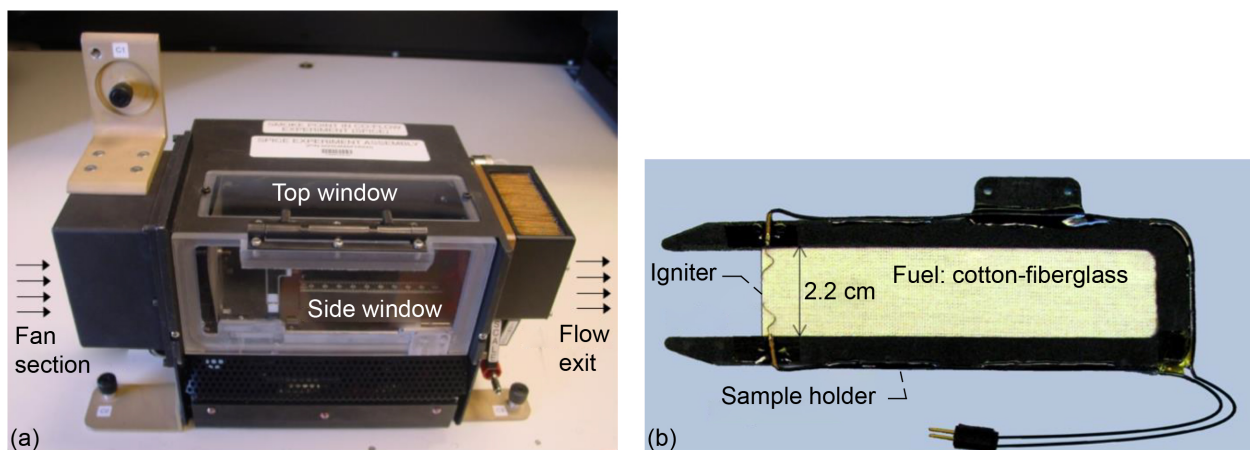
Figure 7.1.—Experimental setup. (a) Small flow duct. (b) Fuel sample, sample holder, and igniter.

camera exposure times were long enough (1/8 to 1/4 s) to easily capture high-quality flame images even for dim flames right before quenching. These still images provide a time history of flame quenching that can be used to compare with transient model results.

7.1.4   Results and Discussion

A total of 27 tests were carried out for the fabric samples in BASS–II, including six quenching tests, three nonignited tests, and one blowoff test. These are listed in Table 7.1. In addition, four tests from the BASS series were selected as listed at the bottom of Table 7.1. These four tests are all 21 percent O_2 cases at a fixed flow velocity during each test. For those cases with flow velocity variations, the starting and the final velocities are indicated in the velocity column. The rate of velocity change varies from case to case depending on the communication between the astronauts and the ground crews and the manual adjustment time by the crew. Many of these tests were used to determine the low-speed quenching limits as a function of O_2 percentage. In some tests, the flame quenched quickly or was not ignited. These samples were reused in additional tests as indicated in Table 7.1. These partially burned samples were ignited with a retractable igniter on one side of the sample at the fuel burnout position. These reused samples in general had a short unburned length and provided less quantitative data, thus will not be discussed in this report.

Figure 7.2 shows flame development stages of a 2.2-cm sample in 10-cm/s flow and 21 percent O_2. Figure 7.2(a) shows side-view flame tracking of flame tip, flame base, and flame length. Figure 7.2(b) shows flame edge-view video still images at different stages. Note in the figure, flow is from right to left. After the igniter was turned on, a strong flame was initiated on both sides of the solid fuel. The flame was stabilized and started to grow and move downstream. At about 19 s, the flame reached a limiting constant length and a steady spread rate relative to the laboratory (Ref. 11). This steady spread state lasted for around 9 s. The flame images look almost identical during this stage, as can be seen at 20.17 and 24.83 s in Figure 7.2(b). Then the flame tip (or more precisely the flame preheating front) moved close to the end of the fuel sample, and the flame decayed in size until complete burnout. The whole combustion process took about 40 s.

Figure 7.3 shows flame development stages of a 2.2-cm sample in 5-cm/s flow and 21 percent O_2. Unlike the flame in 10-cm/s flow in Figure 7.2, the flame from the side-view video is very dim in this case. Figure 7.3 thus shows the top-view images and tracking from those images. Because the flow speed is lower, it took more than 60 s to burn the whole sample. Steady spread time lasts for about 21 s, much longer than the 10-cm/s flow case. Virtually identical images at 35.59 and 45.59 s are shown in Figure 7.3(b). In the top-view images, we can find bright spots behind the flame base when the flame passes. The spots come from the smoldering of a small amount of fuel that is not completely consumed by the flaming combustion. Compared with the 10-cm/s case, the 5-cm/s case has a shorter flame and spreads more slowly.

Steady flame spread rates in different flow speeds and O_2 percentages are plotted in Figure 7.4 for both 2.2- and 1.2-cm samples. Note in some cases flow speed was varied during the test. Steady flame spread here means the flame reached a constant spread rate for more than 20 s. Flames spread more slowly across the narrower samples, at lower flow velocities and at lower O_2 percentages. The trends are consistent with our physical intuition.

TABLE 7.1.—TEST SUMMARY OF FLAT SIBAL[a] FABRICS IN CONCURRENT FLOW IN
BURNING AND SUPPRSSION SOLIDS (BASS AND BASS–II)

Test number	Sample width, cm	Flow, cm/s	O_2, vol%	Comments
GMT45-T1	2.2	10	18.5[b]	---------------------------
GMT45-T2	2.2	10 to 5	18.5[b]	---------------------------
GMT45-T4	2.2	10 to 2.2	18.7	Quenched
GMT45-T15	2.2	10 to 29	18.7	No blowoff
GMT100-T5	2.2	10 to 2.4	18.8	---------------------------
GMT100-T6	2.2	4.5 to 2.6	18.8	---------------------------
GMT100-T13	2.2	4 to 2.2	17.5	Quenched
GMT100-T16	2.2	4 to 3	17.6	---------------------------
GMT175-T9	2.2	10	16.4	No ignition
GMT175-T10	2.2	5	16.4	No ignition
GMT175-T18	2.2	5 to 2.6	17.4	Quenched
GMT178-T11	2.2	4	17.1	---------------------------
GMT178-T12	2.2	5	16.8	No ignition
GMT178-T14	2.2	4 to 2.8	16.9	Quenched
GMT178-T17	2.2	6 to 53	16.9	No blowoff
GMT190-T19	1.2	11	17.2	---------------------------
GMT190-T20	1.2	11 to 3	17.2	Quenched
GMT190-T21	1.2	11 to 47	17.2	Blow-off
GMT190-T22	1.2	10.5 to 5	17.1	Quenched
GMT190-T23	2.2	10	17.2	Reused, did not ignite
GMT190-T24	2.2	10	18.2	Reused, one-sided flame
GMT216-T25	2.2	5 to 2.5	20.8	Reused, ignited
GMT216-T26	2.2	5 to 2.5	20.8	Reused, ignited
GMT216-T27	1.2	5 to 2	20.7	Reused, ignited
GMT216-T28a	1.2	5	20.7	Reused, did not ignite
GMT216-T28b	1.2	5	20.7	Reused, did not ignite
GMT216-T29	1.2	5 to 2	20.7	Reused, ignited
GMT96-T8	2.2	5	21	BASS
GMT96-T7	2.2	10	21	BASS
GMT131-T10	1.2	11	21	BASS
GMT222-T11	1.2	19	21	BASS

[a]Solid Inflammability Boundary at Low Speeds.

[b]O_2 reading in these two tests might be inaccurate.
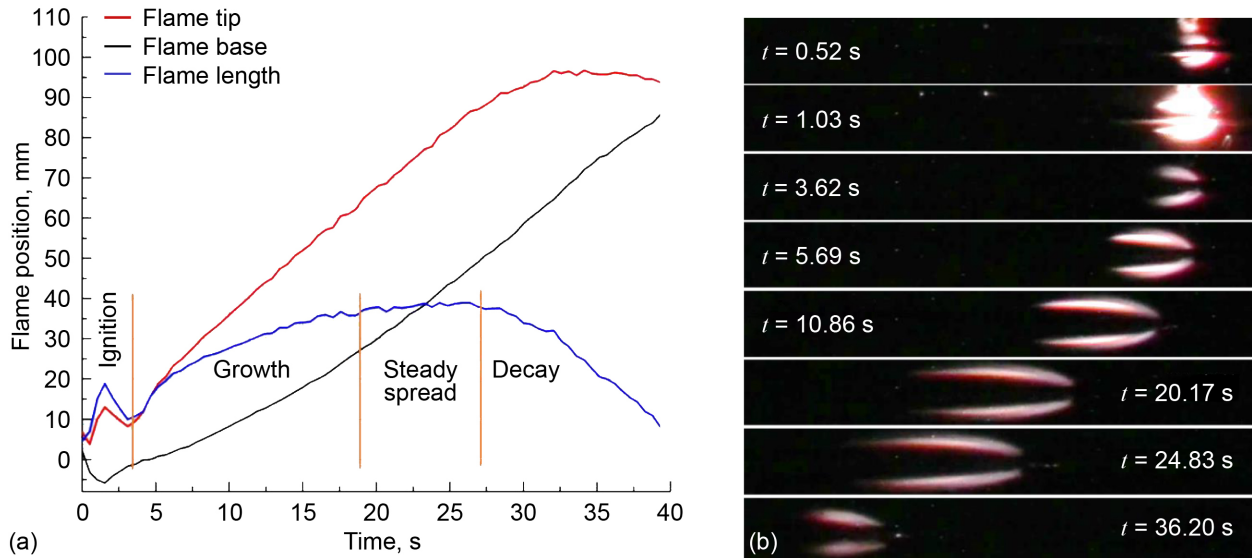
Figure 7.2.—Flame development on 2.2-cm sample in 10-cm/s concurrent flow, 21 percent O_2. (a) Side-view flame tracking. (b) Side-view image sequence over time t. Flow is from right to left.
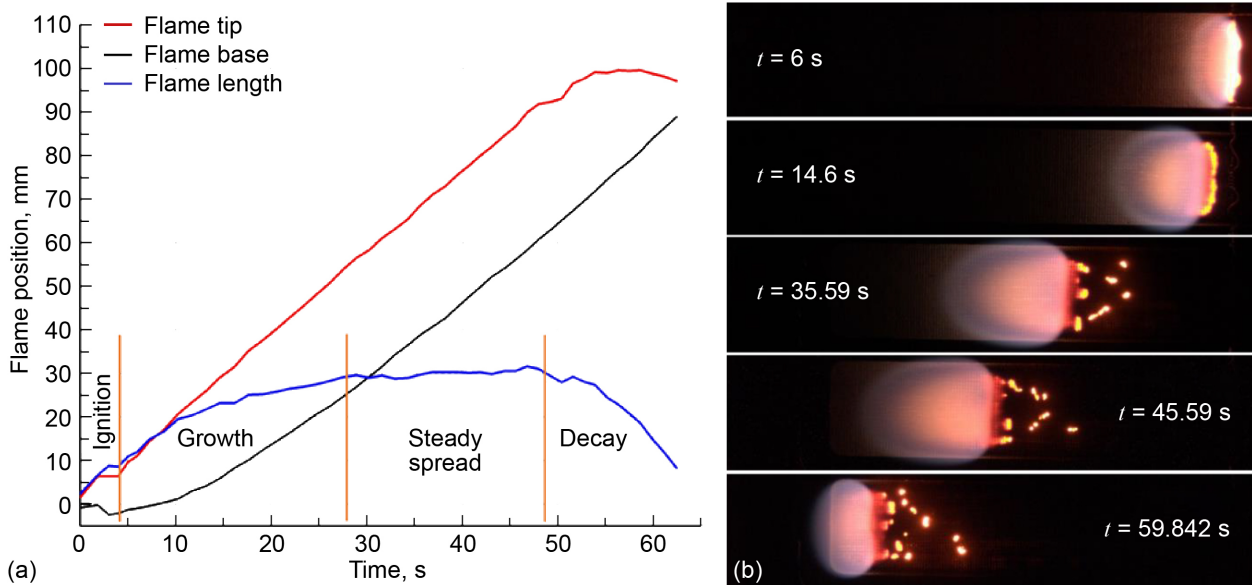
Figure 7.3.—Flame development on 2.2-cm sample in 5-cm/s flow, 21 percent O_2. (a) Top-view flame tracking. (b) Top-view image sequence over time t. Flow is from right to left.
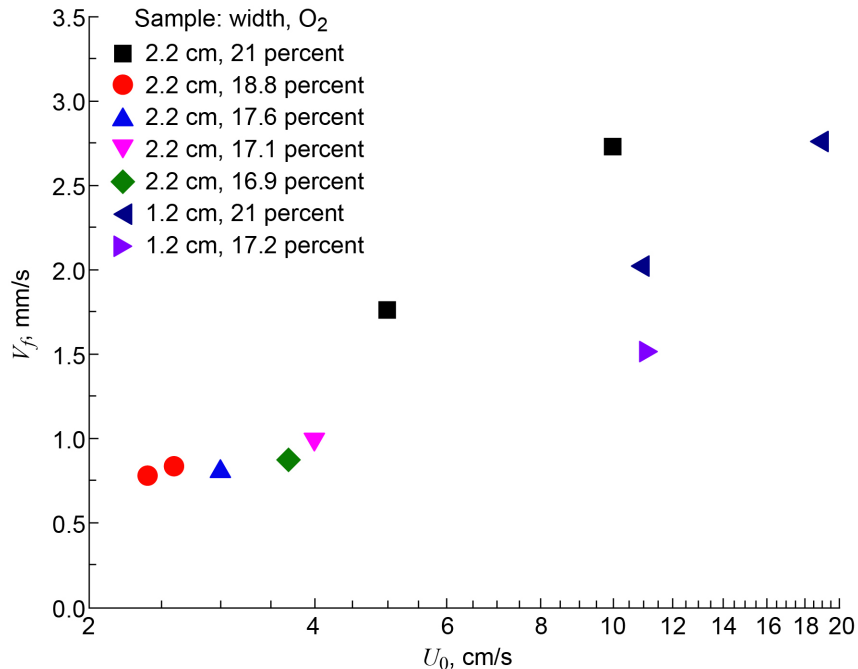
Figure 7.4.—Steady flame spread rate for both 2.2- and 1.2-cm-wide samples.

Figure 7.5 shows a typical flame quenching sequence in the BASS–II experiment. A 2.2-cm-wide sample in 18.7 percent O_2 was first ignited at 10-cm/s flow. Flow speed was decreased to 2.2 cm/s incrementally after ignition. Figure 7.6 shows flame tracking and flow speed versus time. After ignition, the flame started to grow. As the flow speed was reduced, both flame length and flame width dropped accordingly with flow. After 25 s, flow velocity was reduced to 2.2 cm/s and held there for the remainder of the test. As shown in Figure 7.5, both the flame length and flame width continued to decrease approaching a circular-shaped blue flame seen from the top. The size of the flame continues to shrink until extinction is reached. This is typical in a quenching extinction sequence. As the quenching limit is approached (in this case by turning down the flow velocity), the fuel pyrolysis rate and combustion heat release rate (HRR) are reduced, and radiation loss becomes a significant fraction of the HRR from the shrinking flame. When the flame becomes small enough, conduction becomes the additional heat loss. The postburn photo of the sample in Figure 7.5 shows the narrowing of the burnt region as the flame shrinks toward extinction with a substantial part of the fuel left unburnt along the two sides of the sample holder. Although this is a concurrently spreading flame, the quenching sequence shows similar characteristics in opposed flow (Ref. 2); the flame becomes circular, indicating the importance of three-dimensional (3D) heat and mass transfer near the limit.
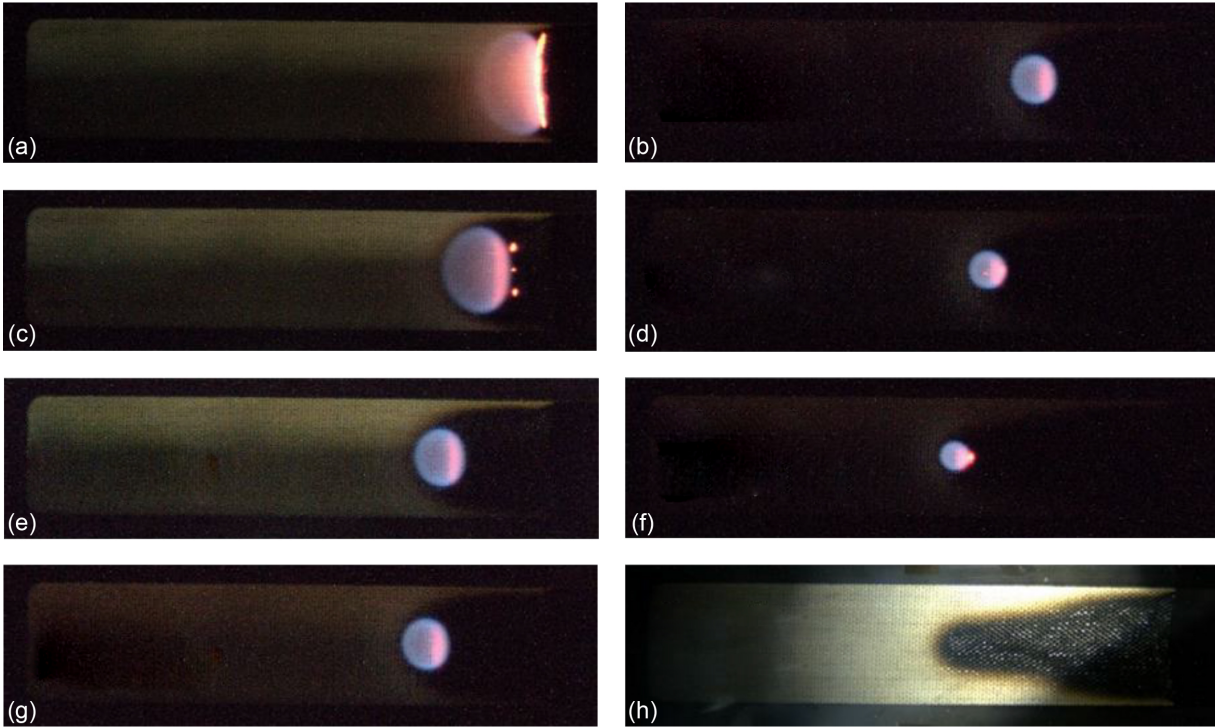
Figure 7.5.—Top view of flame quenching sequence. 2.2-cm-wide sample in 18.7 percent O_2. Ignited at 10-cm/s flow, reduced to 2.2 cm/s. Flow is from right to left. (a) Time t is 6.7 s, velocity V is 8 cm/s. (b) t = 32.6 s. V = 2.2 cm/s. (c) t = 15.7 s. V = 4 cm/s. (d) t = 45.0 s. V = 2.2 cm/s. (e) t = 25.8 s. V = 2.2 cm/s. (f) t = 54.0 s. V = 2.2 cm/s. (g) t = 29.2 s. V = 2.2 cm/s. (h) Postburn.
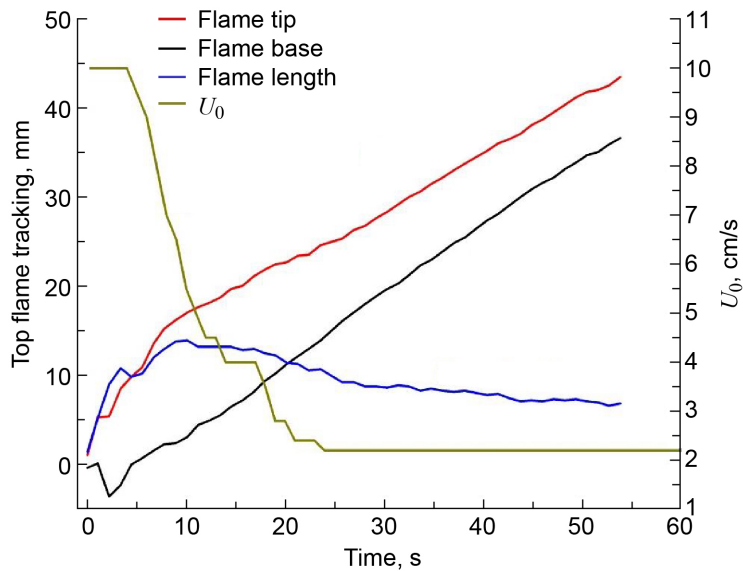
Figure 7.6.—Flame tracking and flow speed U_0 versus time for 2.2-cm-wide sample in 18.7 percent O_2, ignited at 10-cm/s flow, then reduced to 2.2 cm/s.

For this thin fabric fuel in concurrent flow, flame spread rate is relatively large and the sample is not long enough to fine tune the flow speed during the 1 to 2 min of experimental run time. It is difficult to get to the desired near-quenching-limit state every time. Six quenching cases were achieved during BASS–II for the SIBAL sample, four of them were for the 2.2-cm-width samples. Along with the near-limit stable flame data, we were able to draw part of the quenching branch of the flammability boundary as shown in Figure 7.7 for 2.2-cm-wide SIBAL fabric. Quenching flow velocities were found to be between 1 and 5 cm/s with higher velocity at lower O_2 percentage. This trend of the quenching boundary supports the prediction by earlier theoretical models (Refs. 1 and 8). Recently, a 3D transient numerical model has been published (Ref. 6) that is suitable to simulate the present experiment. The model contains many material properties including kinetic rate constants. The bottom part of the flammability boundary that supports combustion in the lowest O_2 environment is expected to be flat in this figure and cannot be determined accurately by this velocity-varying procedure. Very near the boundary, ignition of the sample is sporadic. A procedure with gradually decreasing O_2 is needed. In addition, because of the limited number of tests, the quenching limit for the 1.2-cm-wide sample was not resolved. But it can be seen that the narrow sample has a smaller flammable domain, as expected.
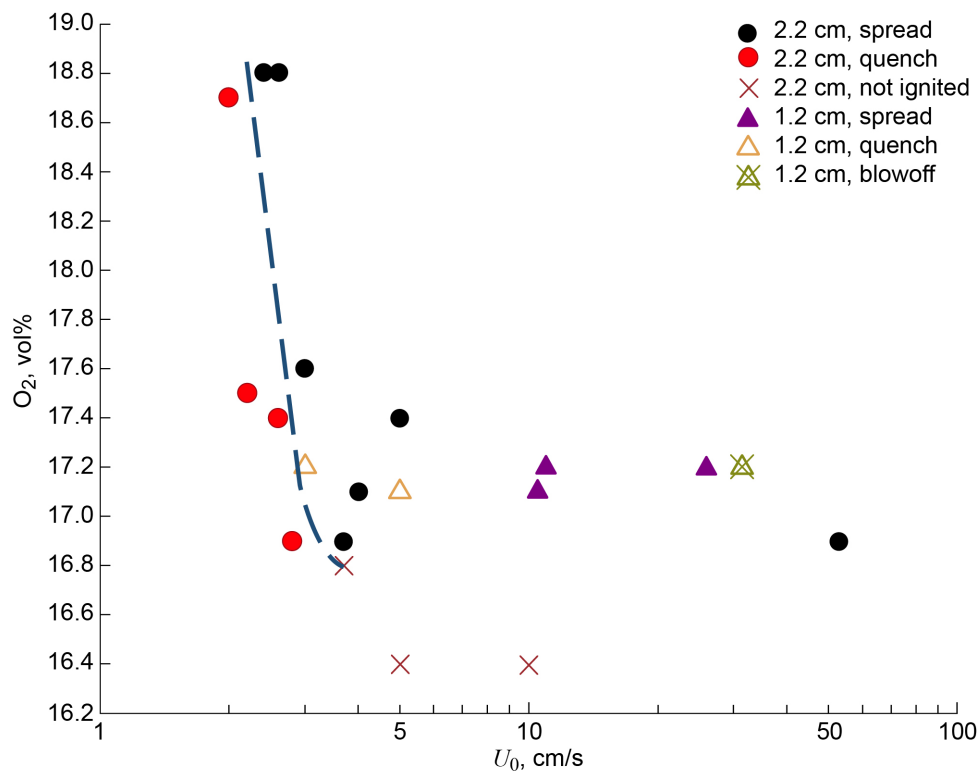
Figure 7.7.—Flammability map for Solid Inflammability Boundary at Low Speeds (SIBAL) fabric in concurrent flow in microgravity. Dotted line marks experimental quenching boundary for 2.2-cm-wide sample. Flow speed (U_0).

7.1.5   Conclusions

Concurrent flame growth and extinction over a thin flat cotton-fiberglass composite fabric sample was studied as part of the Burning and Suppression of Solids (BASS) and BASS–II space experiments aboard the International Space Station. These long-duration microgravity experiments provided rare opportunities for solid fuel combustion studies. By reducing the flow velocity during the tests, quenching extinction limits were obtained accurately. The quenching velocities are small (between 1 and 5 cm/s), and an accurate determination is necessary to resolve the slope of the quenching boundary. The experimental data obtained supports earlier theoretical predictions (at least qualitatively) of solid flammability limits at low flow velocities due to radiative and conductive losses. The flame image sequence at quenching shows the flame shrinks both in length and width and the flame goes out in a three-dimensional manner.

In addition to obtaining quenching limits, the sequence of sample ignition, flame growth, and steady spread to final decay across the entire sample in low-speed purely forced flows were experimentally recorded. These are precious data to help us to understand the entire process of flame development in microgravity. They also provide the basis to check the theoretical model development. Currently, we are measuring and deducing the pyrolysis rate constants for Solid Inflammability Boundary at Low Speeds (SIBAL) fabric in order to perform quantitative comparisons between the model and experiment.

7.1.6   References

1. Ferkul, P.V.; and T'ien, J.S.: A Model of Low-Speed Concurrent Flow Flame Spread Over a Thin Fuel. Combust. Sci. Technol., vol. 99, nos. 4–6, 1994, pp. 345–370.
2. Olson, Sandra L.; Ferkul, Paul V.; and T'ien, James S.: Near-Limit Flame Spread Over a Thin Solid Fuel in Microgravity. Proc. Comb. Inst., vol. 22, no. 1, 1989, pp. 1213–1222.
3. T'ien, J.S., et al.: Mechanisms of Flame Spread and Smolder Wave Propagation. Microgravity Combustion—Fire in Free Fall. H.D. Ross, ed., Academic Press, San Diego, CA, 2001, pp. 299–345.
4. Ferkul, P.V., et al.: Aspects of Fabric in Opposed and Concurrent Air Flow in Microgravity. Presented at the 8th U.S. National Combustion Meeting, Park City, UT, 2013.
5. T'ien, James S.: Diffusion Flame Extinction at Small Stretch Rates: The Mechanism of Radiative Loss. Combust. Flame, vol. 65, no. 1, 1986, pp. 31–34.
6. Zhao, Xiaoyang; and T'ien, James S.: A Three-Dimensional Transient Model for Flame Growth and Extinction in Concurrent Flows. Combust. Flame, vol. 162, no. 5, 2015, pp. 1829–1839. http://dx.doi.org/10.1016/j.combustflame.2014.12.003 Accessed June 23, 2021.
7. Olson, Sandra L., et al.: Results From On-Board CSA–CP and CDM Sensor Readings During the Burning and Suppression of Solids—II (BASS–II) Experiment in the Microgravity Science Glovebox (MSG). ICES–2015–196, 2015.
8. Ferkul, Paul V., et al.: Solid Fuel Combustion Experiments in Microgravity Using a Continuous Fuel Dispenser and Related Numerical Simulations. Microgravity Sci. Tec., vol. 15, no. 2, 2004, pp. 3–12.
9. Kleinhenz, Julie, et al.: One-Sided Flame Spread Phenomena of a Thermally Thin Composite Cotton/Fiberglass Fabric. Fire Mater., vol. 29, no. 1, 2005, pp. 27–37.
10. Johnston, Michael C., et al.: Self Induced Buoyant Blow Off in Upward Flame Spread on Thin Solid Fuels. Fire Saf. J., vol. 71, 2015, pp. 279–286.
11. Tseng, Ya-Ting; and T'ien, James S.: Limiting Length, Steady Spread, and Nongrowing Flames in Concurrent Flow Over Solids. J. Heat Trans., vol. 132, no. 9, 2010, p. 091201

Appendix A.—Test Matrices for Burning and Suppression Solids—II (BASS–II)

These summary test matrices are grouped by principal investigator with Bhattacharjee in Table A.1, Ferkul in Table A.2, Fernandez-Pello in Table A.3, Miller in Table A.4, Olson in Table A.5, and T'ien in Table A.6.

A.1 Bhattacharjee Test Matrix

Details are available at http://flame.sdsu.edu/.

TABLE A.1.—BHATTACHARJEE TEST MATRIX

Actual date (for video display date, add 1 for Leap Year)[a]	Approximate start time and end time (video display time)	As-run test number	Test number	Sample number	Material[b]	Igniter	Flow restrictor	Sample distance	Fan display[c]	Air display	Radiometer gain (1,000; 250; 50; and 10)	Radiometer display	Gaseous nitrogen (GN$_2$) pot	GN$_2$ display	Filter (Y/N)	Release mode (CH/CL)[d]	Exposure Mode (M/A)[e]	Exposure compensation (–#EV)[f]	Bracket frames and exposure bracket (#F/1.0)[g]	Shutter speed, s	F stop	ISO	Shutter hold (s/cont)[h]	Secure digital (SD) card serial number (S/N)	Total frames shot	Calibrated initial O$_2$ vol%	Calibrated final O$_2$ vol%	Initial O$_2$ vol%	Final O$_2$ vol%	Initial CO$_2$ vol%	Final CO$_2$ vol%	Initial CO, ppm	Final CO, ppm	Test observations and anomalies (ignited, spread, extinguished, burn time, color, etc.)[c]
2/19/2014 GMT 2014 050	10:09:50 to 10:10:16	7	B1	147	100-µm PMMA film, 2 cm wide	Integral	2	Opposed	62	5	50	---	8	NA	N	CL	A	–4	off	---	F2	1,000	Cont	7	57	22.2	22.2	20.6	20.6	0.44	0.44	0	6	Ignited very quickly, turned flow off after spread halfway; flame extinguished very quickly; and sooty with blue leading edge
7/7/2014 GMT 188	--------	62	B10	173m	1-cm, 0.2-mm PMMA film	Integral	2	Opposed	1.7 (52), 1.25, 0.9, 0.6, 0.4, 0.35	5, 4, 3, 2, 1	10	---	NA	NA	N	CL	A	–3	NA	---	F2	1,000	Cont	16	123	21.0	20.8	20.1	19.9	0.33	0.44	0	23	Multiple velocities for steady spread, extinguished at pot 0.35
7/7/2014 GMT 188	--------	61	B11	158m	2-cm, 0.2-mm PMMA film	Integral	2	Opposed	2.5 (59), 1.3, 0.7, 0.5, 0.35	5, 3, 1, <1	10	---	NA	NA	N	CL	A	–3	NA	---	F2	1,000	Cont	5	131	21.0	20.7	20.1	19.8	0.33	0.47	0	46	Multiple velocities for steady spread, extinguished at pot 0.35
2/19/2014 GMT 2014 050	12:52:07 to 12:53:12	13	B12	160	300-µm film, 2 cm wide	Integral	2	Opposed	46.5	2	50	---	8	NA	N	CL	A	–4	off	---	F2	1,000	Cont	4	160	22.2	22.1	20.5	20.4	0.51	0.56	17	33	Mostly blue, soot only on bottom
7/7/2014 GMT 188	--------	63	B13	162m	2-cm, 0.4-mm thick film	Integral	2	Opposed	3.5 (68), 1.7, 1.25, 0.9, 0.6, 0.4, 0.35	10, 5, 4, 3, 2, 1	10	---	NA	NA	N	CL	A	–3	NA	---	F2	1,000	Cont	16	311	21.0	20.5	20.1	19.6	0.33	0.65	0	61	Multiple velocities for steady spread, extinguished at pot 0.35
7/2/14 GMT 183	--------	47	B14	174m	1-cm-wide, 200-µm-thick PMMA	Integral	2	Opposed	----------------	5, 3, 2, extinction	250	---	NA	NA	N	CL	A	–4	NA	---	F2	1,000	Cont	5	----	15.0	-----	14.1	-----	0.00	-----	0.2	----	HCl O, only brief ignition, flame extinguished
7/7/2014 GMT 188	--------	59	B15	149m	2-cm, 0.1-mm PMMA film	Integral	0	Opposed	1.4 (50) increase to 10.0 pot	10, max	10	---	NA	NA	N	CL	A	–3	NA	---	F2	1,000	Cont	12	122	21.0	20.8	20.1	19.9	0.33	0.43	0	22	Spread at 10 cm/s, did not blowoff
7/2/14 GMT 183	--------	51	B16	150m	2-cm 100-µm-thick PMMA	Integral	2	Opposed	----------------	3, 5 pot, 0.4 pot	250	---	NA	NA	N	CL	A	–4	NA	---	F2	1,000	Cont	7	94	17.3	17.2	16.5	16.4	0.47	0.51	103	119	HCl 1.1 > 1.3; flame quenched after prolonged burn at 0.4 pot, one-sided flame; spread to top side and quenched immediately; did igniter wire affect top flame?
7/2/14 GMT 183	--------	48	B17	175m	1-cm-wide, 200-µm-thick PMMA	Integral	2	Opposed	----------------	5, 3, pot 0.4	250	---	NA	NA	N	CL	A	–4	NA	---	F2	1,000	Cont	17	190	17.5	17.4	16.6	16.5	0.2	0.34	0	47	Burned steadily at higher flows, extinguished just as we reached a pot of 0.4; vapor jetting more on bottom, possibly because of sample tilted slightly to flow?

[a]Greenwich Mean Time.
[b]Polymethylmethacrylate (PMMA).
[c]Potentiometer (pot).
[d]Continuous high (CH). Continuous low (CL).
[e]Manual (M). Automatic (A).
[f]Exposure value (#EV).
[g]Number of frames and exposure increment (#F/1.0).
[h]Continuous (cont). Seconds (s).

Actual date (for video display date, add 1 for Leap Year)[a]	Approximate start time and end time (video display time)	As-run test number	Test number	Sample number	Material[b]	Igniter	Flow restrictor	Sample distance	Fan display[c]	Air display	Radiometer gain (1,000; 250; 50; and 10)	Radiometer display	Gaseous nitrogen (GN2) pot	GN2 display	Filter (Y/N)	Release mode (CH/CL)[d]	Exposure Mode (M/A)[e]	Exposure compensation (−#EV)[f]	Bracket frames and exposure bracket (#F/1.0)[g]	Shutter speed, s	F stop	ISO	Shutter hold (s/cont)[h]	Secure digital (SD) card serial number (S/N)	Total frames shot	Calibrated initial O2 vol%	Calibrated final O2 vol%	Initial O2 vol%	Final O2 vol%	Initial CO2 vol%	Final CO2 vol%	Initial CO, ppm	Final CO, ppm	Test observations and anomalies (ignited, spread, extinguished, burn time, color, etc.)[c]
7/2/14 GMT 183	--------	49	B18	176m	1-cm-wide, 200-μm-thick PMMA	Integral	0	Opposed	---------------	10, blowoff	250	---	NA	NA	N	CL	A	−4	NA	---	F2	1,000	Cont	11	152	17.4	17.4	16.5	16.5	0.34	0.42	47	78	HCl 0.6 > 0.9, flame blew out at a fan pot of 7.0
7/2/14 GMT 183	--------	52	B19	151m	2-cm, 100-μm-thick PMMA	Integral	0	Opposed	---------------	10, blowoff	250	---	NA	NA	N	CL	A	−4	NA	---	F2	1,000	Cont	2	95	17.3	17.2	16.4	16.3	0.51	0.57	119	131	HCl 1.3 > 1.4; flame blew out at a pot of 6.0
2/19/2014 GMT 2014 050	10:25:54 to 10:26:34	8	B2	155	200-μm PMMA film, 2 cm wide	Integral	2	Opposed	62	5	50	---	8	NA	N	CL	A	−4	off	---	F2	1,000	Cont	7	none	22.2	1.6	20.6	-----	0.44	-----	6	----	No stills taken, cable came loose; not quite a straight on edge view
7/2/14 GMT 183	--------	50	B20	152m	2-cm, 100-μm-thick PMMA	Integral	2	Opposed	---------------	5, 3, pot 0.5	250	---	NA	NA	N	CL	A	−4	NA	---	F2	1,000	Cont	9	111	17.4	17.4	16.5	16.5	0.42	0.47	78	103	HCl 0.9 > 1.1; flame burned entire sample
8/4/14 GMT 216	12:48:30	121	B21	174m	1-cm-wide, 200-μm-thick PMMA	46	1	Opposed	53 and down	5 down to extinction	250	---	NA	NA	N	CL	A	−3	NA	---	F2	1,000	Cont	5	88	20.8	20.6	19.8	19.6	0.36	0.44	−1	18	Ignition at 5 cm/s then fan pot turned down slowly after flame; spreads halfway; flame goes out at 0.355 pot setting
8/4/14 GMT 216	17:56:02	126	B22	176m	1-cm-wide, 200-μm-thick PMMA	39	1	Opposed	53, 42, 41, 40.5	5, 2, 0	250	---	NA	NA	N	CL	A	−3	NA	---	F2	1,000	Cont	8	77	20.7	20.5	19.8	19.6	0.41	0.47	−1	10	Ignition at 5 cm/s then decreased flow in step, fan pot 1.7, 0.5, 0.4, 0.36 (flame out)
2/19/2014 GMT 2014 050	12:26:33 to 12:27:01	11	B3	148	100-μm film, 2 cm wide	Integral	2	Opposed	47	2	50	---	8	NA	N	CL	A	−4	off	---	F2	1,000	Cont	7	253	22.2	21.8	20.9	20.5	0.43	0.49	12	19	Probably 20.6 O2 to start; lower flow flames much more blue overall; still some soot though
2/19/2014 GMT 2014 050	11:56:10 to 11:57:06	9	B4	159	300-μm PMMA film, 2 cm wide	Integral	2	Opposed	61	5	50	---	8	NA	N	CL	A	−4	off	---	F2	1,000	Cont	7	137	22.2	22.2	20.6	20.6	0.44	0.51	−1	10	Bubble layer thickness increases with sample thickness
2/19/2014 GMT 2014 050	12:14:24 to 12:15:07	10	B5	156	200 μm 2 cm wide	Integral	2	Opposed	59	5	50	---	8	NA	N	CL	A	−4	off	---	F2	1,000	Cont	7	206	22.2	21.9	20.9	20.6	0.43	0.43	0	12	Repeat of B2 test conditions, to get top view images; question the 20.9 reading; all others were 20.6 this day
7/7/2014 GMT 188	--------	57	B6	153m	2-cm, 0.1-mm PMMA film	Integral	2	Opposed	0.9, 1.3, 2.75	3, 5, approaching 10	10	---	NA	NA	N	CL	A	−3	NA	---	F2	1,000	Cont	8	80	21.0	20.9	20.1	20.0	0.33	0.41	0	0.3	Steady burning at 3 and 5 cm/s, did not reach 10 cm/s before end of sample, complete burnout, HCl −>0.3
2/19/2014 GMT 2014 050	12:42:23 to 12:43:48	12	B7	161	400-μm film, 2 cm wide	Integral	2	Opposed	47	2	50	---	8	NA	N	CL	A	−4	off	---	F2	1,000	Cont	4	84	22.2	22.1	20.6	20.5	0.45	0.51	1	17	Very long bubble layer
7/7/2014 GMT 188	--------	60	B8	157m	2-cm, 0.2-mm PMMA film	Integral	0	Opposed	1.4, increase to 10.0	10, maximum	10	---	NA	NA	N	CL	A	−3	NA	---	F2	1,000	Cont	12	226	21.0	20.5	20.1	19.6	0.33	0.58	0	131	Spread at 10 cm/s, did not blowoff
7/7/2014 GMT 188	--------	58	B9	154m	2-cm, 0.1-mm PMMA film	Integral	2	Opposed	0.6, 0.35	2, <1	10	---	NA	NA	N	CL	A	−3	NA	---	F2	1,000	Cont	12	45	21.0	20.9	20.1	20.0	0.33	0.35	0	10	Steady burning at 2 cm/s, extinguished at 0.35

[a]Greenwich Mean Time.
[b]Polymethylmethacrylate (PMMA).
[c]Potentiometer (pot).
[d]Continuous high (CH). Continuous low (CL).
[e]Manual (M). Automatic (A).
[f]Exposure value (#EV).
[g]Number of frames and exposure increment (#F/1.0).
[h]Continuous (cont). Seconds (s).

A.2 Ferkul Test Matrix

TABLE A.2.—FERKUL TEST MATRIX

Actual date (for video display date, add 1 for Leap Year)[a]	Approximate start time and end time (video display time)	As-run test number	Test number	Sample number	Material	Igniter	Flow restrictor	Sample distance	Fan display	Air display	Radiometer gain (1,000; 250; 50; and 10)	Radiometer display	Gaseous nitrogen (GN_2) potentiometer	GN_2 display	Filter (Y/N)	Release mode (CH/CL)[b]	Exposure mode (M/A)[c]	Exposure compensation (−#EV)[d]	Bracket frames and exposure bracket (#F/1.0)[e]	Shutter speed, s	F stop	ISO	Shutter hold (s/cont)[f]	Secure digital (SD) card serial number (S/N)	Total frames shot	Calibrated initial O_2, vol%	Calibrated final O_2, vol%	Initial O_2, vol%	Final O_2, vol%	Initial CO_2, vol%	Final CO_2, vol%	Initial CO, ppm	Final CO, ppm	Test observations and anomalies (ignited, spread, extinguished, burn time, color, etc.)
2/19/2014 GMT 2014 050	13:59 to 14:00	14	F1	227	Nomex® (DuPont™) natural (Nomex III)	Integral	2	Concurrent	82	9.5	250		8	NA	N	CL	M	NA	off	1/10	F2	1,000	Cont	4	208	22.2	22.2	20.6	20.6	0.46	0.45	0	2	Ignited briefly but did not spread at all and extinguished while the igniter was still on
7/28/2014 GMT 209	--------	103	F2	228m	Nomex® natural (Nomex III)	Integral	2	Concurrent	92	15	250		NA	NA	N	CL	M	NA	NA	1/10	F2	1,000	Cont	8	72	21	21.0	21	21.0	0.37	0.39	105	82	Tried to ignite, flame would not sustain
8/1/14 GMT 213	8:58:25	115	F3	229m	Nomex® natural (Nomex III)	Integral	1	Concurrent	61	8	50		NA	NA	N	CL	A	−3	NA	------	F2	1,000	Cont	13	46	21.7	0.9	20.8	------	0.36	------	2	---	Brief ignition flash, no sustained flame; no postburn sensor readings taken
6/24/2018	--------	36	F4	39M	Japan Wax candle	Integral	2	Stagnation	See notes	3 ignition	250		NA	NA	N	CH	A	−5	9F 1.0	------	F2	1,600	7 s	3	270	17.4	17.4	16.2	16.2	0.38	0.48	22	56	Long ignition, but blue flame established at 3 cm/s, reduced flow in increments: potentiometers 0.6, 0.4, 0.35, 0.32, 0.31, 0.305 flame extinguished

[a]Greenwich Mean Time.
[b]Continuous high (CH). Continuous low (CL). Shutter
[c]Manual (M). Automatic (A).
[d]Exposure value (#EV).
[e]Number of frames and exposure increment (#F/1.0).
[f]Continuous (cont). Seconds (s).

A.3 Fernandez-Pello Test Matrix

TABLE A.3.—FERNANDEZ-PELLO TEST MATRIX

Actual date (for video display date, add 1 for Leap Year)[a]	Approximate start time and end time (video display time)	As-run test number	Test number	Sample number	Material	Igniter	Flow restrictor	Sample distance	Fan display[b]	Air display	Radiometer gain (1,000; 250; 50; and 10)	Radiometer display	Gaseous nitrogen (GN₂) potentiometer	GN₂ display	Filter (Y/N)	Release mode (CH/CL)[c]	Exposure mode (M/A)[d]	Exposure compensation (−#EV)[e]	Bracket frames and exposure bracket (#F/1.0)[f]	Shutter speed, s	F stop	ISO	Shutter hold (s/cont)[g]	Secure digital (SD) card serial number (S/N)	Total frames shot	Calibrated initial O₂ vol%	Calibrated final O₂ vol%	Initial O₂ vol%	Final O₂ vol%	Initial CO₂ vol%	Final CO₂ vol%	Initial CO, ppm	Final CO, ppm	Test observations and anomalies (ignited, spread, extinguished, burn time, color, etc.)[b]
6/16/14 GMT 167	---------	25	P1	185m	6.35-mm black rod	−22	2	Opposed	-----------	5, 2, slow decrease to extinction	250	----	NA	NA	N	CL	A	−4	NA	----	F2	1,000	Cont	6	307	17.7	17.5	16.6	16.4	0.27	0.44	1	14	Broke −20, −21 igniters, −22 worked; nice flame, got down to extinction at pot 0.315 (finite low flow), very slow increments
7/3/2014 GMT 184	---------	55	P10	187m	6.35-mm black rod	−35	2	Opposed	48, 41	5, pots 0.4, 0.36, 0.32, 0.31, 0.30 extinguished	50	----	NA	NA	N	CL	A	−4	NA	----	F2	1,000	Cont	15	221	17	16.4	16.1	15.5	0.29	0.72	2	44	HCl 0.3 > 0.9, steady burn at multiple velocities, finite quench at pot 0.3
7/29/14 GMT 210	---------	104	P12	199m	9.525-mm black rod	−36	2	Opposed	60, 52, 48, 44.5, 42, 41.5, 41 (2.6, 1.6, 1.2, 0.75, 0.5, 0.4, 0.36, 0.34)	5, 3, 2, 1, 0.5, lower	250	----	NA	NA	N	CL	A	−3	NA	----	F2	1,000	Cont	3	273	17.5	16.8	16.4	15.7	0.29	0.95	2	57	Loss of signal before extinguished, oscillating at 0.36, out immediately at 0.34, multiple steady spread flows
7/14/14 GMT 195	14:30:00	85	P13a	203m	12.7-mm black rod	−37	2	Opposed	Fan pot 1.1 (5cm/s), 0.4, 0.36, 0.32, 0.3, 0.28, 0.26, 0 ext	5 down to extinction	50	----	NA	NA	N	CL	A	−3	NA	----	F2	1,000	Cont	14	255	20.7	19.1	19.8	18.2	0.36	1.63	38	450	Fan pot 1.1 (5 cm/s), 0.4, 0.36, 0.32, 0.3, 0.28, 0.26; flame out when pot turned to 0; HCL 0.5 > 4.1; flame reached front of sample and began to wrap around
7/14/14 GMT 195	16:04:00	86	P13b	203m	12.7-mm black rod	−37	2	Opposed	Fan pot 1.3 (5cm/s), 0.4, 0.36, 0.32 ext	5 down to extinction	50	----	NA	NA	N	CL	A	−3	NA	----	F2	1,000	Cont	10	94	20.6	20.2	19.7	19.3	0.41	0.62	5	72	Fan pot 1.3 (5 cm/s), 0.4, 0.36, 0.32; flame out when pot turned to 0.32
6/23/2014	---------	29	P14	189M	6.35-mm black rod	−22	2	Opposed	46, 41	5, low (0.85, 0.4, 0.32)	250	----	NA	NA	N	CL	A	−4	NA	----	F2	1,000	Cont	4	162	18.4	18.0	17.1	16.7	0.34	0.62	3	90	All blue, extinguished at 0.31
6/23/2014	---------	30	P15	190M	6.35-mm black rod	−22	2	Opposed	46, 41	5, (0.36)	250, 50	----	NA	NA	N	CL	A	−4	NA	----	F2	1,000	Cont	7	170	18.0	17.5	16.7	16.2	0.62	1.11	90	108	Nice stable burn with sooty tail but blue leading edge
7/22/14 GMT 203	---------	93	P16	191m	6.35-mm black rod	−36	2	Concurrent	49, 62, 44, 41.5, 41 (pots 1.3, 2.8, 0.7, 0.4, 0.36, 0.32)	5, 8, 2, low	250, 50	----	NA	NA	N	CL	A	−3	NA	----	F2	1,000	Cont	17	129	18.2	17.4	17.2	16.4	0.30	0.92	0	56	Extinguished at pot 0.32, one high flow setting
7/29/14 GMT 210	---------	105	P17	192m	6.35-mm rod	−36	2	Opposed	60, 52, 48, 233, 48, 41 (2.6, 1.6, 1.2, 10, 1.2, 0.36, 0.34)	5, 3, 2, 22, 2, low	250	----	NA	NA	N	CL	A	−3	NA	----	F2	1,000	Cont	6	186	16.8	16.5	15.7	15.4	0.95	1.34	57	68	A few finite flows, then tried blowoff without success, turned back down to 2 cm/s, then 0.36, 0.34 pots, oscillated and out at 0.34; leading edge receded slightly but did not blowoff
7/30/14 GMT 211	10:46:00	107	P18	193m	6.35-mm black rod	36	2	Opposed	55, 47, etc. (pot 1,2,1,2, etc.)	2, 0, 2, 0, etc.	250	Saturated	NA	NA	N	CL	A	−3	NA	----	F2	1,000	Cont	7	280	20.0	19.0	18.8	17.8	0.34	1.20	1	26	Alternated fan pot between 1 and 2 at 1-min intervals to try to get time constant resolution; finally turned pot down slowly, extinction at fan pot 0.32
7/22/14 GMT 203	---------	94	P19	194m	6.35-mm black rod	−36	2	Concurrent	49, 62, 44, 41.5, 122, 41 (pots 1.3, 2.8, 0.7, 0.4, 0.36, 10., 0.32)	5, 8, 2, maximum, 0	250, 50	----	NA	NA	N	CL	A	−3	NA	----	F2	1,000	Cont	2	279	17.5	16.7	16.5	15.7	0.90	1.61	54	94	Tried blowoff, did not blowoff at pot 10 2 restrictors, flame out at 0.32, sample mostly gone
6/16/2014	---------	26	P2	188M	6.35-mm black rod	−22	2	Opposed	-----------	5, 2.5, 2 (pot 0.9, 0.5, 0.35, 0.33)	250	Nearly saturated	NA	NA	N	CL	A	−4	NA	----	F2	1,000	Cont	7	303	17.4	17.2	16.4	16.2	0.44	0.66	14	26	Nice stable burn at low velocity, mostly blue with some inner soot at higher flow, stable flame at pot 0.33, did not get extinction on stills, but was just fan off, not slow ramp
7/30/14 GMT 211	15:22:22	109	P20	195m	6.35-mm black rod	36	2	Opposed	55, 47. etc. (pot 1, 2, 1, 2, etc.)	2, 0, 2, 0, etc.	50	----	NA	NA	N	CL	A	−3	NA	----	F2	1,000	Cont	2	311	19.0	18.2	17.9	17.1	0.34	1.05	2	78	Alternated fan pot between 1 and 2 at 1-min intervals to try to get time constant resolution; finally turned pot down slowly, extinction at fan pot 0.335
6/23/2014 GMT 174	---------	31	P21a	196M	6.35-mm black rod	−22	2	Opposed	46	5	250	----	NA	NA	N	CL	A	−4	NA	----	F2	1,000	Cont	9	57	16.3	16.3	15	15.0	0.96	1.00	86	94	Flame self-extinguished at 5 cm/s after sample end became flat, dim flame
6/23/2014	---------	32	P21b	196M	6.35-mm black rod	−22	2	Opposed	46	5	250	----	NA	NA	N	CL	A	−4	NA	----	F2	1,000	Cont	9	14	16.3	16.3	15	15.0	1.00	1.03	94	98	Igniter broke after third attempt to ignite flattened end of sample

[a]Greenwich Mean Time.
[b]Potentiometer (pot). Extinction (ext).
[c]Continuous high (CH). Continuous low (CL).
[d]Manual (M). Automatic (A).
[e]Exposure value (#EV).
[f]Number of frames and exposure increment (#F/1.0).
[g]Continuous (cont). Seconds (s).

TABLE A.3.—Concluded.

Actual date (for video display date, add 1 for Leap Year)[a]	Approximate start time and end time (video display time)	As-run test number	Test number	Sample number	Material	Igniter	Flow restrictor	Sample distance	Fan display[b]	Air display	Radiometer gain (1,000; 250; 50; and 10)	Radiometer display	Gaseous nitrogen (GN$_2$) potentiometer	GN$_2$ display	Filter (Y/N)	Release mode (CH/CL)[c]	Exposure mode (M/A)[d]	Exposure compensation (–#EV)[e]	Bracket frames and exposure bracket (#F/1.0)[f]	Shutter speed, s	F stop	ISO	Shutter hold (s/cont)[g]	Secure digital (SD) card serial number (S/N)	Total frames shot	Calibrated initial O$_2$ vol%	Calibrated final O$_2$ vol%	Initial O$_2$ vol%	Final O$_2$ vol%	Initial CO$_2$ vol%	Final CO$_2$ vol%	Initial CO, ppm	Final CO, ppm	Test observations and anomalies (ignited, spread, extinguished, burn time, color, etc.)[b]
7/8/2014 GMT 189	----------	68	P22a	200m	9.525-mm black rod	–35	2	Opposed	5, 0.36, 0.32 extinction after some time	5 down to extinction	250 > 50	----	NA	NA	N	CL	A	–3	NA	----	F2	1,000	Cont	6	83	20.8	0.6	20.2	----	0.32	----	4	----	Extinguished at higher flow, possibly rod not preheated enough by a bit, CO readings elevated, slow response
7/8/2014 GMT 189	----------	69	P22b	200m	9.525-mm black rod	–35	2	Opposed	5, 0.36, 0.34, 0.33, 0.32, 0.31, extinction	5 down to extinction	50	----	NA	NA	N	CL	A	–3	NA	----	F2	1,000	Cont	6	155	20.0	39.1	----	19.1	----	1.09	----	236	Extinguished at lower flow than P22a by a bit, longer slower decrease in flow, CO elevated, slow response
7/30/14 GMT 211	16:18:33	110	P23	201m	9.525-mm black rod	36	2	Opposed	55, 47, etc. (pot 1, 2, 1, 2, etc.)	2, 0, 2, 0, etc.	50	----	NA	NA	N	CL	A	–3	NA	----	F2	1,000	Cont	10	242	18.2	17.0	17.1	15.9	1.05	2.08	78	159	Alternated fan pot between 1 and 2 at 1-min then 2-min intervals to try to get time constant resolution; finally turned pot down slowly, extinction at fan pot 0.38
7/30/14 GMT 211	11:13:35	108	P24	819L	9.525-mm black rod	36	2	Opposed	55, 47, etc. (pot 1,2,1,2, etc.)	2, 0, 2, 0, etc.	250 > 50	----	NA	NA	N	CL	A	–3	NA	----	F2	1,000	Cont	4	308	19.0	17.5	17.8	16.3	1.20	2.24	26	260	Alternated fan pot between 1 and 2 at 1-min intervals to try to get time constant resolution; finally turned pot down slowly, extinction at fan pot 0.30
7/8/2014 GMT 189	----------	70	P25	217m	9.525-mm clear rod	–36	2	Opposed	5, 0.36, 0.34, 0.33, 0.32, 0.31, extinction	5 down to extinction	50	----	NA	NA	N	CL	A	–3	NA	----	F2	1,000	Cont	17	246	20.9	20.2	19.9	19.2	0.38	1.00	43	205	Reburn of 217m in opposed geometry, repeat of P22b, extinguished at same 0.31 pot, more sparklers from flame, and less leading edge vapor jetting, or more central jetting; rod warped downward in video view at end of test, asymmetrical instabilities noted briefly at pot change to 0.32, CO elevated, slow response
6/16/2014	----------	27	P3a	215M	6.35-mm clear rod	–22	2	Opposed	------------	5, 2.5 (1.15, 0.5, 0.35, 0.33. 0.32, 0.315, 0.31, 0.3)	250	----	NA	NA	N	CL	A	–4	NA	----	F2	1,000	Cont	8	304	17.7	17.4	16.6	16.3	0.27	0.51	33	----	Repeat of last test with clear rod; extinguished at 0.3 pot very small flame, but steady spread
6/16/2014	----------	28	P3b	215M	6.35-mm clear rod	–22	2	Opposed	------------	5, very low spread, 0.31 spread, etc. (0.85, 0.32, 0.31, 0.305, 0.30, 0.295)	250	----	NA	NA	N	CL	A	–4	NA	----	F2	1,000	Cont	9	303	17.4	16.8	16.3	15.7	0.51	failed	33	79	Very low velocity test to get limiting spread rate, pot 0.32 spread, 0.31 spread, etc.; power failed to camera?; fan still running; camera power cable needed repair and taping to camera body to make it work
7/3/2014 GMT 184	----------	54	P4	197m	9.525-mm black rod	–35	2	Opposed	48, 41	5, 0.4, 0.36, 0.32, 0.308, .3, off	50	----	NA	NA	N	CL	A	–4	NA	----	F2	1,000	Cont	4	297	18.5	17.1	17.6	16.2	0.62	1.8	64	493	HCl 0.9 > 1.8, long slow burn, steady at multiple pots until turned off flow
7/14/14 GMT 195	13:18:00	83	P5	202m	12.7-mm black rod	–37	2	Opposed	Fan pot 1.5 (5cm/s), 0.9, 0.4, 0.36, 0.32, 0.308, 0.3, 0.29, 0.28, 0, extinction	5 down to extinction	250 > 50	----	NA	NA	N	CL	A	–3	NA	----	F2	1,000	Cont	8	313	19.3	17.6	18.4	16.7	0.32	1.67	0	525	Fan pot 1.5 (5 cm/s), 0.9, 0.4, 0.36, 0.32, 0.308, 0.3, 0.29, 0.28 (flame persisted for all) finally turned down flow to 0 to extinguish; HCL 0 > 4.7; lots of fuel left behind, conical shape
7/3/2014 GMT 184	----------	53	P6	186m	6.35-mm black rod	–35	2	Opposed	48, 41	5, pots 0.4, 0.36, 0.32, 0.31, off	50	----	NA	NA	N	CL	A	–4	NA	----	F2	1,000	Cont	10	162	18.9	18.5	18	17.6	0.3	0.62	0	64	HCl 0 > 0.9, steady burning until turned flow off, multiple pot settings
7/3/2014 GMT 184	----------	56	P8	197m	9.525-mm black rod	–35	2	Opposed	48, 62, 75	5, would not stay lit, 10, 15 ibid	50	----	NA	NA	N	CL	A	–4	NA	----	F2	1,000	Cont	14	66	16.4	16.3	15.5	15.4	0.72	0.81	44	69	HCl 0.9 > 0.9, would not stay lit, tip of sample was flat
7/14/14 GMT 195	13:57:00	84	P9	202m	12.7-mm black rod	–37	2	Opposed	Fan pot 1.5 (5cm/s), 0.9, 0.4, 0.36, 0.32, 0.3, 0.28 extinction	5 down to extinction	50	----	NA	NA	N	CL	A	–3	NA	----	F2	1,000	Cont	15	148	17.6	17.1	16.7	16.2	1.67	2.10	525	535	Fan pot 1.5 (5 cm/s), 0.9, 0.4, 0.36, 0.32, 0.3, 0.28 flame out at 0.28; HCL 4.7 > 4.5; flame did not leave conical portion behind, rather fuel was consumed but final sample shape was very irregular

[a]Greenwich Mean Time.
[b]Potentiometer (pot).
[c]Continuous high (CH). Continuous low (CL). Shutter
[d]Manual (M). Automatic (A).
[e]Exposure value (#EV).
[f]Number of frames and exposure increment (#F/1.0).
[g]Continuous (cont). Seconds (s).

A.4   Miller Test Matrix

TABLE A.4.—MILLER TEST MATRIX

Actual date (for video display date, add 1 for Leap Year)[a]	Approximate start time and end time (video display time)	As-run test number	Test number	Sample number	Material[b]	Igniter	Flow restrictor	Sample distance	Fan display[c]	Air display	Radiometer gain (1,000; 250; 50; and 10)	Radiometer display	Gaseous nitrogen (GN₂) potentiometer	GN₂ display	Filter (Y/N)	Release mode (CH/CL)[d]	Exposure Mode (M/A)[e]	Exposure compensation (−#EV)[f]	Bracket frames and exposure bracket (#F/1.0)[g]	Shutter speed, s	F stop	ISO	Shutter hold (s/cont)[h]	Secure digital (SD) card serial number (S/N)	Total frames shot	Calibrated initial O_2 vol%	Calibrated final O_2 vol%	Initial O_2 vol%	Final O_2 vol%	Initial CO_2 vol%	Final CO_2 vol%	Initial CO, ppm	Final CO, ppm	Test observations and anomalies (ignited, spread, extinguished, burn time, color, etc.)[c]
2/20/14 GMT 2014-051	---------	15	M1	222	1-mm-thick PMMA, one-sided, 2 cm	Integral	2	Opposed	58, 54	10, 8	50	----------	8	NA	N	CL	A	−4	Off	----	F2	1,000	Cont	6	304	22.2	21.9	20.6	20.3	0.45	0.61	0	60	Prolonged ignition, flame initially on both sides, after igniter off and flame moved away from end, bottom flame died and top flame became all blue and small; very slow propagation; changed flow from 10 to 8 cm/s and flame shrank to a circle; spread just over 1/3 of sample when we ran out of camera card, and put flame out by turning off flow
7/23/14 GMT 204	17:38	97	M10	180m	4-mm-thick, 1-cm-wide PMMA slab	Integral	2	Opposed	75, 105, 94/91, 72/69, 63/61 (4.4, 8.0, 6.6/6.3, 4.0/3.7, 3/0/2.7)	10, 17, 14, 10, 8	250, 50, 250	----------	NA	NA	N	CL	A	−3	NA	----	F2	1,000	Cont	16	209	20.1	18.6	19	17.5	0.36	1.59	−1	536	Long burn, quick ignition, flame in seconds, kept it on 40 s + 2nd on for another 10 to 15 s when it was shrinking; multiple flows for steady spreading; flame big at 17, so only left it there 3 min; other flows longer; flame self-extinguished at 8 cm/s after almost 10 min; Alex saw it going out and locked shutter for the last few seconds; pictures start after ignition, about every 8 s
7/11/14 GMT 192	---------	80	M11	181m	1-cm-wide PMMA 5 mm thick	Integral	2	Opposed	3.9, 6.5, 4.6, 3.3, 2.9, 2.8; 62.5, 93, 77, 66, 63, 62	10, 20, 15, 12	250	----------	NA	NA	N	CL	A	−3	NA	----	F2	1,000	Cont	7	247	20.0	18.5	19.1	17.6	0.58	1.68	46	577	29-min burn; extinguished at 12 cm/s., HCl 0.5 > 5.0
7/31/14 GMT 212	14:35:20	114	M12	165m	2-mm-thick PMMA, 2 cm wide	Integral	1	Opposed	41, 42, 41	<1	250 > 50	----------	NA	NA	N	CL	A	−3	NA	----	F2	1,000	Cont	12	271	21.7	20.4	20.7	19.4	0.42	1.42	15	443	Vigorous ignition led to trying to get flame under control; finally had about plateaus at pot = 0.35, 0.4, and again 0.35
7/31/14 GMT 212	12:18:54	112	M13	169m	4-mm-thick PMMA, 2 cm wide	Integral	1	Opposed	52, 47, 43	6, 5, 4	250 > 50	----------	NA	NA	N	CL	A	−3	NA	----	F2	1,000	Cont	11	258	20.8	19.0	19.8	18.0	0.36	1.75	0	487	Mild ignition at 10 cm/s; decreased flow down holding constant for 6 min at pot settings of 1.7, 1.0, and 0.55; finally extinguished by turning pot down to 0.3
2/20/14 GMT 2014-051	---------	16	M14	223	2-mm-thick PMMA, one-sided, 2 cm wide	Integral	2	Opposed	Pot 2.4, 1.87 (54)	10, ~8	50	----------	?	NA	N	S	A	−4	Off	----	F2	1,000	Man	8	259	22.2	21.6	20.6	20.0	0.45	0.98	0	198	Prolonged ignition, followed by flow reduction after flame moved away from igniter region and spread steadily; flame self-extinguished at an air reading of 9 cm/s.
7/7/2014 GMT 188	---------	64	M15	225m	2-cm, 4-mm, one-sided PMMA slab	Integral	2	Opposed	Ignited 10, adjusted down then up to 20, down in increments to 15	10, 8, 7, 8, 10, 20, 18, 16, 15	10, 250	----------	NA	NA	N	CL	A	−3	NA	----	F2	1,000	Cont	7	153	21.0	20.0	20.1	19.1	0.37	1.10	1	220	Ignited and turned flow down to control flame size during end burning, then turned flow up to 20 cm/s and got steady spreading there, turned down flow to 15 and got spreading and slow extinction there.
7/23/14 GMT 204	00:25	99	M16	164m	1-mm-thick PMMA, 2 cm wide	Integral	2	Opposed	73, 57, 59, 48, 45, 43, 75 (4.2, 2.2, 2.4, 1.2, 0.8, 0.5, 4.4)	10, 6, 3, 2, 1, 10	250, 50, 250	----------	NA	NA	N	CL	A	−3	NA	----	F2	1,000	Cont	7	299	19.2	18.7	18.1	17.6	0.95	1.75	118	421	Burned at decreasing flow down to 1 cm/s or so, still fine, at end of sample, turned up flow to 10 cm/s and flame got really long; turned it down but Alex reported some soot on the door and some on the heat sink; dry wipe would not wipe off; try Monday with some other—water?
7/15/14 GMT 196	15:12:00	88	M17	166m	2-cm-wide PMMA, 2 mm thick	Integral	2	Opposed	Fan pot 3.7, 1.7, 1.5, 1.3, 0.8, 0.6, 0.5, 0.3 extinction	10, 5, 3, 0, extinction	250 > 50 > 250	----------	NA	NA	N	CL	A	−3	NA	----	F2	1,000	Cont	11	309	18.8	17.1	17.8	16.1	0.35	1.70	4	485	30-min burn targeted constant flows of 10, 5, and 3; finally turned fan pot to 0 to extinguish. HCl 0.3 > 3.7
7/15/14 GMT 196	12:40:00	87	M18	168m	2-cm-wide PMMA, 3 mm thick	Integral	2	Opposed	Fan pot 3.5, 5 (brief), 3.5, 2.2	10, 15 (brief), 10, 8	50 > 250	----------	NA	NA	N	CL	A	−3	NA	----	F2	1,000	Cont	6	178	17.9	16.8	16.9	15.8	0.32	1.31	0	335	26-min burn; flow briefly at 15 cm/s but flame was too strong so turned down; HCl 0 > 3.1, extinguished 8 cm/s

[a]Greenwich Mean Time.
[b]Polymethylmethacrylate (PMMA).
[c]Potentiometer (pot).
[d]Continuous high (CH). Continuous low (CL). Shutter
[e]Manual (M). Automatic (A).
[f]Exposure value (#EV).
[g]Number of frames and exposure increment (#F/1.0).
[h]Continuous (cont). Seconds (s).

TABLE A.4.—Concluded.

Actual date (for video display date, add 1 for Leap Year)[a]	Approximate start time and end time (video display time)	As-run test number	Test number	Sample number	Material[b]	Igniter	Flow restrictor	Sample distance	Fan display[c]	Air display	Radiometer gain (1,000; 250; 50; and 10)	Radiometer display	Gaseous nitrogen (GN2) potentiometer	GN2 display	Filter (Y/N)	Release mode (CH/CL)[d]	Exposure Mode (M/A)[e]	Exposure compensation (–#EV)[f]	Bracket frames and exposure bracket (#F/1.0)[g]	Shutter speed, s	F stop	ISO	Shutter hold (s/cont)[h]	Secure digital (SD) card serial number (S/N)	Total frames shot	Calibrated initial O2, vol%	Calibrated final O2, vol%	Initial O2, vol%	Final O2, vol%	Initial CO2, vol%	Final CO2, vol%	Initial CO, ppm	Final CO, ppm	Test observations and anomalies (ignited, spread, extinguished, burn time, color, etc.)[c]
7/23/14 GMT 204	23:37	98	M19	170m	4-mm-thick, 2-cm, two-sided PMMA slab	Integral	2	Opposed	75, 105, 94, 75, 77, 79, 59, 61, 57, 55, 53 (4.4, 8.0, 6.6, 4.4, 4.6, 4.8, 2.5, 2.7, 2.2, 2.0, 1.8)	10, 17, 14, 10, 7, 5	250, 50, 250	----------	NA	NA	N	CL	A	–3	NA	----	F2	1,000	Cont	8	201	19.0	17.4	17.9	16.3	0.35	1.60	3	357	Burned with decreasing flows until it went out on its own at 5 cm/s
2/20/14 GMT 2014-051	--------	17	M2	224	3-mm-thick PMMA one-sided, 2 cm wide	Integral	0	Opposed		20, 15, 13	50	----------	?	NA	N	S	A	–4	Off	----	F2	1,000	Man	9	262	22.2	21.2	20.6	19.6	0.46	1.33	12	325	Ignite at 20 cm/s, turn down to 15 cm/s after spread away from igniter; seemed steady, so turned down to 13 cm/s; flame got very dim, so increased flow to 14 cm/s, but it self-extinguished
8/1/14 GMT 213	11:10:50	116	M20	172m	5-mm-thick PMMA, 2 cm wide	Integral	1	Opposed	67, 58	10, 8	50	0.4 > 1.2 > 0.8	NA	NA	N	CL	A	–3	NA	----	F2	1,000	Cont	9	168	18.0	17.4	17.1	16.5	0.30	0.75	0	157	Flame took some time to establish, initially only on bottom of fuel; ignition at 10 cm/s (left 8 min) then flow down to 8 cm/s (flame out after 3 more minutes)
7/11/14 GMT 192	--------	82	M3	226m	2-cm-wide, 5-mm-thick, one-sided PMMA	Integral	2	Opposed	3.0, 3.1, 3.2, 6.4, 5.5, 5.4	10, 20, 18	250 > 50 > 250	----------	NA	NA	N	CL	A	–3	NA	----	F2	1,000	Cont	16	-----	20.8	19.7	19.9	18.8	0.33	1.18	11	300	Extinguished at 18 cm/s; HCl 0.6 > 2.6
7/31/14 GMT 212	13:59:12	113	M4	171m	5-mm-thick PMMA, 2 cm wide	Integral	1	Opposed	52, 47, 43	5, 4, 3	250 > 50	----------	NA	NA	N	CL	A	–3	NA	----	F2	1,000	Cont	16	262	21.8	19.8	20.7	18.7	0.42	2.15	2	561	Mild ignition at 10 cm/s; decreased flow down holding constant for 6 min at pot settings of 1.7, 1.0, and 0.55; finally extinguished by turning pot down to 0.3
2/20/14 GMT 2014-051	--------	18	M5	167	3-mm-thick PMMA, two-sided, 2 cm thick	Integral	0	Opposed		20, 13, 10, 8, 5	50	----------	?	NA	N	S	A	–4	Off	----	F2	1,000	Man	10, 14	300+ +102	22.2	19.0	20.6	17.4	0.44	3.22	9	>500	Rick ignited while we were loss of signal and out of contact with ISS, unfortunately; ignition was ~3 min per his verbal call down when we came back; flame already burning ~1/3 of sample, both sides, long and sooty; more vapor jetting on bottom due to molten ball attached there, visible when lights on to change camera card; turned down to 10 cm/s, then further down in increments to 5 cm/s; extinguished at 5 cm/s after prolonged flashing; during soot cleaning, Rick noticed damage to front door corner by the switches; He sent pictures down for us to evaluate for damage; CO reading posttest was off-scale; came back during purge reading 500
7/31/14 GMT 212	11:12:57	111	M6	163m	1-mm-thick PMMA, 2 cm wide	Integral	1	Opposed	68, 52, 47, 43, 42, 41	10, 5, 3, 0	250	Saturated at start	NA	NA	N	CL	A	–3	NA	----	F2	1,000	Cont	17	269	21.8	20.7	20.8	19.7	0.38	1.27	1	345	Aggressive ignition led to large flame initially; once flame settled down, we kept flow low and had two flow plateaus (pot 0.4 and 0.36); when flame reached end of sample it started backing up and spreading along the edges.
7/11/14 GMT 192	--------	81	M7	177m	1-cm-wide PMMA, 1 mm thick	Integral	2	Opposed	2.6, 1.3, 0.8, 0.7, 0.6, 0.5; 60, 49, 45, 44, 43, 42	10, 6, 5, 4.5, 4, 3	250	----------	NA	NA	N	CL	A	–3	NA	----	F2	1,000	Cont	12	-----	18.9	18.4	18	17.5	1.42	1.84	398	612	18 min burn; burned entire sample; HCl 2.2 > 3.9
7/11/14 GMT 192	---------	79	M8	178m	1-cm-wide PMMA, 2 mm thick	Integral	2	Opposed	3.3, 1.6, 1.0, decrease	10, 5 > 7, 5 decrease	50 > 250	----------	NA	NA	N	CL	A	–3	NA	----	F2	1,000	Cont	5	292	19.1	18.2	18.2	17.3	0.44	1.28	52	467	25-min burn; turned down flow to extinguish, went out at pot 0.4; HCl 0.4 > 4.6
7/11/14 GMT 192	---------	78	M9	179m	1-cm-wide PMMA, 3 mm thick	Integral	2	Opposed	3.3, 4.8; 66, 79	10, 14	50, 250	----------	NA	NA	N	CL	A	–3	NA	----	F2	1,000	Cont	2	156	18.0	17.6	17.1	16.7	0.26	0.54	0	191	Ignited at 10 cm/s, photographs every 5 s or so, turned up flow when flame looked weak; died after 15 min at 14 cm/s; 17-min burn; HCl 0 > 1.7

[a]Greenwich Mean Time.
[b]Polymethylmethacrylate (PMMA).
[c]Potentiometer (pot).
[d]Continuous high (CH). Continuous low (CL).
[e]Manual (M). Automatic (A).
[f]Exposure value (#EV).
[g]Number of frames and exposure increment (#F/1.0).
[h]Continuous (cont). Seconds (s).

A.5 Olson Test Matrix

Actual date (for video display date, add 1 for Leap Year)[a]	Approximate start time and end time (video display time)	As-run test number.	Test number	Sample number	Material[b]	Igniter	Flow restrictor	Sample distance	Fan display[c]	Air display	Radiometer gain (1,000; 250; 50; and 10)	Radiometer display	Gaseous nitrogen (GN₂) potentiometer	GN₂ display	Filter (Y/N)	Release mode (CH/CL)[d]	Exposure Mode (M/A)[e]	Exposure compensation (−#EV)[f]	Bracket frames and exposure bracket (#F/1.0)[g]	Shutter speed, s	F stop	ISO	Shutter hold (s/cont)[h]	Secure digital (SD) card serial number (S/N)	Total frames shot	Calibrated initial O_2, vol%	Calibrated final O_2, vol%	Initial O_2, vol%	Final O_2, vol%	Initial CO_2, vol%	Final CO_2, vol%	Initial CO, ppm	Final CO, ppm	Test observations and anomalies (ignited, spread, extinguished, burn time, color, etc.)[c]
2/18/2014 GMT 2014-049	16:20-	5	O1	207	6.35-mm clear rod	0020-23	2	?	89, 62, 50, 41	20, 10, 5, 2, 1	50	----	8	NA	N	CH	A	−5	9F 1.0	---	F4	1,600	7s	3	62	22.2	21.7	20.6	20.1	0.44	0.85	-1	51	Bracket test with decreasing flows; very sooty long flame at high flows; rod very thinned out and was wobbling due to vapor jetting later in test; Rick broke it off holder during readjustments
7/22/14 GMT 203	13:26	95	O10	210m	6.35-mm clear rod	−31	2	Concurrent	49, 44, 41, 122 (1.3, 0.7, 0.4, 0.36, 0.32, 10)	5, 2, 0, maximum	250	----	NA	NA	N	CL	A	−3	NA	---	F2	1,000	Cont	6	172	16.7	16.1	15.7	15.1	1.61	2.10	94	287	Leading edge (LE) blew out at fan 81, 25 s for rest of flame to blowoff at maximum flow
7/8/2014 GMT 189	--------	65	O11	184m	6.35-mm black rod	−32	2	Stagnation	Ignition, 5, 0.36, 0.32, 0.31, 0.305, blowoff 6.0	5, down then blowoff	250	----	NA	NA	N	CL	A	−3	NA	---	F2	1,000	Cont	11	271	15.4	14.8	14.5	13.9	0.27	0.72	2	290	Repeat of clear rod O8b test, to compare black versus clear for stagnation flame, blowoff at pot of 6.0, fan slightly higher than O8b, HCl 2.8
7/8/2014 GMT 189	--------	67	O12	217m	9.525-mm clear rod	−32	2	Stagnation	pots 1.4, 3, 0.9, 0.7	No ignition at any flow	250	----	NA	NA	N	CL	A	−3	NA	---	F2	1,000	Cont	6	52	13.6	13.5	12.7	12.6	1.72	1.71	+OR	+OR	No sustained flame at any flow, flame with igniter but died immediately upon igniter removal, HCL 12.3
7/21/14 GMT 202	17:22	91	O13a	221m	12.7-mm clear PMMA rod	−29	2	Concurrent	1.3, 0.7, 0.45, 0.36, 0.32, 0.31	49, 44, 42, 41, 41, 40.5 (5, 2, 0)	250	----	NA	NA	N	CL	A	−3	NA	---	F2	1,000	Cont	4	199	15.9	14.6	14.9	13.6	0.91	1.85	389	950	Ignited and burned at 5 pot settings, flame self-extinguished after 3+ min at pot 0.31
7/21/14 GMT 202	17:57	92	O13b	221m	12.7-mm clear PMMA rod	−29	2	Concurrent	1.3, 0.9	7, 4? (49, ?)	250	----	NA	NA	N	CL	A	−3	NA	---	F2	1,000	Cont	17	6	14.6	14.4	13.6	13.4	1.85	2.09	950	Over	Only stayed lit at 0.9 for less than a minute
8/1/14 GMT 213	16:18:00	117	O14	183m	6.35-mm black rod	39	1	Concurrent	52 and down	5 down to extinction	250	----	NA	NA	N	CL	A	−3	NA	---	F2	1,000	Cont	8	279	16.3	15.3	15.3	14.3	0.29	0.86	4	352	Ignition at 5 cm/s then slow pot decreases to quenching pot 0.28
7/28/2014 GMT 209	11:36 msg	100	O15a	218m	9.525-mm clear rod	−31	2	Stagnation	57.5, 47, 42, 41 (2.3, 1.0, 0.5, 0.35, 0.32)	5,0	250	----	NA	NA	N	CL	A	−3	NA	---	F2	1,000	Cont	15	124	17.1	16.7	16	15.6	0.27	0.62	0	176	Decrease flow to extinction at 0.32 pot, from 0.35 pot. 1.5 min at 5 cm/s; 2.5 min pot 1.0; 3.5 min at 0.5; 3.5 min 0.35; slow turn down to 0.32, flame out fairly quickly
7/28/2014 GMT 209	11:59:30 msg	101	O15b	218m	9.525-mm clear rod	−31	2	Stagnation	57.5, 42, 41, 40 (2.3, 0.5, 0.35, 0.34, 0.33, 0.32, 0.31, 0.30, 0.29, 0.28, 0.27)	5, 0	250	----	NA	NA	N	CL	A	−3	NA	---	F2	1,000	Cont	9	316	16.7	15.6	15.6	14.5	0.62	1.63	176	751	Reburn of same rod as previous; decreased flow to extinction at 0.27 pot, much lower than previous; rod heatup effect? 1 min 5 cm/s; 3.5 min pot 0.5; 5 min 0.35; 4 min 0.34; 4 min 0.33; 3 min 0.32; 1 min 0.31; 1 min 0.3; 1 min 0.29; 1.5 min 0.28; 0.27 out
7/29/14 GMT 210	--------	106	O16	219m	9.525-mm clear rod	−31	2	Stagnation	60 (2.6)	5	250	----	NA	NA	N	CL	A	−3	NA	---	F2	1,000	Cont	7	10 postburn only	14.5	14.5	13.4	13.4	0.27	0.32	2	33	Brief flame at end of first ignition, but no joy on sustained flame
7/22/14 GMT 203	--------	96	O17	211m	6.35-mm clear rod	−31	2	Concurrent	49, 46.5, 44, 42,41,72, decrease (1.3, 1.0, 0.7, 0.5, 0.4, 4.0, decrease)	3, 0, 11	250	----	NA	NA	N	CL	A	−3	NA	---	F2	1,000	Cont	12	174	15.1	14.3	14.1	13.3	0.31	0.90	2	377	Stable burns at slightly higher flows, LE blowoff at fan 72 and turned down flow but flame did not recover and extinguished even after flow was down to 43-44
7/28/2014 GMT 209	11:05	102	O18	212m	6.35-mm clear rod	−31	2	Stagnation	57, 51, 47, 72, 51, 72, 51, 47 (2.3, 1.5, 1.0, 4.0, 1.5, 4.0, 1.5, 1.0)	5, 2, 0, 11, 2, 11, 2, 0	250	----	NA	NA	N	CL	A	−3	NA	---	F2	1,000	Cont	5	176	15.2	14.5	14.1	13.4	1.45	1.94	523	816	Got rod hot, blue flame, turned flow up to pot 4.0, stag region blew out, Alex turned down quickly to 1.5 and got it to restabilize; we repeated it but it would not restabilize second time and flame extinguished after multiple oscillations at pot 1.0, after 1.5 would not restabilize
8/1/14 GMT 213	16:49:00	118	O19	213m	6.35-mm clear rod	39	1	Concurrent	52 and down	5 down to extinction	250	----	NA	NA	N	CL	A	−3	NA	---	F2	1,000	Cont	15	266	15.3	14.6	14.3	13.6	0.86	1.51	352	686	Ignition at 5 cm/s then slow pot decreases to quenching pot 0.288
2/18/14 GMT2014-049	--------	6	O2	204	6.35-mm clear rod	0020-23	2	?	0.54 pot and 0.45 pot	0	50	----	8	NA	N	CL	A	−4	Off	---	F4	1,600	Cont	3	287	22.2	21.9	20.6	20.3	0.44	0.59	−1	23	Ignited at 2 cm/s, and got dim flame that got sooty with lots of vapor jetting, reduced flow to 1.5 pot and got less vapor jetting test; still sooty at these low flows

TABLE A.5.—Concluded.

Actual date (for video display date, add 1 for Leap Year)[a]	Approximate start time and end time (video display time)	As-run test number.	Test number	Sample number	Material[b]	Igniter	Flow restrictor	Sample distance	Fan display[c]	Air display	Radiometer gain (1,000; 250; 50; and 10)	Radiometer display	Gaseous nitrogen (GN₂) potentiometer	GN₂ display	Filter (Y/N)	Release mode (CH/CL)[d]	Exposure Mode (M/A)[e]	Exposure compensation (–#EV)[f]	Bracket frames and exposure bracket (#F/1.0)[g]	Shutter speed, s	F stop	ISO	Shutter hold (s/cont)[h]	Secure digital (SD) card serial number (S/N)	Total frames shot	Calibrated initial O₂, vol%	Calibrated final O₂, vol%	Initial O₂, vol%	Final O₂, vol%	Initial CO₂, vol%	Final CO₂, vol%	Initial CO, ppm	Final CO, ppm	Test observations and anomalies (ignited, spread, extinguished, burn time, color, etc.)[c]
6/13/2014 GMT 164	--------	23	O3a	205M	6.35-mm clear rod	–23	2	Concurrent	------------	5, 3	1,000	----	8	NA	N	CL	A	–4	NA	---	F2	1,000	Cont	9	85	18.0	18.0	15.9	15.9	0.25	0.28	16	22	Flame extinguished as soon as he turned flow down, probably overshot, flame sooty at 5 cm/s
	--------	24	O3b	205M	6.35-mm clear rod	–23	2	Concurrent	------------	5, 3, 2, 1, low	1,000 and 250	----	NA	NA	N	CL	A	–4	NA	---	F2	1,000	Cont	9	306	18.0	17.7	15.9	15.6	0.28	0.53	22	116	Flame sooty even at lower flows, didn't get blue until air reading was zero
7/8/2014 GMT 189	--------	66	O4	216m	9.525-mm clear rod	–32	2	Stagnation	5, 0.7, 0.5, 0.4, 0.36 extinction	5 down to extinction	250	----	NA	NA	N	CH	A	–3	NA	---	F2	1,000	Cont	13	249	14.8	13.6	13.9	12.7	0.72	1.72	290	+OR	Larger rod, decreased flow, extinguished at 0.36, HCl 9.7
7/21/14 GMT 202	15:59	89	O5a	220m	12.7-mm clear pmma rod	–41, –42, –30	2	Concurrent	1.3, 2.7, 1.3, 0.7, 0.45, 4.0	5, 10, 5, 2, 0 (49, 62, 49, 44, 42)	250	----	NA	NA	N	CL	A	–3	NA	---	F2	1,000	Cont	13	164	15.1	14.2	14.1	13.2	0.25	1.05	-2	496	Hard to ignite, broke two igniters, burned for 9 min then blew out with pot of 4.0, tried to stay lit but blew off after multiple oscillations.
7/21/14 GMT 202	17:02	90	O5b	220m	12.7-mm clear pmma rod	–30	2	Concurrent	1.3	49, 5 cm/s	250	----	NA	NA	N	CL	A	–3	NA	---	F2	1,000	Cont	4	2	14.2	14.1	13.2	13.1	1.05	1.14	496	590	Would not sustain a flame without igniter on, broke igniter again
6/26/2014	--------	37	O6	206M	6.35-mm clear rod	–24	2	Stagnation	5, 0.36, 0.32, 0.31, 0.305, out 0.275	See fan	250	----	NA	NA	N	CL	A	–4	NA	---	F2	1,000	Cont	2	241	16.7	16.0	15.8	15.1	0.32	0.74	1	232	-------------------------------------
6/26/2014	--------	38	O7	214m	6.35-mm clear rod	–24	2	Stagnation	5, 0.36, 0.32, 0.305, blowoff fan max 10	------------	250	----	NA	NA	N	CL	A	–4	NA	---	F2	1,000	Cont	14	254	16.0	15.5	15.1	14.6	0.74	1.27	232	512	Blowoff fan 97, HCl post 4.9
6/26/2014	--------	39	O8a	208m	6.35-mm clear rod	–24	2	Stagnation	5, 0.36, 0.32, 0.31, extinguished	------------	250	----	NA	NA	N	CL	A	–4	NA	---	F2	1,000	Cont	15	133	15.7	15.3	14.8	14.4	1.23	1.44	436	536	Quench at pot 0.31, HCL 4.8 to 5.9
6/26/2014	--------	40	O8b	208m	6.35-mm clear rod	–24	2	Stagnation	5, 0.36, 0.32, 0.31 blowoff fan pot 6.0	------------	250	----	NA	NA	N	CL	A	–4	NA	---	F2	1,000	Cont	17	152	15.5	15.2	14.4	14.1	1.44	1.74	536	660	Blowoff fan 78, HCl prepost 5.9 to 7.9
6/26/2014	--------	41	O9	209m	6.35-mm clear rod	–24	2	Stagnation	5, 0.36, 0.32 blowoff pot 4.0	------------	250	----	NA	NA	N	CL	A	–4	NA	---	F2	1,000	Cont	13	154	15.0	14.8	14.1	13.9	1.74	1.96	660	794	Blowoff fan 68, HCl 7.5 to 9.3

[a]Greenwich Mean Time.
[b]Polymethylmethacrylate (PMMA).
[c]Potentiometer (pot). Maximum (max).
[d]Continuous high (CH). Continuous low (CL). Shutter
[e]Manual (M). Automatic (A).
[f]Exposure value (#EV).
[g]Number of frames and exposure increment (#F/1.0).
[h]Continuous (cont). Seconds (s).

A.6 T'ien Test Matrix

TABLE A.6.—T'IEN TEST MATRIX

Actual date (for video display date, add 1 for Leap Year)[a]	Approximate start time and end time (video display time)	As-run test number	Test number	Sample number	Material[b]	Igniter	Flow restrictor	Sample distance	Fan display[c]	Air display	Radiometer gain (1,000; 250; 50; and 10)	Radiometer display	Gaseous nitrogen (GN2) potentiometer	GN2 display	Filter (Y/N)	Release mode (CH/CL)[d]	Exposure mode (M/A)[e]	Exposure compensation (-#EV)[f]	Bracket frames and exposure bracket (#F/1.0)[g]	Shutter speed, s	F stop	ISO	Shutter hold (s/cont)[h]	Secure digital (SD) card serial number (S/N)	Total frames shot	Calibrated initial O2, vol%	Calibrated final O2, vol%	Initial O2, vol%	Final O2, vol%	Initial CO2, vol%	Final CO2, vol%	Initial CO, ppm	Final CO, ppm	Test observations and anomalies (ignited, spread, extinguished, burn time, color, etc.)[c]
2/14/2014 GMT 2014-45	12:45:40 to 12:47:10	1	T1	128	SIBAL 2 cm	Integrated	2	1	80	10	50	0.97 maximum	10	0	N	CL	M	NA	NA	1/8	F2	1,000	100 s	2	85	18.5	18.5	17.3	17.3	0.35	0.41	0	40	Compound Specific Analyzer-Combustion Products (CSA-CP) unit 1024; Carbon Dioxide Monitor (CDM) unit 1018; Prefill O2 reading = 20.9 percent; GN2 fill was from video display time 10:53 to 12:31 at maximum GN2 flow rate (pot = 10); Video display time is currently 1 day plus 6 min 10 s ahead of actual GMT; flow velocity held constant
6/24/2018	----------	34	T10	134M	2 cm SIBAL	Integral	2	Concurrent	Pot 1.1	5	250	---------	NA	NA	N	CL	M	NA	NA	----	F2	1,000	Cont	6	43	16.4	16.5	15.2	15.3	0.31	0.33	9	14	Brief ignition but flame extinguished before spreading beyond igniter
6/27/2014	----------	42	T11	135m	2 cm SIBAL	Integral	2	Concurrent	48	5	250	---------	NA	NA	N	CL	M	NA	NA	----	F2	1,000	Cont	12	109	17.1	17.0	16.2	16.1	0.35	0.39	1	45	Burned completely, steady, HCl 0.3 to 0.9
6/27/14 GMT 178	----------	44	T12	136m	2 cm SIBAL	Integral	2	Concurrent	Pot 1.1	5	250	---------	NA	NA	N	CL	M	NA	NA	----	F2	1000	Cont	16	39	16.8	16.9	15.9	16.0	0.7	0.7	113	117	Extinguished quickly
4/10/2014 GMT 100	----------	21	T13	137	2 cm SIBAL	Integral	2	Concurrent		5,1	50	---------	8	NA	n	CL	M	NA	NA	1/8	F2	1,000	Cont	14	55	17.5	17.6	15.9	16.0	0.19	0.20	2	12	HCL 0.2 end, 0.1 start, no HCN, flame extinguished quickly after flow change.
6/27/14 GMT 178	----------	45	T14	140m	2 cm SIBAL	Integral	2	Concurrent		5, 3	250	---------	NA	NA	N	CL	M	NA	NA	----	F2	1,000	Cont	16	119	16.9	16.9	16	16.0	0.7	0.72	117	152	Extinguished as we reduced flow below 3 cm/s
2/14/2014 GMT 2014-45	15:48:35 to 15:49:12	4	T15	138	SIBAL 2 cm	Integrated	0	1	80, 122	9, 29	50	1.68 maximum	10	0	N	CL	M	NA	NA	1/8	F2	1,000	100 s	5	46	18.7	18.7	17.5	17.5	0.45	0.51	72	102	Initial air reading is 15, but Rick did not wait long enough for the anemometer to stabilize; actual airspeed is about 9 cm/s; no flow restrictors installed, but flow only maxed out to 29 cm/s; no blowoff attained
4/10/2014 GMT 100	----------	22	T16	139	2 cm SIBAL	Integral	2	Concurrent		5, 3	50	---------	8	NA	N	CL	M	NA	NA	1/8	F2	1,000	Cont	14	100	17.6	17.5	16.0	15.9	0.21	0.21	17	41	Initial HCl 0.2 final 0.5, no HCN, flame spread whole sample at 3 cm/s
6/27/14 GMT 178	----------	46	T17	142m	2 cm SIBAL	Integral	0	Concurrent		6, 53	250	---------	NA	NA	N	CL	M	NA	NA	----	F2	1,000	Cont	6	83	16.9	16.9	16	16.0	0.72	0.75	152	190	Tried to blowoff, but did not
6/24/2018	----------	35	T18	141M	2 cm SIBAL	Integral	2	Concurrent		5, 2	250	---------	NA	NA	N	CL	M	NA	NA	----	F2	1,000	Cont	5	49	17.4	17.4	16.2	16.2	0.36	0.38	2	22	Brief ignition but flame extinguished as it spread away from igniter, further than previous runs today
7/9/14 GMT 190	----------	71	T19	143m	1 cm SIBAL	Integral	2	Concurrent	68.5, pot 3.6	11	250	---------	NA	NA	N	CL	M	NA	NA	----	F2	1,000	Cont	9	73	17.2	17.2	16.3	16.3	0.29	0.31	1	20	Steady burn, HCL 0.3 > 0.6
2/14/2014 GMT 2014-45	13:08:58 to 13:10:35	2	T2	129	SIBAL 2 cm	Integrated	2	1	80, 59, 55	9, 5, 4	50	0.64 maximum	10	0	N	CL	M	NA	NA	1/8	F2	1,000	100 s	2	100	18.5	18.5	17.3	17.3	0.41	0.45	40	78	Flow velocity changed to 9 to 5 fairly early then very late in the burn changed to 4
7/9/14 GMT 190	----------	72	T20	144m	1 cm SIBAL	Integral	2	Concurrent	3.6, 0.9	11, 3	250	---------	NA	NA	N	CL	M	NA	NA	----	F2	1,000	Cont	9	117	17.2	17.2	16.3	16.3	0.31	0.31	20	34	Quick extinction when we turned air down to 3 cm/s, HCl 0.8 end
7/9/14 GMT 190	----------	73	T21	145m	1 cm SIBAL	Integral	0	Concurrent	1.6 pot, 52	11, maximum (47)	250	---------	NA	NA	N	CL	M	NA	NA	----	F2	1,000	Cont	9	151	17.2	17.2	16.3	16.3	0.31	0.32	34	45	Successful blowoff! HCl still 0.8 end
7/9/14 GMT 190	----------	76	T22	146m	1 cm SIBAL	Integral	2	Concurrent	3.4, 1.7	10, 5	250	---------	NA	NA	N	CL	M	NA	NA	----	F2	1,000	Cont	4	38	17.1	17.0	16.2	16.1	0.59	0.62	140	162	Ignited at 11, turned down to 5 and extinguished, HCl 2.0
7/9/14 GMT 190	----------	74	T23	133m	2 cm SI, moved igniter	Integral	2	Concurrent	3.3, 66	10	250	---------	NA	NA	N	CL	M	NA	NA	----	F2	1,000	Cont	9	203	17.2	17.3	16.3	16.4	0.32	0.32	45	49	Did not ignite with moved igniter, HCl 0.8
7/9/14 GMT 190	----------	77	T24	133m	1 cm SIBAL, top side ign	–29	2	Concurrent	3.3, 66	10	250	---------	NA	NA	N	CL	M	NA	NA	----	F2	1,000	Cont	4	130	18.2	18.2	17.7	17.7	0.51	0.53	85	107	Ignited top of sample with retractable igniter and got steady spread of a one-sided flame

[a]Greenwich Mean Time.
[b]SIBAL is Solid Inflammability Boundary at Low Speeds.
[c]Potentiometer (pot).
[d]Continuous high (CH). Continuous low (CL). Shutter
[e]Manual (M). Automatic (A).
[f]Exposure value (#EV).
[g]Number of frames and exposure increment (#F/1.0).
[h]Continuous (cont). Seconds (s).

Actual date (for video display date, add 1 for Leap Year)[a]	Approximate start time and end time (video display time)	As-run test number	Test number	Sample number	Material[b]	Igniter	Flow restrictor	Sample distance	Fan display[c]	Air display	Radiometer gain (1,000; 250; 50; and 10)	Radiometer display	Gaseous nitrogen (GN2) potentiometer	GN2 display	Filter (Y/N)	Release mode (CH/CL)[d]	Exposure mode (M/A)[e]	Exposure compensation (-#EV)[f]	Bracket frames and exposure bracket (#F/1.0)[g]	Shutter speed, s	F stop	ISO	Shutter hold (s/cont)[h]	Secure digital (SD) card serial number (S/N)	Total frames shot	Calibrated initial O2, vol%	Calibrated final O2, vol%	Initial O2, vol%	Final O2, vol%	Initial CO2, vol%	Final CO2, vol%	Initial CO, ppm	Final CO, ppm	Test observations and anomalies (ignited, spread, extinguished, burn time, color, etc.)[c]
8/4/14 GMT 216	12:13:20	119	T25	138m	SIBAL 2 cm	39	1	Concurrent	53, 45	5, 2.5	250	---------	NA	NA	N	CL	M	NA	NA	1/8	F2	1,000	Cont	14	75	20.8	20.7	19.8	19.7	0.36	0.39	−1	17	Ignition at 5 cm/s then decrease to 2.5 cm/s and hold constant
8/4/14 GMT 216	12:28:44	120	T26	137m	SIBAL 2 cm	39	1	Concurrent	53, 45	5, 2.5	250	---------	NA	NA	N	CL	M	NA	NA	1/8	F2	1,000	Cont	14	87	20.8	20.7	19.8	19.7	0.36	0.43	−1	24	Ignition at 5 cm/s then decrease to 2.5 cm/s and hold constant
8/4/14 GMT 216	17:08:10	122	T27	146m	1 cm SIBAL	39	1	Concurrent	53, 45	5, 2	250	---------	NA	NA	N	CL	M	NA	NA	1/8	F2	1,000	Cont	5	58	20.7	20.6	19.8	19.7	0.41	0.42	−1	9	Ignition at 5 cm/s, then quickly to 2 cm/s (fan pot 0.7); fuel is burned out
8/4/14 GMT 216	17:21:03	123	T28a	144m	1 cm SIBAL	39	1	Concurrent	53	5	250	---------	NA	NA	N	CL	M	NA	NA	1/8	F2	1,000	Cont	5	19	20.7	0.9	19.8	------	0.41	------	−1	----	Tried to get one-sided ignition, but flame only briefly flashed then went out
8/4/14 GMT216	17:29:49	124	T28b	144m	1 cm SIBAL	39	1	Concurrent	53	5	250	--------	NA	NA	N	CL	M	NA	NA	1/8	F2	1,000	Cont	5	27	20.7	40.4	------	19.7	------	0.42	----	2	Tried to get one-sided ignition, but again flame only briefly flashed then went out
8/4/14 GMT 216	17:39:30	125	T29	145m	1 cm SIBAL	39	1	Concurrent	53, 43	5, 2(?)	250	--------	NA	NA	N	CL	M	NA	NA	1/8	F2	1,000	Cont	5	60	20.7	20.5	19.8	19.6	0.41	0.44	−1	10	Alex commented that he thought the angle of the igniter should be reversed to get one-sided ignition, so he tried that; one-sided flame initially but quickly became two-sided; after ignition, fan pot changed to 0.6 and flame went out after a few seconds
6/27/14 GMT 178	----------	43	T3	182m	4 cm spherical section	-24 broke, -25	2	Stagnation	63	10	250	--------	NA	NA	N	CL	A	−4	NA	1/4	F4	1,000	Cont	3, 8	166	17.2	16.8	16.3	15.9	0.42	0.7	45	113	Multiple ignition attempts on card 3, brief flames go out
2/14/2014 GMT 2014-45	15:20:15 to 15:21:15	3	T4	130	SIBAL 2 cm	Integrated	2	1	80, 46	9,1	50	0.19 maximum	10	0	N	CL	M	NA	NA	1/8	F2	1,000	100 s	5	97	18.7	18.7	17.5	17.5	0.44	0.45	59	72	O2 reading creeped up slightly after a long pause in operations; flow velocity changed immediately after ignition down to 1 (fan pot 0.9); extinguished after turning into flamelet
4/10/2014 GMT 100	14:27 to 14:29	19	T5	131	2 cm SIBAL	Integral	2	Concurrent	2.72, 0.50, 0.42	10, 2, 1	50	--------	8	NA	N	CL	M	NA	NA	1/8	F2	1,000	Cont	11	100	18.8	18.9	16.7	16.8	0.20	0.25	2	41	HCN 0 HCL 0.6; ignited at 10, turned down to 2, then 1, sample very small and dim, but seemed to burn full sample length as a flamelet
4/10/2014 GMT 100	14:51 to 15:53	20	T6	132	2 cm SIBAL	Integral	2	Concurrent		5, 2, 1, <1	50	---------	8	NA	N	CL	M	NA	NA	1/8	F2	1,000	Cont	11	117	18.8	18.8	16.7	16.7	0.24	0.28	39	77	HCL 0.9 at the end, still did not extinguish
7/9/14 GMT 190	----------	75	T7	182m	4 cm spherical section	-33, -34	2	Stagnation	3.4, 67	10, 5, 3, 1, decrease	250	---------	NA	NA	N	CL	A	−3	NA	----	F2	1,000	Cont	3	299	17.3	17.1	16.4	16.2	0.32	0.59	49	140	Broke one igniter quickly, took a while to ignite, turned pot down in series ignition at 3.4, 1.6, 1.0, 0.4, 0.36, 0.34, 0.32, 0.31, 0.30, 0.29, 0.285, 0.28 extinction finally, HCl 1.8
6/24/2018	----------	33	T9	133M	2 cm SIBAL	Integral	2	Concurrent	Pot 2.5	10	250	---------	NA	NA	N	CL	M	NA	NA	----	F2	1,000	Cont	6	48	16.4	16.4	15.2	15.2	0.30	0.31	0	9	Brief ignition but flame extinguished before spreading beyond igniter

[a]Greenwich Mean Time.
[b]SIBAL is Solid Inflammability Boundary at Low Speeds.
[c]Potentiometer (pot).
[d]Continuous high (CH). Continuous low (CL). Shutter
[e]Manual (M). Automatic (A).
[f]Exposure value (#EV).
[g]Number of frames and exposure increment (#F/1.0).
[h]Continuous (cont). Seconds (s).

Appendix B.—Microgravity Science Glovebox Work Volume Nitrogen Dilution Continuously Stirred Tank Reactor Model and On-Orbit Verification Testing of Model

B.1 Symbols

C_{in} concentration of O_2 entering work volume, $= 0$ (pure N_2)
C_o initial concentration of O_2 in the work volume
C_{out} concentration of O_2 exiting the work volume, $= c(t)$, a continuously stirred tank reactor (CSTR) property
$c(t)$ concentration of O_2 in the work volume as a function of time
r flow rate of gaseous N_2, 0.0005 m^3/min maximum, adjustable
T temperature
V volume of Microgravity Science Glovebox (MSG) working volume, 0.25 m^3

B.2 Information

The continuously stirred tank reactor (CSTR) model is based on a mole balance on O_2 as follows:

1. The control volume is the working volume, with an input of N_2 and a leak rate of well-mixed gas.
2. Boundary and conditions:
   a. Concentration of O_2 coming into the work volume $C_{in} = 0$ (pure N_2)
   b. $C_{out} = c(t)$ (CSTR property)
   c. Initial concentration of O_2 in the work volume $C(0) = C_o$

The rate of change of the O_2 concentration $c(t)$ with time t within the work volume V equation is given by the flow of gaseous N_2 (r) multiplied by the difference between the inlet (C_{in}) and outlet O_2 concentrations (C_{out})

$$\frac{dc}{dt}V = r(C_{in} - C_{out}) = -rC_{out} = -rc(t) \tag{B.1}$$

3. Integrating and applying initial conditions:

$$c(t) = C_o \exp\left(\frac{-r}{V}t\right) \tag{B.2}$$

Astronaut Chris Cassidy conducted a calibration test on the morning of GMT (Greenwich Mean Time) 2013-095 in the Microgravity Science Glovebox (MSG) using a Compound Specific Analyzer-Combustion Products (CSA-CP) sensor taking O_2 readings of the MSG working volume at intervals during the dilution. During dilution, the Burning and Suppression of Solids (BASS) duct fan was turned to maximum, and the working volume air circulation was deactivated. To validate the model, we used the following values in the model based upon the test conditions:

- MSG working volume (Ref. 1) $= 0.255$ m^3
- BASS–II hardware $= {\sim}0.005$ m^3
- Net volume $V = {\sim}0.25$ m^3

- N_2 flow rate in = 493 cm^3/min or 0.000493 m^3/min
- Initial O_2 concentration $c(0) = C_o$
- CSA-CP sensor $C(0) = 20.9$ percent O_2
- International Space Station Major Constituents Analyzer (MCA) = 21.48 percent O_2 (data available from NASA Johnson Space Center)

Figure B.1 shows the calibration data compared to the model predictions for both the CSA-CP readings and corrected for the offset from the MCA. The model agrees very well with CSA-CP readings directly and corrected for the offset to provide a calibrated O_2 level with time. The curvature is minimal due to the slow rate of N_2 flow into the large volume.

This model was used for subsequent BASS–II operations to determine the N_2 flow rate and flow time to achieve the desired test O_2 concentration based upon the initial O_2 concentration and operational crew time constraints. It worked very well, and postdilution CSA-CP readings agreed extremely well with the model predictions over a range of dilution rates, as shown in Figure B.2. The CSA-CP readings were then corrected for the offset from the MCA readings for that day to provide a calibrated O_2 reading for each test.
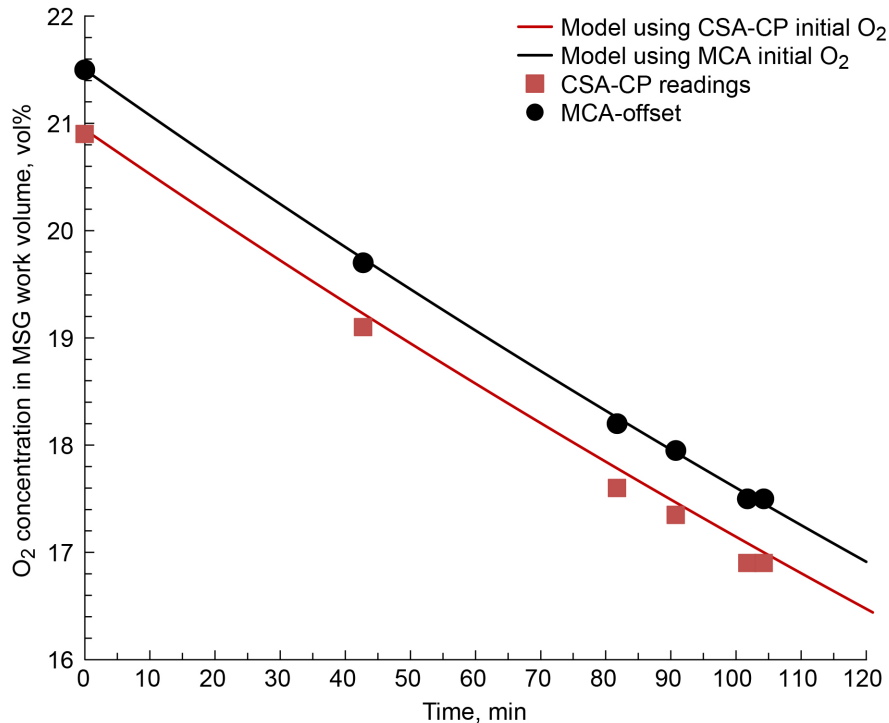

Figure B.1.—Model verification of continuously stirred tank reactor (CSTR) modeling the Microgravity Science Glovebox (MSG) dilution using Compound Specific Analyzer-Combustion Products (CSA-CP) sensor O_2 readings. Sensor data taken at intervals during dilution show how measurements agree with model curve (Eq. (B.2)). Data symbols are sized to ±0.1 percent O_2, resolution of sensor. Raw CSA-CP data and corrected data for Major Constituents Analyzer (MCA) offset are shown with model predictions using initial reading as starting value.
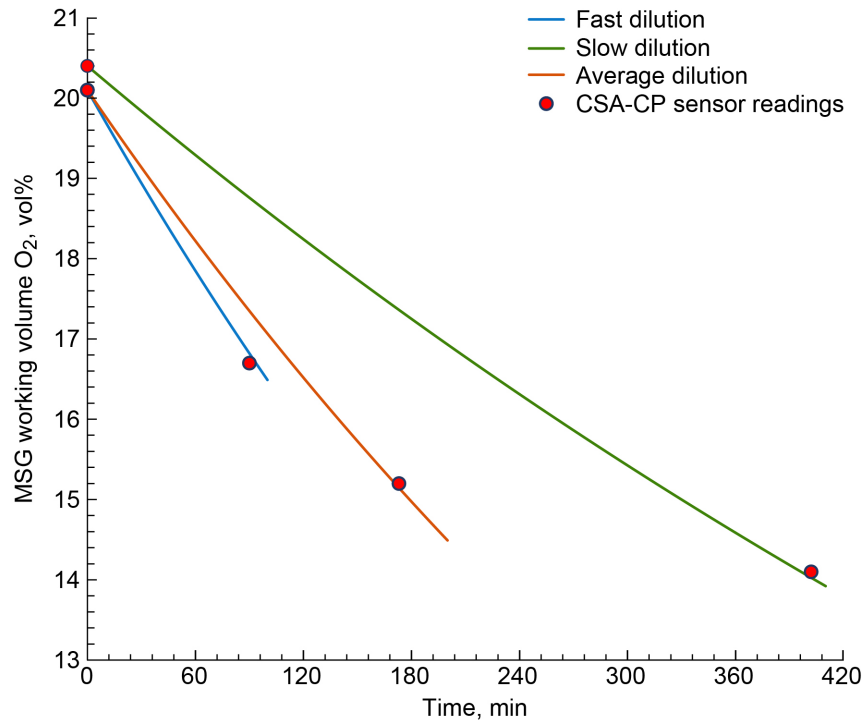
Figure B.2.—Dilution model compared to fast, slow, and average dilution rates during Burning and Suppression of Solids—II (BASS–II) operations. Data from three BASS–II tests and continuously stirred tank reactor (CSTR) model (Eq. (B.2)) results show range of dilution times and O_2 levels obtained. Control of both flow rate and dilution time allowed us to work around crew schedules while still obtaining desired working volume O_2 concentration for test. Compound Specific Analyzer-Combustion Products (CSA-CP).

B.3   References

1   Spivey, Reggie A., et al.: An Overview of the Microgravity Science Glovebox (MSG) Facility, and the Gravity-Dependent Phenomena Research Performed in the MSG on the International Space Station (ISS). AIAA 2008–812, 2008.

Appendix C.—List of Preflight, In-Flight, and Postflight Anomalies

1. An anomaly occurred on 2014 Greenwich Mean Time (GMT) 51, where the lower right corner of the Lexan door overheated and bubbled due to a flow leak at that spot during a very long burn. The damage affected the door interlock switches, as was found during inspection on GMT 58. A repair plan to recover switch functionality and seal the door leaks was implemented successfully on GMT 86 and 91, as shown in Figure C.1, and operations have continued since then without further door damage.

2. After the end of operations on GMT 167, the experiment video dropped out and was intermittent. Inspection on GMT 168 indicated it was the connector on the back of the camera, and a repair to the cable was successfully implemented on GMT 170, as shown in Figure C.2, that restored the experiment video. A backup plan to utilize a different camera was not required. For future operations, a new camera cable will be launched.

3. During operations on GMT 205, during a high-flow blowoff attempt with a flat polymethylmethacrylate sample, some flame briefly vapor-jetted out from the open sides of the sample holder toward the window before the flame was extinguished. The crew noted a soot spot that did not come off with a dry wipe. On the next operations day, GMT 209, prior to the start of operations, the crew used a wet wipe to remove the residue, and operations continued nominally without further incident.

Figure C.1.—Repaired duct door seal and interlocks, showing bubbled lower right corner.

Figure C.2.—Video cable repair and strain relief.

Appendix D.—Heat Release Rate and Hardware Temperature Rise Estimates for Burning and Suppression of Solids—II Thick Polymethylmethacrylate Slab Samples

D.1 Symbols

$\dot{Q}$ steady total heat release

$\dot{Q}_{air}$ kJ/min of energy carried out of the Burning and Suppression of Solids (BASS) flow duct

ρ density of air; 1.2 kg/m^3

c_p heat capacity of air 1 kJ/kg K

H duct height; 7.5 cm = 0.075 m

m mass

r_0 initial regression rate

r_{max} peak regression rate

t time

U flow velocity; 30 cm/s = 0.3 m/s = 18 m/min

W duct width; 7.5 cm = 0.075 m

ΔT change in temperature

D.2 Introduction

The principal investigator Sandra L. Olson wrote this report on January 10, 2014.

D.3 Purpose of the Analysis

Burning and Suppression of Solids—II (BASS–II) samples are larger than previously flown samples, and there is a concern that the hardware will become overheated and be damaged by the burning of these large samples. This analysis is to estimate the temperature rise of the BASS experiment assembly for a worst-case flame for this large thick sample. It should be noted that we have no plans to run a test like this.
Assumptions:

- The worst-case sample is the 0.5-cm-thick, 8.5-cm-long, and 2-cm-wide polymethylmethacrylate (PMMA) slab sample.
- The worst-case flame is a concurrent flame, which is expected to be larger than an opposed flame. Note that these samples are actually expected to be used only for opposed flow, but we do not want to restrict ourselves so assume the larger flame for these calculations.
- The worst-case flame is a two-sided burn, assumed to burn symmetrically.
- The sample will burn stoichiometrically.
- The flame will grow to reach a steady-state size.
- The ambient flow condition will be air at 30 cm/s, three times the highest flow in the test matrix for these samples, again, so that we are not restricted by the current test plan.
- The maximum burn time is the time it takes to burn the largest sample completely.
- The air leaving the flow duct is in equilibrium temperature with the exhaust hardware.
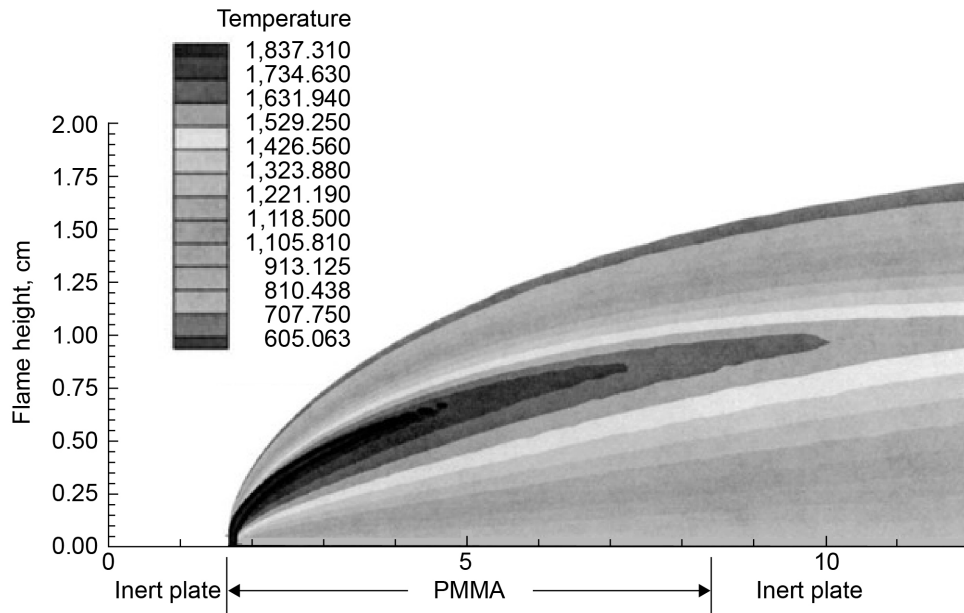
Figure D.1.—Predicted flame temperature profile for flame in forced flow velocity U of 60-cm/s flow, from Reference 1. Polymethylmethacrylate (PMMA).

D.4 Background

The basis for the burning rate estimates presented here are based on both a computational study looking at the burning rate distribution for boundary layer flow combustion of a PMMA plate in forced flow, shown in Figure D.1, (Ref. 1), and BASS test results from a 1-cm PMMA sphere burning in a stagnation flow (which captures the burning of the exposed base of the sample). A thick PMMA slab will take time to ignite and grow to a steady-state size, and the sample burning rate distribution is an important quantity to determine how much heat is being generated by the flame.

D.5 Analysis

As can be seen in Figure D.2, the base of the flame (at $x = 0$) has the highest burning rate and there is an exponential decay in the regression rate away from that peak burning rate. Using peak regression rate (r_{max}) for the four flow profiles given, we can extrapolate down to the 30-cm/s flow of interest.

The exposed base of the flame (the upstream most point) will be the strongest part of the flame, and the burning rate is expected to be a maximum there. Based on data in the Section D.7 from a 1-cm-sphere BASS test, we estimate the regression rate to be 3.05 mm/min, which is in keeping with the estimates from Figure D.2, as shown in Figure D.3. The downstream regression rates will decay exponentially from there, as shown in Figure D.2.
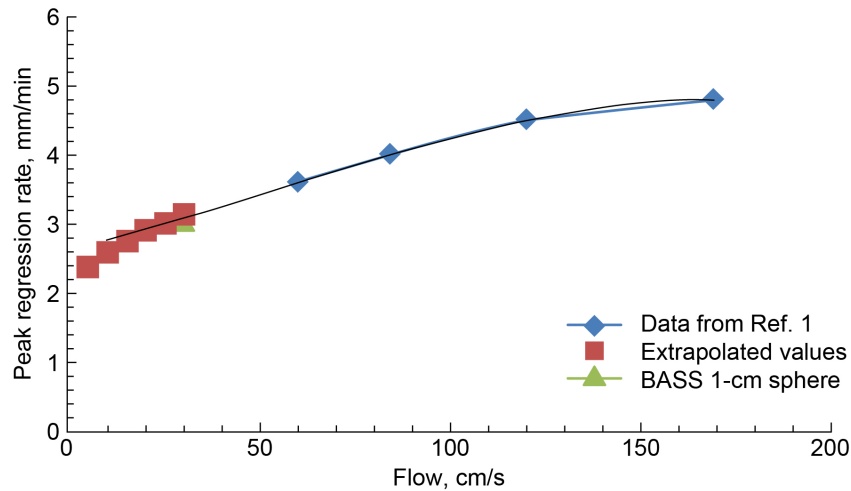
Figure D.2.—Peak regression rates from Figure D.2 curve fit with expected square root trend as flow is reduced (Ref. 2). Fit is used to calculate extrapolated points. At 30 cm/s, peak regression rate is estimated to be 3.13 mm/min.
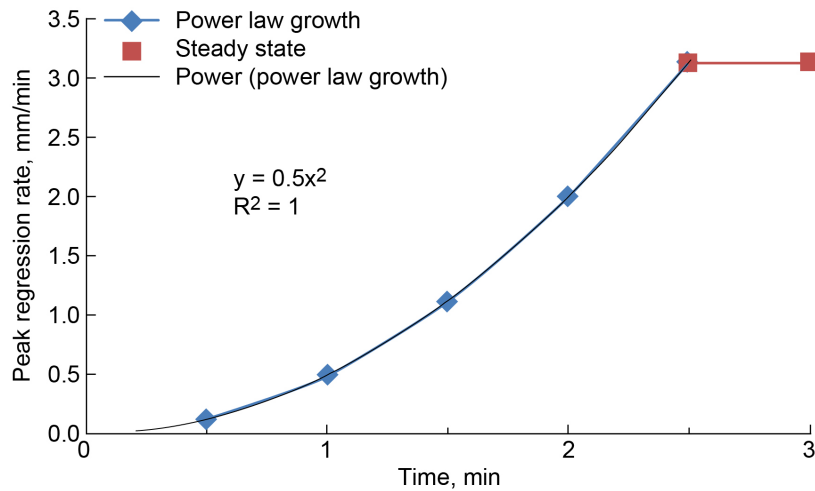

$y = 0.5x^2$
$R^2 = 1$

Figure D.3.—Power law growth pattern used to predict flame size as function of time.

The sample is 8.5 cm long, so at 3.05 mm/min, it will take ~28 min for the flame base to regress the entire length of the sample. Note that this is way beyond the still camera card limit of 7 min.

The flame will take some time to grow the steady-state size. To estimate the growth rate, we use an expected power law growth rate (Ref. 3) and estimate the flame will grow to a steady-state size in approximately 2.5 min, as shown in Figure D.3.

This growth rate is quite reasonable, since a previous BASS test showed that a PMMA slab sample took over 3 min to grow to steady size, as shown in the Section D.7. Using the experimental growth history and peak regression rates, we can estimate the regression rate profiles as a function of time.

These regression profiles (which occur on both sides of the sample) can then be used to determine how much fuel is being consumed each minute. We do this by adding up the regression at each x location (basically, the area under the curves) and also multiplying that value by the width of the sample (2 cm).

Note that these profiles are derived from steady slab burning where a significant fraction of the heat release is returned to the fuel for preheating or reradiated to the environment.
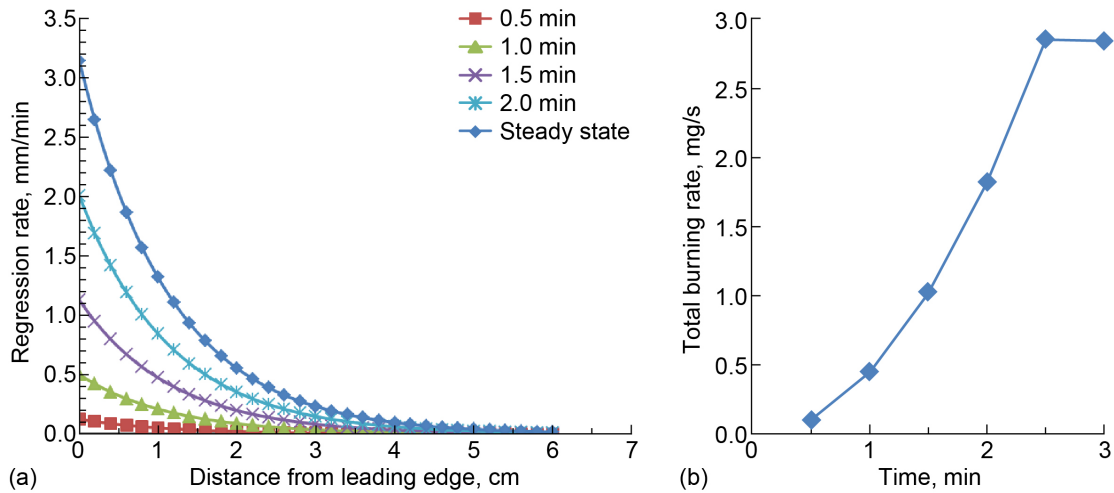
Figure D.4.—Estimated regression rate profiles at different times for 30-cm/s flame. Also shown, total burning rate with time during transient.

The total cubic mm of fuel per minute can then be converted to a heat release rate by assuming stoichiometric burning on both sides of the fuel, and an O_2 consumption calorimetry-based heat release rate of 13.1 kJ/g of O_2.

$$C_5H_8O_2 + 6\ O_2 \rightarrow 5\ CO_2 + 4\ H_2O$$
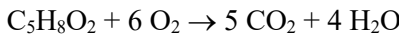
$$\frac{mm^3}{minimum\ side} \times \frac{2\ sides}{sample} \times \frac{gram\ fuel}{mm^3} \times \frac{gmol\ fuel}{gram\ fuel} \times \frac{stoichiometric\ gmol\ O_2}{stoichiometric\ gmol\ fuel}$$

$$\times \frac{gram\ O_2}{gmol\ O_2} \times \frac{13.1\ kJ}{gram\ O_2} \times \frac{1,000\ J}{kJ} = \dot{Q}_{comb}\left(\frac{J}{min}\right)$$

Values used:

- 1.19 g/cc fuel density (1.19 mg/mm^3)
- 100 g/gmol fuel
- 32 g/gmol O_2
- 6 gmol O_2/1 gmol fuel

The steady total heat release rate $\dot{Q}$ is 72 W based on these regression rates and properties. Ignition energy is estimated by using 4-A current through a 1-Ω igniter or 16 W. This heat is carried through the flow duct and out into the Microgravity Science Glovebox (MSG). The experiment housing will absorb some of this heat.

The rate at which the combustion energy is carried out of the hardware by the air can be calculated:

$$\frac{\dot{Q}_{air}}{\Delta T}\ \left(\frac{kJ}{min \cdot °C}\right) = \rho c_p UHW$$

where $\dot{Q}_{air}$ is the kJ/min of energy carried out of the BASS flow duct, ΔT is the temperature change, the density of air ρ is 1.2 kg/m^3, the heat capacity of air c_p is 1 kJ/kg K, the forced flow velocity U is 30 cm/s, 0.3 m/s, or 18 m/min, and the duct height H and width W is 7.5 cm or 0.075 m.

The air carries $\dot{Q}_{air}/\Delta T$ = 121.5 J/min Δ°C. The heat exchanger components the hot exhaust gas passes through can be found in Table D.1. These are connected to the main housing of the experiment assembly, which is about 1,580 g of aluminum, and more remotely, the total mass of the Experiment Assembly is 6.94 kg.

To determine the hardware temperature with time (t), we simply sum the mass (m) times the heat capacity (c_p) of each hardware component times a temperature change:

$$\dot{Q}t = \left[\left(\rho c_p UHW \right)_{air} + \sum mc_p \right] \Delta T_{exhaust}$$

where $\dot{Q}$ is the total heat release rate in watts and $T_{exhaust}$ is the temperature of the exhaust gas after passing through each component and solve for ΔT. This is shown in Figure D.5 for just the exhaust hardware, the main housing, and the total experiment assembly.

TABLE D.1.—HEAT EXCHANGER COMPONENTS

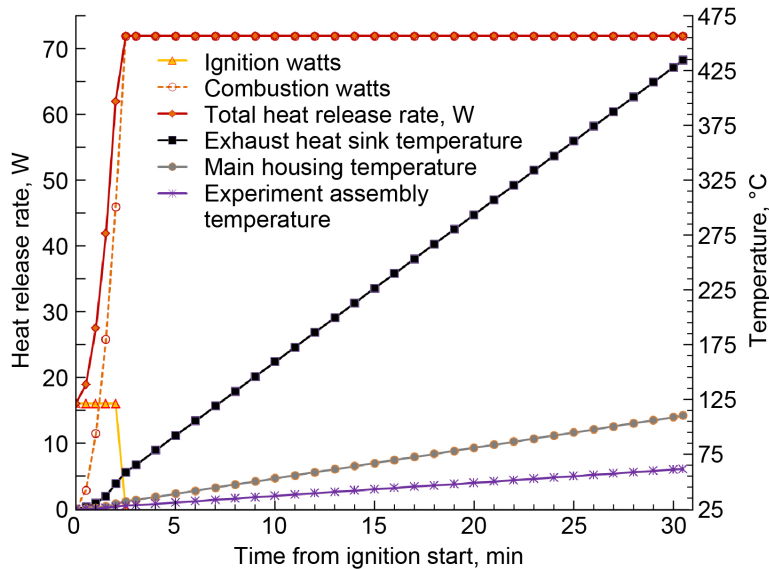| Hardware	Mass, g	Material	Heat capacity, kJ/kg°C	Melting temperature, °C
Heat sink	250	Copper	0.4	1,085
Soot housing	58	Aluminum	0.9	660
Soot cover	32	Aluminum	0.9	660
Screens	50	Bronze	0.4	950

Figure D.5.—Estimated heat release rate and associated temperature rise with time for various total mass quantities.

The maximum burn time is assumed to be the 2.5-min growth phase plus the 28-min sample regression phase, for a total of 30.5 min, as plotted in Figure D.5. The maximum temperatures reported in the following information are for this maximum burn time.

The heat release in the early phase is dominated by the ignition energy. Once the combustion heat release approaches steady state, the igniter is turned off and the flame is sustained.

The maximum temperature will occur in the exhaust hardware. This metal (primarily copper) hardware is built to take the hot combustion gases and cool via conduction to the other hardware. The maximum temperature if all of the combustion energy is only deposited in this heat sink under these worst-case assumptions, is 434 °C, which is below the melting point of the lowest melting material (aluminum at 660 °C) so this absolute worst-case maximum temperature will not cause damage to the hardware. This maximum temperature will not be realized in actuality because the heat will quickly dissipate to the main housing, which reaches a maximum temperature of 110 °C if all of the heat is distributed only there. The experiment assembly dissipates the heat further, and the maximum temperature of the entire experiment assembly is 62 °C.

During the 10-min cooldown for these thick samples, both the flow through the BASS duct and the MSG air circulation fans help dissipate the heat. The MSG air cooling loop has a 125-W capacity, which would dissipate the energy in 18 min, assuming no dissipation via conduction to the MSG hardware.

Based on this worst-case analysis, it is not expected that the hardware will suffer any damage from the worst-case, largest flames that could be achieved with the BASS–II samples.

D.6   References

1. Ananth, Ramagopal; Ndubizu, Chuka C.; and Tatem, P.A.: Burning Rate Distributions for Boundary Layer Flow Combustion of a PMMA Plate in Forced Flow. Combust. Flame, vol. 135, nos. 1–2, 2003, pp. 35–55.
2. Olson, S., et al.: Sounding Rocket Microgravity Experiments Elucidating Diffusive and Radiative Transport Effects on Flame Spread Over Thermally Thick Solids. Combust. Sci. Technol., vol. 176, 2004, pp. 557–584.
3. Olson, Sandra, et al.: Pressure Response in Enclosures During and After Large-Scale Flame Spread: Testing and Modeling. AIAA 2013–3412, 2013.
4. Olson, S.: Convective Heat Transfer Scaling of Ignition Delay and Burning Rate With Heat Flux and Stretch Rate in the Equivalent Low Stretch Apparatus. Fire Saf. Sci., vol. 10, 2011, pp. 959–970.

D.7   Appendix—Polymethylmethacrylate Growth to Steady Size

In Figure D.6, a one-sided PMMA slab was burned at a slow flow. The 1-cm-wide sample took 7.5 min for the total test time, with the ignition taking over 1 min. Flame reached steady size in about 3 min and was only 15 mm long. The spread rate was 0.037 mm/s (0.0037 cm/s or 2.2 mm/min).

The BASS 1-cm sphere had an initial mass of 617.5 mg. Sample 19 (1-cm PMMA sphere) was completely consumed in four tests (various high- and low-flow speeds) with the burn durations in Table D.2.

The total burn time was 5 min and 25 s (325 s). The average burning rate was 617.5/325 = 1.9 mg/s. Assume this occurs over the surface of the sphere where $A = 4\pi r^2 = 3.14 \times 0.5^2 \times 4 = 3.14$ cm^2. So, 1.9 mg/s ÷ 1.19 mg/mm^3 ÷ 314 mm^2 = 0.005 mm/s × 60 s/min = 0.3 mm/min. Note this is 0.0005 cm/s, which is equivalent to a stretch rate of 10 s^{-1}, a reasonable 0g level for burning rates for PMMA from (Ref. 4) as seen in Figure D.7.
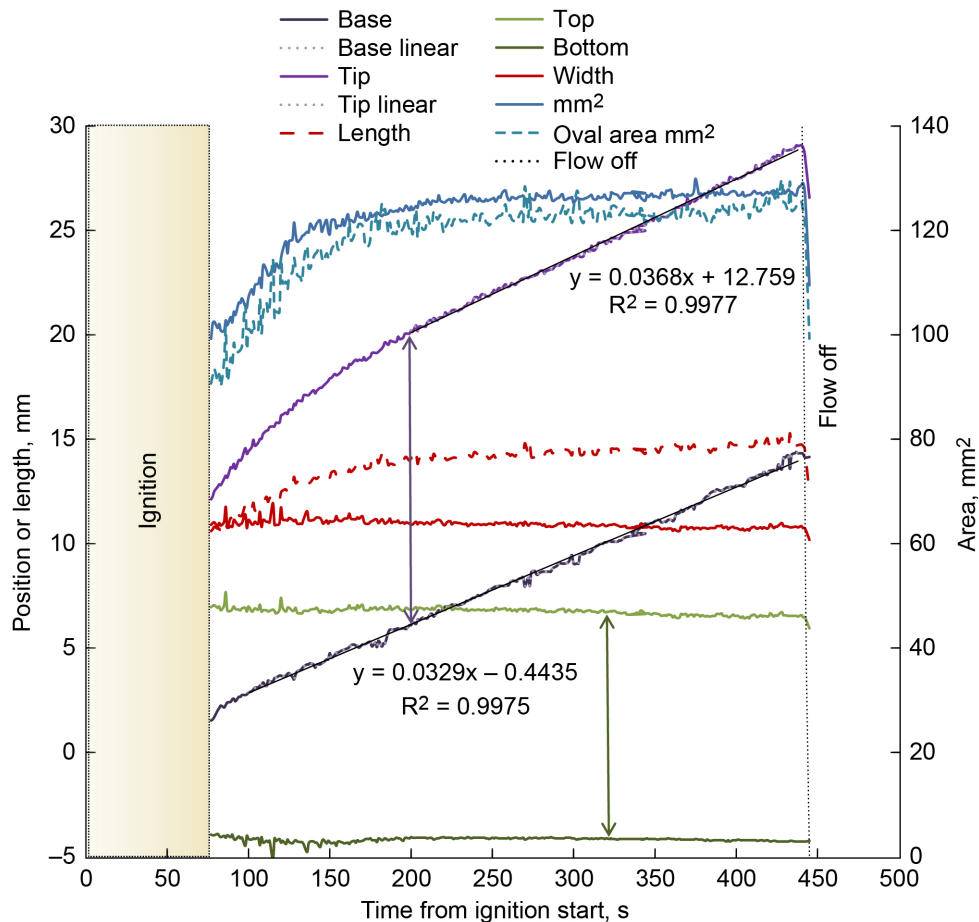

Figure D.6.—Burning and Suppression of Solids (BASS) one-sided polymethylmethacrylate (PMMA) slab burn at slower flow, 1-cm-wide sample.

TABLE D.2.—BURN DURATIONS

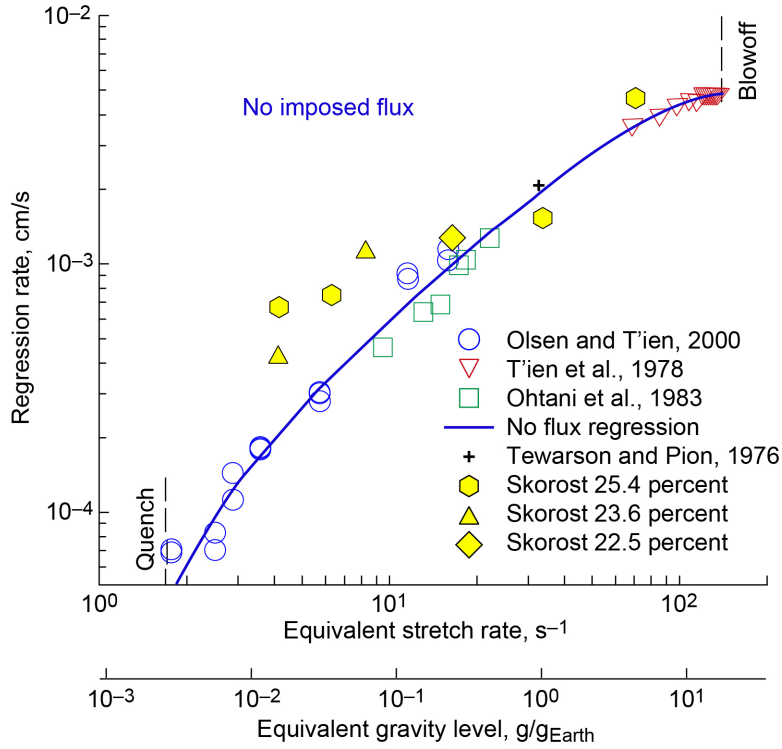| Test	Start	End	Total
18	14:45:25	14:47:05	00:01:40
19	10:37:40	10:38:30	00:00:50
20	10:55:25	10:56:40	00:01:15
21	11:17:35	11:19:05	00:01:40

Figure D.7.—Polymethylmethacrylate (PMMA) stagnation point burning rate data from Reference 4.

Appendix E.—Burning and Suppression Solids (BASS) and BASS–II Papers and Presentations

The following is a list of Burning and Suppression of Solids (BASS) and BASS–II papers and presentations, going from newest to oldest through summer 2020.

1. Thomsen, Maria, et al.: Buoyancy Effect on Downward Flame Spread Over PMMA Cylinders. Fire Technol., vol. 56, 2020, pp. 247–269.
2. Endo, Makoto, et al.: Flame Growth Around a Spherical Solid Fuel in Low Speed Forced Flow in Microgravity. Fire Technol., vol. 56, 2020, pp. 5–32.
3. Carmignani, L.; and Bhattacharjee, S.: Burn Angle and Its Implications on Flame Spread Rate, Mass Burning Rate, and Fuel Temperature for Downward Flame Spread Over Thin PMMA. Combust. Sci. Technol., vol. 192, no. 8, 2020, pp. 1617–1632.
4. Thomsen, Maria, et al.: Downward Burning of PMMA Cylinders: The Effect of Pressure and Oxygen. Proc. Comb. Inst., vol. 38, no. 3, 2020, pp. 4837–4844.
5. Carmignani, L.; Dong, K.; and Bhattacharjee, S.: Radiation From Flames in a Microgravity Environment: Experimental and Numerical Investigations. Fire Technol., vol. 56, 2020, pp. 33–47.
6. Hossain, Sarzina, et al.: Opposed Flow Flame Spread Over Thermally Thick Solid Fuels: Buoyant Flow Suppression, Stretch Rate Theory, and the Regressive Burning Regime. Combust. Flame, vol. 219, 2020, pp. 57–69.
7. Carmignani, Luca: Opposed-Flow Flame Spread Over Solid Fuels in Different Burning Regimes. Ph.D. Dissertation, Univ. of California San Diego, 2019.
8. Winter, Kelsey Gloria: Experimental Measurements of PMMA Combustion in Simulated Microgravity Along the Normoxic Curve. M.S. Thesis, San Diego State Univ., 2019.
9. Olson, Sandra L., et al.: Flammability Limits From BASS–II Testing in Microgravity Compared to Normal Gravity Limits. ICES–2019–101, 2019.
10. Thomsen, Maria, et al.: Opposed Flow Burning of PMMA Cylinders in Normoxic Atmospheres. Fire Saf. J., vol. 110, no. 102903, 2019.
11. Marcum, Jeremy W.; Ferkul, Paul V.; and Olson, Sandra L.: PMMA Rod Stagnation Region Flame Blowoff Limits at Various Radii, Oxygen Concentrations, and Mixed Stretch Rates. Proc. Comb. Inst., vol. 37, no. 3, 2019, pp. 4001–4008.
12. Olson, Sandra L.; Ferkul, Paul V.; and Marcum, Jeremy W.: High-Speed Video Analysis of Flame Oscillations Along a PMMA Rod After Stagnation Region Blowoff. Proc. Comb. Inst., vol. 37, no. 2, 2019, pp. 1555–1562.
13. Huang, Xinyan, et al.: Transition From Opposed Flame Spread to Fuel Regression and Blow Off: Effect of Flow, Atmosphere, and Microgravity. Proc. Comb. Inst., vol. 37, no. 3, 2019, pp. 4117–4126.
14. Hernández, N., et al.: Piloted Ignition Delay Times on Optically Thin PMMA Cylinders. Proc. Comb. Inst., vol. 37, no. 3, 2019, pp. 3993–4000.
15. Carmignani, Luca, et al.: Boundary Layer Effect on Opposed-Flow Flame Spread and Flame Length Over Thin Polymethyl-Methacrylate in Microgravity. Combust. Sci. Technol., vol. 190, no. 3, 2018, pp. 535–549.
16. Lage, Nicholas Alexander: Two Dimensional Heat Transfer in Non-Thermally Thin Poly(Methyl Methacrylate) During Combustion in a Narrow Channel Apparatus. M.S. Thesis, San Diego State Univ., 2018.

17. Chan, Ryan Lesley: Effect of Oxygen Concentration on Flame Spread Over Thin Fuels in Different Regimes: A Numerical Investigation. M.S. Thesis, San Diego State Univ., 2018.
18. Link, Shmuel, et al.: The Effect of Gravity on Flame Spread Over PMMA Cylinders. Sci. Rep., vol. 8, no. 120, 2018.
19. Carmignani, L.; Sato, S.; and Bhattacharjee, S.: Flame Spread Over Acrylic Cylinders in Microgravity: Effect of Surface Radiation on Flame Spread and Extinction. ICES–2018–311, 2018.
20. Johnston, Michael C.: Growth and Extinction Limits: Ground Based Testing of Solid Fuel Combustion in Low Stretch Conditions in Support of Space Flight Experiments. Ph.D. Dissertation, Case Western Reserve Univ., 2018.
21. Johnston, Michael C.; and T'ien, James S.: Gravimetric Measurement of Solid and Liquid Fuel Burning Rate Near and at the Low Oxygen Extinction Limit. Fire Saf. J., vol. 91, 2017, pp. 140–146.
22. Marcum, Jeremy; Olson, Sandra; and Ferkul, Paul: Mixed Convection Blowoff Limits as a Function of Oxygen Concentration and Upward Forced Stretch Rate for Burning PMMA Rods of Various Sizes. ICES–2017–370, 2017.
23. Olson, Sandra; and Ferkul, Paul V.: Microgravity Flammability Boundary for PMMA Rods in Axial Stagnation Flow: Experimental Results and Energy Balance Analyses. Combust. Flame, vol. 180, 2017, pp. 217–229.
24. Bhattacharjee, Subrata, et al.: Measurement of Instantaneous Flame Spread Rate Over Solid Fuels Using Image Analysis, Fire Saf. J., vol. 91, 2017, pp. 123–129.
25. Bhattacharjee, Subrata, et al.: Radiative, Thermal, and Kinetic Regimes of Opposed-Flow Flame Spread: A Comparison Between Experiment and Theory, Proc. Comb. Inst., vol. 36, no. 2, 2017, pp. 2963–2969.
26. Zhao, Xiaoyang, et al.: Concurrent Flame Growth, Spread, and Quenching Over Composite Fabric Samples in Low Speed Purely Forced Flow in Microgravity. Proc. Comb. Inst., vol. 36, no. 2, 2017, pp. 2971–2978.
27. Link, Shmuel, et al.: The Effect of Gravity on Flame Spread Over PMMA Cylinders in Opposed Flow With Variable Oxygen Concentration. ICES–2016–79, 2016.
28. Shah, Tirthesh Jayesh: Flame Spread Over Thick Polymethylmethacrylate Samples in a Simulated and Actual Microgravity Environment. M.S. Thesis, San Diego State Univ., 2016.
29. Pham, Thao; and Miller, Fletcher: A Narrow Channel Apparatus to Study Radiative Heat Loss of Solid Fuel in Microgravity Combustion. Poster presented at the 32nd Annual Meeting of the American Society for Gravitational and Space Research (ASGSR), Cleveland, OH, 2016.
30. Endo, Makoto: Numerical Modeling of Flame Spread Over Spherical Solid Fuel Under Low Speed Flow in Microgravity: Model Development and Comparison to Space Flight Experiments. Ph.D. Dissertation, Case Western Reserve Univ., 2016.
31. Marcum, Jeremy; Olson, Sandra; and Ferkul, Paul: BASS–II Microgravity Forced Flow Rod Blowoff Limits Compared to Normal Gravity Mixed Convective Blowoff Limits. Presented at the 32nd Annual Meeting of the American Society for Gravitational and Space Research (ASGSR), Cleveland, OH, 2016.
32. Endo, Makoto, et al.: Experimental Data Analysis and Numerical Modeling of Flame Spread on a PMMA Sphere in Microgravity. Presented at the 32nd Annual Meeting of the American Society for Gravitational and Space Research (ASGSR), Cleveland, OH, 2016.
33. Carmignani, Luca; and Bhattacharjee, Subrata: Flame Spread Over PMMA Samples and Blow-Off Extinction for Different Angles. Presented at the 32nd Annual Meeting of the American Society for Gravitational and Space Research (ASGSR), Cleveland, OH, 2016.

34. Miller, Fletcher, et al.: Experimental Measurements and Numerical Modeling of Solid Fuel Combustion in a Narrow Channel Apparatus to Simulate Microgravity. Presented at the 32nd Annual Meeting of the American Society for Gravitational and Space Research (ASGSR), Cleveland, OH, 2016.

35. Miller, Fletcher: Developing the Narrow Channel Apparatus for Material Flammability Tests in Normal Gravity: A Comparison to Data Obtained on ISS. Presented at the ISS R&D Conference, San Diego, CA, 2016.

36. Bhattacharjee, Subrata; Simsek, Aslihan; and Carmignani, Luca: Boundary Layer Effect on Opposed-Flow Flame Spread in the Microgravity Regime. ICES–2016–387, 2016.

37. Link, Scmuel, et al.: The Effect of Gravity on Flame Spread Over PMMA Cylinders in Opposed Flow With Variable Oxygen Concentration. ICES–2016–79, 2016.

38. Marcum, Jeremy W.; Olson, Sandra L.; and Ferkul, Paul V.: Correlation of Normal Gravity Mixed Convection Blowoff Limits With Microgravity Forced Flow Blowoff Limits. Presented at the 2016 Spring Technical Meeting Central States Section of the Combustion Institute, Knoxville, TN, 2016.

39. Chu, Yanyan; and Wichman, Indrek S.: Laminar Opposed Flow Flame Spread Over Degrading Combustible Materials. Presented at the 2016 Spring Technical Meeting Central States Section of the Combustion Institute, Knoxville, TN, 2016.

40. Wichman, Indrek S., et al.: Fire in Microgravity. Am. Sci., vol. 104, no. 1, 2016, pp. 44–51.

41. Bhattacharjee, S., et al.: The Critical Flow Velocity for Radiative Extinction in Opposed-Flow Flame Spread in a Microgravity Environment: A Comparison of Experimental, Computational, and Theoretical Results. Combust. Flame, vol. 163, 2016, pp. 472–477.

42. Bhattacharjee, S., et al.: Opposed-Flow Flame Spread: A Comparison of Microgravity and Normal Gravity Experiments to Establish the Thermal Regime. Fire Saf. J., vol. 79, 2016, pp. 111–118.

43. Olson, S.L.: Concurrent Flow Blowoff Boundary Extrapolation to Zero Stretch: A Proposed New Materials Flammability Test Method. Presented at the FLARE International Workshop, Sapporo Japan, 2016.

44. Shah, Tirthesh J.; Olson, Sandra L.; and Miller Fletcher J.: Modeling and Analysis of Intermediate Thickness PMMA Sheets in Microgravity Opposed Flow. Presented at the 31st ASGSR Annual Meeting, Alexandria, VA, 2015.

45. Olson, Sandra L.; Ferkul, Paul V.: Critical Damkohler Number Flammability Boundary Analysis for PMMA Cylinders Burning in Axial Forced Concurrent Flow. Presented at the 31st ASGSR Annual Meeting, Alexandria, VA, 2015.

46. Link, Shmuel, et al.: Downward Flame Spread Over PMMA Cylinders in Opposed Flow Under 1g and μg Conditions. Presented at the 31st ASGSR Annual Meeting, Alexandria, VA, 2015.

47. Bhattacharjee, Subrata: Opposed-Flow Flame Spread: A Comparison of Microgravity and Normal Gravity Experiments Establishing the Thermal Regime. Presented at the 31st ASGSR Annual Meeting, Alexandria, VA, 2015.

48. Bhattacharjee, Subrata, et al.: Opposed-Flow Flame Spread: A Comparison of Microgravity and Normal Gravity Experiments Establishing the Thermal Regime. Presented at the 31st ASGSR Annual Meeting, Alexandria, VA, 2015.

49. Shah, Tirthesh J., et al.: Modeling and Analysis of Intermediate Thickness PMMA Sheets Burning in Microgravity Opposed Flow. Presented at the Western States Section of the Combustion Institute—Fall 2015 Meeting, paper 134HC–0056, 2015.

50. Bhattacharjee, Subrata, et al.: Temperature and CO_2 Fields of a Downward Spreading Flame Over Thin Cellulose: A Comparison of Experimental and Computational Results. Proc. Combust. Inst., vol. 35, no. 3, 2015, pp. 2665–2672.

51. Bhattacharjee, Subrata, et al.: Experimental Validation of a Correlation Capturing the Boundary Layer Effect on Spread Rate in the Kinetic Regime of Opposed-Flow Flame Spread. Proc. Combust. Inst., vol. 35, no. 3, 2015, pp. 2631–2638.

52. Olson, Sandra L., et al.: Results From On-Board CSA–CP and CDM Sensor Readings During the Burning and Suppression of Solids—II (BASS–II) Experiment in the Microgravity Science Glovebox (MSG). ICES–2015–196, 2015.

53. Bhattacharjee, S., et al.: The Critical Flow Velocity for Radiative Extinction in Opposed-Flow Flame Spread in a Microgravity Environment: A Comparison of Experimental, Computational, and Theoretical Results. Presented at the 9th Mediterranean Combustion Symposium, Rhodes, Greece, 2015.

54. Olson, Sandra L.; and Ferkul, Paul V.: Microgravity Flammability of PMMA Rods in Concurrent Flow. Presented at the 9th U.S. National Combustion Meeting, Cincinnati, OH, 2015.

55. Zhao, Xiaoyang, et al.: Concurrent Flame Growth, Spread and Extinction Over Composite Fabric Samples in Low Speed Purely Forced Flow in Microgravity. Presented at the 9th U.S. National Combustion Meeting, Cincinnati, OH, 2015.

56. Bornand, Garrett; Shah, Tirthesh; and Miller, Fletcher: Experiments and Modeling of Flame Spread in a Narrow Channel Apparatus and on the International Space Station. Presented at the 9th Southern California Symposium on Flow Physics, San Diego, CA, 2015.

57. Hamdan, Ghaleb; and Miller, Fletcher: Computational Modeling of a Laminar Flow in a 2D Planar Couette Channel at Low Reynolds Numbers. Presented at the 9th Southern California Symposium on Flow Physics, San Diego, CA, 2015.

58. Olson, Sandra: Development of an ISS Experiment to Study Spacecraft Materials Flammability Evaluation Test Methods. Presented at the 30th Annual Meeting of the American Society for Gravitational and Space Research (ASGSR), Pasadena, CA, 2014.

59. Shah, Tirthesh, et al.: Model and Experiments of Burning Intermediate Thickness PMMA Sheets in Microgravity Opposed Flow. Presented at the 30th Annual Meeting of the American Society for Gravitational and Space Research (ASGSR), Pasadena, CA, 2014.

60. Bornand, Garrett, et al.: Using a Narrow Channel Apparatus to Study Thermally-Intermediate Fuel Combustion in a Simulated 0g Environment. Poster presented at the 30th Annual Meeting of the American Society for Gravitational and Space Research (ASGSR), Pasadena, CA, 2014.

61. Endo, M., et al.: Experiment and Modeling of Flame Spread on PMMA Sphere in Low-Speed Forced Flow in Microgravity. Presented at the 30th Annual Meeting of the American Society for Gravitational and Space Research (ASGSR), Pasadena, CA, 2014.

62. Link, S., et al.: Gravitational Effects on Flame Spread Rates for Clear and Black PMMA Cylinders in Opposed Flows. Presented at the 30th Annual Meeting of the American Society for Gravitational and Space Research (ASGSR), Pasadena, CA, 2014.

63. Bornand, Garrett; Sullivan, Greg; and Miller, Fletcher: Polymethylmethacrylate Combustion in a Simulated Microgravity Environment. Poster presented at the 35th International Symposium on Combustion, San Francisco, CA, 2014.

64. Bornand, Garrett; and Miller, Fletcher: Computational Modeling of Polymethylmethacrylate Combustion in a Narrow Channel Apparatus. Poster presented at the 35th International Symposium on Combustion, San Francisco, CA, 2014.

65. Bornand, Garrett R.; Sullivan, Greg J.; and Miller, Fletcher J.: Flame Spread Over Thermally Thick Polymethylmethacrylate in a Narrow Channel Apparatus. Paper 087EF–0034, Western States Section of the Combustion Institute Spring Meeting, Pasadena, CA, 2014.

66. Olson, S.L., et al.: Burning and Suppression of Solids—II Fire Safety Investigation for the Microgravity Science Glovebox. Presented at the 29th Annual Meeting of the American Society for Gravitational and Space Research (ASGSR) and the 5th International Symposium on Physical Sciences in Space (ISPS), Orlando, FL, 2013.

67. Takahashi, Fumiaki, et al.: Burning Characteristics of Paraffin and Japan Wax Candle Flames in a Low-Speed Oxidizing Stream in Microgravity. Presented at the 29th Annual Meeting of the American Society for Gravitational and Space Research (ASGSR) and the 5th International Symposium on Physical Sciences in Space (ISPS), Orlando, FL, 2013.

68. Ferkul, Paul V., et al.: Thickness and Fuel Preheating Effects on Material Flammability in Microgravity From the BASS Experiment. Presented at the 29th Annual Meeting of the American Society for Gravitational and Space Research (ASGSR) and the 5th International Symposium on Physical Sciences in Space (ISPS), Orlando, FL, 2013.

69. Bhattacharjee, Subrata, et al.: A Novel Apparatus for Flame Spread Study. Proc. Combust. Inst., vol. 34, no. 2, 2013, pp. 2513–2521.

70. Ferkul, P.V., et al.: Flammability Aspects of Fabric in Opposed and Concurrent Air Flow in Microgravity. Presented at the 8th U.S. National Combustion Meeting, Park City, UT, 2013.

71. Bornand, G.R., et al.: Opposed-Flow Flame Spread in a Narrow Channel Apparatus Over Thin PMMA Sheets. Presented at the 8th U.S. National Combustion Meeting, paper 070FR–0418, 2013.

72. Endo, M., et al.: A Numerical Simulation of Flame Growth and Decay Over a Spherical Solid in Microgravity. Presented at the 2012 Central States Section Spring Technical Meeting of the Combustion Institute, Dayton, OH, 2012.